1987

Picosecond excitation transport in disordered systems

David Edward Hart
Iowa State University

Order Number 8805080

Picosecond excitation transport in disordered systems

Hart, David Edward, Ph.D.

Iowa State University, 1987

U·M·I
300 N. Zeeb Rd.
Ann Arbor, MI 48106

PLEASE NOTE:

In all cases this material has been filmed in the best possible way from the available copy. Problems encountered with this document have been identified here with a check mark __✓__.

1. Glossy photographs or pages _____
2. Colored illustrations, paper or print _____
3. Photographs with dark background _____
4. Illustrations are poor copy _____
5. Pages with black marks, not original copy _____
6. Print shows through as there is text on both sides of page _____
7. Indistinct, broken or small print on several pages __✓__
8. Print exceeds margin requirements _____
9. Tightly bound copy with print lost in spine _____
10. Computer printout pages with indistinct print _____
11. Page(s) _____ lacking when material received, and not available from school or author.
12. Page(s) _____ seem to be missing in numbering only as text follows.
13. Two pages numbered _____. Text follows.
14. Curling and wrinkled pages _____
15. Dissertation contains pages with print at a slant, filmed as received __✓__
16. Other _____

_____

_____

Picosecond excitation transport in disordered systems

by

David Edward Hart

A Dissertation Submitted to the
Graduate Faculty in Partial Fulfillment of the
Requirements for the Degree of
DOCTOR OF PHILOSOPHY

Department: Chemistry
Major: Physical Chemistry

Approved:

Signature was redacted for privacy.

In Charge of Major Work

Signature was redacted for privacy.

For the Major Department

Signature was redacted for privacy.

For the Graduate College

Iowa State University
Ames, Iowa

1987

TABLE OF CONTENTS

CHAPTER I. INTRODUCTION

The nonradiative transfer of electronic energy between like or unlike molecules is a subject of considerable scientific and technical interest. Elucidation of the dynamics of energy transport would greatly enhance our understanding of numerous physical systems. The transport of energy between chlorophyll a molecules in the photosynthetic unit shows a considerably different time dependence than transport among chlorophyll a molecules at a comparable concentration in vitro [1]. The difference suggests a nonrandom structure to the assembly of chlorophyll a molecules in vivo. The details of this structure which may be ascertained from a comprehensive theory describing energy transport might eventually lead to a synthetic device used to harvest the energy of the sun. Also, the dependence of energy transport dynamics on the spatial separation and relative orientation of the energy donor and acceptor has prompted some to use it as a probe of polymer and micellar structure [2,3].

The theoretical considerations required to describe energy transport in the above systems [4,5] are necessarily more complex than those required for a system of chromophores randomly distributed and oriented in an effectively infinitely extending array such as a solution of dye molecules. It is important, therefore, that energy

transport in disordered systems is adequately understood so that the theory can be confidently extended to more complex systems. It is within this context that this work is presented. In order to evaluate the development of electronic excitation transport theory in disordered systems, a body of precise data from well characterized systems is needed. The experimental methods employed in this work represent significant progress in obtaining that data.

For a description of the energy transport phenomenon consider the assembly of molecules represented in Fig. 1.1. Two types of molecules are distributed randomly in space with their absorption dipoles randomly oriented relative to one another. When a donor molecule, represented by an oval, is electronically excited it can relax to the ground state via several pathways. Nonradiative relaxation can take place by internal conversion or intersystem crossing [6]; a fluorescence photon can be emitted; or, the energy can be transferred nonradiatively to another molecule. If the energy accepting molecule is another donor type (not necessarily an identical molecule), the same possibilities exist for energy dissipation as for the initially excited molecule. If, however, the energy is transferred to a trap molecule, represented by a rectangle, fluorescence and energy transfer are quenched and the excited trap relaxes through some nonradiative intramolecular process.

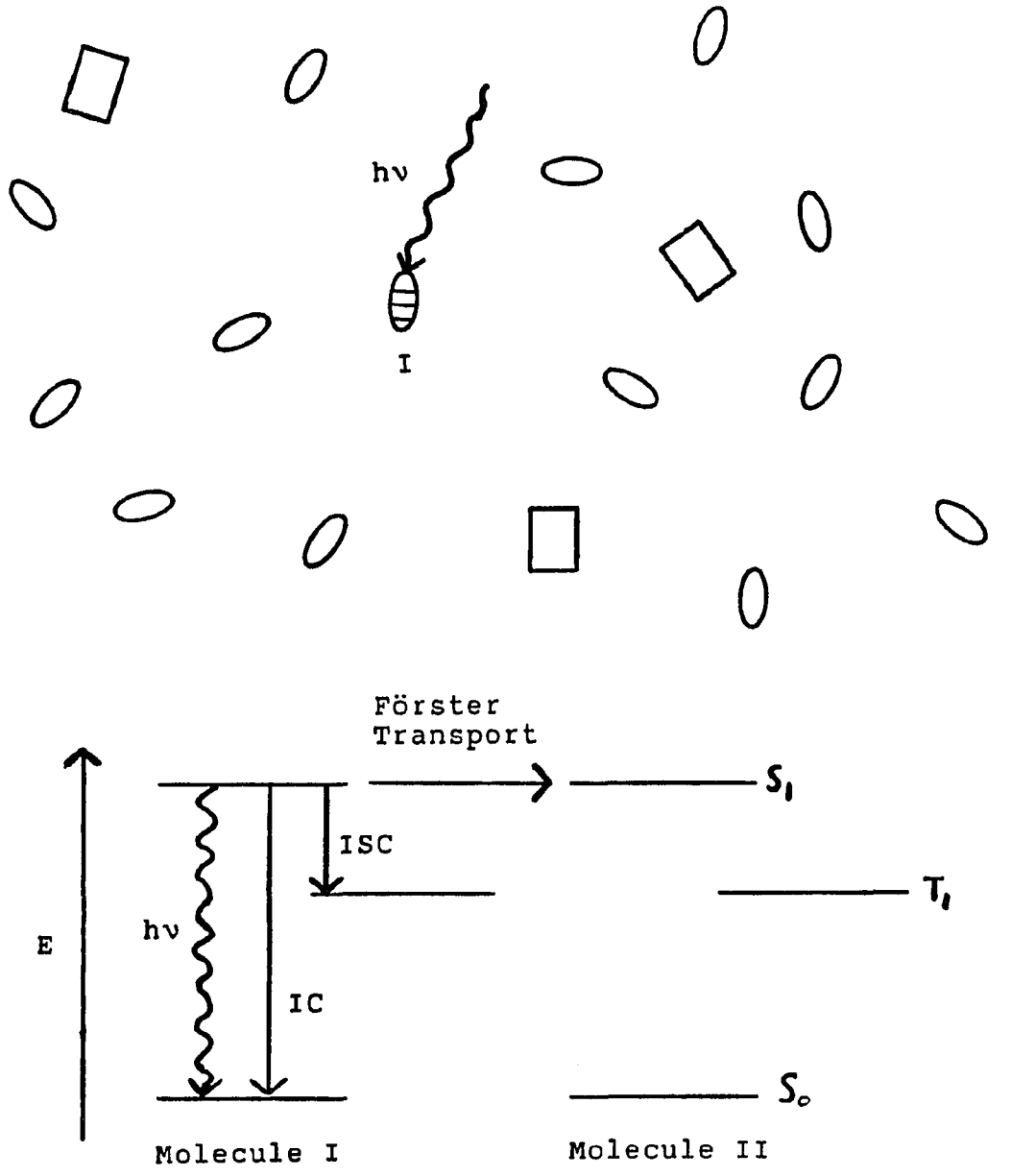

Figure 1.1 Energy transfer between randomly distributed and oriented dipoles. The ovals represent energy donors and the rectangles represent energy traps

Förster described the probability for energy transfer between a pair of molecules in terms of an allowed dipole-dipole transition [7,8]. The transfer rate from molecule j to k is

$$w_{jk} = \frac{3}{2\tau}\left[\frac{R_o}{r_{jk}}\right]^6 \left[\hat{d}_j\cdot\hat{d}_k - 3(\hat{d}_j\cdot\hat{r}_{jk})(\hat{d}_k\cdot\hat{r}_{jk})\right]^2 \qquad (1.1)$$

where

τ = fluorescence lifetime of the donor molecule in the absence of acceptor molecules,

r_{jk} = separation between the molecules,

$\hat{r}_{jk}$ = unit vector along the line joining the two molecules, and

$\hat{d}_j$ and $\hat{d}_k$ = unit vectors in the direction of the molecular transition dipole moments j and k, respectively.

R_o, the Förster critical transfer parameter, has units of length and is given by [9]

$$R_o^6 = \frac{9000\ln 10\ \Phi_D}{128\pi^5\eta^4 N}\int_o^\infty \frac{f_D(\bar{\nu})\ \varepsilon_D(\bar{\nu})}{\bar{\nu}}\, d(\bar{\nu}). \qquad (1.2)$$

R_o relates the probability for energy transfer to the overlap between the donor fluorescence spectrum $f_D(\bar{\nu})$, the acceptor absorption spectrum $\varepsilon_D(\bar{\nu})$, the quantum yield of donor fluorescence Φ_D, and the index of refraction of the solvent η. A wavenumber scale is used in Eq. 1.2 and $f_D(\bar{\nu})$

is normalized to unity. N is equal to Avogadro's number. Mechanisms for energy transfer based on other interactions [10] such as dipole-quadrupole, electron exchange effects, and electric dipole-magnetic dipole have been shown to have much smaller contributions to the energy transfer probability and may be considered in systems which do not have allowed dipole-dipole transitions.

Sensitized luminescence experiments provided the first experimental evidence of nonradiative energy transfer [8,10]. In this case, fluorescence from the acceptor is detected at some time after the initial donor excitation. The absorption spectrum of the acceptor does not overlap with the initial excitation energy and other energy transfer pathways such as molecular collisions and reabsorption of donor fluorescence have been eliminated leaving only energy transfer to excite the acceptor.

Much more difficult to distinguish is energy transfer between identical molecules [11,12]. No longer does the frequency of the emitted radiation discriminate between the acceptor ensemble and the initially excited donor ensemble as the source of the fluorescence. A probe for this type of energy transfer is the quenching of the polarization of the fluorescence from a sample initially excited with linearly polarized light.

The probability of exciting a molecule with polarized light decreases with the $\cos^2$ of the angle between the

molecular transition dipole moment and the electric field vector of the light. An anisotropic distribution of excited state dipoles is created initially with the preferred orientation of the dipoles being parallel to the direction of polarization of the exciting light.

This unequal distribution of excited state dipole directions is reflected in the relative intensities of the components of the sample fluorescence oriented parallel and perpendicular to the polarization of the exciting light. Two terms are in general use to describe the distribution of intensity between the parallel and perpendicular components of the fluorescence [13], the polarization,

$$P = \frac{I_{\parallel}(t) - I_{\perp}(t)}{I_{\parallel}(t) + I_{\perp}(t)} \tag{1.3}$$

and the anisotropy

$$r = \frac{I_{\parallel}(t) - I_{\perp}(t)}{I_{\parallel}(t) + 2I_{\perp}(t)} \tag{1.4}$$

The polarization defines the fraction of light which is linearly polarized along a single axis (Fig. 1.2). It is the ratio of the polarized component of the light to the total intensity along the axis. As such, the polarization is best suited to describe a light source directed along an axis. The anistropy is the ratio of the polarized component of the light to the total emitted intensity. Dipolar emission such as that from a fluorescing molecule is symmetrically distributed in directions perpendicular to the

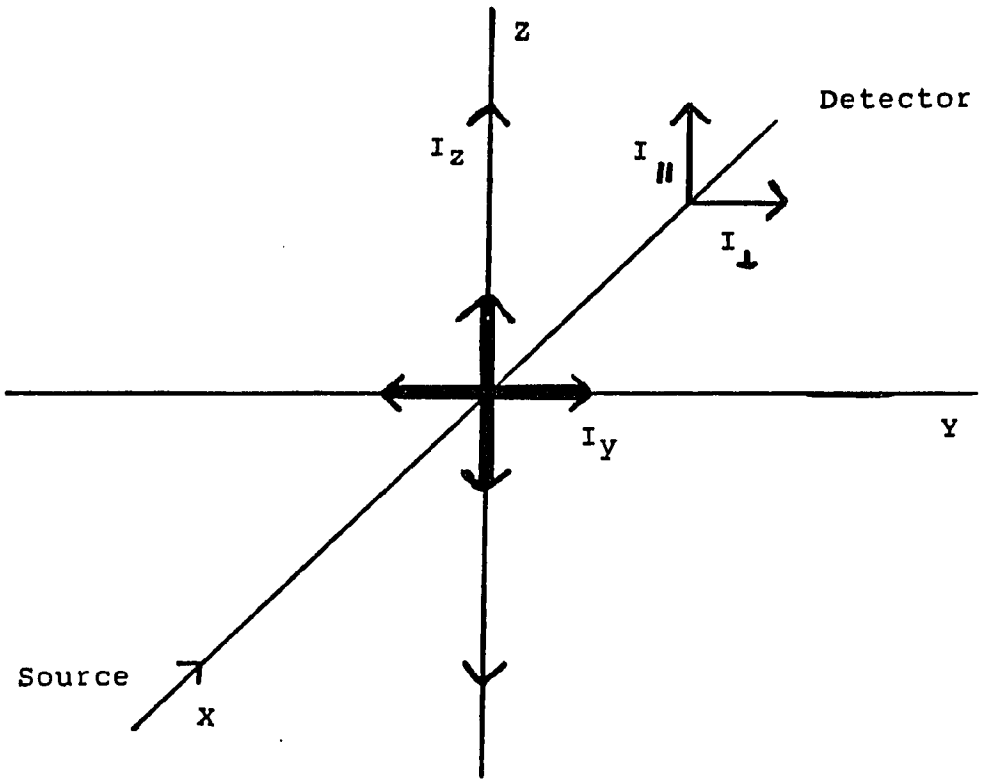

Figure 1.2 Polarization of light. $I_{\parallel} - I_{\perp}$ is the component in excess of the natural (unpolarized) component of light directed along an axis. The total detected intensity is $I_{\parallel} + I_{\perp}$

dipole transition moment. When an isotropic distribution of dipoles is excited by light polarized parallel to the z-axis (Fig. 1.3), the fluorescence parallel to the x-axis I_x, and the y-axis I_y, is equally intense. If $I_{//} = I_z$ and $I_{\perp} = I_x = I_y$, then the total fluorescence intensity is the sum of all fluorescence along the three orthogonal axes, $I_{//} + 2I_{\perp}$. This definition makes the anisotropy better suited to describe emission of a fluorophore. Also, in contrast to the polarization, contributions to the anisotropy r_i from independent species are additive if appropriately weighted by the fraction of the total fluorescence f_i which they represent.

$$r = \sum_i f_i r_i \tag{1.5}$$

The anistropy of the emission from a randomly oriented ensemble of dipoles excited by polarized light is 2/5 [13]. If an initially excited donor nonradiatively transfers its excitation to a neighboring acceptor with a randomly oriented dipole transition moment before fluorescence occurs, the anisotropy is seen to decrease.

The degree to which this anisotropy is decreased can be used as an indication of the probability for nonradiative energy transfer if the system meets certain criteria [11]. The absorption and emission transition dipoles should be parallel with respect to the molecular frame in order to avoid intrinsic depolarization. Also, rotation of the

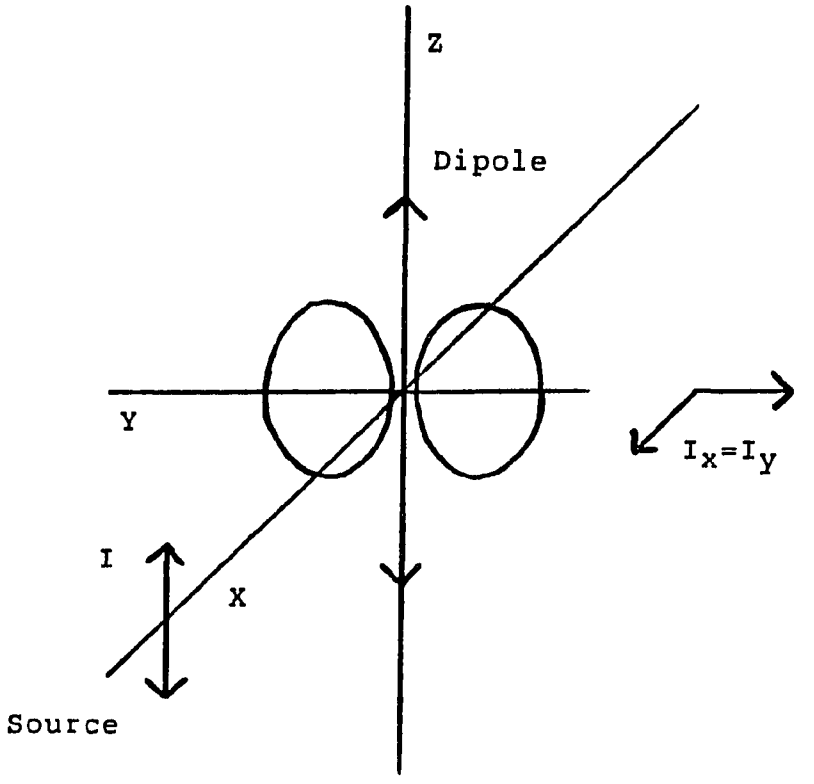

Figure 1.3 Anisotropy of light. The emitted radiation is distributed symmetrically about the z-axis. $I_{//} - I_{\perp}$ is the component in excess of the natural (unpolarized) component of the emitted light. The total detected intensity is $I_{//} + 2I_{\perp}$

molecules should be slow compared to the lifetime of the excited state in order to avoid depolarization due to a change in the orientation [14] of the initially excited dipole before fluorescence occurs.

The early development of energy transfer theory was based on the modeling of the decay in the anisotropy of steady-state fluorescence emission as the concentration of the transport sites in the sample increased (concentration quenching of the fluorescence polarization). Galanin [15] demonstrated that the initial polarization of an ensemble of randomly oriented dipoles excited with linearly polarized light is almost completely lost after only a single energy transfer step. Therefore, only the ensemble of initially excited molecules should represent a significant contribution to the observed anisotropy of the sample. Contributions to the anisotropy from ensembles made up of molecules excited after one or more energy transfers should be negligible (Eq. 1.5). This point will be addressed further in a later chapter in relation to some of the work presented here.

Describing the probability that the excitation energy will be on the initially excited site, G^S, is a formidable task. (Note that even though the symbol G^S is associated with a particular theory of energy transfer it will be used here to establish a consistent set of symbols throughout this work.) Figure 1.4 shows only a few of the infinite

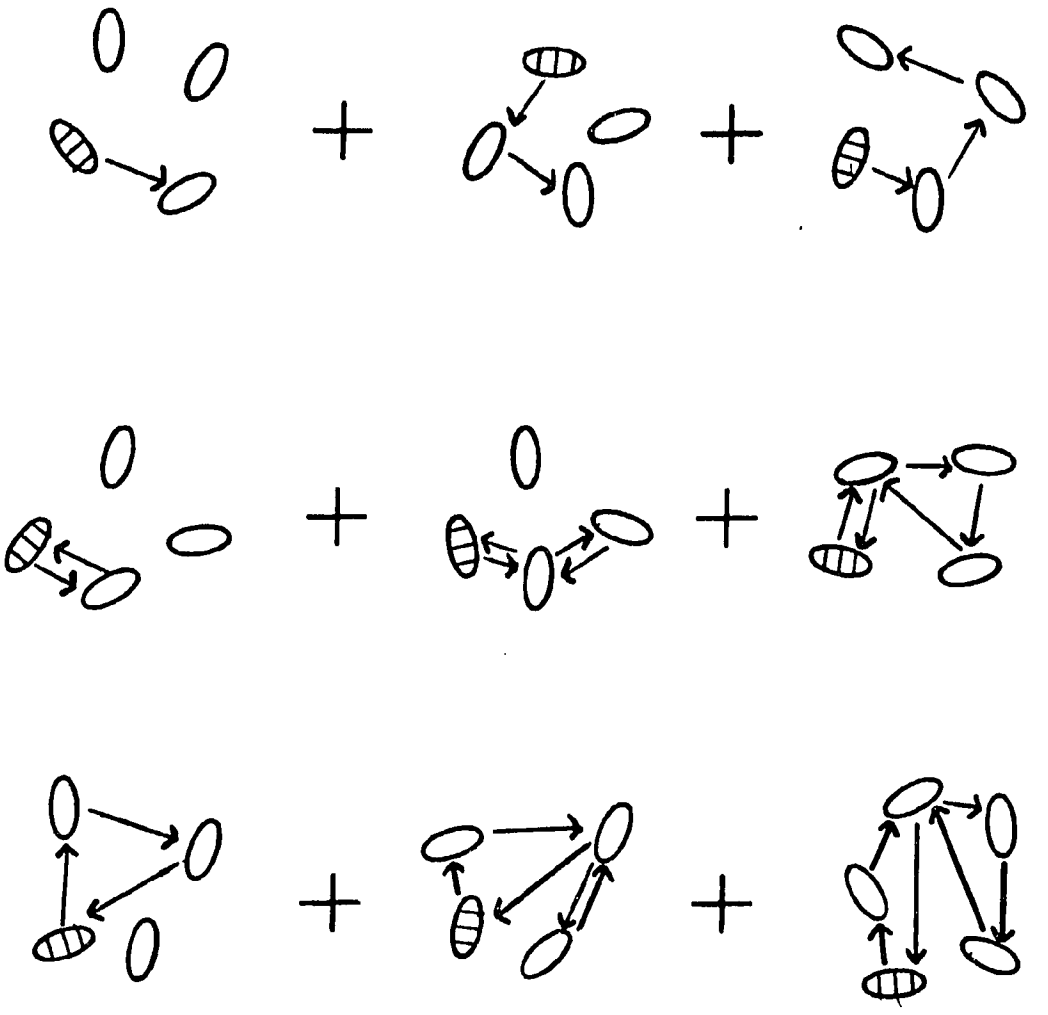

Figure 1.4 Trajectories for energy transport. The initially excited molecule is striped. An infinite number of trajectories would exist in the thermodynamic limit of an infinite number of interacting molecules

number of trajectories the excitation could follow in a solution of randomly distributed dipoles. A completely accurate description of G^S would require a summation of the contributions from each of the trajectories. For a system of N interacting molecules the probability that the jth molecule is excited $p'_j(t)$ must satisfy the master equation describing the energy transfer rate [8]

$$\frac{dp'_j(t)}{dt} = \frac{-p'_j(t)}{\tau} + \sum_{k=1}^{N} w_{jk}(p'_k(t) - p'_j(t)) \tag{1.6}$$

where it is assumed that kT is much larger than the inhomogeneous linewidth of the dipole transition so that $w_{jk} = w_{kj}$. The first term of this equation describes the natural decay of the excited state with lifetime τ. The natural decay term can be eliminated by the substitution

$$p_j(t) = p^s_j(t) \exp(t/\tau) \tag{1.7}$$

so that

$$\frac{dp_j(t)}{dt} = \sum_{k=1}^{N} w_{jk}(p_k(t) - p_j(t)) \tag{1.8}$$

The Förster transfer rate w_{jk} is defined in Eq. 1.1. If we require that the probability that the excitation resides on the initially excited site at t = 0 is unity,

$$p_j(0) = \delta_{j1} \tag{1.9}$$

then

$$G^S(t) = p_1(t). \tag{1.10}$$

Modeling the decay of fluorescence anisotropy in steady-state experiments is achieved by calculating the lifetime-averaged probability that the excitation will be on the initially excited site

$$\bar{G}^S = \frac{1}{\tau} \int_0^\infty G^S(t)dt. \tag{1.11}$$

Theories which account for physically significant energy transfer trajectories away from and possibly back to the initially excited site should be the most successful. Knox [11] presents a theory of concentration quenching of fluorescence polarization and critically examines the theoretical contributions of Förster [7], Weber [16], and Jablonski [17]. Hedstrom [18] reviews this work in addition to the work of others. A Förster type interaction (Eq. 1.1) between pairs of molecules is always assumed. Many of the differences between the theories arise in the definitions of the subsets of molecules among which the excitation can transfer.

Steady-state experiments and theories on concentration quenching of fluorescence polarization provided estimates

for the Förster parameter R_0 of Eq. 1.2 for a number of systems. Information pertaining to the number of molecules participating in the transfer process is also obtainable from these theories. Application of the various theories to the same data yields widely varying results [11]. The validity of any theory was difficult to ascertain because of the lack of precise experimental data available for comparison [12]. With the experimental methods available, each data point in the anisotropy vs. concentration curve required the preparation of a new sample. Thus, to accurately map this curve over a large dynamic range of concentrations would require a large experimental effort.

Hemenger and Pearlstein [12] demonstrated the utility of using time-resolved experiments to study energy transport. By studying the time-dependence of fluorescence depolarization as opposed to the concentration dependence, a single sample can be used to collect the data necessary to provide the same information about the system as the steady-state experiments. In this instance the time-dependent probability that the excitation energy resides on the initially excited site, $G^S(t)$ of Eq. 1.11, is used to determine the time-dependent anisotropy of the fluorescence emission.

$$G^S(t) \propto r(t) \tag{1.12}$$

A Green's function solution to the master equation, (Eq. 1.8), expanded in powers of density was formulated by Haan and Zwanzig [19]. The number density of molecules was replaced by the dimensionless reduced concentration

$$C = \frac{4}{3} \pi R_o^3 \rho \tag{1.13}$$

representing the number of donor molecules within the distance R_o from the initially excited state. The series was truncated after the second order term in concentration and used to estimate the time derivative of the average mean squared displacement of the excitation, $d\langle x(t)^2\rangle/dt$. In the short-time, low-concentration limit valid for the truncated series, this derivative is nonzero. This means that energy transport is nondiffusive in the short-time limit among randomly distributed sites in three dimensions as opposed to the diffusive behavior found for a periodic lattice [7].

This behavior might well be expected from a randomly distributed system of molecules [20]. At short times the excitation has a high probability of repeated transfers among molecules in small clusters which would not exist in a periodic lattice. This correlated motion of the excitation will reduce the value of the mean squared displacement at short times. As time progresses, the probability increases that the excitation escapes the initial cluster and moves in a more uniform or diffusive manner. Haan and Zwanzig [19] find a $t^{5/6}$ dependence to the mean squared displacement at

short times. However, due to the limitations of their truncated density expansion they can only speculate that diffusive behavior occurs at longer times or high concentrations where the excitation could more easily transfer to distant molecules.

The Green's function solution to the master equation derived by Haan and Zwanzig [19] was the basis for the theory of energy transport in solution developed by Gochanour, Andersen, and Fayer (hereafter GAF) [20]. A diagrammatic expansion of the Green's function is used to obtain an expression for $G^s(\varepsilon)$, the Laplace transform of $G^s(t)$. This diagrammatic approach takes into account all terms of Haan and Zwanzig's truncated density expansion plus many higher order terms. In its highest level of approximation, the so-called 3-body approximation, GAF theory predicts nondiffusive excitation transport in the short-time, low-density regime and diffusive behavior at long times and high densities. The diffusion coefficient predicted by the 3-body GAF theory is shown to have the form proved necessary by Haan and Zwanzig [19] for diffusive motion in a randomly distributed 3-dimensional system. Further discussion of GAF theory will be found in Chapter II.

The methods of GAF have also been applied to energy transport in 2-dimensional systems [21]. What is needed is a body of experimental data which can provide a critical

evaluation of the development in the theory of 2- and 3-dimensional excitation transport. The work presented here describes the development and characterization of 2- and 3-dimensional arrays of dye molecules from which such data can be collected.

Also described is an experimental apparatus based on the method of time-correlated single photon counting which was used to collect the fluorescence depolarization data applicable to energy transport studies. It is believed that this work represents a significant improvement in the understanding of the artifacts inherent in the types of systems studied and in the technique of time-correlated photon counting. Unaccounted for, these artifacts can obscure an accurate description of the energy transport process.

Explanation of Dissertation Format

Chapters V and VI are published works pertaining to energy transport in 3-dimensional dye assemblies. Chapters VII and VIII are published works pertaining to energy transport in 2-dimensional dye assemblies. Each of these chapters contain a description of the experimental apparatus and data analysis procedure used for the specific experiment. However, a more detailed presentation of the time-correlated photon counting apparatus and the computer

modeling of experimental fluorescence depolarization data will be given in Chapters III and IV, respectively. Two appendices are included which, hopefully, will elucidate the discussion in Chapter IV. The appendicies include a Fortran program representative of those used to analyze our data and a glossary of the common variables used in this type of program.

The second chapter of this dissertation will focus on a discussion of GAF electronic excitation transport [20] and a model proposed by Huber et al. known as the 2-particle theory [22]. A brief description of each theory will be provided. The final chapter will summarize the accomplishments of this work.

CHAPTER II. THEORY

Recent development of the theory of excitation transport has been based on the study of approximate time-dependent solutions to the master equation

$$\frac{dp_j(t)}{dt} = \sum_{k=1}^{N} w_{jk}(p_k(t) - p_j(t)) \tag{1.8}$$

For this work in particular we will be interested in the solutions provided by GAF theory [20] and Huber et al. [22].

GAF theory expresses the Green's function solution to the master equation as the sum of two terms

$$G(\vec{r},\vec{r}',t) = G^s(\vec{r},\vec{r}',t) + G^m(\vec{r},\vec{r}',t) \tag{2.1}$$

The Green's function describes the probability of finding the excitation at $\vec{r}$ at time t assuming that it was at $\vec{r}'$ at t = 0. $G^s(\vec{r},\vec{r}',t)$ is the probability of finding the excitation in the ensemble of initially excited molecules and $G^m(\vec{r},\vec{r}',t)$ is the probability of finding the excitation at a site not excited initially.

Working with the Laplace-Fourier transform of the Green's function

$$G(\vec{k},\varepsilon) = G^s(\varepsilon) = G^m(\vec{k},\varepsilon) \tag{2.2}$$

GAF expanded each of the two terms as functions of ε and a transfer rate w_{jk}. In the thermodynamic limit where the number of interacting molecules $N \to \infty$ these expansions for $G^s(\varepsilon)$ and $G^m(\vec{k},\varepsilon)$ produce, in each case, and infinite series of products of w_{jk} factors. Each product in the series can be represented as a diagram of circles representing the energy donors and arrows describing the trajectories of the energy transfer among the circles (Fig. 2.1). Through a process of topological reduction, the complexity of the resulting set of diagrams for $G^m(\vec{k},\varepsilon)$ can be reduced to a subset of diagrams from which the original set of $G^m(\vec{k},\varepsilon)$ diagrams can be generated. The expression for this subset of diagrams is in terms of factors of $G^s(\varepsilon)$

$$G^m(k,\varepsilon) = \frac{\rho G^s(\varepsilon)^2 \Sigma_n(k,G^s(\varepsilon))}{[1 - \rho G^s(\varepsilon)\ \Sigma_n(k,G^s(\varepsilon))]} \tag{2.3}$$

where ρ is a density term and

$$\Sigma_n(k,G^s(\varepsilon)) = \frac{1}{\rho G^s(\varepsilon)^2} x \begin{bmatrix}\text{sum of the reduced set} \\ \text{of diagrams for } G^m(k,\varepsilon)\end{bmatrix} \tag{2.4}$$

In the thermodynamic limit Eq. 2.4 should contain diagrams with an infinite number of circles. The subscript n refers to the maximum number of circles in the set of diagrams summed in the approximation of Eq. 2.4. Approximate expressions for $G^s(\varepsilon)$ are obtained from the summation. If

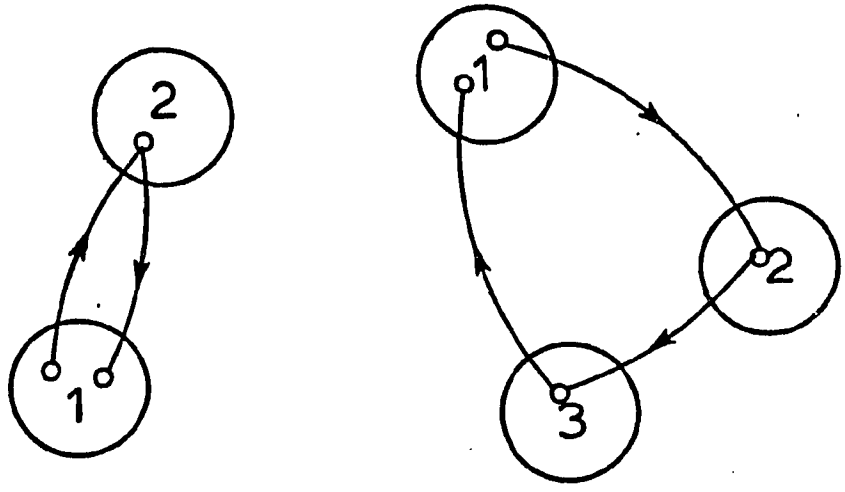

$w_{12}w_{21}$ $w_{12}w_{23}w_{31}$

Figure 2.1 Examples of GAF diagrams representing the product of w_{jk} factors

all of the reduced set of diagrams containing two circles are summed the expression for $G^s(\varepsilon)$ is referred to as the 2-body approximation. The 3-body approximation to $G^s(\varepsilon)$ results when the three-circle diagrams are summed in addition to the 2-body terms. The complexity of the problem has prevented any higher order approximations in GAF theory.

For a 3-dimensional disordered system the GAF 3-body approximation yields

$$G^s(\varepsilon) = \tau\{\pi^2C^2/4\ [1 - [1 + (32/\pi^2C^2)(\varepsilon\tau - 0.1887C^2)]^{1/2}] + 4(\varepsilon\tau - 0.1887C^2)\}/[4(\varepsilon\tau - 0.1887C^2)^2] \qquad (2.5)$$

where τ is the fluorescence lifetime of the chromophore and C is defined by Eq. 1.13. The inverse Laplace transform [23] of Eq. 2.5 gives $G^s(t)$ the probability that the energy resides on the initially excited site at time t. Recall from Chapter 1 that a sample excited with linearly polarized light loses memory of its initial state of polarization (Eq. 1.3) after a single energy transfer step [15]. In fact, Anfinrud and Struve [24] have recently used computer simulated fluorescence profiles to demonstrate the validity of this approximation even with the high precision afforded by current experimental techniques. With this approximation, $G^s(t)$ for molecules randomly distributed in 3 dimensions can be related to the time-dependent components of the polarized fluorescence by [25]

$$I_{//}(t) = P(t)[1 + 0.8\ G^{S}(t)]$$

$$I_{\perp}(t) = P(t)[1 - 0.4\ G^{S}(t)] \qquad (2.6)$$

where P(t) describes the isotropic decay of the excited state population. P(t) can be recovered by taking a linear combination of $I_{//}(t)$ and $I_{\perp}(t)$ such that the effects of fluorescence depolarization are obscured

$$P(t) = I_{//}(t)\cos^2\theta + I_{\perp}(t)\sin^2\theta \qquad (2.7)$$

Experimentally this is achieved by rotating an analyzing polarizer (Fig. 2.2) to the so-called magic-angle ($\theta = 54.7°$) with respect to the polarization of the incident light. Chapter III will deal with the details of the experimental apparatus.

A much simpler approximation to $G^{S}(t)$ has been developed by Huber et al. [22]. Only repeated energy exchange between pairs of donors is considered. In this 2-particle model, the second term of Eq. 1.8 is identified as the loss of excitation probability from the initially excited site $j = 1$. The second term then corresponds to the back transfer of excitation to the site $j = 1$. A disordered 3-dimensional array of donors is approximated by a periodic lattice with a small fraction f of the sites randomly occupied. After averaging over all possible configurations

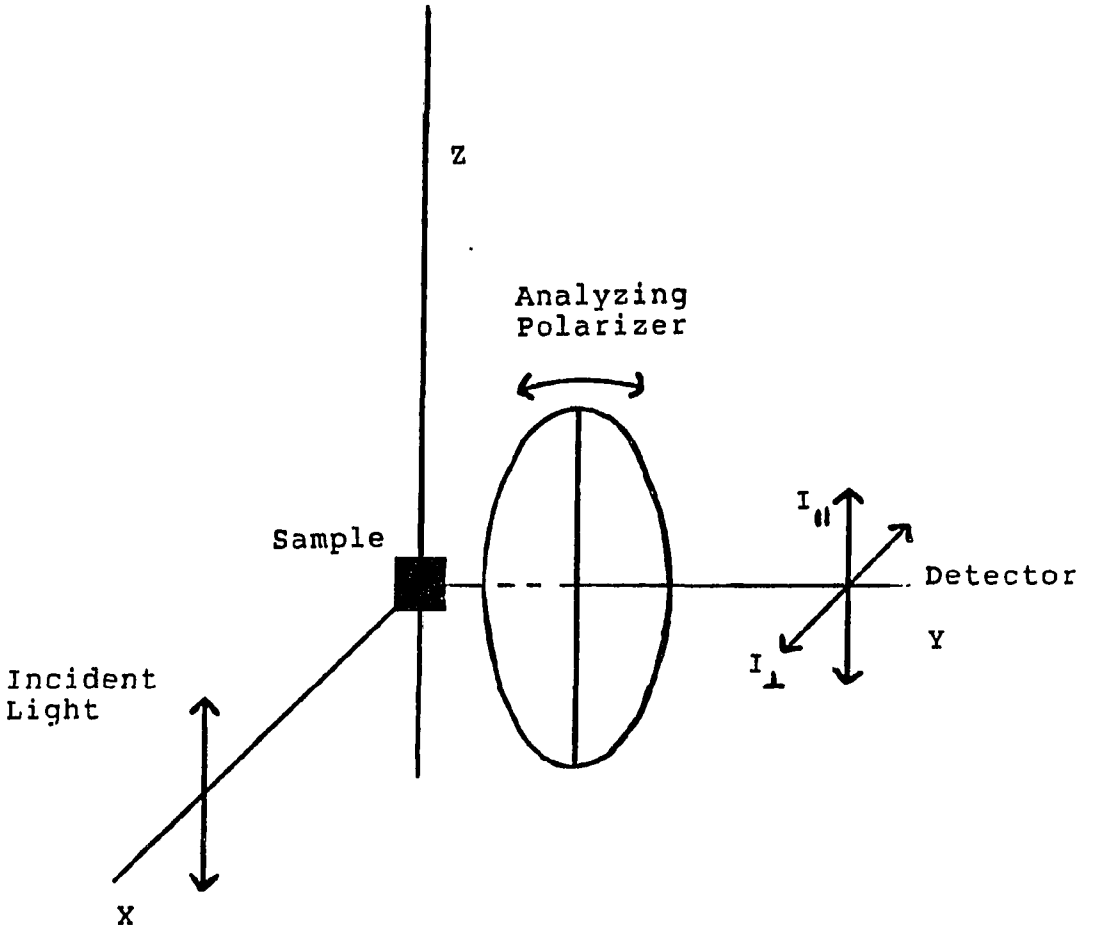

Figure 2.2 Schematic diagram for the collection of the polarized components of fluorescence emission. $I_{\parallel}$, $I_{\perp}$, and P(t) are collected by rotating the transmission axis of the analyzing polarizer to 0°, 90, or 54.77° (3-dimensional, isotropic distribution of dipoles) with respect to the direction of polarization of the incident light

of the donors on the lattice, the probability of finding the excitation on the initially excited molecule of a given pair is [26]

$$p(t) = e^{-w(r)t}\cosh(w(r)t)$$
$$= 1/2(1 + e^{-2w(r)t}) \qquad (2.8)$$

The probability of finding an excitation on an initially excited site is then the product over the N lattice sites of finding the excitation on a particular site.

$$G^S(t) = \prod_{i=1}^{N} fP_i(t) + (1 - f) \qquad (2.9)$$

The first term in the expansion of the logarithm of Eq. 2.9 in powers of f is retained. The summation over discrete lattice point is replaced by an integration over a continuous spatial distribution in 3-dimensions, $4\pi r^2$. When w(r) is given by the Förster transfer rate (Eq. 1.1),

$$G^S(t) = \exp\left[- C\left[\frac{\pi t}{2\tau}\right]^{1/2}\right]. \qquad (2.10)$$

where C and τ are defined the same way as in Eq. 2.5.

Knoester and Van Himbergen [27] have demonstrated that Eq. 2.5 is equal up to second order to the exact density expansion solution for the probability of finding the excitation on an initially excited site. They have also shown that the Eq. 2.10 is equal up to first order in the

same density expansion and that the second order coefficient is in error by only 3%.

An analytical expression in the time regime for the GAF Eq. 2.5 has been developed by Fedorenko and Burshtein [28]. The short and long time limits established for the behavior of $G^s(t)$ [29] can be compared to the analytic expression of GAF 3-body theory. At $t<<5.7\tau/C^2$ the limiting expression is exactly the 2-particle model in Eq. 2.10. The Fedorenko and Burshtein analytic expression also shows the proper behavior in the short time limit.

At long times ($t>>5.7\tau/C^2$) the limiting expression for $G^s(t)$ is

$$G^s(t) = \left[\frac{2\tau}{\pi C^2 t}\right]^{3/2} \tag{2.11}$$

The Fedorenko and Burshtein expression for $G^s(t)$ in this limit is

$$G^s(t) = \frac{8}{\pi^{1/2}}\left[\frac{8\tau}{\pi^2 C^2 t}\right]^{3/2} \exp(-0.1197C^2 t/\tau) \tag{2.12}$$

This lack of agreement between the GAF 3-body theory and the long time limiting behavior is a major criticism levied by Fedorenko and Burshtein against GAF theory. It should be pointed out, however, that this is not an experimentally accessible time regime at reasonable values of C (~1). Currently it is more productive to assess the validity of a

given theory in the short to intermediate time range where comparison with experimental data is possible.

Figure 2.3 illustrates the close agreement between the 2-particle theory of Huber and the GAF 3-body theory at experimentally interesting times ($t \simeq 6\tau$) and $C = 1.0$. The advantages of a simple analytic expression in time for G^S are obvious. The use of Eq. 2.10 instead of Eq. 2.5 reduces the computational effort needed by eliminating the need to perform the inverse Laplace transform of $G^S(\varepsilon)$ to recover $G^S(t)$. The 2-particle expression is likely to be more tractable when modification to the theory are necessary to look at more complicated systems. The experiments presented in Chapter VI indicate that the fits to real data provided by Eqs. 2.5 and 2.10 are indistinguishable.

Loring and Fayer (LF) [21] have applied the diagrammatic approach of GAF to 2-dimensional systems. In this case a 2-body approximation is the highest order expression available for $G^S(t)$. The 2-body 3-dimensional GAF results decays ~10% too fast at longer times when compared to the 3-body 3-dimensional results [20]. Deviations of similar magnitude have been observed between the 2-body 2-dimensional results and a 2-dimensional model developed by Baumann and Fayer based on Huber's 2-particle theory [26]. In addition, the LF 2-body 2-dimensional model is encumbered by mathematical complexity similar to that of the GAF results. The LF 2-

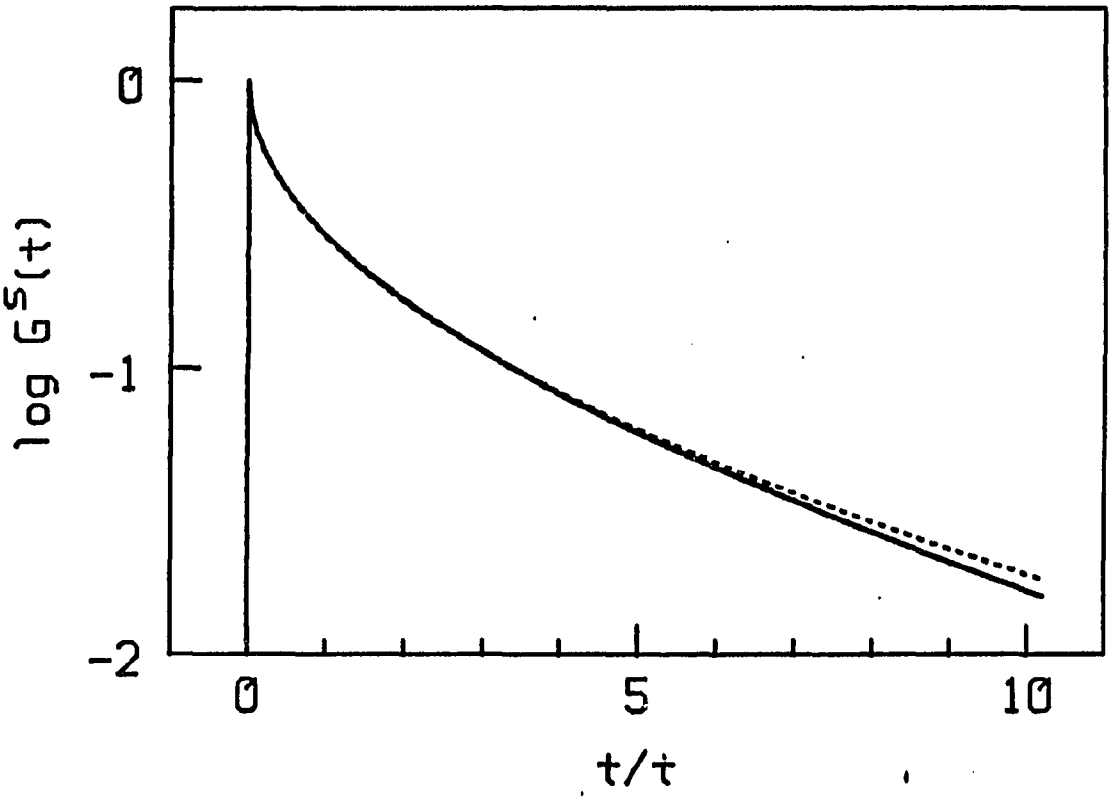

Figure 2.3 Comparison of the decay in $G^S(t)$ represented by the GAF 3-body theory (solid line) and the 2-particle theory (dashed line). The agreement is very close in the region of experimental interest ($t \simeq 6\tau$ at a reduced concentration of $C = 1.0$)

body model was used to analyze the data from the experiments presented in Chapter VII.

In the 2-particle 2-dimensional theory

$$G^S(t) = \exp[-1.354\ C\ (t/4\tau)^{1/3}] \tag{2.13}$$

where the reduced surface concentration is

$$C = \pi R_O^2 \rho \tag{2.14}$$

and ρ is the surface number density of donors. As mentioned above the 2-particle 2-dimensional model for $G^S(t)$ decays more slowly and is expected to be more accurate than the LF 2-body 2-dimensional model [26]. The 2-particle 2-dimensional model for $G^S(t)$ was utilized in the data analysis of Chapter VIII. For the orientational distribution of chromophore transition dipoles operative in the Langmuir-Blodgett film experiments of Chapter VIII, $G^S(t)$ can be related to the observable polarized components of the time-dependent fluorescence emission by

$$I_{//}(t) = P(t)[1 + 0.5G^S(t)]$$

$$I_{\perp}(t) = P(t)[1 - 0.5G^S(t)] \tag{2.15}$$

As is the case with Eqs. 2.6, Eqs. 2.15 assume that excitation transport is the sole mechanism for depolarization of the fluorescence. The magic-angle in this case (Eq. 2.7) is $\theta = 45°$.

CHAPTER III. EXPERIMENTAL

Photon Counting

In each of the experiments presented in Chapters V-VIII the time dependence of fluorescence emission is recorded using the method of time-correlated single photon counting. This technique has the advantages of high sensitivity, a wide dynamic range, and well understood noise characteristics in the data collected.

The high sensitivity and wide dynamic range are realized because photon counting measures the arrival times of single fluorescence photons at a detector relative to the excitation time of the sample rather than fluorescence intensity [30]. Thus, the technique is applicable in very low light level situations where analog methods may fail. Examples of these situations may include low concentrations of fluorophores, inefficient fluorophores, or situations where the study of decay dynamics several fluorescence lifetimes away from the initial excitation time is important.

A general description of the photon counting method as it applies to the measurement of fluorescence decay times is in order before the topic of noise characteristics in the data is discussed. The time-dependent fluorescence intensity distribution is due to the probability

distribution of emission of a single photon after excitation. By exciting the sample a large number of times and observing the time of single photon emission after each excitation, the probability distribution can be constructed [30]. At present we will consider δ-function excitation and δ-function response of the light detector and associated electronics. A timing reference pulse is generated for each excitation pulse. A photon from the sample fluorescence following an excitation is detected by a photomultiplier tube. The output anode pulse of the photomultiplier corresponding to the detection of a single photon at the photocathode is used to trigger (START) the charging of a capacitor with a constant current in a time-to-amplitude converter (TAC). The arrival of the timing reference pulse at the TAC will STOP the charging of the capacitor. The amount of charge stored will be proportional to the delay time between the START and STOP pulses at the TAC inputs. The delay time will vary depending on how the sample modulates the excitation pulse. That is, if the sample merely scattered the δ-function excitation energy without interacting with it the delay time would be constant. The output of the TAC is a voltage pulse whose amplitude depends on the accumulated charge (delay between the START and STOP pulses). A multichannel analyzer (MCA) operating in the pulse height analysis mode receives the analog pulse from the TAC and assigns to it a digital value proportional to

its amplitude. One of a sequence of discrete memory channels representing equal time intervals after the initial excitation is incremented depending on the digital value derived from the TAC output. The accumulated counts in the MCA memory channels constitute a histogram representing the time-dependent probability for single photon emission from the sample.

Only one STOP pulse is available for each excitation cycle of the sample. In any case, the response time of the electronics is not fast enough to allow us to time the arrival of each fluorescence photon which may result from a single excitation pulse. Only the first single photon anode pulse from the photomultiplier per excitation of the sample is recorded. In order to insure that we are sampling the entire distribution for single photon emission, i.e., that the probability of receiving a count in any channel of the MCA per excitation is equal, the fluorescence intensity should be kept low enough to minimize the probability of multiple photon emission. In order to achieve this, the ratio of the number of detected anode pulses N_D to the number of excitations N_E should be lower than ~0.01 [30]. Allowing N_D/N_E to increase much above 0.01 will distort the histogram collected on the MCA to reflect the higher probability of detecting a prompt fluorescence photon at high detection count rates. The counts in the later time channels of the MCA will be depressed relative to their true

probability of occurrence. This counting error is known as pulse pile-up. Its relative magnitude is greatest in the last channel of data collected and at that point is nearly equal to N_D/N_E. The actual value of N_D/N_E should be chosen based on the amount of error which can be tolerated in a given experiment. The value of 0.01 was chosen as a rule of thumb value assuming ~100 counts in the last channel. Although the effects of pulse pile-up can be corrected for [31] it is usually more desirable and a simple matter to avoid it. Cavity dumped laser sources offer excitation rates from several kilohertz to tens of megahertz so that data collection times can be kept relatively short (high N_D per second) while N_D/N_E is kept well below 0.01.

The probability of detecting a fluorescence photon is given by the Poisson probability function [32]. The mean, μ, of a Poisson distribution for a counting experiment is equal to the average number of events occurring per unit time interval. The mean is also equal to the variance, σ^2, of a Poisson distribution.

$$\sigma^2 = \mu \tag{3.1}$$

$$\sigma = \sqrt{\mu} \tag{3.2}$$

Photon counting experiments carried out under the conditions described insure that the probability of detecting a fluorescence photon during any of the equal time intervals defined by the MCA memory channels is equal for each excitation cycle. The number of counts in each channel

is then the estimate of the mean of the Poisson probability function of observing a count in that time interval. From equation 3.2 the standard deviation σ in the number of counts N in a given channel i is

$$\sigma_i = \sqrt{N_i} \tag{3.3}$$

In addition to the noise contributed by the counting statistics, counts due to dark current in the photomultiplier tube can add a constant background to all channels of the MCA. If an estimate for the number of background counts is available the data can be corrected in a straightforward manner. Data manipulation will be discussed in Chapter IV.

Apparatus

The same general experimental apparatus was used in each of the experiments described in Chapters V-VIII (Fig. 3.1). However, some important modifications were made to the instrument during different experiments in order to improve its performance. These changes will be discussed when appropriate during a description of the components of the apparatus.

The rear mirror of a Coherent Innova 90, 5 watt argon ion laser was removed so that its cavity could be extended to accommodate a Harris Corporation H-401 acoustooptic mode-locking crystal with a resonance frequency of 48 MHz. The

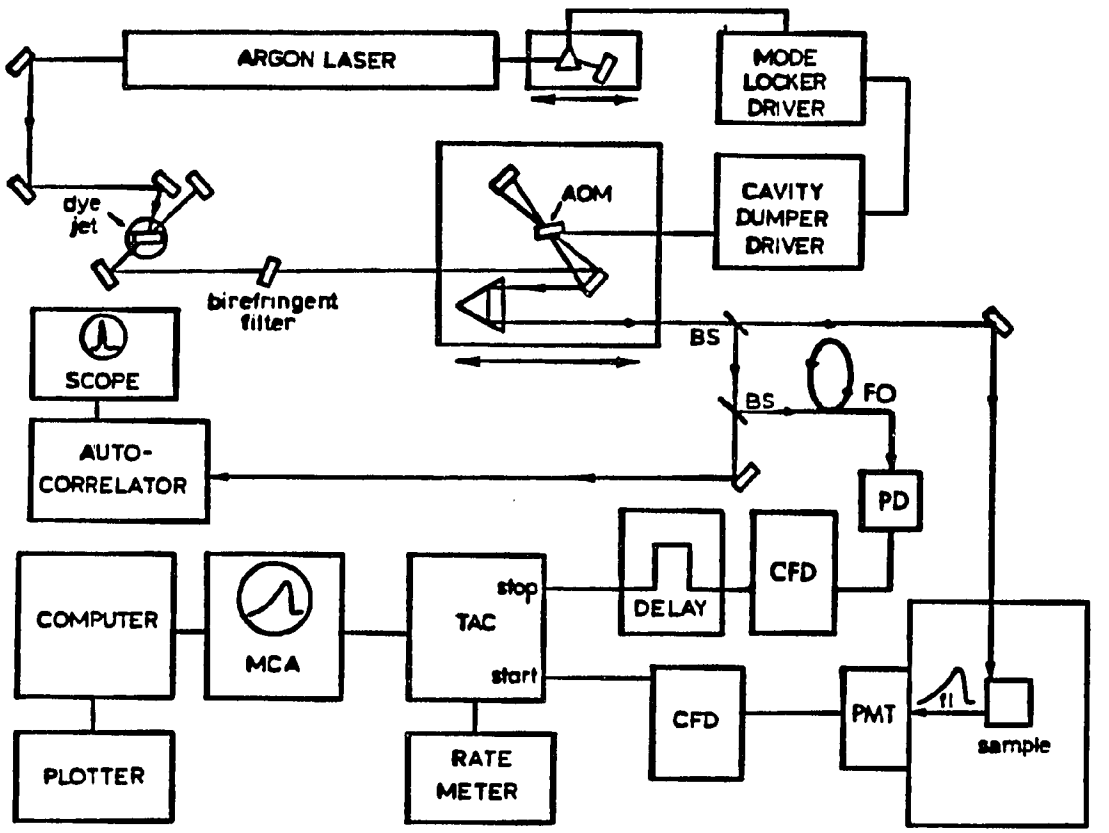

Figure 3.1 Time-correlated single photon apparatus. AOM, acousooptic modulator; BS, beam splitter; FO, fiber optic; PD, photodiode; CFD, constant fraction discriminator; PMT, photomultiplier tube; TAC, time-to-amplitude converter; MCA, multichannel analyzer

mode-locked output of the Ar^+ laser is a train of pulses at 96 MHz, twice the mode-locking frequency. Although the proper equipment was not available with which to characterize these pulses, they are believed to be approximately 100-150 ps in duration at the full width at half maximum (FWHM) [9]. The Ar^+ laser output is used to synchronously pump a Coherent CR599-01 rhodamine 590 dye laser. The output optic of the standard dye laser has been removed and the cavity extended to match the cavity length of the Ar^+ laser. The dye laser is cavity dumped allowing the repetition rate of the dye laser to be adjusted to submultiples of the mode-locking frequency. A dye laser output rate of 4.8 MHz is used in all work presented here. The wavelength of the rhodamine 590 dye laser is tuned between ~570 nm and ~620 nm with a three-plate quartz birefringent filter. A detailed discussion of cavity-dumping and mode-locking by acoustooptic modulation or synchronous pumping as they apply to this laser system is presented by Hedstrom [18].

Time-correlated photon counting experiments are insensitive to intensity fluctuations in the excitation source [30]; but, the timing is influenced by variations in the pulse shape. Several steps have been taken to insure stable operation of the laser system and thereby minimize changes in the shape of the output pulse.

First, the quality of the dye laser pulses is constantly monitored with a real-time autocorrelator [33]. A fraction of the laser intensity is sampled and split into two pulses with a 50% beam splitter. One of these pulses travels a fixed optical path length and is focussed into a thin second harmonic generating (SHG) crystal (Type I $LiIO_3$ or KDP) [9,18]. A dual mirror assembly rotating at 30 HZ gives the second pulse an optical path length which varies by $\pm\delta$ about the fixed optical path length of the first pulse (variable time delay). The magnitude of the difference in path length δ is determined by the separation between the mirrors in the rotating assembly. The second pulse is also focussed into the SHG crystal so that it spatially overlaps with the first pulse. The time profile of the second pulse sweeps past that of the first pulse. When the optical path lengths for each pulse are identical the pulses overlap in space and time and a maximum in the intensity of the second harmonic generated is observed.

The UV pulses produced by the SHG crystal (285 nm if the fundamental laser wavelength is 570 nm) are not collinear with the crossed beams of the laser. Spatial discrimination as well as optical filtering can be used against the fundamental wavelength. The second harmonic signal is detected on a zero-background with a photomultiplier tube and displayed on an oscilloscope. The intensity of the second harmonic is a function of the square of the sum of

the electric field vectors of the overlapping pulses. Sweeping one pulse past the other generates a waveform on the oscilloscope which is directly related to the laser pulse shape and thus can be used as a guide when optimizing the operation of the laser system. The cavity length of the argon ion laser and the optical alignment of the laser cavities are adjusted to yield a waveform on the oscilloscope with maximum amplitude and near-minimum width at the FWHM. The proper FWHM is most easily identified by increasing the sensitivity of the oscilloscope so that changes in the baseline region are easily detected. The FWHM of the waveform should not be decreased to the point at which satellite pulses or "wings" are observed of either side in the baseline region. This indicates a cavity length mismatch between the two lasers and the creation of more than one pulse in the dye laser cavity per argon ion pump pulse. This condition can adversely affect the precision of a photon counting experiment.

Laser stability was enhanced in the time period just prior to performing the work presented in Chapters VI and VIII. This was achieved by improving the stability and quality of the mode-locking in the argon ion laser. This, in turn, improves the stability of the synchronously pumped dye laser pulses [34]. The mode-locking element consists of a quartz crystal to which is bonded a piezoelectric transducer. A quartz crystal oscillator in the mode-locker

drive circuitry produces a stable radio frequency (rf) of 48.078654 MHz ±2 Hz which is amplified and delivered to the piezoelectric transducer at a power level of ~0.5 W. If the rf matches a resonance frequency of the mode-locker crystal, a standing acoustic wave is generated in the crystal. THe acoustic wave modulates the refractive index of the mode-locker crystal producing a diffraction grating. Diffraction off of the standing wave introduces a periodic loss of intracavity laser power. This forces the approximately 40 longitudinal modes around the 514.5 nm Ar^+ line [18] to resonate in the cavity with their phases locked in such a way that there is periodic constructive interference of the modes. The result is a train of pulses at a repetition rate twice that of the mode-locker frequency. Optimum performance is obtained when the cavity length L is adjusted so that the round trip time for a pulse in the cavity is $t = 2L/c$ where c is the speed of light.

The resonance frequency of the mode-locking crystal increases with temperature. The room temperature is controlled to within ±1.0°C and the mode-locking crystal is mounted in a temperature controlled oven. However, the temperature of the crystal also is determined by the amount of rf power being absorbed by the crystal and the amount of intracavity laser power absorbed by the mode-locker assembly. At the rf power levels necessary to achieve quality mode-locking with low noise between pulses in the

argon ion laser (~0.5-1.0 W) [34], the large amount of energy which must be dissipated by the crystal leads to temperature instability and fluctuations in the mode-locking crystal resonance frequency.

We have employed a feedback circuit based on the design of Klann et al. [34] to control the resonance frequency instability. The rf power not absorbed at the mode-locking crystal is reflected back to the source. If the transmitted rf drive frequency matches an acoustic resonance of the crystal, the reflected rf signal is in phase with the transmitted signal. A crystal resonance frequency lower or higher than the rf drive frequency causes the reflected rf signal to have a positive or negative phase difference with the transmitted signal, respectively. A phase detector in the mode-locker drive circuitry generates a positive or negative error voltage in response to the corresponding phase difference. The error voltage is amplified and applied to the control voltage of the rf power amplifier driving the mode-locker. A positive phase difference results in an increase in rf drive power and energy dissipation at the mode-locking crystal. The resulting increase in the crystal temperature shifts the crystal acoustic resonance upward toward the fixed rf drive frequency. The converse is true for a negative phase difference. The error voltage resulting from the phase difference is constantly monitored. After allowing

approximately two hours for the laser system to warm up and the room temperature to equilibrate, the phase difference is typically stable to ±0.03°.

The dye laser pulses have a time duration of ~5 ps at FWHM. An accurate determination of the pulse width would require a knowledge of the function describing the pulse shape and deconvolution of the autocorrelation function [35]. Approximately 80% of the 10 mW average power at 570 nm from the dye laser is split off and used to operate the autocorrelator and trigger two EG&G Ortec FOD-100 photodiodes. The remaining light is then dispersed by an equilateral prism so that the continuous spontaneous emission from the dye laser can be spatially discriminated against before the sample is excited. The light then passes through a light-baffled tube into a closed aluminum box housing the sample and additional optics (Fig. 3.2). Inside the box the light is directed by a pair of mirrors through a polarizer with its transmission axis in the horizontal plane (y-polarized). In all experiments the sample lied in the xy-plane and the exciting laser light made an angle between 10-15° with the surface normal (z-axis). Sample fluorescence is collected along the z-axis.

Determining the excitation polarization and aligning the analyzing polarizer at specific positions relative to it is a critical aspect of the optical alignment. The excitation polarizer is the last optical element before sample

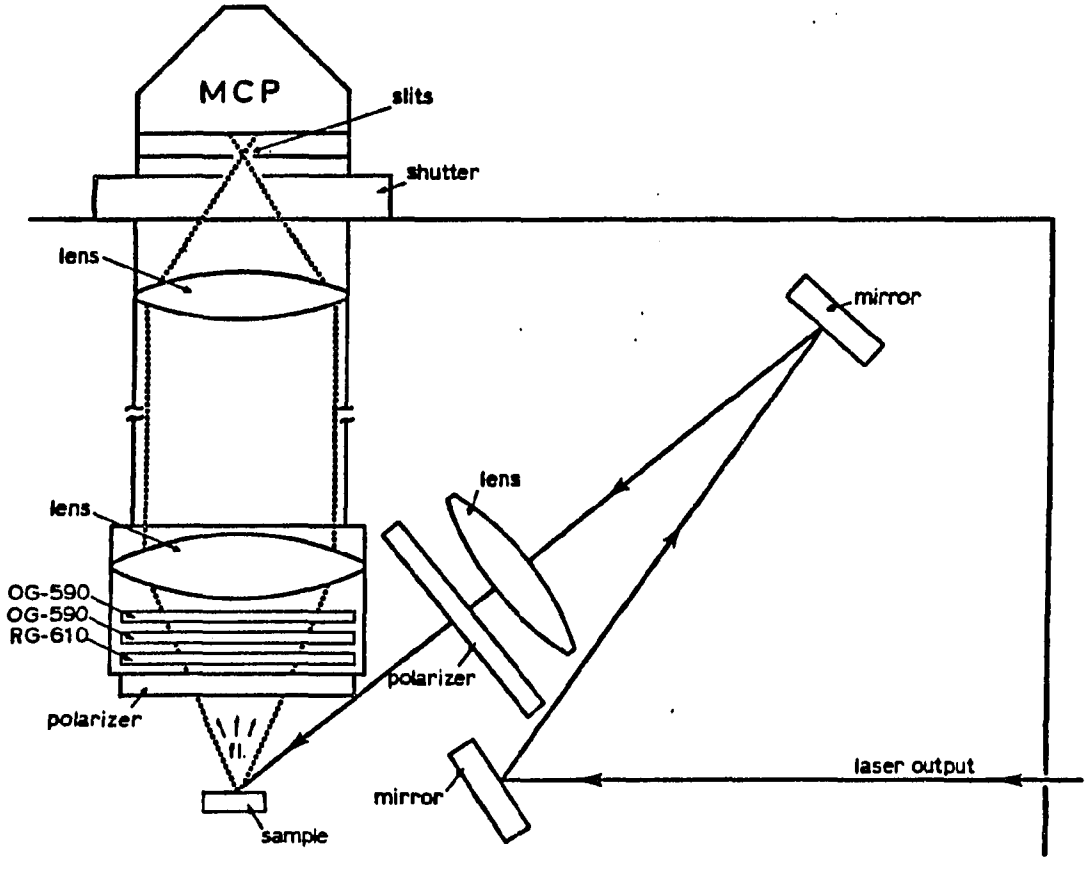

Figure 3.2 Beam geometry and optical arrangement in the light box of the photon counting apparatus

excitation. This prevents other optical elements from adulterating the purity of the linearly polarized exciting light. Also, the analyzing polarizer is the first optical element in the detection optics. This insures that the intensity collected is from the desired polarization component of the fluorescence. Each polarizer is set in a machined mount designed to permit precise rotation of the polarizer 90°, 54.7°, and 45° from its initially established position.

To align the excitation polarizer, vertically polarized light is directed into the box and through the polarizer. The transmitted light is reflected off of a piece of optically flat quartz located at the sample position (Fig. 3.2). The quartz piece is rotated about the y-axis until the reflected beam intensity is minimized. This occurs at the Brewster angle. Through an iterative process the polarizer and quartz piece are each rotated slightly until a minimum in the reflected intensity is found. The transmission axis of the excitation polarizer is now aligned vertically. At this point the polarizer is rotated precisely 90° in its machined mount so that only horizontally (y-axis) polarized light is transmitted. The quartz piece is now rotated so that the reflection is directed straight through the collection optics and onto a white card positioned at the exit slits. The machined mount of the analyzing polarizer is set to the "perpendicular"

position and the polarizer is rotated until a null in the transmitted intensity is obtained. The excitation polarizer remains fixed and the analyzing polarizer can be rotated in its machined mount so that its transmission axis is parallel, perpendicular, 54.7°, or 45° relative to the exciting polarization.

Dielectric-coated interference or colored-glass absorption filters are used to discriminate against scattered laser light. The fluorescence is collimated and focused onto a pair of adjustable slits by a pair of synthetic fused silica plano-convex lenses. The adjustable slits make it possible to spatially discriminate against fluorescence from any place other than the initially excited region of the sample.

The light detector is a Hamamatsu Model R1564U microchannel plate photomultiplier tube (MCP) with a bialkali photocathode. This type of phototube is used because it has superior timing characteristics over dynode chain photomultipliers [36,37]. The relatively high electric field strengths at the photocathode and short trajectories of the initial photoelectrons yields a short transit time spread for photoelectrons and fast risetimes on the anode pulse. Furthermore, unlike dynode chain photomultipliers, the timing characteristics of the MCP are insensitive to the wavelength of the detected photons. Our

MCP has a transit time spread of 76 ps and a rise time of the anode pulse of 206 ps when operated at -3000V [38].

The shape of the anode pulse from the MCP is preserved by amplifying with a B&H Electronics AC3011 MIC 3.15 GHz, 21 dB preamplifier. This signal inverting preamplifier is equipped with input protection circuitry which suppresses high voltage transients and provides a ground pathway for DC current. The amplified anode pulses from the MCP are then processed by a Tennelec TC455 quad constant fraction discriminator (CFD). For all of the work presented in Chapters V and VII and some of the work in Chapter VI it was necessary to invert the polarity of the amplified anode pulse from the MCP with an EG&G IT100 inverting transformer before sending it to the CFD because only negative going pulses could be processed. The 1 GHz inverting transformer attenuates the signal and modifies it by slowing the rise time. Modifications were then made to one channel of the TC455 CFD allowing positive going pulses to be processed eliminating the need for the inverting transformer.

Constant fraction discrimination eliminates the timing error due to the variability of input pulse heights. Figure 3.3 illustrates the timing error due to varying pulse heights inherent in leading edge discrimination. The TC455 CFD divides the input pulse into two portions, the larger of which will be called the main pulse. A user supplied external delay cable whose length depends on the fraction of

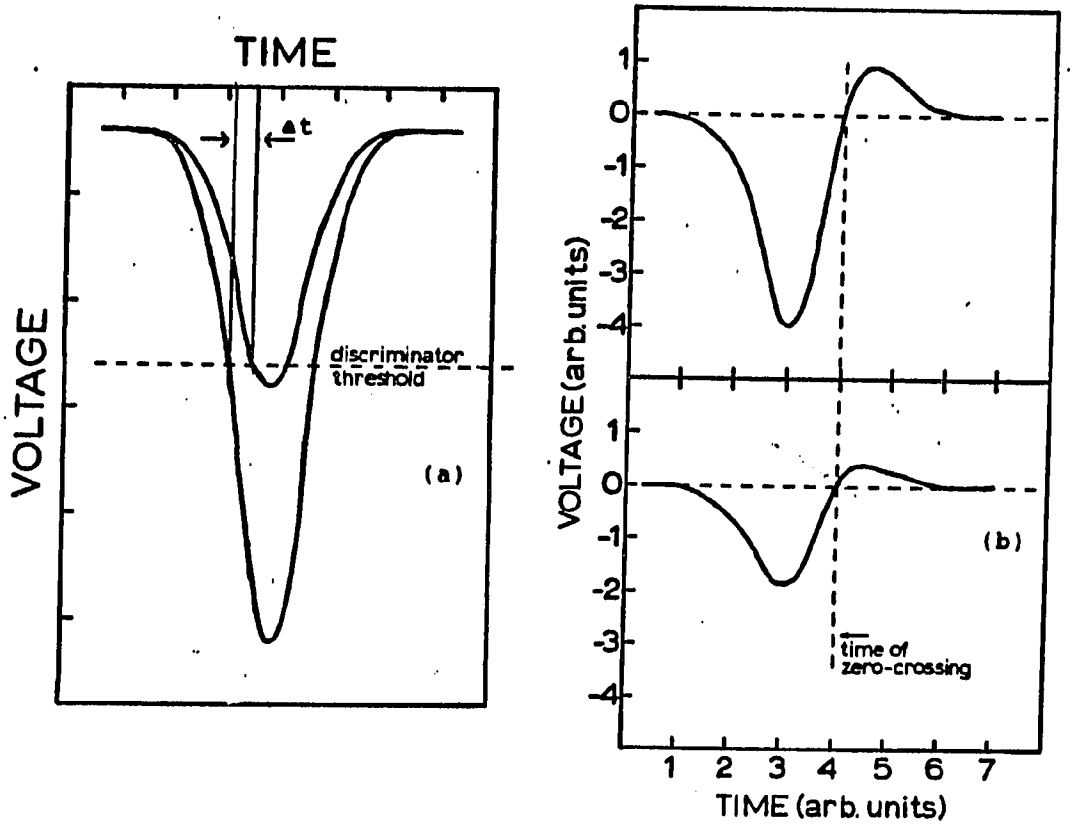

Figure 3.3 Leading edge vs. constant fraction discrimination.
a) Variations in the pulse heights lead to dispersion in the timing of events with a common origin in time.
b) The threshold crossing is constant in time for a wide dynamic range of pulse heights

intensity split off and the rise time t_r between 10 and 90% of the input pulse height [39] is introduced into the path of the main pulse.

$$t_{delay} = [t_r(1 - f) + 0.3] \tag{3.4}$$

where

$$f = \frac{\text{height of the undelayed pulse}}{\text{height of the delayed pulse}} \tag{3.5}$$

The delayed and undelayed portions of the pulse are directed to separate inputs of an integrated circuit comparator chip. In effect, one pulse is subtracted from the other. When the difference crosses a predefined voltage (walk) the comparator outputs a logic pulse. For a given pulse shape the crossing point is fixed in time for a wide dynamic range of input pulse heights. The CFD produces a NIM-standard fast negative logic pulse for each comparator logic pulse provided the initial input pulse exceeded a user set minimum voltage threshold.

As purchased the TC455 CFD was capable of processing negative going pulses with $t_r \geq 1$ nsec. Interference from reflections of high frequency components of the much faster rise time pulses of the MCP-B&H preamplifier combination and a large RC time constant for the CFD circuit caused significant distortion of the pulse shape. True constant fraction discrimination could not be performed.

Several modifications were made to the Tennelec TC455 CFD in order to improve performance. Plug-in modules were

originally used to house resistor networks which define the input voltage range and the fraction of intensity to be split from the input pulse. The plug-ins and their sockets were removed from the circuit board and replaced by copper strips and precision resistors soldered directly to the circuit board. The external delay cable which attached through LEMO type cable connectors was replaced with an internal delay soldered directly to the circuit board. Six diodes originally installed as circuit protection devices were removed to reduce the capacitance of the circuit. These changes significantly improved the high frequency transmission characteristics of the CFD circuitry. In addition, modifications were made to one channel which allow the processing of positive going pulses from the MCP-B&H preamplifier combination.

Timing error due to CFD performance is directly related to the input noise of the comparator chip. Figure 3.4 demonstrates how the timing error is reduced by increasing the slope of the signal passing through the crossing point. The slope is maximized by using fast rise time pulses and adjusting the fraction and delay so that the steepest slope of the rising edge of the delayed main pulse coincides in time with the region at approximately 90% of the peak value of the undelayed pulse on its falling edge. The optimum fraction for fast risetime pulses is ~0.5 (Eq. 3.5). In

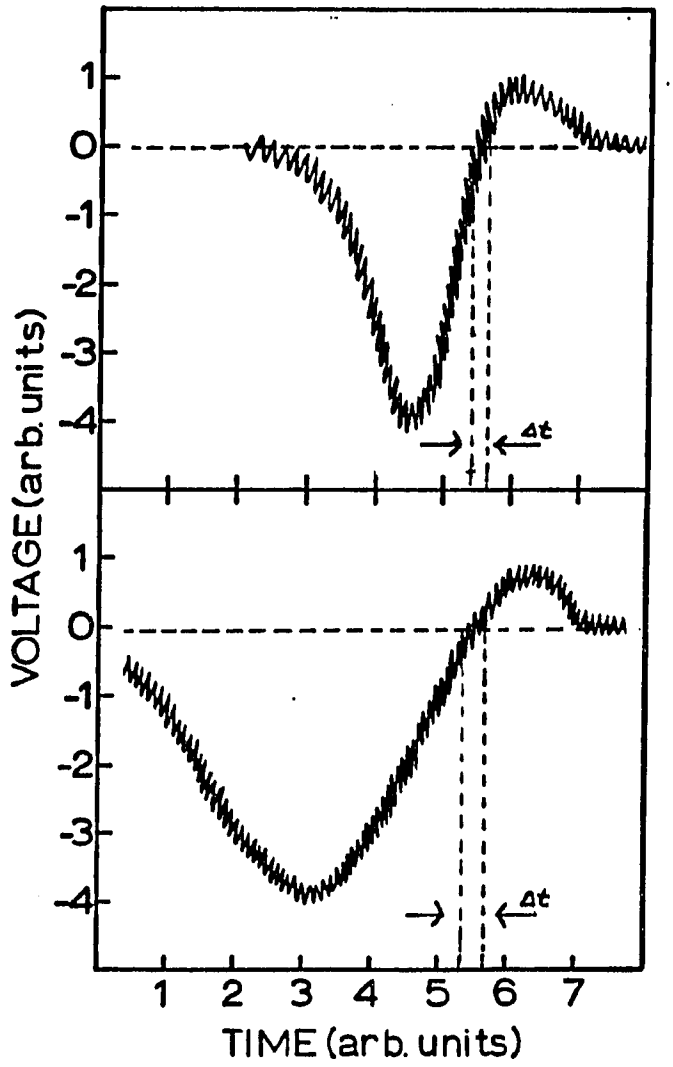

Figure 3.4 Illustration of the timing error contributed by noise on the input of the constant fraction discriminator comparator chip. A steeper slope through the threshold crossing region reduces the timing dispersion

practice, values of t_{delay} are determined empirically. An internal delay of ~0.5 ns was required to optimize the CFD performance.

The CFD logic pulse derived from the MCP anode pulse provides one input to the TAC. The other TAC input is a CFD logic pulse derived from a photodiode sampling the dye laser pulses. This is the timing reference pulse discussed previously. The EG&G Ortec FOD-100 photodiode has a pulse rise time of < 1 ns. Therefore, a second channel of the quad TC455 CFD was modified in a manner similar to that described above. However, the modification which allowed the processing of positive going pulses was not necessary.

The general operation of the TAC was described earlier in this chapter. In practice the TAC is used in an inverted operating configuration [40] in which the randomly arriving photoanode pulses are used to START the TAC and the timing reference pulses from the photodiode are used to STOP it. Initially this was done to maximize the data collection efficiency of the photon counting system. After receiving a START input the TAC is disabled from receiving another until a STOP input is registered or until the time set on the TAC range has expired (50 ns in this work). In the latter case no TAC output is sent to the MCA. The excitation rate with our cavity-dumped dye laser is 4.8 MHz. If the photodiode sampled pulses were used as the START input for the TAC (conventional operating configuration) it would be

necessary, with our cavity dumper, to reduce the laser repetition rate to 96 kHz so that the maximum input rate of the TAC (~150 kHz) would not be exceeded. A necessary condition for proper single-photon counting is that the rate of detected anode pulses be far less than the rate of excitation. There would be a great number of excitation cycles in which the TAC would cycle through the entire 50 ns time range without registering a count in the MCA because there would be no detected fluorescence photon to provide the STOP pulse. If, on the other hand, the single-photon anode pulses are used to START the TAC every START accepted would register as a count since a reference STOP pulse exists for every excitation event. The dead time of the TAC would be minimized.

The inverted configuration is used in all work presented here. However, a problem was discovered which required additional modification of the TAC operating configuration. START count rates faster than ~1 kHz introduced noticeable broadening in the time response of the instrument. Above a count rate of ~1 kHz a significant fraction of the randomly arriving START pulses retrigger the TAC charging cycle before the circuitry has completely recovered from the previous cycle. This means that two fluorescence events which occur at identical lengths of time from excitation could produce TAC output pulses of different heights due to the varying initial state of the TAC circuitry. To remedy

this count rate dependence of the TAC performance a Tektronix PG101 pulse generator was used to gate the START input of the TAC off for 125 μs after each accepted (TRUE) START input received by the TAC. This allowed the TAC circuitry to reset to a common qiescent state before accepting the next START pulse. An output pulse generated by every TRUE START of the TAC was used to trigger the pulse generator. The gating circuit eliminated the TAC count-rate dependence for count rates up to the 8 kHz corresponding to the 125 μs reset time. At an excitation rate of 4.8 MHz the photon counting condition of low N_D/N_E could be met with gated count rates of ~5 kHz (~20 kHz ungated). This is still more efficient than data collection in the conventional TAC operating configuration. The TAC gating procedure was used for the work presented in Chapters VI and VIII. Bebelaar [36] also noticed a count rate dependence to the instrument time response.

The time response of the instrument is evaluated by replacing the sample with a light scatterer. The laser-wavelength absorbing filters are replaced with transmitting filters and the laser intensity is attenuated to achieve the same count rates used for the collection of fluorescence (~4-5 kHz gated TRUE STARTS). The instrument response so collected has a FWHM of ~47 ps in a 10 ns time window of the MCA. Figure 3.5 shows the instrument time response. The scatterer is a 0.15 mm thick glass microscope slide

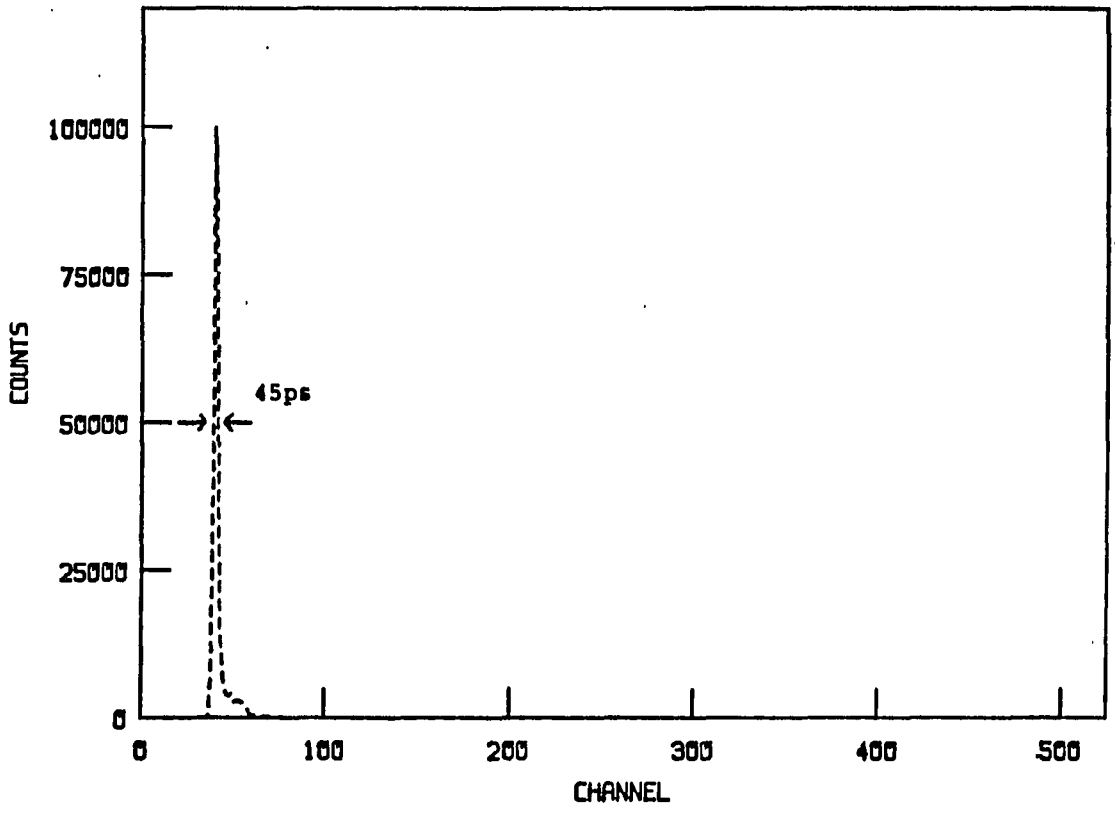

Figure 3.5 Instrument response function of the photon counting apparatus. The time resolution is 20 ps per channel

coverslip with one side ground on fine sandpaper. The importance of minimizing the thickness of scatter is clear when one considers that light scattered from the bottom surface of the coverslip travels ~0.3 mm farther and is ~1 ps delayed relative to light from the top surface. Thicker scatterers introduce correspondingly more dispersion in the arrival times of scattered photons and artificially broaden the instrument response function.

It has been found that an apparent nonlinearity in the time-to-amplitude conversion of the TAC can be attributed to two main sources. Depending on the settings chosen for the TAC (time range, gain, bias level) proper timing between the START and STOP pulses requires the use of a delay line in the path of one or the other. In this instrument the delay is introduced into the path of the STOP pulse which is derived from a photodiode sampling the 4.8 MHz cavity-dumped laser output. The delay can be introduced before or after the pulse is processed by the TC455 CFD. It is important, however, that the photodiode pulse does not arrive at the CFD while the MCP anode pulse is being processed in another channel of the same CFD. The high frequency nature of these fast rise time pulses causes crosstalk between the channels of the CFD and can adversely affect the timing of events. Interference between the pulses in the CFD can manifest itself as unwanted structure in the decay profile viewed on the MCA.

In the experiments of Chapters V and VII the possibility of crosstalk between CFD channels was eliminated by using two separate CFDs. The STOP pulse derived from the photodiode was processed by an Ortec Model 934 quad CFD. The START pulse from the MCP anode was processed by the Tennelec TC455 quad CFD. This work was performed before the modifications to the TC455 CFD enabling it to process faster rise time pulses were made. In this application comparable performance could be obtained from each CFD. However, after modification of the TC455 CFD superior performance of the photon counting apparatus could be obtained by processing both pulses using two channels of the same quad CFD.

The second main cause of an apparent nonlinear response of the TAC is radiofrequency pick-up by signal transmission cables. It is desirable to keep the length of coaxial transmission cables to a minimum. This means that the MCP-B&H amplifier should be located as closely as possible to the CFD. Also, as much of the delay in the STOP pulse as possible should be done by optical means rather than through coaxial delay cable. Visible ripple on the decays viewed on the MCA revealed the same periodicity as the pulse of 384 MHz rf used in firing the cavity dumper. Furthermore, the position and intensity of the ripples could be affected by repositioning of coaxial delay cables indicating pick-up of rf noise by the cables. Much of this cable can be eliminated by delaying the optical pulse through a length of

fiber optic before exciting the photodiode. Extraneous rf noise cannot be coupled with the signal through the optical fiber.

The final major modification to the photon counting apparatus was the addition of integrating and gating circuitry which adjusted data collection times to compensate for laser intensity fluctuations. When measuring the time-dependent fluorescence of dye molecules dispersed in an organized monolayer of lipid molecules at an air-water interface (Chapter VIII) an appreciable background signal from the water can distort the decay. At the lowest dye surface densities studied, ~10^{-4} chromophore/$Å^2$, the background signal can contribute ~10% of the fluorescence count rate. The background signal is Raman scattering from the water and has a time profile that is nearly identical in shape to the scattered laser light used to measure the instrument response function. Even though the background signal represents a small fraction of the total count rate, those counts can have a large effect on the shape of the fluorescence decay because they are distributed over a small range of channels in the MCA representing early times.

The fluorescence decay profile can be corrected by subtracting a background-signal curve from it. In order to do this accurately it is imperative that the background profile and the fluorescence profile are collected under conditions which assure that each sample has been exposed to

the same total light intensity. A portion of the laser intensity is sampled by an EG&G Ortec FOD-100 photodiode separate from the one used to supply the STOP pulse to the TAC. The photodiode supplies the control voltage to a voltage controlled oscillator (VCO). The frequency of oscillation of the VCO depends on the intensity of the light sampled by the photodiode. The output of the VCO is gated off whenever the TAC is gated off for 125μs after receiving a TRUE START. The gated output pulses from the VCO represent the light hitting the sample during "live" data collection time. These pulses are counted by a microprocessor and the MCA is gated on for data collection until a preset number of counts is registered in the microprocessor.

In practice, the microprocessor used to count the VCO output is a Commodore 64. The nominal VCO frequency is 700 kHz. The Commodore 64 cannot count at this high rate. Therefore, a decade counter is used to divide the VCO count rate by 10 before the microprocessor receives it. This reduction in the count rate does not impair the resolution afforded by the high frequency of the VCO. Gating of the VCO circuit is performed before the division by 10 so that the decade counter registers all VCO pulses occurring during the gated on period.

Sample Preparation

The study of excitation transport in three-dimensional systems was carried out in solutions of laser dye in glycerol. The high viscosity of the solvent (1490 cp at 20°C) inhibits molecular rotation on the time scale of the fluorescence lifetimes of the chromophores used. Molecular rotation is a mechanism for fluorescence depolarization. Its suppression is important if we wish to simplify our model describing fluorescence depolarization to include only an excitation transport mechanism.

For the work presented in Chapter V, rhodamine 590 perchlorate (rh 6G, Fig. 3.6a) purchased from Exciton Chemical Company was used to prepare the glycerol solutions by weight. The purity of the dye was ascertained by thin layer chromatography on Analtech silica gel G analytical plates. Only one spot was observed with three different solvent systems prepared by volume; ethanol/acetone, 35:65; ethanol/acetic acid, 65:35; 1-propanol/formic acid, 80:20.

The sample was formed by compressing a drop of a solution between two $\lambda/4$ fused silica plates. Absorption measurements on these types of samples indicate an ~10 μm absorption path length. The extinction coefficient derived from the absorption measurement of a standard rh 6G solution in a 1.0 cm cell was used in this determination.

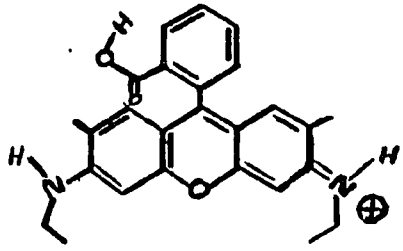

(a)

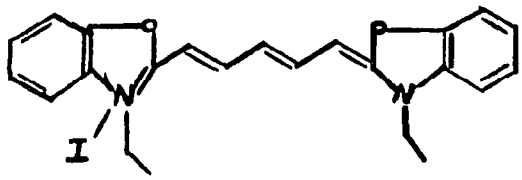

(b)

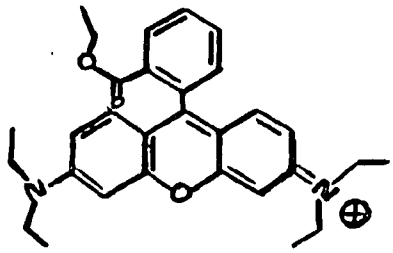

(c)

Figure 3.6 Dyes used in excitation transport studies.
a) rhodamine 6G (rh 6G)
b) 3,3'-diethyloxadicarbocyanine iodide (DODCI)
c) rhodamine 3B (R3B)

In samples with such high extinction coefficients (1.2×10^5 $L \cdot mol^{-1} cm^{-1}$ for rh 6G in glcerol), fluorescence self-absorption can have a significant effect on the apparent fluorescence lifetime even in 10 μm cells [41]. Dilation of the fluorescence lifetime caused by reabsorption and the subsequent reemission of emitted photons is shown to be severe for rh 6G in glycerol in Fig. 3.7. The decrease in lifetime evident at the highest concentration, 4.12 mM, is due to the rapid onset of fluorescence quenching by rh 6G dimer traps.

Fluorescence self-absorption affects not only the isotropic decay, but also the decay of the polarized emission profiles. The effects of this artifact were alleviated in future experiments (Chapter VI) by reducing the optical density of the samples. Dilute hydrofluoric acid was used to etch the Al/MgF_2 coating from a 9 mm diameter circular area of a front surface reflector. The remainder of the coated area was masked with Parafilm "M" Laboratory Film. The reflector substrate is a $\lambda/20$, 2.5 cm diameter, 1.0 cm thick fused silica flat. A drop of glycerol solution is placed in the etched area and compressed with a similar uncoated substrate. The remaining Al/MgF_2 coating acts as a very thin spacer between the flat substrates. Thick substrates are used to prevent distortion of the cell upon compression. Also, an aluminum mount was machined which allowed uniform pressure at reproducible

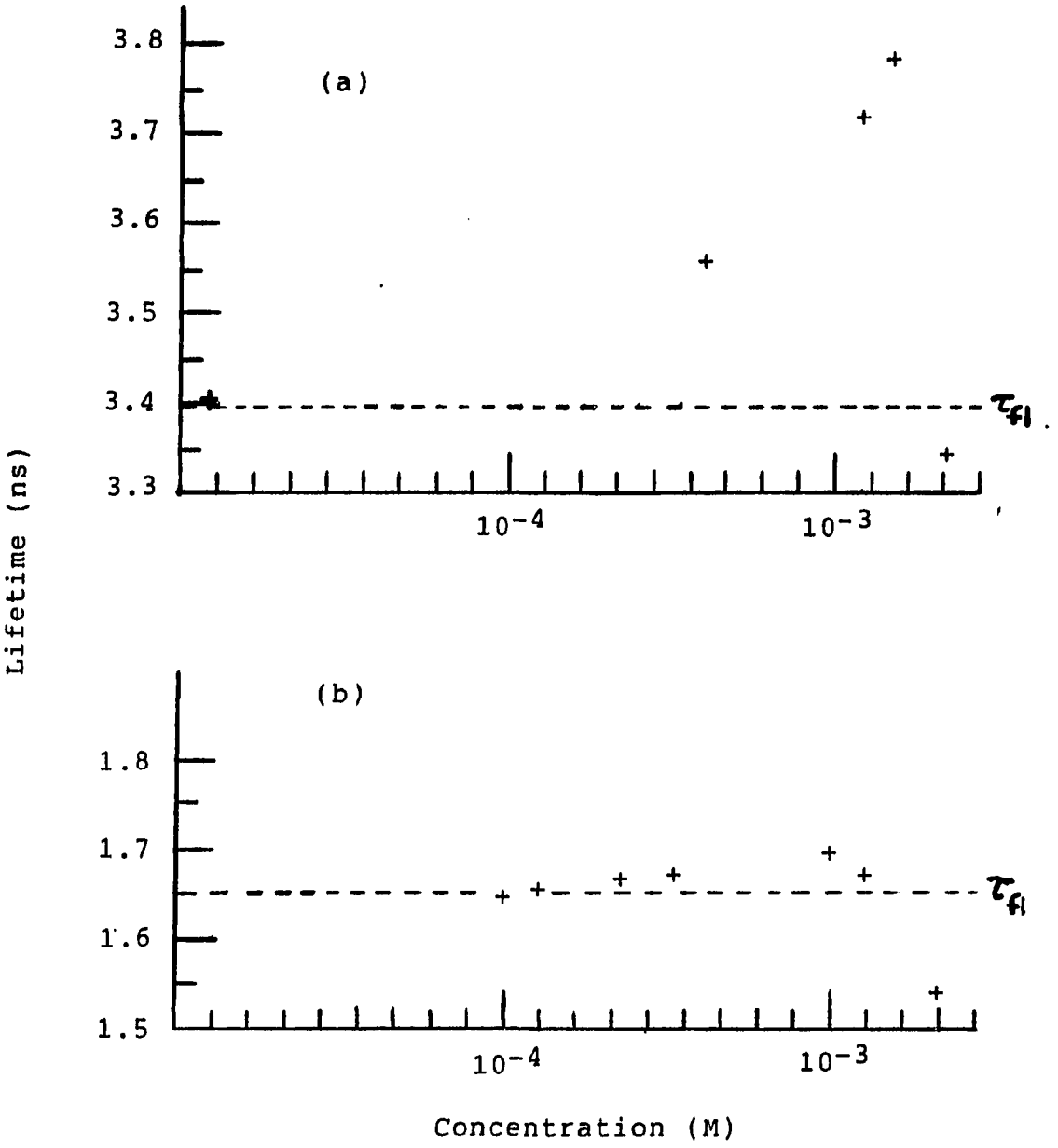

Figure 3.7 The effects of fluorescence self-absorption on the isotropic fluorescence lifetime.
a) rh 6G in glycerol in a ~10 μm cell
b) DODCI in glycerol in a ~2 μm absorption cell

levels to be applied around the rim of the cell during compression. Absorption measurements with standard rh 6G in glycerol solutions indicate an absorption path length of ~2 μm.

The ~2 μm cell was utilized in the work in Chapter VI. In addition, the laser dye studied was changed from rh 6G to 3,3'-diethyloxadicarbocyanine iodide (DODCI, Fig. 3.6b). DODCI has a shorter isotropic decay time τ than rh 6G (~1.7 ns vs. ~3.4 ns) in glycerol. With ~10 ns observation window available to us we can follow the decay for ~5.5 fluorescence lifetimes providing a large dynamic range for testing time-dependent models of excitation transport. The effects of self-absorption on DODCI in glycerol in the ~2 μm cell are minimal (Fig. 3.7b). As in the case with rh 6G, the fluorescence lifetime is shortened dramatically by the effects of trapping by dimers at high concentrations.

Two-dimensional excitation transport was studied in two very different media. The first experiments (Chapter VII) were performed on rhodamine 3B (R3B Fig. 3.6c) adsorbed onto optically flat $\lambda/4$ fused silica substrates. A different approach was taken in a second set of experiments (Chapter VIII) in an attempt to create a better 2-dimensional system. The dye octadecylrhodamine B (ODRB) was dispersed in the lipid dioleoylphosphatidylcholine (DOL) in organized monolayers at air-water interfaces. The structures of these molecules are shown in Fig. 3.8.

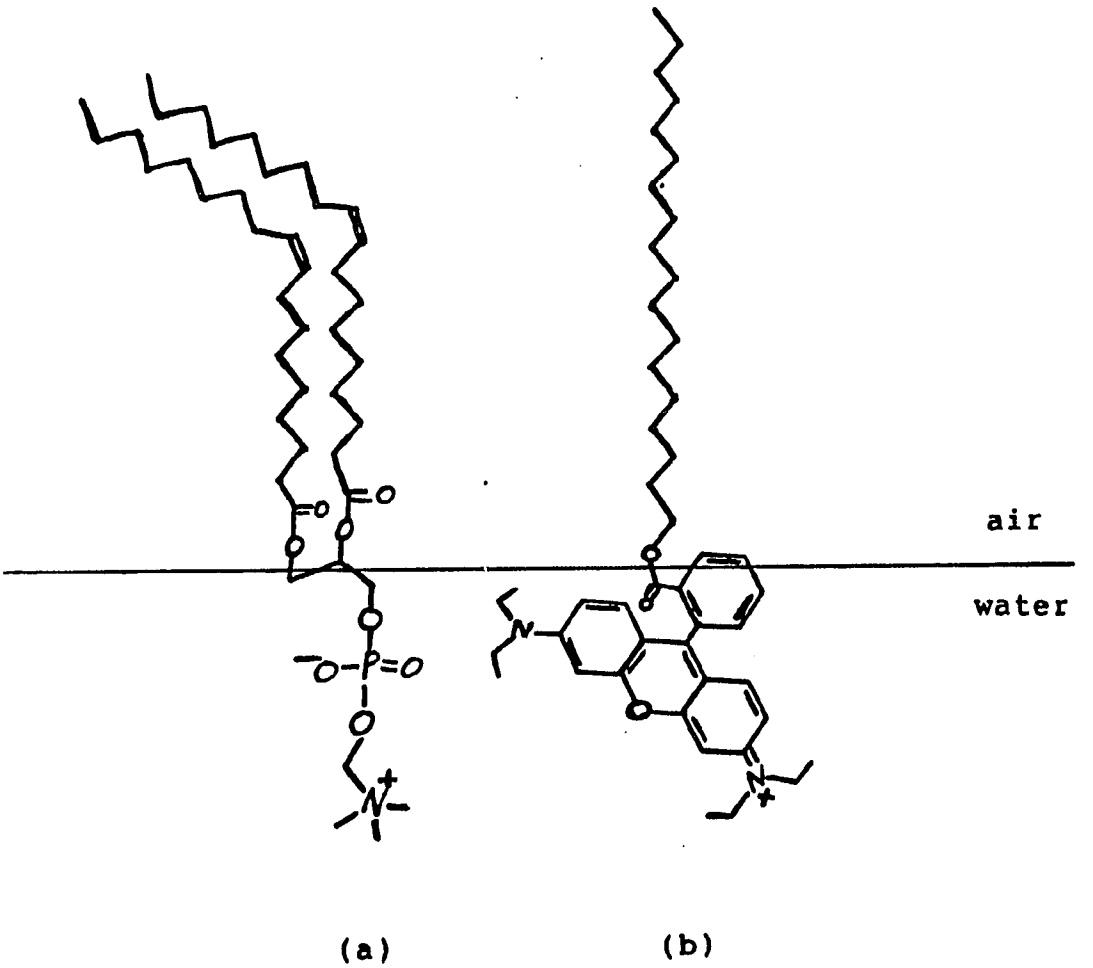

Figure 3.8 Constituents of the Langmuir-Blodgett film.
a) dioleoylphosphatidylcholine (DOL)
b) octadecylrhodamine B (ODRB). The air-water interface is added for conceptual purposes only and does not represent a proven orientation of the species at the interface

The R3B was obtained from Kodak Laser Products. Thin layer chromatography with the same solvent systems and plates described for rh 6G revealed only one spot. Samples were prepared by dipping (~10 min) fused silica substrates into aqueous solutions of R3B varying in concentration from 3.7×10^{-9} M to 7.4×10^{-7} M. The dye surface coverage on clean fused silica substrates proved to be nonuniform. When the total fluorescence intensity is collected from the surface as a computer controlled stepper-motor translates the sample through the focussed (~0.1 mm spot size) 575 nm laser beam, sharp peaks in the intensity are observed. Surface flaws such as scratches where dye can accumulate are believed to cause the peaks. Fluorescence decay profiles were collected only from areas where the dye coverage was uniform.

The uniformity of surface dye coverage could be improved if the fused silica substrate was treated with dichloro-dimethylsilane prior to dipping into the dye solution (Fig. 3.9). The procedure for cleaning and treating the substrates is given elsewhere [18]. This treatment renders the surface hydrophobic. The samples emerge from the aqueous dye solutions dry, eliminating the possibility of puddling dye solution on the surface. The fluorescence decay profiles were not affected by the surface treatment.

Preparation of 2-dimensional systems by the above method was deficient in several ways. The adsorption isotherms for the system are unknown and the dye surface coverage was too

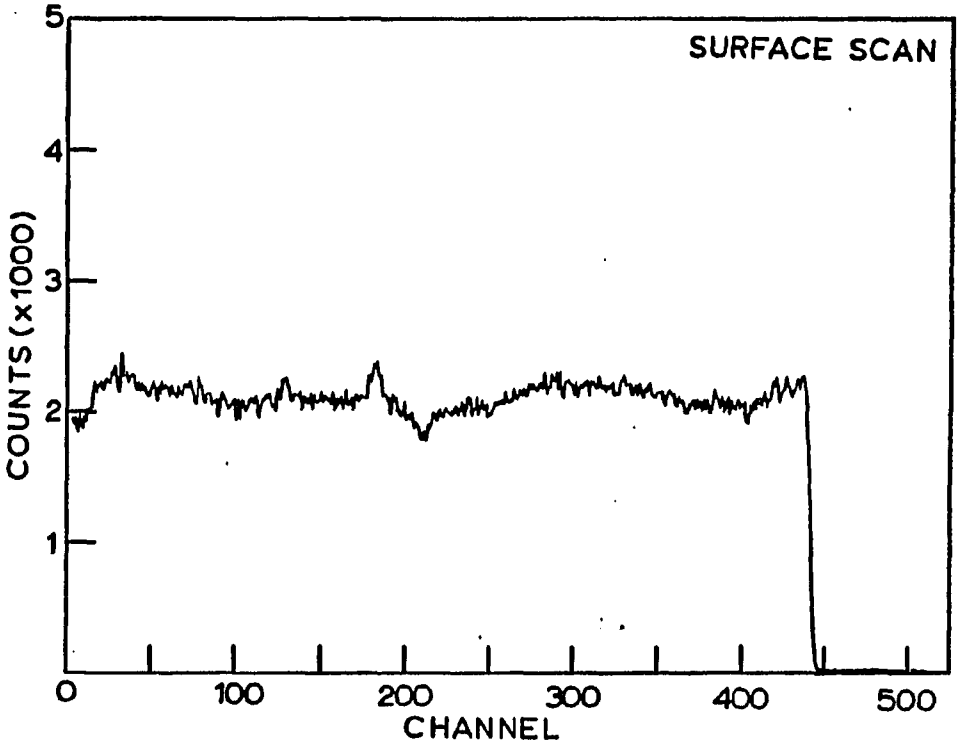

Figure 3.9 Uniformity of surface coverage for R3B on fused silica. The total fluorescence intensity is collected as the focussed laser beam scans the surface. The fused silica has been rendered hydrophobic by pretreatment with dichlorodimethylsilane

low for direct measurement by absorption spectroscopy except at the highest surface coverage. The optical density in this case was 0.002 ± 0.00025 as measured by a Perkin-Elmer 320 UV-VIS spectrophotometer. Therefore, the actual surface densities of chromophores is not known. Also, the optically flat surface may not be flat on the molecular level. This and the unknown homogeneity of surface adsorption sites make it difficult to know the orientational distribution of transition dipole moments on the surface, a necessary parameter for models of excitation transport.

Some of these problems are overcome in a 2-dimensional system consisting of a Langmuir-Blodgett (LB) film at an air-water interface. An LB film consists of molecules which have a polar hydrophilic and a nonpolar hydrophobic portion. Referring to Fig. 3.8, the phosphatidylcholine portion of the DOL is miscible in water while the two long hydrocarbon chains are not; likewise, the charged chromophore of the ODRB is miscible in water while the 18 carbon hydrocarbon chain is not. When properly formed the hydrophilic portions of the DOL and ODRB will be mixed in the water phase, the hydrophobic portions will be mixed in the air phase, and an organized monolayer of ODRB in DOL results at the air-water interface.

The trough used to form the LB films is shown in Fig. 3.10. The open area is 2.5x5.0 cm^2 and 2.0 cm deep. A 2.5 cm fused silica window in the bottom of the tray passes the

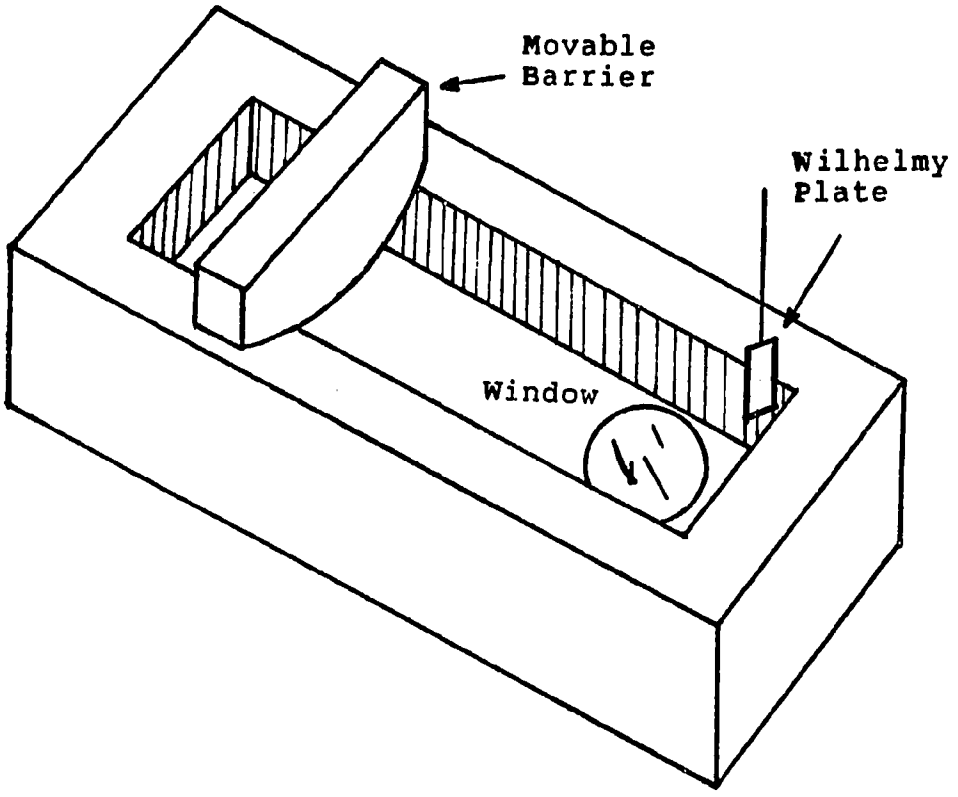

Figure 3.10 Langmuir-Blodgett trough, movable barrier, and Wilhelmy plate. The trough and barrier are constructed of Teflon. The trough is 2.0 cm deep with an open surface area of 2.5x5.0 cm^2. A 2.5 cm diameter fused silica window is mounted in the bottom. The Wilhelmy plate is a 0.5 cm wide strip of filter paper attached to an electronic balance

laser intensity transmitted by the LB film in order to avoid excessive scattered light. The trough and movable barrier were machined from Teflon. Great care was necessary to insure smooth, parallel, 90° edges on the tray and a smooth matching surface on the cylindrical face of the barrier. Very sharp machine tools and light sanding with 600 grit or finer wetted siliconcarbide paper provides a very smooth surface. The LB film leaks past a poorly machined trough-barrier edge when compressed.

Cleanliness also proved to be important in reproducibly forming stable LB films. The trough and barrier were rinsed with methanol and chloroform immediately prior to use. The water used was tap distilled water further purified with ion exchange and charcoal columns to a specific resistivity of 18 MΩ. The water was introduced into the trough through a 0.2 μm micropore. Dust settling on the water surface can be removed by dragging a lint-free lens tissue over the surface.

Surface pressure Π in the trough was constantly monitored during each experiment by the Wilhelmy plate method [43]. The 0.49 cm wide (measured when wet) Wilhelmy plate was fashioned from Whatman #1 Qualitative filter paper. The plate was attached via a thin wire to a stainless steel rod which was mounted on the pan of a Mettler AE100 electronic balance. The use of an electronic balance rather than one with a fulcrum and lever arm allows

measurements to be made while keeping the Wilhelmy plate stationary. The LB trough height was adjusted so that ~1 mm of the Wilhelmy plate was submerged. The adhesive attraction of the water to the Wilhelmy plate exerts a downward force on the paper proportional to the surface tension of the water. The balance is zeroed so that we have a reference of $\Pi = 0$ dyne/cm for a clean water surface. The introduction of the ODRB:DOL monolayer decreases the surface tension of the pure water and a negative reading is registered on the balance. This decrease in the surface tension of pure water is referred to as the surface pressure.

The cleanliness of the water surface prior to LB film formation was checked by advancing the movable barrier from one end of the trough (maximum surface area 12.5 cm^2) to within ~0.5 cm of the other (minimum surface area 1.25 cm^2). The surface was considered clean if there was no change in Π after this large reduction in surface area. If this was not the case, the trough was cleaned, the Wilhelmy plate was rinsed in clean water, and the cleanliness of the surface was retested. The barrier is advance with a Newport Research Corporation Model 850-2 linear actuator.

The Wilhelmy plate was positioned in a corner of the trough out of the path of the laser beam. With this placement, the advancing barrier never came close enough to the Wilhelmy plate to affect the measurement of Π.

Curvature of the water surface at the edges of the trough can also affect the reliability of the Π measurement. The curvature was minimized by keeping the water level flush with the top of the trough. With this precaution the Wilhelmy plate could be placed quite close to the edge of the trough and still measure Π reliably.

Essential to obtaining reproducible compression curves and stable monolayer assemblies was maintaining a high ambient humidity. A pan of water with ~500 cm^2 surface area was placed in the aluminum box holding the sample (Fig. 3.1). The stability of the LB film was also checked in a nitrogen atmosphere. No difference was found from the film stability in air.

Glass distilled $CHCl_3$ (Mallinckrodt Nanograde) was used to prepare stock solutions of ODRB purchased from Molecular Probes, Eugene, Oregon. Aliquots of the stock solutions were mixed with 1.00 cm^3 of chloroform solution of DOL purchased from Avanti Polar Lipids, Birmingham, Alabama. All solutions were diluted to 25.00 ml in volumetric flasks. The movable barrier was moved to the back of the trough to expose the maximum surface area. The ODRB:DOL:$CHCl_3$ samples were delivered to the clean water surface in a 1.6 μl drop from a 10.0 μl syringe. The $CHCl_3$ rapidly evaporates from the water surface leaving ODRB dispersed in DOL at the air-water interface. The DOL concentration used in all samples was chosen so that an easily measured amount of solution

could be applied to the maximum trough water surface area without noticeably changing the surface pressure; yet, the surface area could be reduced by more than a factor of two with the movable barrier before the desired surface pressure (usually 25 dyne/cm) was reached. The DOL monolayer breakdown pressure of 44 dyne/cm [42] could also be reached before the barrier reached the end of travel.

After the initial deposition of the sample, the barrier was advanced at a rate of ~2 mm/min until Π increased by 0.1 dyne/cm. The rate of compression was then decreased to ~0.35 mm/min in order to obtain a near-equilibrium compression of the monolayer to the desired surface pressure. A typical compression to 25 dyne/cm takes ~45 minutes. The LB film was allowed to stand for 10 minutes following compression to assure that the film had stabilized at the desired surface pressure before fluorescence data was collected. Figure 3.11 shows a compression curve for a LB film of one of our samples. Note the slight discontinuity at 25 dyne/cm. This is where the barrier was stopped for ~2.5 hours to allow data collection. LB films prepared in this manner were stable to within $\pm$0.1 dyne/cm over a period of at least several hours.

Unlike the case of R3B adsorbed onto fused silica, the surface density ρ of ODRB in the LB film can be estimated accurately. The molecular weights of ODRB and DOL are M_{ODRB} = 731.5 g/mol and M_{DOL} = 786.15 g/mol. Tancrede et

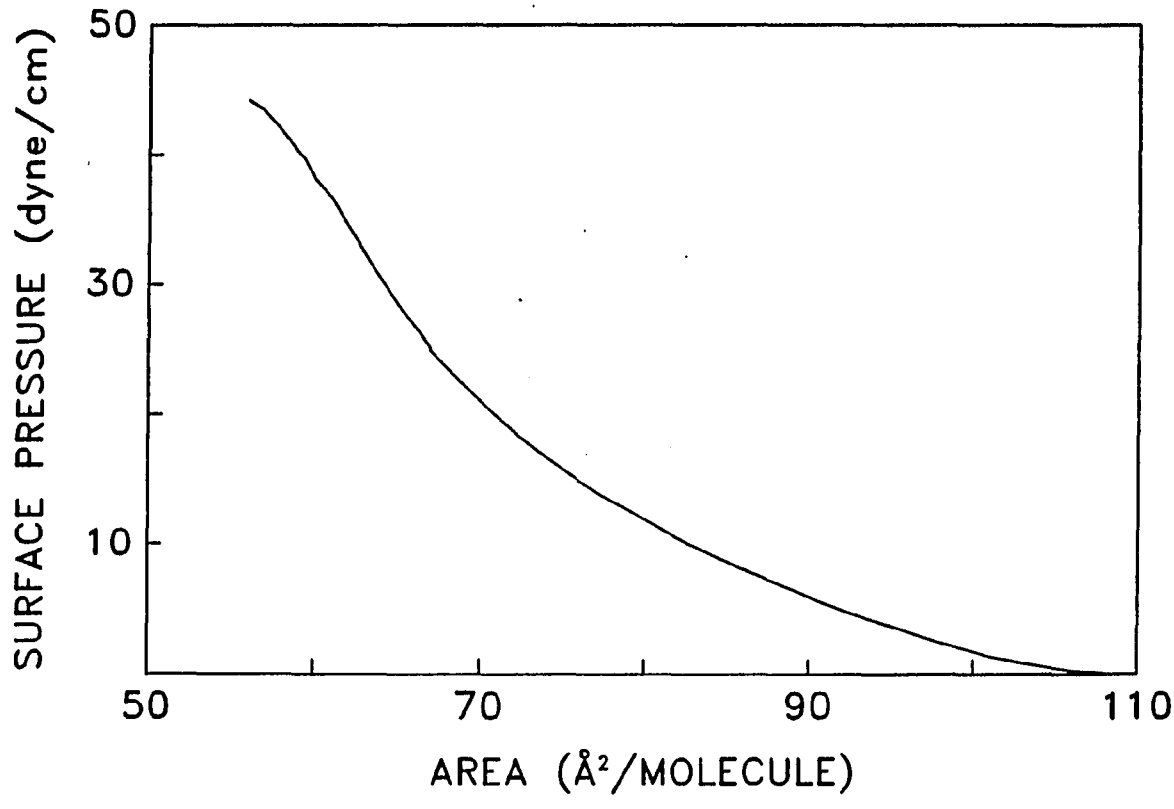

Figure 3.11 Surface pressure vs. area for a Langmuir-Blodgett film of ODRB dispersed in DOL at an air-water interface. The compression rate is ~0.35 mm/min along the long axis of the trough (Fig. 3.10). The mole fraction of ODRB is ~0.05

al. estimate that DOL occupies ~70Å^2/molecule at Π = 25 dyne/cm [42] while we obtain an estimate of 67Å^2/molecule (Fig. 3.11) at a much slower compression rate. Fatty acids such as arachidic acid occupy 20Å^2/molecule and a dialkylated dye such as dioctadecylthiacyanine occupies just twice this area of 40Å^2/molecule [43]. Therefore, an estimate of 20Å^2/molecule for ODRB should be reasonable. With this information and a knowledge of the solution compositions it is easy to estimate a dye number density ρ in the monolayer.

$$\rho = \frac{X_{ODRB}}{X_{ODRB}A_{ODRB} + X_{DOL}A_{DOL}} \qquad (3.6)$$

where X_i and A_i are the mole fractions and areas occupied per molecule, respectively.

CHAPTER IV. DATA ANALYSIS

The analysis of the time-dependent fluorescence decays to yield information about the energy transport dynamics is performed with the aid of a computer. A Digital Equipment Corporation (DEC) Minc-23 based on a PDP 11/23 microprocessor or a DEC VAX 11/780 was used for all computations. All programming was done in Fortran.

Programming Strategy

A convolute-and-compare strategy [44] is employed in the programs used. A user determined model is convoluted with an experimentally determined instrument response function and compared to an experimentally determined instrument response function and compared to an experimentally determined fluorescence decay. The Marquardt algorithm for nonlinear least-squares parameter estimation [45] is used to allow simultaneous variation of the fitting model parameters for each iteration of the convolute-and-compare procedure. The iterations continue until the chi-squared

$$\chi^2 = \sum_{i=M}^{N} (C_i - Y_i)^2/Y_i \qquad (4.1)$$

is minimized. C_i is the value of the convolution and Y_i is the number of counts in channel i of the MCA. From the discussion of photon counting statistics in Chapter III, Y_i

is also the variance of the counts. The range of data channels analyzed is given by (M,N).

Each experiment requires specific modifications to the general program. The fitting model must address the physics of a particular experimental situation. Chapters V-VIII discuss the specific models and data manipulation strategies for individual experiments. This chapter will concentrate on the general methods used for data analysis. The functions and requirements of the various subroutines will be discussed. The methods used to determine the goodness of a fit will also be presented.

The program is divided into several subroutines. This makes reading the program or modifying certain functions much easier. One version of the program titled NGSRR2.FOR is supplied in Appendix A for reference. The MAIN portion of the program is subject to many variations depending on user preference. One of the primary functions of this section of the program is to receive the input of model parameters, experimental data files, and various other parameters which establish how the data are to be fit. The input is menu driven so that the large number of data can be entered quickly and changed if necessary.

Some data formatting and manipulation takes place in MAIN in preparation for the nonlinear least-squares determination of the model parameters. Since the TAC is used in an inverted configuration [40], the channels of the

MCA corresponding to early times after sample excitation are on the right side of the screen with the higher numbered memory locations. MAIN reverses the files to read left to right beginning with the early time channels. Any model parameters with units of time are converted to numbers of channels corresponding to the time-calibrated channels of the MCA. Also, the average background counts contributed from phototube dark current are subtracted from the data files point by point [46]. The estimate for the average background counts is obtained from a range of data channels which precede the fluorescence emission and, so, receive only "dark" counts.

The uncertainty in the number of counts in any channel of the MCA is given by Eq. 3.3. The relative uncertainty in the number of counts in a given channel decreases with higher counts. Therefore, the contribution to χ^2 from each channel of data must be weighted by a factor of the reciprocal variance of that channel (Eq. 4.1) [32]. MAIN calculates and stores these weighting factors in the array WTS.

$$WTS_i = 1/\sigma_i^2 = 1/Y_i \qquad (4.2)$$

If the data are modified in any way (background subtracted, scaled) the propagated error should be determined [32, 47] and WTS modified to reflect the true uncertainty in the number of counts contained in channel i. In practice the background counts contributed by the MCP photomultiplier are

very low and we do not adjust the WTS to include the error introduced by their subtraction. The average background counts are $\lesssim 5$ even for long counting times and peak counts of $\sim 10^5$.

Prior to initiating the variation of model parameters in the nonlinear least-squares estimating section of the program, MAIN estimates values for a shift parameter B(1) and any model scaling parameters (preexponential factors, for example) unless it is required that their values be fixed at the user input values. Shifting the zero-time of the instrument response by an amount B(1) corrects to first-order time drift of the instrument response relative to the fluorescence profile and distortions in the instrument response due to collecting it at a different wavelength than the fluorescence profile. MAIN initially sets B(1) so that the peak of the instrument response datafile in array X(I) corresponds to the channel of the rising edge of fluorescence datafile in array Y(I) which has approximately half the number of counts as the peak channel in Y(I). The instrument response for the apparatus described in Chapter II is very stable in time and the MCP phototube dynamic response does not exhibit any wavelength dependence. Shift parameters are typically 0-1 channels. Scale parameters are estimated as the ratio of the peak counts of the fluorescence datafile to the product of the peak (zero-time) response of the decay model and the integrated area of the

instrument response. This product is simply a convolution of the instrument response with a single time interval of the decay model and yields an estimate of the peak of the computer generated fitted curve.

The fluorescence datafile collected are not simply the time-response N(t) of the chromophores to δ-function excitation. If this were true we could compare them directly with the decay model. However, the excitation pulse has a finite time-width. Molecules excited by early arriving photons will be decaying as photons in the tail of the excitation pulse are exciting other molecules [30]. The excitation pulse can be thought of as a sum of δ-function pulses with varying amplitudes E(t) at any time t. Referring to Fig. 4.1, the number of excited molecules at time t depends on the amplitude of the δ-pulse E(t). At a time t′ after the excitation at t, the number of excited molecules will be given by the initial population times the decay law E(t)N(t′-t). The total fluorescence intensity at time t′ is proportional to the sum over all t up to t′ of the excited molecules at t′

$$I(t) \alpha \int_0^{t'} E(t)\, N(t' - t)\, dt \qquad (4.3)$$

Equation 4.3 represents the convolution of the chromophore decay function with the excitation function. I(t) reveals how the δ-function response of the chromophore

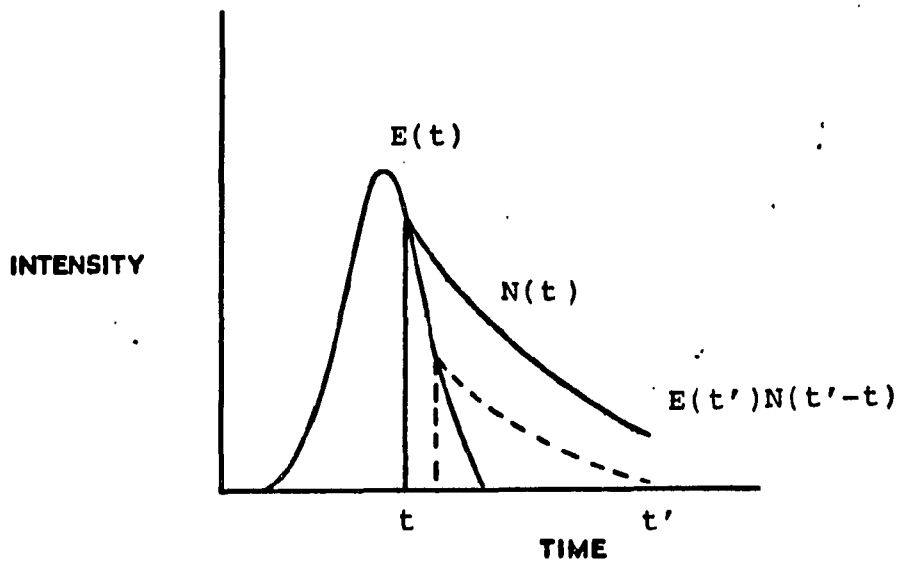

Figure 4.1 The effects of convolution. E(t) is the excitation pump profile. N(t) is the decay law for the sample. The value of the convolution at time t' is the sum of all contributions to the decaying population from times preceding t'

is distorted by excitation with a time-broadened pulse. The convolution can also be represented as

$$I(t) \propto E(t) \otimes N(t). \qquad (4.4)$$

The photon counting detection system does not have a δ-response to a δ-pulse excitation due to the transit time spread of photoelectrons in the photodetector and timing jitter in the electronics. The instrument response X(t) and the detection system response S(t)

$$X(t) = E(t) \otimes S(t). \qquad (4.5)$$

It can be shown [30] that the convolution of the instrument response with the decay law N(t) represents the distorted fluorescence decay C(t) collected and stored in the MCA.

$$C(t) = X(t) \otimes N(t) \qquad (4.6)$$

A convolution is an infinite sum over smoothly varying functions (Eq. 4.3). In our convolute-and-compare program we wish to convolute a histogram representing the response function with a continuous function representing the fluorescence decay. The channel counts in our histogram representations of the instrument response and distorted fluorescence decay profile are not the values of these functions at some instant in time, rather they represent the integrated area under the function over a time interval Δt, defined by the calibration of the MCA channels. The integral implied in Eq. 4.6 can be replaced by the infinite sum

$$C_n = \sum_{i=1}^{n} X(i - s)\, N(n - i) \qquad (4.7)$$

where C_n is the number of counts in the nth channel of the fluorescence decay, X(i - s) is the channel count of the instrument response appropriately shifted by S channels, and N(n - i) is the value of the decay model at a time (n - i) after the excitation.

A more accurate formulation of the discrete convolution of Eq. 4.7 would result if, instead of an instantaneous value for N(t), we used the integrated value of the function over a time interval Δt centered about time (n - i). The time interval Δt is the same one represented by a channel of the MCA. The error is especially acute for the initial value of the decay model. The integrated value of the interval centered at t = 0 will be less than half of the instantaneous value of the decay model at t = 0. The error that this introduces to the convoluted function is increasingly important as the instrument response function becomes narrower (i.e., it is represented by fewer channels).

Current versions of our programs use an integrated value of the decay model N(t) when performing convolutions. A discussion of how these values are obtained will be included

in the following description of the nonlinear least-squares parameter estimation portion of the program.

LSQENP is an acronym which refers to the least-squares estimation of nonlinear parameters. It is in this subroutine that the model parameters are simultaneously varied by the appropriate magnitudes and in the appropriate directions so that they converge to the set of values judged by LSQENP to provide the best fit to the experimental data. LSQENP is called only from MAIN. Information about the model parameters such as their number, the initial values, and which are to be fixed at constant values while others are varied are sent to LSQENP along with the experimental data, X(I) the instrument response, Y(I) the fluorescence decay, and WTS(I) the weighting factors. BLOCK DATA contains constant parameters required by LSQENP. These parameters are used to determine when to terminate a fit and the magnitude of the changes imposed on the model parameters. More will be said about the principles of operation in LSQENP in a later section of this chapter.

LSQENP is a general algorithm which can be used to fit any function for which the partial derivatives with respect to the function parameters can be found. For our purposes the function is generally one which describes the decay of fluorescence intensity with time. The function used range from a single exponential to model the natural decay of fluorescence emission to much more complex expressions which

model fluorescence depolarization via a combination of energy transport and restricted rotational motion of the chromophore. The values of the model function and its partial derivatives which are required by LSQENP are accumulated in separate subroutines FCODE and PCODE, respectively.

FCODE defines the model function being used in the fit. The parameter values designated by LSQENP are used to evaluate the function at time intervals (channels) corresponding to the time intervals defined by the channels of the MCA. The values of the function are accumulated in the array DEC. Important to note is that the value of the function at t = 0 is computed and stored in DEC0. This value is not collected experimentally but its omission during convolution can cause significant error in the convoluted function. FCODE also calls the subroutine SHIFT which changes the position of the instrument response file X(I) relative to the fluorescence file Y(I). The shift can be a fraction of a channel and is done in a way which preserves the integrated area under the instrument response curve. The new value of X for a fractional channel shift is found by linear interpolation between the value in the channel to be shifted and the value in the adjacent channel in the direction of the shift.

Before convolution of the model function with the experimental instrument response, FCODE sends DEC0 and the

array to the subroutine HIST. HIST uses Simpson's rule to approximate the areas of intervals Δt about the instantaneous function values represented in DEC0 and DEC. If an analytic integral is available for the function, integration over the proper time interval can replace the Simpson's rule approximation. DEC0 and DEC are thus transformed into histogram representations of the model function. (Refer to Eq. 4.7 and the subsequent discussion.)

The convolution is performed in the subroutine CONVOL called by FCODE. The two histograms representing the model function and instrument response function are convoluted according to Eq. 4.7 and the results replace the contents of the array DEC. The values of the convoluted function are returned to LSQENP as required.

The subroutine PCODE operates in a manner analogous to FCODE. LSQENP calls PCODE to calculate the partial derivatives of the model function with respect to each variable in the fit. The subroutines VHIST and VONVOL perform the same functions in PCODE as HIST and CONVOL perform in FCODE. The difference in these subroutines is that VHIST and VONVOL use virtual arrays exclusively. This is necessary because of the large number of arrays used in PCODE and a shortage of directly addressable memory in the MINC-23 computer to handle them. Virtual memory is a software controlled memory reallocation scheme which extends the memory capacity available to a program. Data access

time is sacrificed when virtual arrays are addressed so their use should be avoided for frequently called arrays.

Least Squares Estimation of Nonlinear Parameters

LSQENP uses the values of the convoluted function from FCODE and the convoluted partial derivatives from PCODE to conduct its search for the best fit between the experimental decay and the convoluted function. The value of χ^2 (Eq. 4.1) is calculated for each iteration of LSQENP and the search is terminated when χ^2 is minimized. The search algorithm was developed by Marquardt [45] and is also discussed by Bevington [32]. This algorithm utilizes features of two methods of minimizing χ^2.

If we think of χ^2 as mapping a hypersurface in K-dimensional space where K is the number of parameters in the model function, a gradient search can be used to indicate the direction of a minimum of the χ^2 surface. The gradient of χ^2 [32]

$$\nabla\chi^2 = \sum_{j=1}^{k} \left[\frac{\partial\chi^2}{\partial a_j} \hat{a}_j\right] \tag{4.8}$$

is the vector indicating the direction of steepest ascent of χ^2. The components of the gradient indicate the direction and rate of change of χ^2 with respect to the individual parameters. A step size is chosen for the parameters. The

parameters are changed so that χ^2 changes in the opposite direction of that indicated by the gradient.

The search works well at the early stages of the search. As the minimum in χ^2 is approached (i.e., the partial derivatives get very small) it becomes difficult for the gradient search to precisely locate the minimum. A smaller step size for the parameters would increase the precision of the search at the expense of an increased number of the computations.

An alternative to the gradient search would be to define an analytic function which describes the χ^2 as a function of the parameters can approximate the shape of the hypersurface as a parabola and the function parameters which provide a minimum in the value of χ^2 can be derived. This method is efficient and precise if the starting position is near the minimum. If the starting position is not near the minimum, the parabolic approximation of the χ^2 hypersurface is not valid and this method cannot be expected to find the neighborhood of the minimum.

The Marquardt algorithm combines the best features of these two types of searches. The result is an algorithm which interpolates between the two extremes of the gradient and Taylor's series search [32]. The direction and step size are determined for the search based on the signs and magnitudes of the partial derivatives calculated in PCODE.

In order to eliminate unnecessary calculations, the subroutine BCHECK is called by LSQENP to look for values of the parameters which represent physically unreasonable situations. Restrictions on the sign or range of values for a parameter can be imposed in BCHECK. If LSQENP has assigned a parameter value outside of the restrictions, control is returned to a point in LSQENP which reevaluates the parameters before FCODE is called to calculate function values based on the "unphysical" parameters. BCHECK must be modified to accommodate each new model used in FCODE.

Global Data Analysis

The foregoing discussion has assumed that a single set of data is being fit to a single decay model. In the sample program in Appendix B and in many other data fitting situations, we use a global approach to simultaneously fit data described by different model decays [48]. While an independent fit of each set of data to the appropriate decay model could be carried out, that type of analysis ignores relationships which may exist between the decay models. These relationships may incur additional restrictions on the value of a parameter so that its value can be determined more accurately. A subset of the total parameters can be linked together so that common values for these linked

parameters are found which satisfy all of the model functions. Fits for each model in the global analysis contribute to the total χ^2 which is now the quantity to be minimized.

For example, $I_{//}(t)$ and $I_{\perp}(t)$ (Eqs. 2.6) are fit simultaneously for each donor concentration C_D studied. These two fitting models are forced to have the same value of C_D. This is physically reasonable since the data were collected from the same sample. The value of the combined χ^2 is minimized. Since a change in C_D has an opposite effect in the rates of decay of $I_{//}(t)$ and $I_{\perp}(t)$, linking the two fits forces C_D to converge to a value appropriate for the model rather than fitting possible systematic artifacts in the data.

Linking parameters in a global fit also reduces the covariance (coupling) between different parameters. $I_{//}(t)$ depends on both the reduced concentration of donors C_D and the fluorescence lifetime τ. The increase in the decay of $I_{//}(t)$ resulting from an increase in C_D can be compensated for by decreasing τ. This means that with noise present in the data the fitting procedure may not find the unique set of parameters C_D and τ which represent the true decay. Additional constraints placed on the parameters by the inclusion of another set of data with a different fitting model can alleviate this type of coupling and lead to more accurate determination of parameter values.

Table III of Chapter V indicates the accuracy of parameter recovery for simulated data. Simulated $I_{\parallel}(t)$ and $I_{\perp}(t)$ profiles are fit independently and globally with the parameters τ and C linked. Note that the quality of the fit for the independently fit functions is better as indicated by the lower values of the reduced χ^2. However, the accuracy in the recovered parameters is better in the linked fit.

In the Fortran program, the linking of common parameters between model functions is controlled with the 2-dimensional array IMAP. The number of rows is equal to the largest number of parameters used in an included model function. The number of columns is equal to the number of model functions included in the fitting procedure. In general, IMAP can be extended to include any number of functions; there need not be a one-to-one correspondence between the parameters of the various functions. In Appendix A, IMAP includes two functions each with the same five parameters. The indices of the 1-dimensional arrays IFIX and ILINK have a one-to-one correspondence with the rows (parameters) of IMAP. IFIX indicates which row of parameters should remain fixed at the initially input values throughout the fitting procedure. ILINK indicates which parameters should be linked together and which should have their values varied independently throughout the fitting procedure.

Including more than one model necessarily results in a more complicated program. FCODE must include each model; PCODE must include the partial derivatives for each model; and LSQENP must calculate the χ^2 contribution for each model and sum them.

Termination of Parameter Search

LSQENP terminates its search for the set of parameters which minimize χ^2 when one of several criteria are met. Table 4.1 lists the value of the variable IDONE in LSQENP corresponding to a particular convergence test along with a description of the test. Further details of the convergence criteria are given by Marquardt [45]. Figure 4.2 is a flowchart indicating the possible pathways for the termination of the search in LSQENP.

Quality of Fit

Several criteria can be used to judge the quality of the fit obtained. The value of χ^2 is an indication of the dispersion between the observed function values and the expected values [32]. The observed deviation is divided by the expected deviation (Eq. 4.1). If the observed and expected deviations are approximately equal for all data points, $\chi^2 \simeq N$ the number of data points. Dividing the χ^2

TABLE 4.1 Explanation of convergence criteria for the subroutine LSQENP

IDONE	TEST	CONDITION
1	FORCE OFF	No convergence criteria were met after the completion of a user defined number of iterations.
2	EPSILON	This is the preferred convergence criteria. The step size for each parameter has become very small relative to the parameter value. The limits on the relative size are set by the constants TAU and E in BLOCKDATA.
3	CHI-SQUARED	The change in χ^2 after the completion of an iteration is <0.01%.
4	GAMMA EPSILON	The EPSILON TEST is passed only after the step size has been cut in half one or more times. It is assumed that χ^2 is minimized within computing round-off error if this test is passed.
5	GAMMA LAMBDA	Computer round-off error is determining the step size. This usually indicates high parameter correlation.

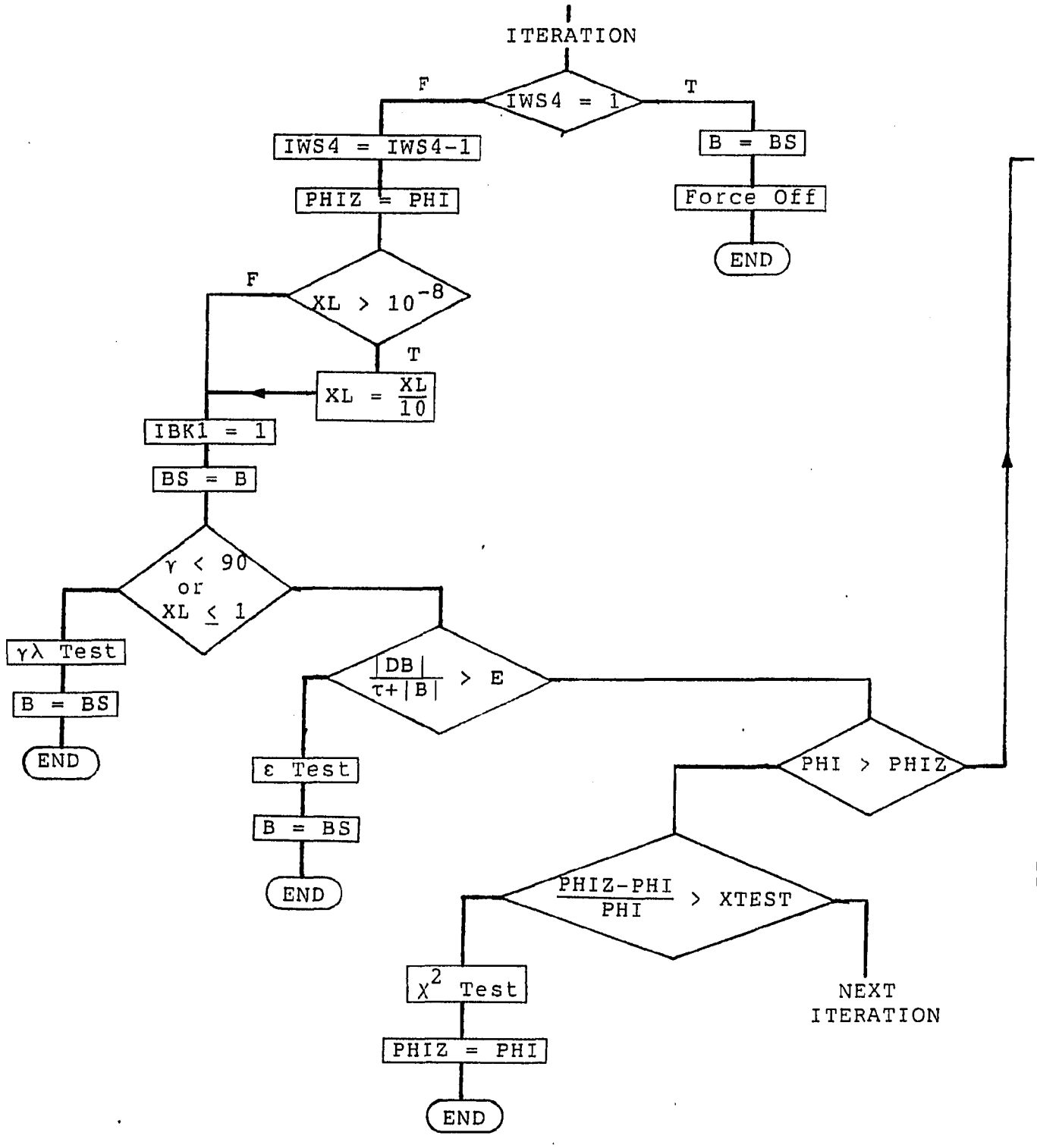

Figure 4.2 Convergence flowchart for LSQENP

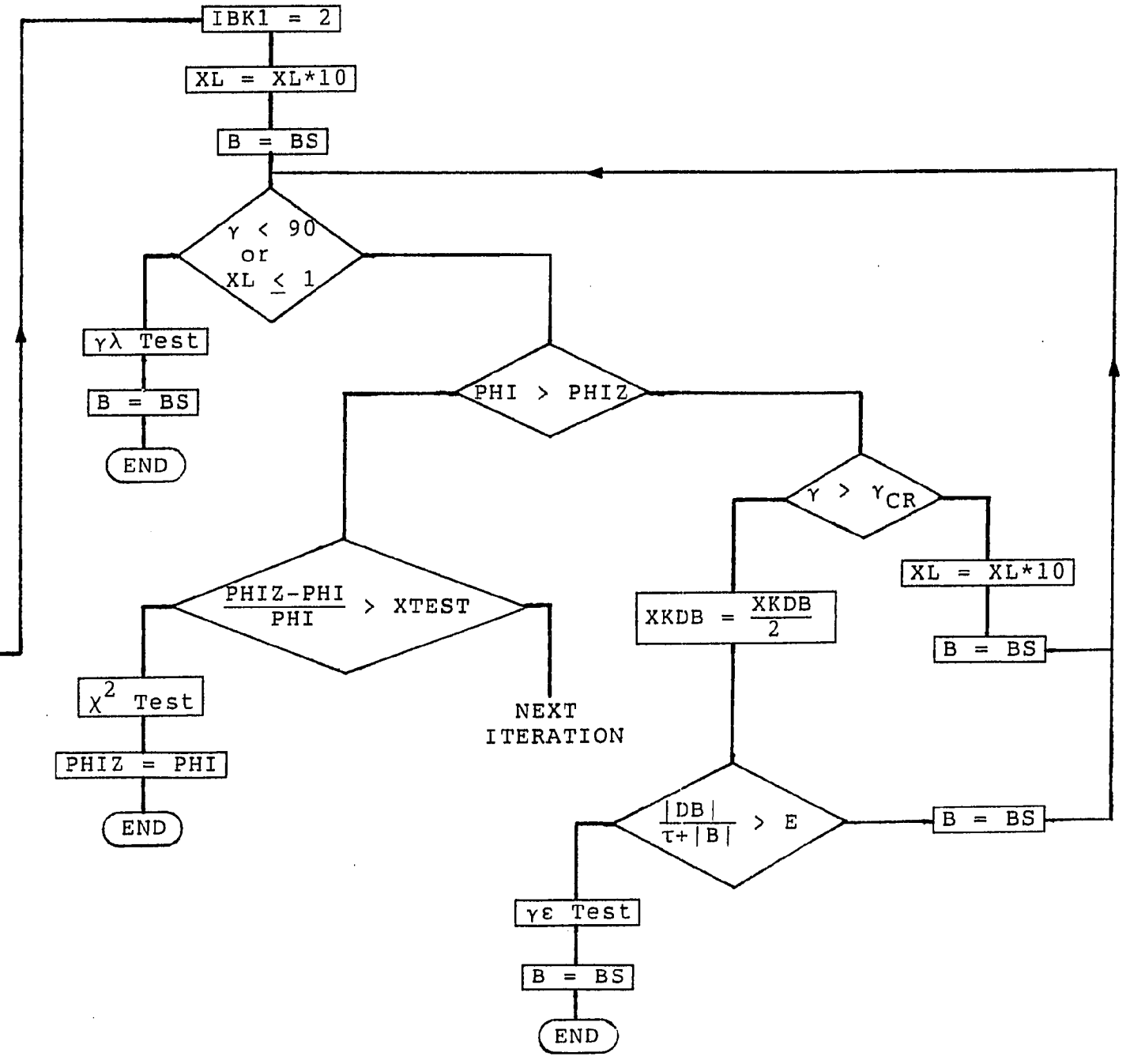
IBK1 = 2
XL = XL*10
B = BS
γ < 90 or XL ≤ 1
γλ Test
B = BS
END
PHI > PHIZ
γ > γCR
XL = XL*10
B = BS
XKDB = XKDB/2
(PHIZ-PHI)/PHI > XTEST
χ2 Test
PHIZ = PHI
END
NEXT ITERATION
|DB|/(τ+|B|) > E
B = BS
γε Test
B = BS
END

by the number of degrees of freedom

$$\nu = N - n - 1 \tag{4.9}$$

where n is the number of variable parameters yields the reduced χ_r^2

$$\chi_r^2 = \chi^2/\nu. \tag{4.10}$$

A $\chi_r^2 \simeq 1$ indicates that the chosen model describes the observed dispersion well. Higher values of χ_r^2 may indicate that modifications to the model are needed.

Values of $\chi_r^2 > 1$ may be an artifact of the fitting procedure. When fitting the entire range of data collected in one of our experiments, deviations in the rising edge from the model can contribute significantly to χ^2. This is especially true since our instrument response function is represented by so few channels (~3-4 channels FWHM). The values for the rising edge of the convoluted function result from very few terms of the summation of Eq. 4.5 and can contain large errors. If the rising edge channels are omitted from the calculation of χ_r^2 values near 1 can be obtained with the proper model.

Values of $\chi_r^2 \simeq 1$ may also be obtained even if an improper model function is used in the fit if there is sufficient noise in the data. When the proper model is used the observed deviations should fluctuate randomly about the model. An incorrect model exhibits nonrandom fluctuations of the data around it although the value of χ^2 may not be significantly different.

A test of the randomness of scattering of the data points around the model function is to observe the autocorrelation of the weighted residuals [44]. Recalling the definitions of terms in Eqs. 4.1, 4.2, and 4.7, the autocorrelation of residuals is

$$A_n = \frac{2N'}{(N - M)} \frac{\sum_{i=1}^{(N-M)/2} Y_i^{-1/2}(C_i - Y_i)Y_{i+n}^{-1/2}(C_{i+n} - Y_{i+n})}{\frac{1}{N'} \sum_{i=1}^{N'} (C_i - Y_i)^2/Y_i} \quad (4.11)$$

with the additional term N′ equal to the number of channels in the fluorescence data set. Random scatter of the data points about the model function will yield an autocorrelation of the weighted residuals with low amplitude, high frequency fluctuations about the zero-line (Fig. 4.3a). Nonrandom scatter will show up as a low frequency modulation of the autocorrelation about the zero-line (Fig. 4.3b).

As the signal-to-noise ratio of the photon counting data becomes greater, the autocorrelation of the weighted residuals is increasingly influenced by artifacts of data collection. The apparent nonlinearity of the TAC is manifested as low frequency oscillations in the autocorrelation function. The number of peak counts obtained before the artifact induced oscillations become apparent depends on the fluorescence lifetime τ_f of the sample. Longer-lived species such as rhodamine 640

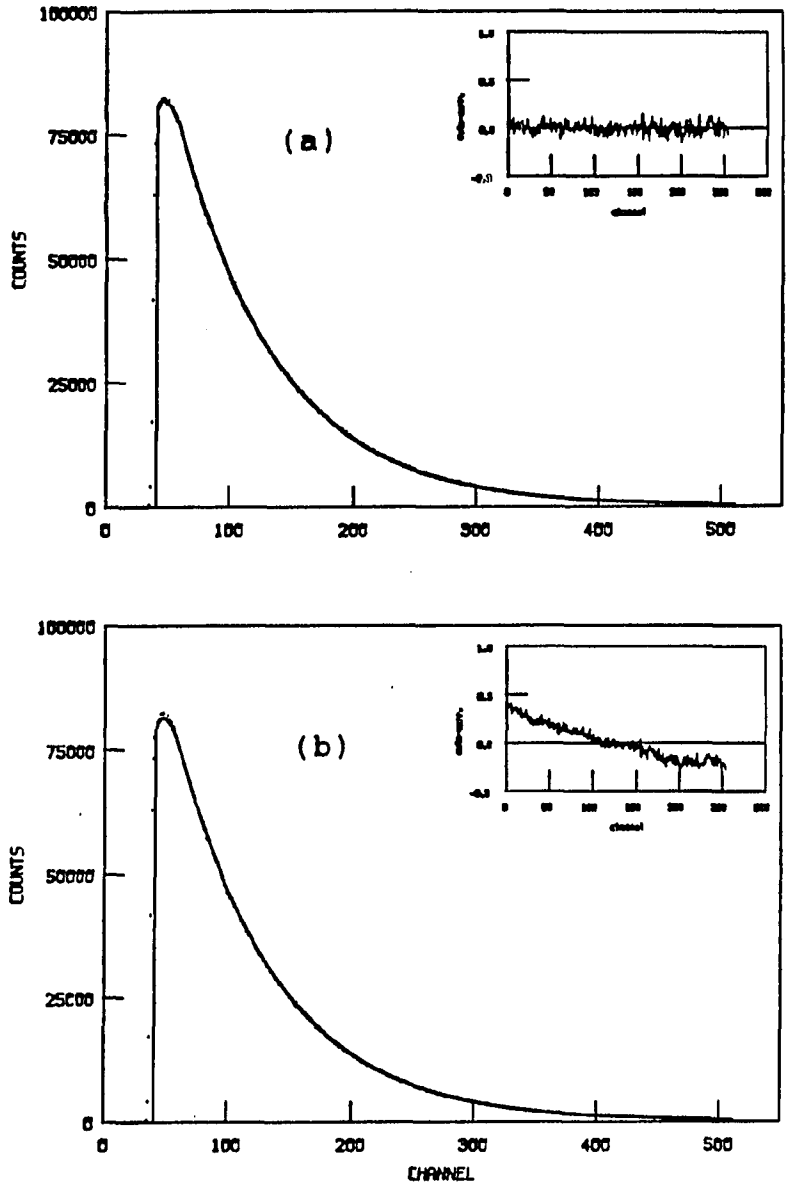

Figure 4.3 Fitted fluorescence profiles showing the autocorrelations of the weighted residuals. The fit in (a) appears to be good and the autocorrelation of the residuals indicates random scatter of the data about the fitting model. The fit in (b) appears to be good but the modulation of the autocorrelation of the residuals indicates systematic deviations of the data from the fitting model

(τ_f = 3.4 ns in glycerol) have a high signal-to-noise ratio in the tail region as well as the peak in our 10 ns window and the oscillations can be seen when ~$6x10^4$ counts are accumulated in the peak channel. For shorter-lived species such as DODCI (τ_f = 1.7 ns in glycerol) the oscillations are not noticed even when ~10^5 counts are accumulated in the peak channel. The autocorrelation of the weighted residuals has a decreased utility as a test for the appropriateness of a given model function when the signal-to-noise gets very high. It can be, however, a useful tool for the diagnosis of systematic artifacts which may affect data collected on the system.

FLUORESCENCE DEPOLARIZATION OF RHODAMINE 6G IN GLYCEROL: A PHOTON-COUNTING TEST OF 3-DIMENSIONAL EXCITATION TRANSPORT THEORY

David E. Hart, John F. Hedstrom, Philip A. Anfinrud, and Walter S. Struve

Department of Chemistry and Ames Laboratory - USDOE
Iowa State University, Ames, Iowa 50011

CHAPTER V. FLUORESCENCE DEPOLARIZATION OF RHODAMINE 6G IN GLYCEROL: A PHOTON-COUNTING TEST OF 3-DIMENSIONAL EXCITATION TRANSPORT THEORY

Introduction

It has been long recognized that accurate modeling of fluorescence concentration depolarization in solution is a formidable theoretical problem. Early attempts to describe the influence of Förster dipole-dipole excitation transport [1] on fluorescence depolarization frequently assumed that transfer was limited to one or two excitation hops from the initially excited molecule [2, 3], or that excitation was exchanged only between nearest and next-nearest neighbor molecules in solution [4-6]. To our knowledge, the first realistic calculations of the probability $G^S(t)$ that excitation is found on the initially excited molecule at time t were provided by Gochanour, Andersen, and Fayer [7], who worked out diagrammatic Green's function expansions of solutions to the excitation transport master equation [8] and obtained successive self-consistent approximations to $G^S(t)$. The latter Green's function is related to the fluorescence depolarization in solution by [9]

$$G^S(t) = 2.5 \frac{I_{//}(t) - I_{\perp}(t)}{I_{//}(t) + 2I_{\perp}(t)} \qquad (1)$$

where $I_{//}(t)$ and $I_{\perp}(t)$ are the fluorescence intensity components polarized parallel and normal to the excitation polarization. (This equation holds if the solvent is viscous enough to inhibit rotational depolarization during the fluorescence lifetime, if the molecular absorption and emission transition moments coincide, and if the excitation pulse energy is small enough so that the orientational distribution of unexcited molecules is random.) Gochanour and Fayer [9], (hereafter GF) tested their second-lowest (three-body) self-consistent approximation to $G^s(t)$ by measuring the experimental time-dependent fluorescence components

$$\begin{aligned} I_{//}(t) &= Ae^{-t/\tau}\,[1 + 0.8G^s(t)] \\ I_{\perp}(t) &= Ae^{-t/\tau}\,[1 - 0.4G^s(t)] \end{aligned} \qquad (2)$$

for rhodamine 6G (rh6G) in glycerol. By computing the three-body Green's function $G^s(t)$, which depends on the known rh 6G concentration and on the isotropic dye lifetime τ (which they measured at sufficiently high dilution so that $G^s(t) \to 1$ for all t), they were able to check experimental fluorescence intensities against convolutions of their Gaussian experimental response function with theoretical profiles generated from Eqs. 2. Excellent visual agreement was obtained, with divergences of $\lesssim 5\%$ for times up to $\sim 2.5\tau$ ($\sim$8 ns).

GF obtained their fluorescence profiles by KDP sum-frequency mixing of rh 6G fluorescence with variably delayed 1.06 μm pulses from a CW mode-locked Nd:YAG laser, and the resulting 390-nm up-converted pulses were detected by a cooled photomultiplier and lock-in amplifier. In this paper, we use time-correlated photon counting to obtain time-dependent fluorescences for rh 6G in glycerol. This technique [10] offers far superior data statistics, and autocorrelation functions of the residuals [11] can elicit systematic deviations between data and theoretical profiles which are too small to observe using sum-frequency mixing. Our data analysis (Experimental Section) provides a check on whether the polarized fluorescence components actually exhibit the form of Eqs. 2, or whether the single-exponential factors are distorted, e.g., by excitation trapping at rh 6G dimers, which accelerates fluorescence decay and renders it nonexponential in highly concentrated solutions. Our analysis also avoids parameter correlation (covariance) between the rh 6G concentration (which influences $G^S(t)$) and τ in Eqs. 2, so that it is unnecessary to rely on independent low-concentration measurements to obtain the isotropic dye lifetime τ. This advantage is important, because τ varies significantly with rh 6G concentration even in 10 μm path length fluorescence cells due to self-absorption [12] and (at the higher concentrations) excitation trapping. It develops that

because the absorption and fluorescence spectra of rh 6G overlap so much near 540 nm [12], self-absorption cannot be even approximately suppressed in such thick cells at the millimolar concentrations over which excitation transport competes efficiently with intramolecular decay. At the lowest rh 6G concentrations, our fluorescence decay profiles prove to be indistinguishable from theoretical profiles calculated using the three-body Green's function $G^S(t)$ in Eqs. 2 when the autocorrelation of residuals are examined. Nonstatistical autocorrelations are obtained at higher rh 6G concentrations, but these differences are shown to arise largely from nonexponentiality in the isotropic decay function (i.e., excitation trapping by rh 6G dimers) and from self-absorption, rather than from inaccuracies in the three-body Green's function.

Experimental Section

An acousto-optically mode-locked argon ion laser (Coherent Innova 90 with 5 W plasma tube operated at 26 A) pumped a cavity-dumped rhodamine 590 dye laser (Coherent CR-599-01 tuned with three-plate birefringent filter) to produce tunable picosecond pulses which exhibited zero-background autocorrelations with ~8 ps fwhm. The mode locker was a Harris Corporation H-401 unit driven at 48 MHz.

The 4.8-MHz cavity dumper included a Harris Corporation H-100 acousto-optic modulator and H-102 driver, with folding reflectors mounted on Newport Research Corporation beam directors and Line Tool Co. translators. Laser performance was monitored and optimized with a rotating-mirror real-time autocorrelator [13].

Commercial rhodamine 590 chloride (rh 6G) was obtained from Exciton; the unpurified dye showed only one TLC spot using Analtech silica gel G plates and three different solvent systems (ethanol/acetone, ethanol/acetic acid, and 1-propanol/formic acid). Fluorescence cells were formed from $\lambda/4$ fused quartz flats by compressing a drop of solution between two flats. Optical density measurements on rh 6G solutions of known concentration in such cells showed that this procedure typically yielded solutions with ~10μm path length. Thinner cells (~2 - 4μm) could be obtained by etching the Al coating from a ~ 4mm diameter circular area of an optically flat front-surface reflector, and then bounding the sample between a surface so treated and a fused quartz flat.

Horizontally polarized 575 nm dye laser pulses were incident on the horizontal rh 6G cell surface at ~75° from normal. Fluorescence was collected vertically with a 5 cm focal length quartz lens and was focused by a 10 cm focal length lens through a variable rectangular aperture prior to detection by a Hamamatsu R1564U microchannel plate phototube

(MCP) with bialkali photocathode and borosilicate glass window. The MCP exhibited ~6 x 10^5 gain at -3000 V, 500 nm and a transit time spread of 76 ps at 3200 V. Laser scatter and filter fluorescence were minimized by two 3 mm Schott OG-590 filters and a 3 mm Schott RG-610 filter. Excitation pulses were focused with a 10 cm focal length quartz lens to ~0.1-mm diameter at the cell surface. The excitation and analyzer polarizers were Promaster Spectrum 7 photographic polarizers; the analyzer was placed between the cell and the collecting lens. The differential detector sensitivity to fluorescence photons polarized parallel and normal to the excitation polarization was conservatively less than 2%.

MCP photocurrent pulses were amplified and inverted using a B&H Electronics AC3011 MIC (3.15 GHz) 21 dB preamplifier and an EG&G IT100 inverting transformer. Amplified pulses were passed through a Tennelec TC455 quad constant-fraction discriminator (CFD) and served as START pulses in an Ortec 457 time-to-amplitude converter (TAC). An EG&G FOD-100 photodiode operating in the photoconduction mode sampled dye laser pulses; its signal was processed through an Ortec 934 quad CFD to provide STOP pulses. TAC output was stored in a Canberra Series 30 MCA operated in the PHA mode to yield 5.0, 10.0, or 20.0 ps channel resolution. Instrument functions for deconvolution of raw data were obtained by scattering 575-nm laser pulses from a clean quartz substrate, and typically exhibited ~80 ps fwhm.

After transfer to a Digital Equipment Corporation MINC-23 system with dual floppy disk drive operating in an RT-11 environment with FB monitor, fluorescence profiles were analyzed with a Marquardt nonlinear regression [14] program.

Data Analysis

For a given fluorescence decay law N(t), the convolute-and-compare analysis forms the convolution C_n in the nth channel of N(t) with the instrument function x(t),

$$C_n = \sum_{i=1}^{N} x(i - s)N(n - i) \qquad (3)$$

where s is a variable, integral shift parameter. For the trial function N(t), we use $I_s(t)$ or $I_p(t)$ in Eqs. 2, with the three-body approximation [9] to the Green's function given by the numerical inverse Laplace transform [15] of

$$G^s(\varepsilon) = \tau\{(\pi^2\gamma^2C^2/4\,[1 - [1 + (32/\pi^2\gamma^2C^2)(\varepsilon\tau - 0.1887\gamma^2C^2)]^{1/2}] + 4(\varepsilon\tau - 0.1887\gamma^2C^2)\}/[4(\varepsilon\tau - 0.1887\gamma^2C^2)^2] \qquad (4)$$

Here $\gamma = 0.846$ is a constant which arises from the dipole-dipole orientational dependence of the excitation transfer probability [9], and the reduced concentration

$$C = \frac{4}{3}\pi R_o^3 \rho \tag{5}$$

depends on the dye molecule number density ρ and on the Förster parameter R_o which characterizes the excitation hopping rate w_{jk} between molecules with transition moments oriented along d_j and d_k separated by distance R_{jk},

$$w_{jk} = \frac{3}{2\tau}\left(\frac{R_o}{R_{jk}}\right)^6 K_{jk}^2$$
$$K_{jk} = \hat{d}_j \cdot \hat{d}_k - 3(\hat{d}_j \cdot \hat{R}_{jk})(\hat{d}_k \cdot \hat{R}_{jk}) \tag{6}$$

Since $G^s(t)$ depends on the reduced concentration C and on the isotropic lifetime τ, convolutions of the model functions in Eqs. 2 with the instrument function contain four adjustable parameters: A, τ, C, and s. (Cavity-dumping at 4.8 MHz made it unnecessary to include the base line as an adjustable parameter, or to build the mode-locked laser pulse periodicity into the modeling function as was done in earlier work [16].) These four parameters can be simultaneously optimized in the nonlinear regression program to minimize the statistically weighted χ^2

$$\chi^2 = \sum_{i=M}^{N} (C_i - Y_i)^2 / Y_i \tag{7}$$

where Y_i is the number of fluorescence counts accumulated in channel i and (M, N) is the channel range used in the analysis. Our 80 ps fwhm instrument function was not wide compared to the 20 ps channel spacing. Since the convolute-and-compare analysis was restricted to integral shift parameters s, choosing M = 1 produced disproportionate contributions to χ^2 from the rising-edge portion of the fluorescence profiles. Channel M was instead typically placed on the rising edge at 90% peak counts, and the continuous curves representing optimized fits to our data profiles (Results and Discussion Section) begin with channel M.

Covariance can compromise the uniqueness of fits based on simultaneous variation of C and τ, because increases in C can be compensated by increases in τ to yield a Green's function which is nearly unchanged over the analyzed channel range. The isotropic lifetime τ was therefore extracted from single-exponential fits to magic-angle fluorescence profiles, which were accumulated at all rh 6G concentrations with an analyzing polarizer aligned at 54.7° from the excitation polarization to yield profiles proportional to $I_{//}(t) + 2I_{\perp}(t)$. The results of such single-exponential fits to magic-angle profiles are summarized in Table I for five rh 6G concentrations between 1.43×10^{-5} and 4.12×10^{-3} M. The cell thickness in all cases was 10 μm. The visual quality of the fits is shown for four of the samples in

Table I. Magic-angle fits of rhodamine 6G fluorescence profiles

Sample	Concentration, M	τ, ns	χ^2_r
1	1.43×10^{-5}	3.40	1.180
2	6.29×10^{-4}	3.56	1.944
3	1.62×10^{-3}	3.72	2.306
4	2.45×10^{-3}	3.78	3.237
5	4.12×10^{-3}	3.32	3.782

Figure 1. Reduced χ^2 values tend to increase with concentration, and they range from ~1.1 to 3.8. The relative inaccuracy of the single-exponential fit in the latter case arises from nonexponential decay behavior introduced by excitation trapping [17] by rh 6G dimers, which are more numerous at the higher concentrations. The autocorrelations of residuals [13]

$$A_n = \frac{2N'}{(N - M)} \frac{\sum_{i=1}^{(N-M)/2} Y_i^{-1/2}(C_i - Y_i)Y_{i+n}^{-1/2}(C_{i+n} - Y_{i+n})}{\sum_{i=1}^{N'} Y_i^{-1}(C_i - Y_i)^2} \qquad (8)$$

with N′ equal to the number of channels comprising the fluorescence profile, provide a more discriminating test for quality of fit. The nearly statistical autocorrelation which is shown for the lowest concentration in Figure 1 shows that the magic-angle profile is nearly indistinguishable from single-exponential decay under present counting statistics.

Of particular interest in Table I is the marked variation of the optimized lifetime τ with rh 6G concentration. Though all of the magic-angle profiles in this table were obtained with 10 μm fluorescence cells, self-absorption (which dilates the fluorescence lifetime without sensibly affecting its exponentiality [12])

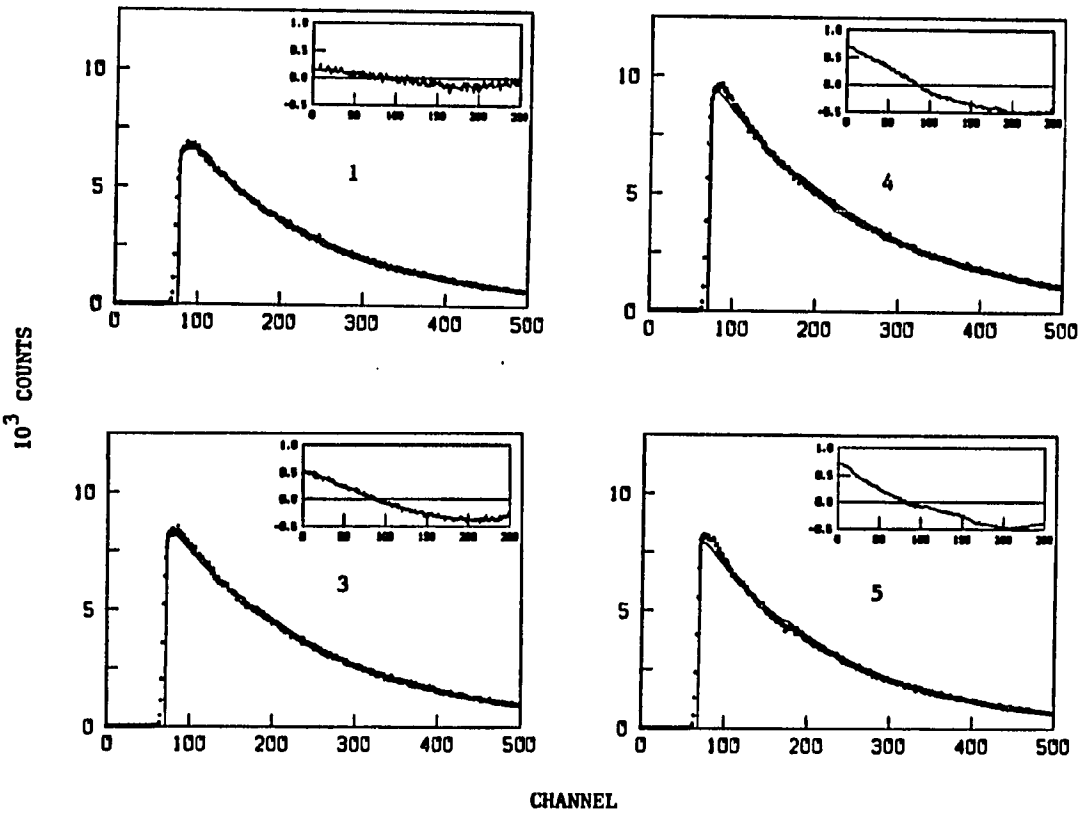

Figure 1. Magic-angle fluorescence profiles for samples 1, 3, 4, and 5 in Table 1. Continuous curves are optimized convolutions of single-exponential decay functions with the instrument function Inset plots show autocorrelations of residuals. Time calibration is 20 ps per channel. Cell thickness was 10 μm in each case

increases τ from 3.40 to 3.78 ns in samples 1 - 4; excitation trapping reduces τ to 3.32 ns at the highest concentration (sample 5). Much larger τ variation with rh 6G concentration (up to 4.83 ns at 2.45×10^{-3} M) was observed in a 100-μm cell. Following Hammond [12], the isotropic lifetimes τ may be converted into lifetimes τ_c corrected for self-absorption via

$$\tau_c = \tau(1 - aQ_o) \tag{9}$$

with

$$aQ_o = 2.65cl \int_o^\infty \varepsilon_F E(\lambda)(0.0039 - \log A_F)\, d\lambda \tag{10}$$

$E(\lambda)$ is the rh 6G emission spectrum normalized to the fluorescence quantum yield Q_o, ε_F is the rh 6G absorption coefficient at the fluorescence wavelength, A_F is the sample absorbance at the fluorescence wavelength, c is the solution concentration, and l is the cell length. Using values of ε_F, $E(\lambda)$, and Q_o for rh 6G in ethanol [12], one obtains the lifetimes τ_c corrected for self-absorption in Table II. For the four lowest concentrations, τ_c is between 3.32 and 3.39 ns; this mutual consistency strongly suggests that self-absorption is the primary origin of lifetime dilation in samples 1-4, and that a 10-μm cell is not thin enough to

Table II. Lifetime corrections for self-absorption

Sample	Path length, μm	a	τ, ns	τ_C, ns
1	10	0.003	3.40	3.39
2	10	0.058	3.56	3.37
3	10	0.106	3.72	3.35
4	10	0.131	3.78	3.32
5	10	0.160	3.32	2.82

completely remove this artifact at any of these concentrations. The correction is almost negligible ($\lesssim$0.3%) in sample 1, but amounts to ~12% in sample 4. For sample 5, τ_C is ~500 ps shorter than those found at lower concentrations, indicating that trapping is rapid at 4.12×10^{-3} M.

The magic-angle profile analyses provide initial τ values for deconvolution of the $I_{//}(t)$ and $I_{\perp}(t)$ profiles using Eqs. 2 and 4 as model functions. Both of these profiles are deconvoluted <u>simultaneously</u>, with C and τ linked by minimization of their combined χ^2 [18]. This procedure effectively eliminates parameter correlation, because the effects of changing C (or τ) have opposite sign in $I_{//}(t)$ and $I_{\perp}(t)$ according to Eqs. 2. This was demonstrated in trial deconvolutions of simulated profiles, computed by convoluting a 100 ps fwhm Gaussian instrument function with $I_{//}$ and $I_{\perp}$ decay laws calculated using Eqs. 2 and 4 with C = 0.5 and τ = 4.0 ns. Independent deconvolution of these simulated $I_{//}$ and $I_{\perp}$ profiles yielded optimized lifetimes of 4.016 and 4.008 ns, and optimized reduced concentrations of 0.535 and 0.468, respectively (Table III). In the linked deconvolution, the common values of τ and C converge to 3.996 ns and 0.5008 instead. Table III also shows that considerably larger fractional differences in C are obtained between independent and linked deconvolutions when C = 0.1 instead of C = 0.5 is used to

Table III. Deconvolutions of simulated $I_{//}$ and $I_{\perp}$ profiles

	τ = 4.000 ns, C = 0.500			
	independent		linked	
	$I_{//}$	$I_{\perp}$	$I_{//}$	$I_{\perp}$
A	0.1129	0.3049	0.1122	0.3025
τ, ns	4.0156	4.0077	3.9961	3.9961
C	0.5349	0.4684	0.5008	0.5008
χ_r^2	1.024	1.022	1.032	1.032

	τ = 4.000 ns, C = 0.100			
	independent		linked	
	$I_{//}$	$I_{\perp}$	$I_{//}$	$I_{\perp}$
A	0.1092	0.3206	0.1085	0.3188
τ, ns	4.0305	4.0257	3.9960	3.9960
C	0.1311	0.0797	0.0998	0.0998
χ_r^2	1.024	1.023	1.032	1.032

simulate the data profiles; this occurs because $G^S(t)$ is less sensitive to C when the latter is small. In each of these tests, Gaussian noise was added to the simulated profiles.

Covariance can thus be ruled out as a source of artifacts in our data analysis. The magic-angle analyses we have described show that excitation trapping by dimers considerably distorts the isotropic decay behavior at the highest concentration, and that lifetime dilation by self-absorption is difficult to suppress in rh 6G solutions. These phenomena affect the fluorescence anisotropy (and the measured Green's function $G^S(t)$) in ways which are difficult to correct for rigorously. Excitation trapping reduces the fluorescence depolarization and the apparent value of C, because excitation transport is interrupted at a lifetime shorter than the intramolecular lifetime τ_D. Self-absorption leads to inflated values of the measured reduced concentration, because absorption and reemission of fluorescence in solution contributes an additional mechanism for depolarization. A realistic assessment of these effects is important in a careful experimental test of excitation transport theory.

Results and Discussion

The polarized fluorescence profiles are displayed with the optimized convolutions of Eqs. 2 with the instrument function for samples 1, 3, 4, and 5 in Figure 2. These profiles exhibit the expected trend from slight to strong fluorescence depolarization over the rh 6G concentration range 1.43×10^{-5}, 4.12×10^{-3} M within the displayed time period of ~10 ns. In Table IV, we list the final fitting parameters for these $I_{//}(t)$ and $I_{\perp}(t)$ profiles. The visual fits, the reduced χ^2 values in Table IV, and the autocorrelations of residuals shown in Figure 2 all tend to worsen at the highest rh 6G concentrations. The origin of part of these discrepancies is clearly the fact that the magic-angle profiles are not precisely single-exponential (Figure 1), especially at the highest concentrations, so that the single-exponential isotropic factors in Eqs. 2 cannot represent the true decay behavior. The least-squares program attempts to compensate for this nonexponentiality by adjustment of the parameters in $G^s(t)$ when fitting $I_{//}(t)$ and $I_{\perp}(t)$, with the result that the autocorrelations in some cases (samples 2 and 3) are markedly better for the $I_{//}(t)$ profile than for the magic-angle profile. The trend in optimized reduced concentrations C vs. rh 6G molarity M is summarized in Figure 3 for samples 1-5, with additional data points added for a sample with $M = 1.76 \times 10^{-4}$ M. Solutions

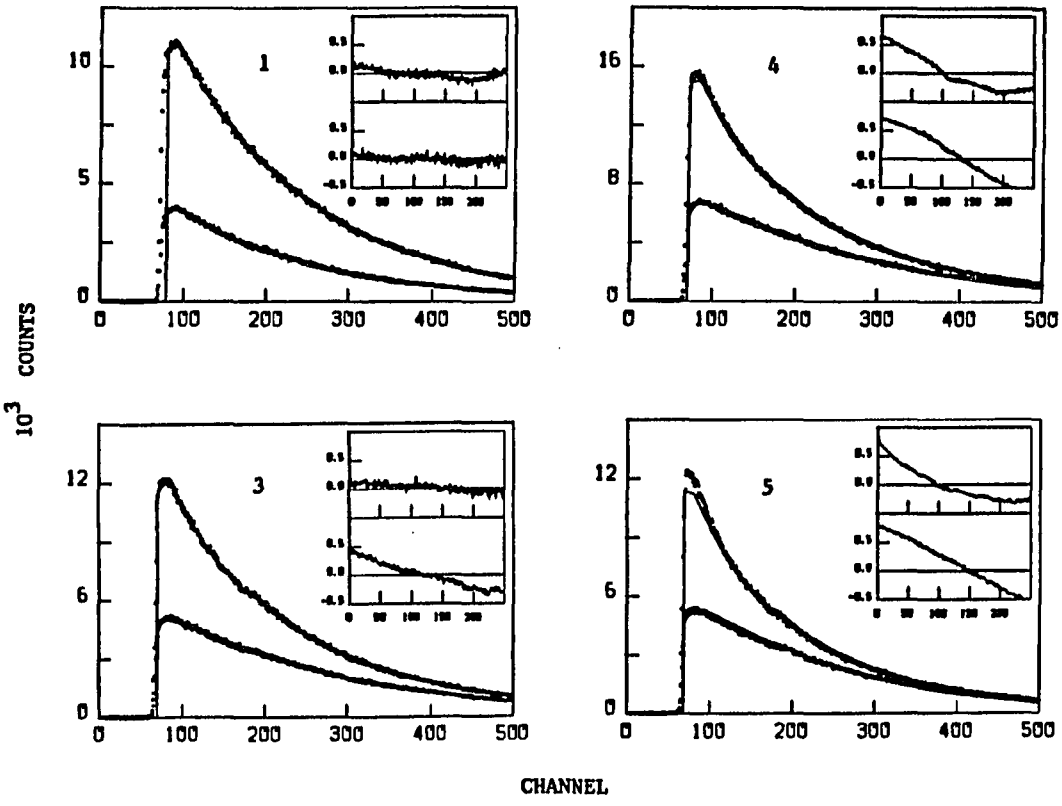

Figure 2. Fluorescence profiles $I_{//}(t)$ and $I_{\perp}(t)$ for samples 1, 3, 4, and 5 in Table 1. Continuous curves are optimized convolutions of model functions computed from Eqs. 2 and 4 with the instrument function. Upper and lower inset plots show autocorrelations of residuals for $I_{//}(t)$ and $I_{\perp}(t)$, respectively. Time calibration is 20 ps per channel; cell thickness was 10 μm in each case

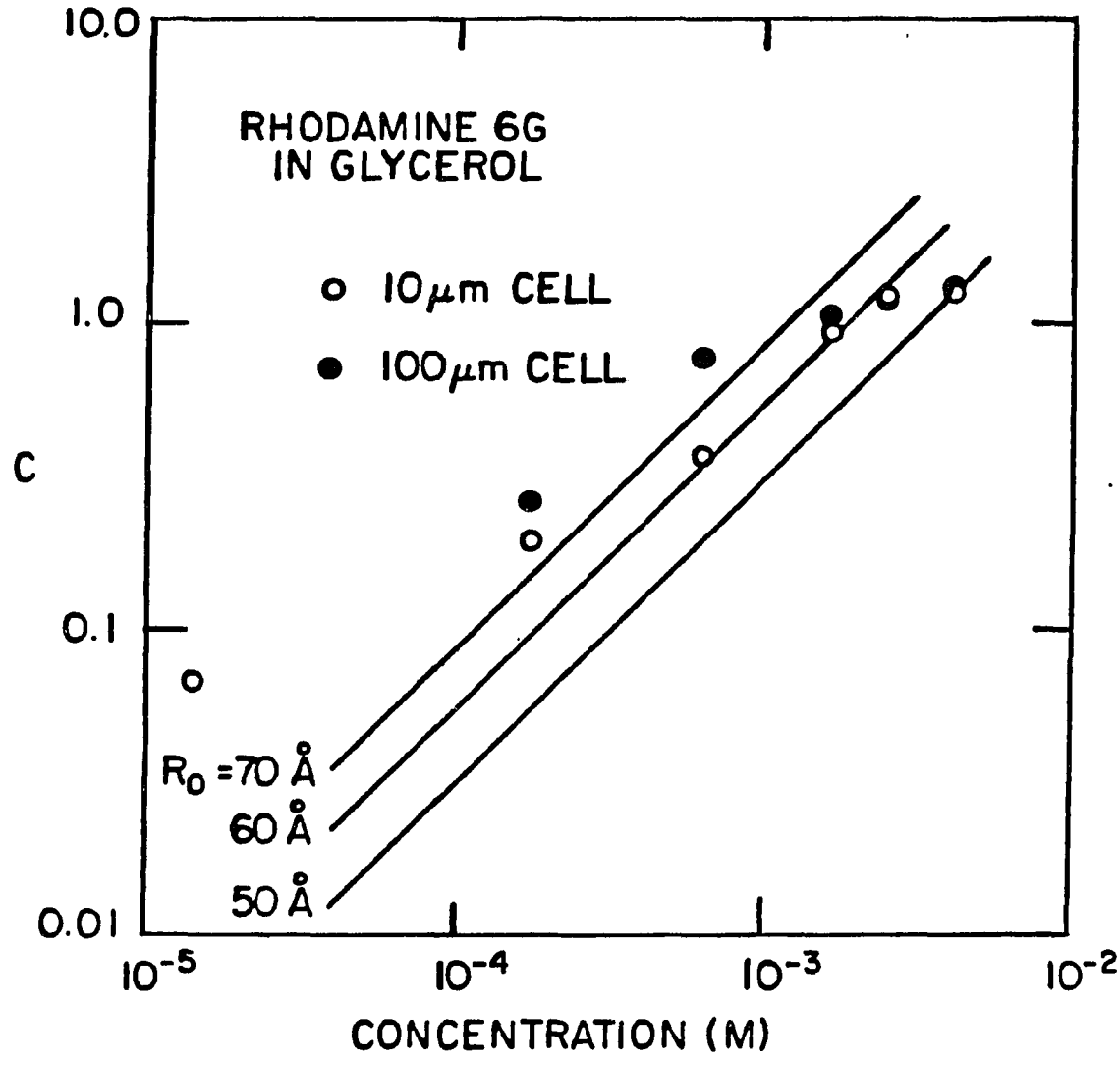

Figure 3. Optimized reduced concentrations C of rh 6G solutions, from nonlinear least-squares fits to $I_{//}(t)$ and $I_{\perp}(t)$ profiles of model functions calculated from three-body Green's function $G^{s}(t)$. Data points are included for solutions in 10-μm cell (O) and 100-μm cell (●). Straight lines give actual reduced concentration vs. rh 6G solution molarity for dyes with Förster parameters R_0 = 50, 60, and 70 Å

Table IV. Fitting parameters for anisotropic fluorescence profiles

$$I_{//}(t) = Ae^{-t/\tau}[1 + 0.8G^S(t)]$$

$$I_{\perp}(t) = Ae^{-t/\tau}[1 - 0.4G^S(t)]$$

Sample	τ, ns	C	χ^2_r
1	3.41	0.0675	1.141 1.172
2	3.68	0.368	1.318 1.926
3	3.77	0.927	1.270 2.153
4	3.69	1.22	3.006 4.501
5	3.22	1.26	6.170 5.268

with cell thicknesses of both 10 μm and 100 μm (the 100 μm sample profiles and fitting parameters are not shown) are included in this plot. C should in principle be proportional to M through Eq. 5, this is approximately obeyed only by the 10-μm samples over the limited concentration range 6×10^{-4}, 2.4×10^{-3} M, where the proportionality factor corresponds to R_0 ~60 Å. At higher concentrations, C values obtained in both 10-μm and 100-μm cells level off due to excitation trapping, which artificially depreciates the apparent reduced concentration. The separations between the 10-μm and 100-μm data points at the other concentrations are a consequence of greater self-absorption in the thicker samples, and they show that this effect can materially influence the measured fluorescence anistropy as well as the isotropic lifetimes in our samples (Table II).

Our method of data analysis formally differs from that of GF in that these authors varied C to most closely match their profiles with convolutions of Eqs. 2 at one concentration (2.6×10^{-3} M, comparable to that of our sample 4). This optimized value of C (0.83) was used to infer that R_0 = 50 Å, and this value of the Förster parameter was used to calculate theoretical decay profiles for comparison with their data obtained at other concentrations, yielding visually excellent results. If they were so handled, our data would have yielded similar

results, but with a somewhat larger empirical value of R_0 between 50 and 60 Å (Figure 3). What our present analysis shows is that the apparently small differences between the calculated and experimental profiles arise primarily from self-absorption and excitation trapping artifacts, rather than from discrepancies between the three-body and true Green's functions $G^S(t)$. Avoiding such artifacts would require better sample design: thinner sample cells and more effective inhibition of rh 6G aggregation. GF employed cells ranging from 300 to 5 μm in thickness, and we used 10 μm cells at all of our concentrations. Figure 3 and Table II together suggest that cells thinner than ~2μm should be used, at least at the highest concentrations. We constructed such cells by etching 4mm diameter areas of Al coating from $\lambda/4$ glass substrates using HF solution, only to find that the substrate material itself fluoresced in the red under 575 nm laser excitation. Experiments with well-constructed cells ~1μm thick are planned in our laboratory. Excitation trapping is clearly a more persistent problem, particularly in the dynamically interesting high-concentration regime in which breakdowns in any self-consistent approximation to $G^S(t)$ will first become apparent. Self-absorption can be minimized in well-designed transient-grating experiments [19] to test the excitation transport theory. Such experiments do not offer data with the statistical quality available in photon counting, and

their results are similarly influenced by excitation trapping if the latter is not properly taken into account.

Our data points for the two lowest concentrations in Figure 3 lie significantly higher than would be expected for physically reasonable Förster parameters R_o. Self-absorption is not likely to contribute significantly at such concentrations; the large divergences are in part a consequence of the relative insensitivity of $G^s(t)$ to C for $t \leq 2\tau$ when $C \lesssim 0.1$.

Very recently, Fedorenko and Burshtein [20] demonstrated that the inverse Laplace transform of Eq. 4 can be inverted analytically, and compared the long-time asymptotic behavior of the three-body $G^s(t)$ with the known asymptotic behavior [21] of the true Green's function. Considerable emphasis was placed on the fact that the three-body theory exhibits incorrect long-time behavior. In "static-quenching" situations in which the reduced dye concentration C is negligible compared to the reduced trap concentration C_T, $G^s(t)$ is given exactly by [22]

$$G^s(t) = \exp[-C_T(\pi t/\tau)^{1/2}] \qquad (11)$$

It is readily shown in such cases (cf. Fig. 1 in Ref. 20) that the three-body Green's function is a very good approximation to the true $G^s(t)$ for $C_T \lesssim 1$ when $t \lesssim 2\tau$ (the experimental time regime investigated by GF and by us), but

progressively worsens at longer times. It seems reasonable a priori that the three-body $G^S(t)$ will exhibit similar behavior in the present systems ($C_T << C$), for which exact Green's functions have not been calculated. Indeed, our rigorous least-squares analysis of polarized photon-counting fluorescence profiles from rh 6G in glycerol shows that differences between the theoretical and experimental decay curves are dominated by trapping and self-absorption artifacts, rather than by errors in the three-body approximation. These differences are not very large (especially when viewed on a linear scale as in Figure 2), and in this sense the 3-body Green's function does provide a very good approximation.

It is obviously of interest to explore these systems' fluorescence profiles at longer times where the three-body approximation breaks down, since no current theory describes this regime accurately. This can be achieved using longer counting times in sample cells short enough to inhibit dynamic self-absorption effects, provided excitation trapping can be suppressed by minimizing dye aggregation. Such experiments are being developed in our laboratory.

Acknowledgment

The Ames Laboratory is operated for the U.S. Department of Energy by Iowa State University under Contract No. W-7405-Eng-82. This work was supported by the Office of Basic Energy Sciences. We thank Professor Michael Fayer for valuable discussions, and are indebted to Robert Crackel for his help with the corrections for self-absorption.

References

1. Förster, T. Discuss. Faraday Soc. 1959, 27, 7.
2. Galanin, M. D. Trudy Fiz. Inst. 1950, 5, 339.
3. Vavilov, S. I. Zh. Eksp. Teor. Fiz. 1943, 13, 13.
4. Craver, F. W.; Knox, R. S. Mol. Phys. 1971, 22, 385.
5. Craver, F. W. Mol. Phys. 1971, 22, 403.
6. Ore, A. J. Chem. Phys. 1959, 31, 442.
7. Gochanour, C. R.; Andersen, H. C.; Fayer, M. D. J. Chem. Phys. 1979, 70, 4254.
8. Förster, Th. Ann. der Phys. 1948, 6, 55.
9. Gochanour, C. R.; Fayer, M. D. J. Phys. Chem. 1981, 85, 1989.
10. O'Connor, D. V.; Phillips, D. "Time-correlated Single Photon Counting"; Academic Press: New York, 1984.
11. Grinvald, A.; Steinberg, I. Z. Anal. Biochem. 1974, 59, 583.
12. Hammond, P. R. J. Chem. Phys. 1979, 70, 3884.

13. Yasa, Z. A.; Amer, N. M. Opt. Commun. 1981, 36, 406.

14. Marquardt, D. W. J. Soc. Ind. Appl. Math. 1963, 11, 431.

15. Stehfest, H. Commun. ACM 1970, 13, 47.

16. Anfinrud, P.; Crackel, R. L.; Struve, W. S. J. Phys. Chem. 1984, 88, 5873.

17. Loring, R. F.; Andersen, H. C.; Fayer, M. D. J. Chem. Phys. 1982, 76, 2015.

18. Knutson, J. R.; Beechem, J. M.; Brand, L. Chem. Phys. Lett. 1983, 102, 501.

19. Miller, R. J. D.; Pierre, M.; Fayer, M. D. J. Chem. Phys. 1983, 78, 5138.

20. Fedorenko, S. G.; Burshtein, A. I. Chem. Phys. 1985, 98, 341.

21. Vugmeister, B. E. Phys. Status Solidi 1978, 906, 711.

22. Förster, Th. Z. Naturforsch., A: Astrophys., Phys. Phys. Chem. 1949, 4A, 321.

EXCITATION TRANSPORT IN SOLUTION: A QUANTITATIVE COMPARISON BETWEEN GAF THEORY AND TIME-RESOLVED FLUORESCENCE PROFILES

David E. Hart, Philip A. Anfinrud, and Walter S. Struve

Department of Chemistry and Ames Laboratory - USDOE
Iowa State University, Ames, Iowa 50011

CHAPTER VI. EXCITATION TRANSPORT IN SOLUTION: A QUANTITATIVE COMPARISON BETWEEN GAF THEORY AND TIME-RESOLVED FLUORESCENCE PROFILES

Introduction

There has been a resurgence of interest in the problem of electronic singlet excitation transport in solution, where the transport rates are governed by Förster dipole-dipole coupling [1]. One of the properties which characterizes transport in a system of N identical molecules which are randomly distributed in space is $G^s(t)$, the time-dependent probability that the excitation resides on the molecule which was initially excited at t=0. The calculation of $G^s(t)$ is a challenging theoretical problem: excitation can return to the initial site via hopping trajectories with unlimited length and topology, and an infinite-order density expansion must be summed to evaluate $G^s(t)$ exactly.

Gochanour, Andersen, and Fayer [2] (hereafter GAF), formulated diagrammatic expansions of the Laplace transform $\hat{G}^s(\varepsilon)$ of $G^s(t)$ in powers of ε. Using a series of self-consistent approximations, they obtained compact analytic expressions for infinite-order partial sums of the $\hat{G}^s(\varepsilon)$ expansions. These approximations to the Laplace transform were inverted numerically for selected molecule number

densities to obtain the two lowest-order self-consistent approximations (the 2-body and 3-body approximations) to $G^s(t)$. An intriguing feature of the GAF theory was the relative simplicity of its expressions for $\hat{G}^s(\varepsilon)$, since no assumptions limiting either the number of excitation hops [3, 4] or the number of neighboring molecules involved [5] were made. The 2-body and 3-body approximations both yielded mean-squared displacements $\langle r^2(t)\rangle$ approaching 6Dt at long times, where the diffusion coefficent D exhibited a correct number density dependence. D itself varied with t at early times, suggesting that the self-consistent approximations can at least qualitatively describe the transition from the nondiffusive (short-time, low-density) to diffusive (long time, high density) regimes.

There is no guarantee that the series of self-consistent approximations converges rapidly to the true Green's function $G^s(t)$. Fedorenko and Burshtein [6] recently analyzed the 2- and 3-body theories by showing that $\hat{G}^s(\varepsilon)$ can be inverted analytically. They demonstrated that while the exact Green's function must behave as [7]

$$G^s(t) \rightarrow \left[\frac{2\tau}{\pi C^2 t}\right]^{3/2} \qquad (1)$$

for times $t >> 18\tau/\pi C^2$ (where τ is the isolated-molecule excited state lifetime and C is a dimensionless molecule number density defined in Experimental Section and Data

Analysis Section), the 3-body Green's function behaves as

$$G^s(t) \rightarrow \frac{8}{\pi^{1/2}}\left[\frac{8\tau}{\pi^2 C^2 t}\right]^{3/2} \exp(-0.1197 C^2 t/\tau) \qquad (2)$$

at long times. The asymptotic 2-body Green's function differs from this only in the substitution of 0.3084 for the number 0.1197 in Eq. 2, so that the 3-body theory does not substantially correct the 2-body theory in this regime. The basic validity of the self-consistent equation used for generating the partial sums has also been questioned [8].

From the experimental perspective, the pertinent time regime is not so much the asymptotic region where Eq. 1 applies ($t \gtrsim 6\tau$ for $C = 1$, where the fluorescence count rate falls to $< 2 \times 10^{-3}$ times the peak count rate), but rather the physically interesting regime where $G^s(t)$ is falling violently during the transition from nondiffusive to diffusive behavior. In the absence of excitation traps (the "migration limit"), there is no expression for $G^s(t)$ whose accuracy has been confirmed at such times. In 3-dimensional disordered systems, $G^s(t)$ is related to the fluorescence intensity components $I_{//}(t)$ and $I_{\perp}(t)$ polarized along and normal to the laser excitation polarization by [9]

$$I_{\parallel}(t) = P(t)[1 + 0.8\ G^{S}(t)],$$

$$I_{\perp}(t) = P(t)[1 - 0.4\ G^{S}(t)] \qquad (3)$$

when the solvent is viscous enough to inhibit rotational depolarization, when the absorption and fluorescence transition moments are parallel, and when the exciting beam is sufficiently weak not to perturb the random orientational distribution of transition moments in unexcited molecules. P(t) is the isotropic decay function, which is single-exponential in the absence of excitation trapping of other artifacts. Gochanour and Fayer [9] measured polarized fluorescence profiles for rhodamine 6G in glycerol, and compared them with convolutions of their experimental response function with the 3-body approximation to $G^{S}(t)$. They obtained excellent visual agreement for $t<2.5\tau$ and concentrations up to 5.3×10^{-3} M. Anfinrud et al. [10] obtained a more stringent test of the 3-body theory for rhodamine 6G in glycerol using time-correlated photon counting, which can afford higher S/N ratios than profiles generated by KDP frequency-mixing of dye fluorescence with delayed 1.06 μm pulses from a Q-switched mode-locked Nd:YAG laser [9]. The photon-counting profiles were closely simulated using Eqs. 3 with the 3-body $G^{S}(t)$ for dye concentrations between 1.7×10^{-4} and 2.4×10^{-3} M. However, the experimental profiles proved to be strongly

distorted by self-absorption [11] (which dilates the measured isotropic lifetime τ and artificially inflated the observed depolarization) and by excitation trapping (which renders the isotropic decay nonexponential and truncates the depolarization). These artifacts dominated the differences between the experimental and optimized theoretical profiles.

In this work, we report photon-counting profiles for DODCI in glycerol. The large overlap between the absorption and fluorescence spectra in xanthene and carbocyanine dyes requires the use of fluorescence cells $\lesssim 2$ μm thick to avert self-absorption effects a millimolar concentrations [11]; cell thicknesses of 10 μm [10] and 5 to 300 μm [9] were used in earlier work. DODCI has a shorter isotropic lifetime τ than rhodamine 6G in glycerol (~1.7 vs. ~3.4 ns), giving an expanded dynamic range for testing $G^S(t)$ with our observation window (~10 ns). Longer counting times were employed to yield ~10^5 counts (S/N ~ 300) in the peak channel. With these modifications, the residuals between the experimental and 3-body theoretical profiles are no longer dominated by either self-absorption or trapping effects at concentrations below ~10^{-3} M.

It should be stressed here that extremely high precision is needed to achieve meaningful tests of transport theories using polarized fluorescence profiles. For illustration, we show convolutions in Fig. 1 of an instrument response function (generated by numerical convolutions of a 100 ps

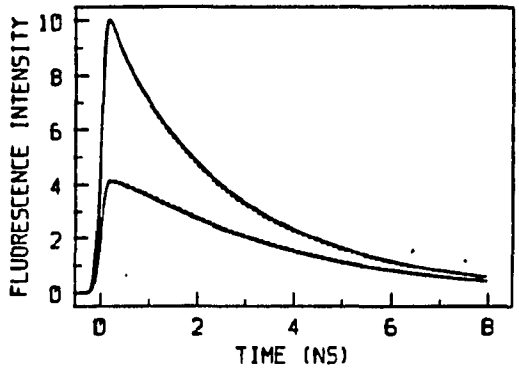

Figure 1. Convolutions of a model instrument function (generated by numerical convolution of a 100 ps FWHM Gaussian function with a 140 ps FWHM Gaussian function) with Eqs. 3 for $I_{//}(t)$ and $I_{\perp}(t)$. The GAF 2-body and 3-body approximations are used for $G^{s}(t)$. From top to bottom, the plotted curves are 3-body $I_{//}(t)$, 2-body $I_{//}(t)$, 2-body $I_{\perp}(t)$, and 3-body $I_{\perp}(t)$. The reduced concentration C and isotropic lifetime τ are 0.83 and 3.1 ns, respectively

FWHM Gaussian excitation pulse with a 140 ps FWHM Gaussian detection pulse to simulate the experimental conditions reported by Gochanour and Fayer [9]) with Eqs. 3 for $I_{\parallel}(t)$ and $I_{\perp}(t)$ using the 2-body and 3-body approximations to $G^{s}(t)$ with $C = 0.83$, $\tau = 3.1$ ns. It is clear that earlier tests of GAF theory [9, 10] were barely precise enough to differentiate between the 2-body and 3-body theories for $C \sim 1$, let alone test details of the 3-body theory. In our earlier photon-counting work [10] we accumulated $\sim 10^4$ counts in the peak channel, yielding $S/N \lesssim 10^2$; larger fluctuations characterized the profiles generated by frequency-mixing gating [9]. This underscores the need for a careful study of possible experimental artifacts. In addition to self-absorption and trapping, we have considered and eliminated intrinsic depolarization, 2-dimensional (thin-cell) effects, solvent reorganization, scattered light, background emission, filter fluorescence, polarizer alignment, and rate dependence in the photon counting time-to-amplitude converter as important contributions to the differences between our experimental and theoretical profiles.

Experimental Section and Data Analysis

The mode-locked argon ion laser, synchronously pumped rhodamine 590 laser, and cavity dumper produced tunable pulses with ~8 ps FWHM and 4.8 MHz repetition rate as

described previously [10]. Commercial DODCI was obtained from Excitation. A $\lambda/20$, 2.5 cm dia fused silica substrate was commercially coated with Al and MgF_2 overcoat (CVI Laser Corporation); a 9mm dia region of this coating was removed by etching with HF solution. Solutions of DODCI in glycerol were compressed between this optic and an uncoated $\lambda/20$ fused silica substrate. Absorption spectra of rhodamine 6G solutions in this cell (in which the unetched Al/MgF_2 coating served as a spacer), combined with the absorption coefficient derived from spectra of standard rhodamine 6G solution in a 1 cm cell, indicated that the ultrashort cell thickness was between 1.5 and 2.0 μm.

In the first set of fluorescence experiments reported in this paper, the optics and photon-counting electronics were nearly identical to those used in the rhoodamine 6G work [10]. Horizontally polarized dye laser pulses entered the ultrashort cell at ~75° incidence from the surface normal, and fluorescence was collected along the normal with a 10 cm focal length quartz lens. Two 3mm Scott OG-590 filters and one CVI multilayer dielectric sharp-cutoff filter (hereafter referred to as filter combination A) screened lased scatter from the detector. The fluorescence detection and photon-counting system were built around Hamamatsu R1564U microchannel plate phototube (MCP), a B&H Electronics AC3011 MIC (3.15 GHz) 21dB preamplifier, Tennelec TC 455 and Ortec 934 quad constant-fraction discriminators (CFDs), and an

Ortec 457 time-to-amplitude converter (TAC). Since the discriminators accepted only negative-going pulses, an EG&G IT100 inverting transformer processed the positive-going output from the B&H preamplifier. The TAC output was stored in a Canberra Series 30 multichannel analyzer operated in the pulse height analysis mode with 20 ps/channel resolution. The excitation wavelength was 575 nm. Instrument functions for deconvolution were obtained by scattering 575 nm pulses from a clean silica substrate, and were typically ~80 ps FWHM.

In a second series of fluorescence experiments, several modifications were incorporated in the optics and electronsic. One channel of the Tennelec TC455 constant-fraction discriminator was modified to accept positive-going input pulses directly from the preamplifier, obviating the EG&G IT100 inverting transformer used in earlier work. The input circuitry leading to the zero-crossing comparator in the TC455, designed for triggering by pulses with ~1 ns rise time, was rebuilt to accommodate the somewhat faster rise time pulses from the MCP/preamplifier. Time-to-amplitude conversion in the TAC proved to be influenced by the count rate, causing instrument function broadening that could be minimized by restricting the count rate to below ~1kHz [12]. A 125 μs gating pulse was derived from the true START output of the TAC using a Tektronix PG501 pulse generator, and was used to gate the TAC off for this time

period. This effectively eliminated TAC rate dependence for count rates up to ~8kHz, the limit imposed by the 125 μs gating period. Shorter gating periods produced detectable instrument function broadening at count rates $\gtrsim$ 1kHz; omission of gating yielded ~15 ps broadening at 10 kHz count rate. Discrimination of START and STOP pulses was accomplished using two channels of the Tennelec TC455 CFD, rather than one channel in each of the Ortec 934 and Tennelec TC455 discriminators. With these changes, a ~47 ps FWHM instrument function was obtained which was independent of count rate. The latter was typically ~5 kHz. DODCI samples in this series were excited at 570 rather than 575 nm, and 3 mm Schott filters (filter combination B) superseded the filters (combination A) used in the first series. The instrument function sharpening and the change in excitation wavelength had minimal effects on the measured fluorescence dynamics. Altering the filter combination produced observable changes; the experimental conditions pertinent to each data set are specified in what follows by naming the filter combination used.

For each DODCI sample, fluorescence profiles were accumulated with an analyzing polarizer (Promaster Spectrum 7) aligned in each of three positions: along the excitation polarization, normal to the excitation polarization, and at the magic angle $\theta = 54.7°$ from the excitation polarization. These yielded the experimental profiles $I_{//}(t)$, $I_{\perp}(t)$, and

$I_{//}(t)\cos^2\theta + I_{\perp}(t)\sin^2\theta = P(t)$, respectively, according to Eqs. 3. The differential apparatus sensitivity to fluorescence photons polarized was less than 2%.

Fluorescence profiles were transferred to a DEC MINC-23 minicomputer equipped with Winchester and dual floppy disk drives operating in a TSX-Plus multiuser environment. The convolute-and-compare analysis employed Marquardt nonlinear least-squares regression [13] to minimize χ^2, the sum of weighted squares of residuals between the number of fluorescence counts in each channel n and the discrete convolution

$$C_n = \sum_{i=1}^{n} x(i - s)I(n - i) \qquad (4)$$

of the instrument function x(t) with the decay law I(t). Here s is an adjustable integer (the shift parameter), and I(t) is an arbitrary model function with an arbitrary number of adjustable parameters. For magic-angle profiles accumulated with filter combination A, a single-exponential model function $P(t) = A \exp(-t/\tau)$ with adjustable lifetime τ was initially used. Equations 3 were then used as model functions for the anisotropic profiles $I_{//}(t)$ and $I_{\perp}(t)$, with $G^s(t)$ given in the GAF 3-body approximation by the inverse Laplace transform of

$$\hat{G}^S(\varepsilon) = \tau\{(\pi^2\gamma^2C^2/4)[1-[1 + (32/\pi^2\gamma^2C^2) \times (\varepsilon\tau - 0.1887\gamma^2C^2)]^{1/2}] + 4(\varepsilon\tau - 0.1887\gamma C^2)\}/[4(\varepsilon\tau - 0.1887\gamma C^2)^2]. \quad (5)$$

The constant $\gamma = 0.846$ results from the dipole-dipole orientation dependence of the transport probability w_{jk} between molecules j and k. C is the dimensionless reduced concentration

$$C = \frac{4}{3}\pi R_o^3 \rho, \quad (6)$$

with ρ equal to the dye molecule number density and R_o equal to the Förster parameter [1] characterizing the transport probability

$$\omega_{jk} = \frac{3}{2\tau}\left[\frac{R_o}{r_{jk}}\right]^6 [\hat{d}_j\cdot\hat{d}_k - 3(\hat{d}_j\cdot\hat{r}_{jk})(\hat{d}_k\cdot\hat{r}_{jk})]^2 \quad (7)$$

between dye molecules separated by $\vec{r}_{jk}$ and having transition moments along $\hat{d}_j$ and $\hat{d}_k$.

$G^S(t)$ depends on two parameters, the isotropic lifetime τ and the reduced concentration C. In the earlier experimental runs obtained with filter combination A, covariance between τ and C in fitting $I_{//}(t)$ and $I_{\perp}(t)$ was effectively suppressed by first obtaining an initial value of τ at each concentration from single-exponential

convolute-and-compare analysis of the magic-angle profile. Using this initial choice for τ, the $I_{//}$ and $I_{\perp}$ profiles could be deconvoluted in tandem by minimizing their combined χ^2 [10, 14] with respect to A, s, τ, and C. Tests of this fitting procedure on simulated polarized fluorescence data with Gaussian noise [10] indicate that it inhibits covariance because changes in τ (or C) have opposite effects on $I_{//}(t)$ and $I_{\perp}(t)$ via Eqs. 3. The optimum shift parameter s was determined by fitting profiles over the entire MCA channel range. The final fit was then performed with fixed shift parameter over a range beginning with a channel on the rising edge at ~90% peak counts, since the discreteness of the 20 ps channel spacing otherwise resulted in artificially large contributions to χ^2 from earlier channels on the rising edge.

Apart from yielding τ values for deconvolution of the anisotropic profiles, analysis of the magic-angle profiles provides a useful diagnostic for data artifacts. Figure 2 shows a magic-angle profile for 2.28×10^{-3} M DODCI in glycerol, which typifies our counting statistics (72,000 - 120,000 peak channel counts) and quality of single-exponential fits. In Table I, we list the results of single-exponential fits to magic-angle profiles for DODCI concentrations between 1.19×10^{-5} and 2.49×10^{-3} M. For concentrations up to 1.23×10^{-3} M, the lifetimes vary insignificantly (<2%) from a mean of 1.72 ns - implying that

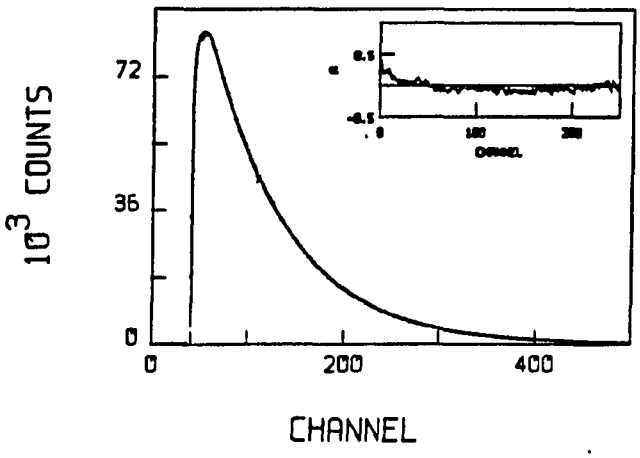

Figure 2. Magic angle fluorescence profile for 2.28×10^{-3} M DODCI in glycerol, obtained using 2μm cell length and filter combination A (see text). Continuous curve is optimized convolution of instrument function with single-exponential model function (τ = 1.61 ns, χ^2_r = 1.836). Inset shows autocorrelation of weighted residuals. Time calibration is 20 ps/channel

Table I. Magic angle fits of DODCI fluorescence profiles[a]

$I(t) = A \exp(-t/\tau)$

Concentration, M	τ,ns	χ_r^2
1.19×10^{-5}	1.71	2.407
	1.68	1.478
	1.69	1.354
1.63×10^{-4}	1.70	1.138
	1.72	1.320
	1.71	2.110
2.54×10^{-4}	1.72	1.734
3.88×10^{-4}	1.74	2.370
	1.74	2.721
5.85×10^{-4}	1.71	2.898
	1.73	4.406
1.23×10^{-3}	1.74	4.828
1.95×10^{-3}	1.67	3.297
2.28×10^{-3}	1.61	1.836
	1.61	2.009
2.49×10^{-3}	1.59	2.783
	1.60	2.317

[a]Accumulated using filter combination A (see the text).

effects of self-absorption on τ have been virtually eliminated at these concentrations by using 2 μm cell length. Quantitative calculation of the expected distortion in τ due to self-absorption [11], using the absorption and fluorescence spectra of DODCI in glycerol, predicts <3% dilation for concentrations as high as 10^{-3} M in a 2 μm cell. Much larger τ variation was observed in 10 μm rhodamine 6G solutions over a similar concentration range due to self-absorption [10]. At higher concentrations, τ becomes increasingly shortened by excitation trapping by dye aggregates whose density increases with dye concentration.

Figure 2 exemplifies an additional artifact, which shows up as a small discrepancy between the experimental magic-angle profile (discrete points) and the convolution of the optimized single-exponential decay law with the instrument function (continuous curve) over the first ~10 channels near the peak. This phenomenon is readily seen only under present of superior counting statistics. It arises from solvent reorganization: the first few solvent coordination layers react to the dipole moment change accompanying the $S_1 \leftarrow S_o$ transition and the fluorescence spectrum dynamically shifts [15], altering the fraction of the fluorescence spectrum transmitted by the cutoff filters. The inset plot in Fig. 2 displays the autocorrelation of weighted residuals [10, 16], which consists of statistical fluctuations about zero autocorrelation in the case of a perfect fit [17].

This autocorrelation is dominated by nonstatistical contributions in the first few channels. To confirm that these discrepancies arise from solvent reorganization, the filter combination A used in the first set of experiments was replaced with combination B. The accompanying change in spectral sensitivity is shown in Fig. 3, which contrasts the sensitivities of combination A and combination B when used with the Hamamatsu R1564U MCP photocathode. For comparison, we superimposed the DODCI fluorescence spectrum from 10^{-3} M glycerol solution in a thin cell (normalized to photocathode response and Jobin-Yvon H-20 monochromator transmission). The peak sensitivities using combination A (~645 nm) and combination B (~605 nm) lie considerably to the red and slightly to the blue, respectively, of the DODCI fluorescence maximum at ~610 nm. The nonexponential behavior detected in magic-angle profiles using both of these filter combinations was characterized by fitting them with the biexponential function $A_1 \exp(-t/\tau_1) + A_2 \exp(-t/\tau_2)$, in which the long-component lifetime τ_2 is similar to the single-exponential lifetimes τ in Table I and the preexponential factor A_1 is a measure of the early-time nonexponentiality. Negative A_1 were generally required for good biexponential fits to profiles accumulated with combination A (Table II): the fluorescence spectrum at early times is blue-shifted from the static spectrum shown in Fig. 3, and at such times the reduced overlap between the

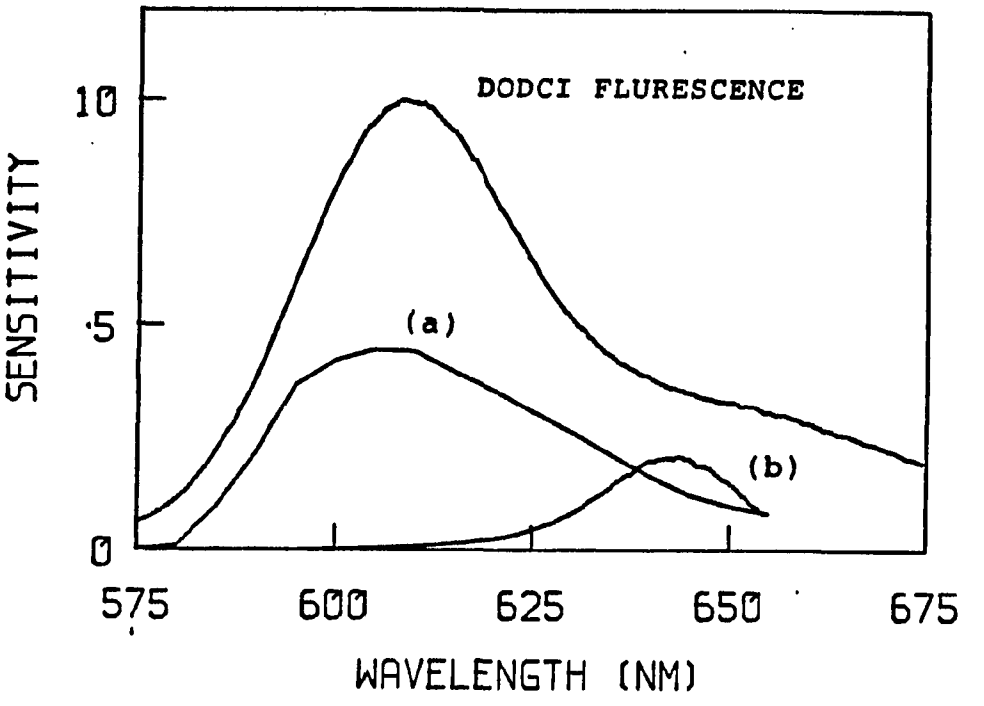

Figure 3. Spectral sensitivity of microchannel plate detector with (a) filter combination A and (b) filter combination B, superimposed on fluorescence spectrum of 1×10^{-3} M DODCI in glycerol. All spectra were evaluated using a Jobin-Yvon H20 monochromator ($\Delta\lambda$ = 0.5 nm) and Philips 56DUVP phototube; spectral sensitivity curves are corrected for MCP response using published sensitivities of MCP and 56DUVP phototubes

Table II. Magic angle fits of DODCI fluorescence profiles[a]

$$I(t) = A_1 \exp(-t/\tau_1) + A_2 \exp(t/\tau_2)$$

Concentration, M	A_1	τ_1,ns	A_2	τ_2,ns	χ_r^2
1.19×10^{-5}	-0.0624	0.252	1.062	1.70	0.9619
	-0.0060	0.927	1.006	1.68	1.479
1.63×10^{-4}	-0.0161	0.441	1.016	1.69	0.9859
	-0.0463	1.03	1.046	1.70	1.115
	-0.0514	0.899	1.051	1.69	1.394
2.54×10^{-4}	-0.0461	0.776	1.046	1.70	1.053
3.88×10^{-4}	-0.0543	0.640	1.054	1.72	0.9874
	-0.1027	1.15	1.103	1.70	2.197
5.85×10^{-4}	-0.0699	0.605	1.070	1.69	1.100
	-0.0834	0.495	1.083	1.70	1.133
1.23×10^{-3}	-0.1024	0.296	1.102	1.72	1.224
1.95×10^{-3}	-0.1090	0.146	1.109	1.66	1.190
2.28×10^{-3}	-0.1577	0.039	1.158	1.61	1.161
	-0.0482	0.065	1.048	1.61	1.857
2.49×10^{-3}	-0.0722	0.041	1.072	1.59	2.679
	-0.1093	1.14	0.8907	1.64	1.353

[a]Accumulated using filter combination A.

fluorescence spectrum and the spectral sensitivity depresses the photon counts. (This effect is apparent in the magic-angle profile of Fig. 2, which was obtained using combination A.) Optimal biexponential fits to profiles taken using combination B yielded positive A_1 (Table III), since the sensitivity of this combination overlaps the early-time blue-shifted spectrum somewhat more than it overlaps the static spectrum. In the latter case, near-perfect biexponential fits were obtained (χ_r^2 = 0.995 to 1.257, as compared to χ_r^2 = 1.1387 to 4.828 for the single-exponential fits in Table I). The long-component lifetimes τ_2 in Tables II and III exhibit trends similar to that of the lifetimes τ in Table I: τ_2 varies by less than 3% except at the highest concentrations, where the decay is significantly accelerated by trapping. At such concentrations, comparisons of our anisotropic fluorescence data with transport theory become suspect. In our view, the contrasting early-time deviations from exponentiality in magic-angle profiles obtained using the two filter combinations is convincing evidence that they originate from dynamic spectral shifts accompanying solvent reorganization. We have observed similar trends in nonexponentiality of isotropic profiles from rhodamine 640 in glycerol.

Table III. Magic angle fits of DODCI fluorescence profiles[a]

$$I(t) = A_1 \exp(-t/\tau_1) + A_2 \exp(t/\tau_2)$$

Concentration, M	A_1	τ_1,ns	A_2	τ_2,ns	χ_r^2
1.84×10^{-4}	0.0658	0.779	0.9342	1.651	0.995
3.25×10^{-4}	0.0528	0.8250	0.9472	1.662	1.148
5.70×10^{-4}	0.0708	1.043	0.9294	1.674	1.152
9.95×10^{-4}	0.2211	1.381	0.7789	1.690	1.044
1.78×10^{-3}	0.2135	1.195	0.7865	1.663	1.257
3.00×10^{-3}	0.1850	0.8561	0.8150	1.535	1.077

[a]Accumulated using filter combination B.

Results and Discussion

Results of convolute-and-compare analysis of the anisotropic fluorescence profiles using the 3-body Green's function for $G^s(t)$ are summarized in Tables IV and V for data accumulated using filter combination A and B, respectively. Profiles obtained using combination A were fitted with the functions $I_{//}(t)$ and $I_{\perp}(t)$ in Eqs. 3, using the isotropic function $P(t) = b_1 \exp(-t/\tau)[1 - b_2 \times \exp(-t/\tau')]$. Only C, b_1, and τ were floated. The initial τ values were taken from the long-component lifetimes t_2 from the biexponential fits in Table II, while the τ' values were fixed at $(1/\tau_1 - 1/\tau_2)^{-1}$ and the b_2 values were fixed at A_1/A_2. For profiles obtained using combination B, the isotropic decay function P(t) in Eqs. 3 was represented by biexponential decay functions in which A_1, A_2, τ_1, and τ_2 were fixed at the values listed in Table III. Only C and a scaling parameter were allowed to vary for these profiles; the lifetime parameter τ in $G^s(t)$ [Eq. 5] was held at 1.665 ns, which well approximates τ_2 from biexponential fits to the isotropic profiles at all but the highest DODCI concentration (Table III). Representative plots of anistropic photon-counting profiles with optimized convolutions of the instrument function with Eqs. 3 are shown in Fig. 4 for two contrasting concentrations (1.63×10^{-4} and 2.28×10^{-3}M). The physical depolarization is

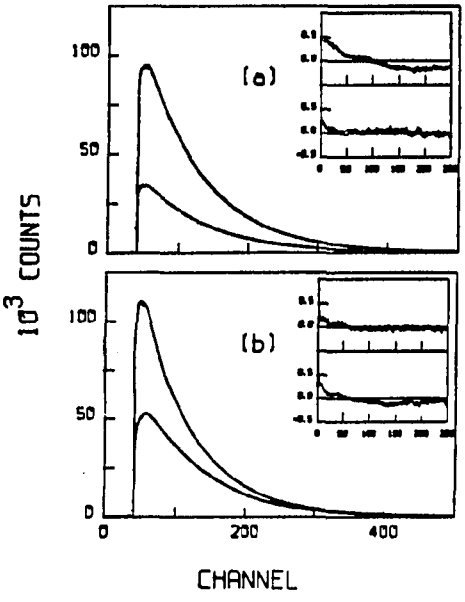

Figure 4. Fluorescence profiles $I_{//}(t)$ and $I_{\perp}(t)$ for (a) 1.63×10^{-4} M and (b) 2.28×10^{-3} M DODCI in glycerol, obtained using 2 μm cell length and filter combination A. Continuous curves are optimized convolutions of Eqs. 3, using 3-body Green's function, with the instrument function. Upper and lower inset plots show autocorrelations of weighted residuals for $I_{//}(t)$ and $I_{\perp}(t)$, respectively. Time calibration is 20 ps/channel

Table IV. Fitting parameters for anisotropic fluorescence profiles[a]

Concentration, M	τ,ns	C	χ_r^2
1.19×10^{-5}	1.71	0.079	2.270
	1.69	0.063	1.421
	1.68	0.056	2.081
1.63×10^{-4}	1.71	0.124	1.767
	1.72	0.116	1.702
	1.72	0.118	2.190
2.54×10^{-4}	1.72	0.163	2.590
3.88×10^{-4}	1.76	0.233	3.636
	1.75	0.226	2.402
5.85×10^{-4}	1.71	0.318	2.797
	1.74	0.307	4.931
1.23×10^{-3}	1.75	0.540	5.359
1.95×10^{-3}	1.67	0.691	3.572
2.28×10^{-3}	1.63	0.775	2.358
	1.61	0.726	2.197
2.49×10^{-3}	1.61	0.797	2.652
	1.61	0.819	2.694

[a]Accumulated using filter combination A.

Table V. Fitting parameters for anisotropic fluorescence profiles[a]

Concentration, M	C	χ_r^2 (combined)
1.84×10^{-4}	0.116	1.788
3.25×10^{-4}	0.212	1.841
5.70×10^{-4}	0.331	1.599
9.95×10^{-4}	0.492	1.463
1.78×10^{-3}	0.668	1.594
3.00×10^{-3}	0.846	1.472

[a]Accumulated using filter combination B.

noticeably more rapid at the higher concentration (Fig. 4b), where the $I_{//}$ and $I_{\perp}$ profiles merge to within a standard deviation well before the end of the window. The quality of fit (as judged by the autocorrelations of weighted residuals in the inset plots) is not markedly different in Figs. 4a and b, because the residuals are dominated in the first 50 channels by solvent reorganization effects which appear independently of concentration. The reorganization artifacts were not apparent in our earlier rhodamine 6G work [10], in which ~12,000 peak channel counts were typically collected.

The optimized reduced concentrations $C \equiv (4/3)\pi R_0^3 \rho$ vary smoothly with actual DODCI concentration M, as shown in Fig. 5a and b for data obtained using filter combinations A and B, respectively. Data points for concentrations lower than 1.63×10^{-4}M are not included in this figure, because $\partial G^S(t)/\partial C$ became so small at such concentrations that the Marquardt algorithm does not converge with the present S/N ratios. The points at higher concentrations should ideally form a locus with constant Förster parameter R_0. The R_0 value computed [1] from DODCI absorption and fluorescence spectra and the refractive index of glycerol is ~64Å. The points in Fig. 5 lie near R_0 ~63 to 65Å at the lowest DODCI concentrations, but skew systematically toward smaller R_0 at higher concentrations. Since artificially small R_0 values are then required for the 3-body theory to replicate the

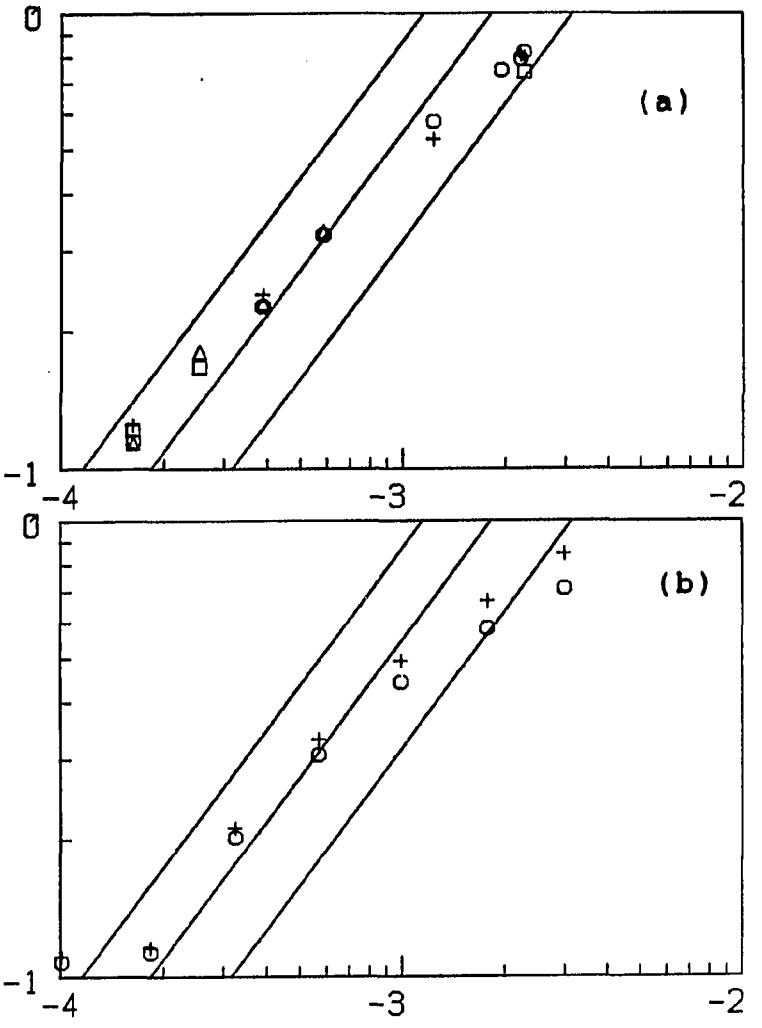

Figure 5. Optimized reduced concentrations C vs. actual DODCI concentrations M, from linked deconvolutions of $I_{//}$ and $I_{\perp}$ profiles collected using (a) filter combination A and (b) filter combination B. Straight lines give loci of true reduced concentrations vs. M for (from left) R_0 = 70, 60, and 50Å. In (a), different symbols represent 3-body fits to anisotropic profiles from different experimental runs. In (b), a single run at each concentration is analyzed using the 2-body (O) and 3-body (+) approximation to $G^s(t)$

experimental profiles, the observed decay in $G^S(t)$ is slower than that predicted by the 3-body theory by an amount which increases with dye concentration. This skewing trend is clearly unaffected by the filter combination used to accumulate the profiles. Since the nonexponential deviations attending solvent reorganization in the magic-angle profiles exhibit opposite signs for the two filter combinations, the similarity of Figs. 5a and b is evidence that the skewing is not a solvent reorganization artifact. The anisotropic profiles collected using combination A were also deconvoluted using single-exponential functions with floating τ for $P(t)$ in $I_{\parallel}(t)$ and $I_{\perp}(t)$. This procedure generated a plot similar to those in Fig. 5, implying that these results are not sensitive to details of modeling the isotropic decay. It should be noted that optimized reduced concentrations C are displayed in Fig. 5b for fits using the 2-body as well as 3-body approximation for $G^S(t)$. The C values for the 2-body fits are systematically lower than those for the 3-body fits, because the 2-body approximation to $G^S(t)$ decays more rapidly than the 3-body approximation by an amount which increases with C [2]. The skewing in Fig. 5 indicates that the true $G^S(t)$ in our DODCI solutions decays more slowly than either of these approximations. The distinctions which show up in Fig. 5(b) between the 2-body and 3-body fits would be difficult to measure with the S/N available in earlier depolarization experiments [9, 10].

The deviations exhibited at the higher concentrations in Fig. 5 are physically large. Since excitation trapping by DODCI aggregates visibly distorts the magic-angle profiles at the three highest concentrations in Table I and the two highest concentrations in Table III, the points extracted from anisotropic profiles at these concentrations in Figs. 5a and b respectively may be influenced by this artifact. However, appreciable skewing is evident at lower concentrations ($\leqslant 10^{-3}$M), where analyses of isotropic profiles show little distortion from self-absorption or trapping. Fitting the anisotropic profiles between ~10^{-4} and 6 × 10^{-4}M in Fig. 5a required adjustment of R_o from ~65 to ~60Å; this artificially decreases the strength of the Förster dipole-dipole interaction (which varies as R_o^6) by a factor of 1.6.

Another phenomenon considered as a source of artifacts was intrinsic depolarization, arising from noncoincidence between the directions of the absorption and emission transition moments in the dye. When these moments form an angle $\lambda \neq 0$, the function $G^s(t)$ in Eqs. 3 must be replaced [18] by $G^s(t)P_2(\cos\lambda)$, where $P_2(\cos\lambda)$ is the second-order Legendre polynomial in $\cos\lambda$. For a number of molecules, λ is small [15]; the value $\lambda = 7.4°$ has been reported for the $S_1 \leftarrow S_o$ transition in DPH [19]. Several of our anisotropic profiles were fitted using variable λ initially set at 10°. The nonlinear least-squares algorithm forced λ toward 0°

(final values of 0.02° to 0.09° were typical). Allowance for intrinsic depolarization did not improve the quality of the fits, nor did it materially influence the optimized C values. Residual emission and laser scatter from a solution cell filled with pure glycerol accumulated peak channel counts which were lower than those characteristic of our fluorescence profiles by factors of $\gtrsim 10^2$, indicating that emission sources other than DODCI contributed negligibly to our profiles. Analyzing polarizer alignment errors were minimal, because the alignment of the perpendicular polarization was accurately set by minimizing the transmission of the polarized laser beam reflected directly off a cell window, and because the alignment benchmarks for the parallel and magic angle positions were machined into the polarizer mount to within an accuracy of ~0.1°. Effects of reduced system dimensionality accompanying the use of 2 μm cells are unlikely, because this cell thickness corresponds to ~300 R_o for DODCI in glycerol; this migration distance is not typically approached for our solutions during our photon-counting time window.

The 3-body theory is expected to exaggerate the rate of decay in $G^s(t)$ in principle, since it omits 4-body and higher-order processes by which excitation can be returned to the initial donor molecule. GAF compared the decay in $G^s(t)$ in the 2-body and 3-body approximations for $0<t<\tau$ and $C = 1.0, 5.0$; they found that the lower-order 2-body

approximation decays more rapidly. However, it can be argued that at our present concentrations the probability of four donors being close enough together to produce significant 4-body contributions to $G^S(t)$ is negligibly small [20]. Our discrepancies may not be caused by errors in the 3-body theory, but may arise because dye solutions do not resemble the model on which the theory is based. Since the dye tends to aggregate at millimolar concentrations, the probability of finding tightly grouped monomers may be significantly higher than in the random spatial distributions envisioned by the theory.

The question arises why one should focus on testing the GAF theory, because simpler theories for $G^S(t)$ are available. The long-time behavior [7] described in Eq. 1 is expected to become accurate for $t/\tau >> 6/C^2$, which translates into $t >> 10ns/C^2$ for DODCI. This regime is marginally reached at long times in our profiles for the highest concentrations and is not reached in the lower concentrations at all. At the short times where $t/\tau << 6/C^2$, Huber, Hamilton, and Barnett showed that $G^S(t)$ is expected to behave as [21]

$$G^S(t) \rightarrow \exp[- C(\frac{\pi t}{2\tau})^{1/2}]. \qquad (8)$$

In Fig. 6, we show comparative plots of Eq. 8 and the 3-body approximation to $G^S(t)$ for C = 1.0 (which exceeds the

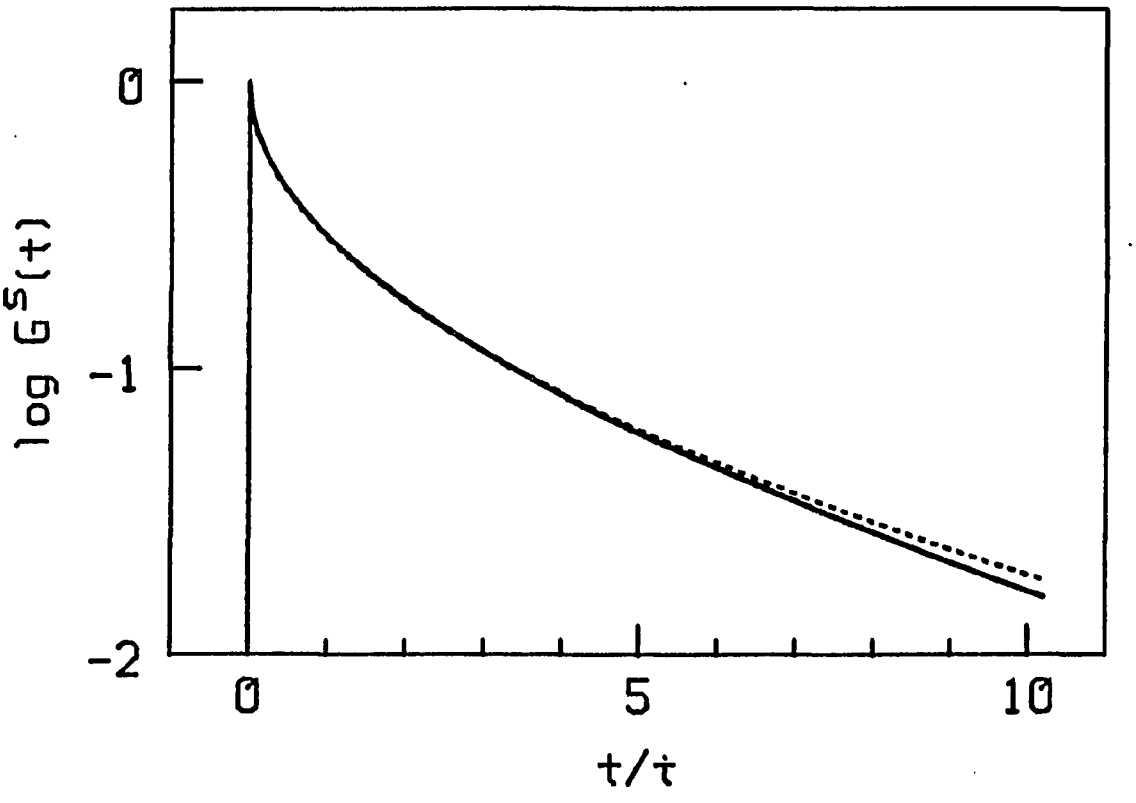

Figure 6. Comparison of the 3-body approximation to $G^S(t)$ (solid curve) and the short-time asymptotic expression (Eq. 8, dashed curve), computed for C = 1.0

highest concentration for which our data are valid) and times out to 10τ. The two functions are remarkably similar. Deconvolutions of representative data were repeated using Eq. 8 instead of the 3-body function for $G^S(t)$, and optimized C values nearly identical to those in Table IV were obtained. It appears fair to say that for the present experimental times and concentrations of interest ($t \lesssim 6\tau$, $C \lesssim 1.0$), Eq. 8 provides as accurate an approximation to $G^S(t)$ as the 3-body theory. The mutual agreement between these theories, coupled with their disagreement with our data, suggests that the discrepancies shown in Fig. 5 arise because real solutions of DODCI in glycerol are not well represented by the assumptions underlying the theories. We have obtained experimental plots similar to those in Fig. 5 for rhodamine 6G in glycerol [10], and thus such discrepancies may be a general property of cyanine and xanthene dyes in alcoholic solution.

Acknowledgments

The Ames Laboratory is operated for the U.S. Department of Energy by Iowa State University under Contract No. W-7405-Eng-82. This work was supported by the Office of Basic Energy Sciences. We thank Professor Michael Fayer and Shaul Mukamel for valuable discussions.

References

1. Förster, T. Discuss. Faraday Soc. 1959, 27, 7.
2. Gochanour, C. R.; Andersen, H. C.; Fayer, M. D. J. Chem. Phys. 1979, 70, 4254.
3. Galanin, M. D. Tr. Fiz. Inst. Akad. Nauk USSR 1950, 5, 339.
4. Vavilov, S. I. JETP 1943, 13, 13.
5. Craver, F. W.; Knox, R. S. Mol. Phys. 1971, 22, 385.
6. Fedorenko, S. G.; Burshtein, A. I. Chem. Phys. 1985, 98, 341.
7. Klafter, J.; Silbey, R. J. Chem. Phys. 1980, 72, 843.
8. Vodunov, E. N.; Malyshev, V. A. Fiz. Tverd. Tela (Leningrad) 1984, 26, 2990.
9. Gochanour, C. R.; Fayer, M. D. J. Phys. Chem. 1981, 85, 1989.
10. Anfinrud, P. A.; Hart, D. E.; Hedstrom, J. F.; Struve, W. S. J. Phys. Chem. 1986, 90, 2374.
11. Hammond, P. R. J. Chem. Phys. 1979, 70, 3884.
12. Bebelaar, D. Rev. Sci. Instrum. 1986, 57, 1116.
13. Marquardt, D. W. J. Soc. Ind. Appl. Math. 1963, 11, 431.
14. Knutson, J. R.; Beechem, J. M.; Brand, L. Chem. Phys. Lett. 1984, 88, 5873.
15. Lakowicz, J. R. "Principles of Fluorescence Spectroscopy"; Plenum: New York, 1983; chapter 5.
16. Anfinrud, P.; Crackel, R. L.; Struve, W. S. J. Phys. Chem. 1984, 88, 5873.
17. Grinvald, A.; Steinberg, I. Z. Anal. Biochem. 1974, 59, 583.
18. Chuang, T. J.; Eisenthal, K. B. J. Chem. Phys. 1972, 57, 5094.

19. Shinitzky, M.; Barenholz, Y. J. Biol. Chem. 1974, 249, 2652.

20. Fayer, M. D. Dept. of Chem., Stanford University, private communication.

21. Huber, D. L.; Hamilton, D. S.; Barnett, B. Phys. Rev. B. 1977, 16, 4642.

EXCITATION TRANSPORT AND FLUORESCENCE ANISOTROPY OF RHODAMINE 3B ON AMORPHOUS QUARTZ

David E. Hart, John F. Hedstrom, Philip A. Anfinrud, and Walter S. Struve

Department of Chemistry and Ames Laboratory - USDOE
Iowa State University, Ames, Iowa 50011

CHAPTER VII. EXCITATION TRANSPORT AND FLUORESCENCE ANISOTROPY OF RHODAMINE 3B ON AMORPHOUS QUARTZ

Introduction

Electronic excitation transport and trapping in disordered systems have provided challenging problems to theorists interested in predicting time-dependent observables such as excited state populations, fluorescence depolarization, and the transient grating effect [1]. Such properties may be extracted from solutions to the couples master equations which govern the set of probabilities p_j that electronic excitation resides on molecule j at time t. In the absence of excitation trapping, these master equations assume the form [2]

$$dp_j/dt = \sum_k^N w_{jk}(p_k - p_j) - p_j/\tau_D \qquad (1)$$

for a system of N identical donor molecules with intramolecular excited state lifetime τ_D. The coefficients w_{jk} are Förster dipole-dipole transition rates [3]

$$w_{jk} = \frac{3}{2\tau_D}\left[\frac{R_o}{r_{jk}}\right]^6 \left[\hat{d}_j\cdot\hat{d}_k - 3(\hat{d}_j\cdot f_{jk})(\hat{d}_k\cdot f_{jk})\right]^2 \qquad (2)$$

where $\vec{r}_{jk}$ is the position of molecule j relative to that of molecule k, $\hat{d}_j$ and $\hat{d}_k$ are unit vectors along the respective

transition moments, and R_0 is the intermolecular separation at which excitation transport and intramolecular decay have equal probability. Since excitation can migrate from molecule to molecule in sequences with unlimited length and topology, exact solutions to the master equations have not been achieved for arbitrary donor molecule number densities in system of any dimensionality. Early attempts to approximate the master equation solutions tended to assume either that one or two excitation migrations occurred at most during the donor excited state lifetime [4, 5] or that excitation sharing was limited to nearest [6] or nearest and next-nearest neighbors [7].

Beginning in 1979, Andersen, Fayer, and their co-workers developed Green's function expansions of the master equation solutions [8-11] to yield successive self-consistent approximations to $G^S(t)$, the time-dependent probability that electronic excitation will be found on the photon-excited donor molecule. $G^S(t)$ is experimentally observable using the transient grating effect [12], and is also related to the time-dependent fluorescence depolarization [13] by

$$G^S(t) = 2.5\frac{I_{//}(t) - I_{\perp}(t)}{I_{//}(t) + 2I_{\perp}(t)} \qquad (3)$$

in three-dimensional systems, where $I_{//}(t)$ and $I_{\perp}(t)$ are the fluorescence intensity components polarized parallel and normal to the linearly polarized excitation. It has been verified [13] that the next-lowest (three-body) self-

consistent approximation to $G^s(t)$ in three dimensions [8] yields calculated fluorescence polarization components in excellent agreement with those observed in concentrated dye solutions, and the master equation has been considered essentially solved for three-dimensional disordered systems.

For two-dimensional systems (e.g., molecules adsorbed onto a flat surface), comparable master equation solutions are not available because in two dimensions the three-body Green's function $G^s(t)$ fails to converge at long times [14]. The lowest order, two-body approximation [11] is expected to be less reliable in two than in three dimensions, because density expansions tend to converge less rapidly in systems with lower dimensionality. No experimental measurements of two-dimensional $G^s(t)$ have been reported to our knowledge. In this work, we have measured fluorescence anisotropies for rhodamine 3B (R3B) adsorbed onto optically flat fused quartz. Our experimental fluorescence components $I_{||}(t)$ and $I_{\perp}(t)$ are deconvoluted with model decay functions which incorporate the two-dimensional, two-body Green's function $G^s(t)$ for donor molecules randomly distributed on a flat surface. At very low coverages, we find that essentially no fluorescence depolarization occurs within several donor lifetimes (or equivalently that $G^s(t) \to 1$ for all t); this implies that dye reorientation contributes negligibly to the observed fluorescence depolarization, which then arises exclusively from excitation transport among motionless,

adsorbed donors. R3B was chosen for the donor species because it dimerizes much less in our surface coating procedure than many dyes (including cresyl violet [15]), is free of acid-base equilibria which complicate the fluorescence profiles of rhodamine B [16, 17], and exhibits an $S_1 \leftarrow S_o$ absorption band (ε_{max} ~1.2 x 10^5 at 555 nm in ethanol; ~10 nm red shift on quartz) which can be pumped by a rhodamine 590 synchronously pumped dye laser.

The relationship between $G^S(t)$ and the fluorescence components $I_{//}(t)$ and $I_{\perp}(t)$ depends on the angular distribution of fixed donor transition moments on the surface [18], so a knowledge of this distribution is important to the data analysis. It is possible a priori that R3B molecules adsorbed on $\lambda/4$ fused quartz can experience microscopic surface roughness with a mean periodicity small enough to produce transition moments which are nearly randomly oriented in three dimensions. Second-harmonic anisotropy measurements on "optically flat fused quartz" substrates coated with less than one monolayer of xanthene dyes (rhodamine 6G, rhodamine B, and acidic fluorescein [19, 20])have implied that the transition moments in these systems form characteristic fixed angles θ^* from the macroscopic surface normal (Figure 1), with random distributions in the azimuthal adsorption angle ϕ. The derived adsorption angles (e.g., $\theta^* = 52 \pm 4°$ and $55 \pm 4°$ for the long-axis polarized $S_1 \leftarrow S_o$ transitions in rhodamine

6G and rhodamine B respectively) support the hypothesis that adsorption occurs through bonding of the -COOH or -COOR groups to the fused silica substrate. Since these substrates are not absolutely flat on a molecular scale, our transition moment distributions cannot actually be restricted to single, sharp cones of half-angle θ^*. This is demonstrated in Figure 2a, which compares fluorescence profiles (obtained by techniques described in the Experimental Section) horizontally and vertically polarized laser pulses. The fluorescence was collected along the vertical surface normal in both cases without an analyzing polarizer. The two profiles should exhibit identical time dependence if the transition moments are restricted to a single cone with its symmetry axis parallel to the surface normal. They would differ materially if the transition moments were randomly oriented in three dimensions, and they would then correspond to $I_{//}(t) + I_{\perp}(t)$ and $2I_{\perp}(t)$ in the three-dimensional notation of Eq. 3. Since the profiles in Fig. 2a in fact do not coincide, they give dynamic evidence that the dye transition moments are not adsorbed at a uniform angle θ^* from the excited fluorescence profiles collected from the same R3B/quartz sample (i) with an analyzing polarizer oriented perpendicular to the excitation polarization (Fig. 1) and (ii) with no analyzing polarizer. Since the difference between the pair of profiles in Figure 2b is much larger than that in Figure 2a, fluorescence

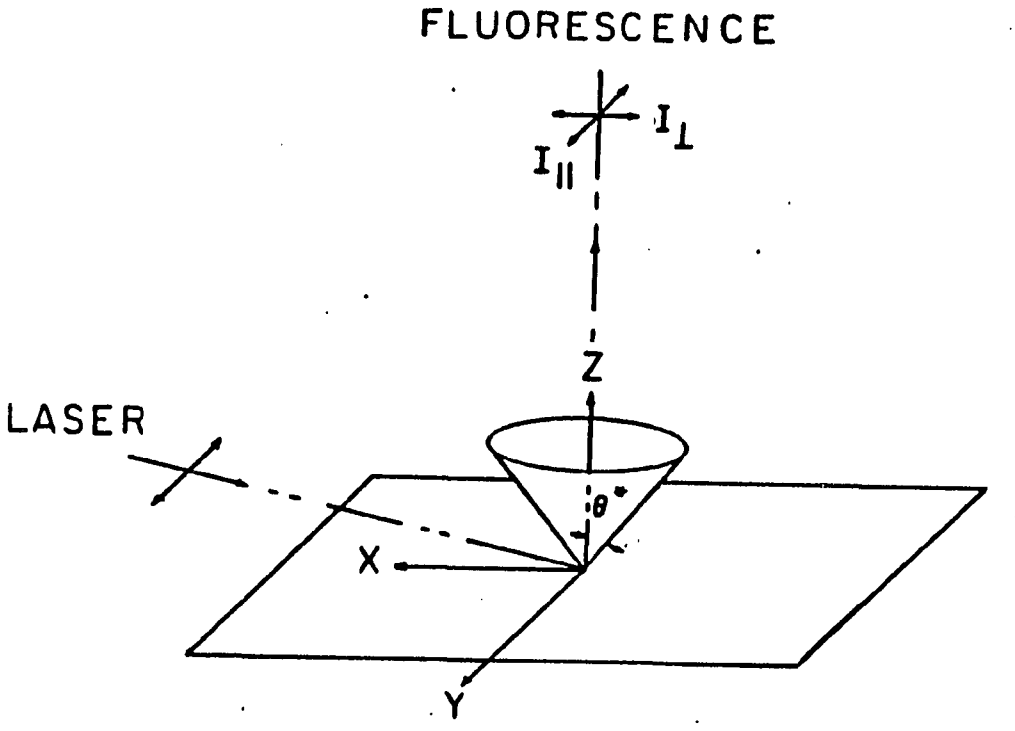

Figure 1. Experimental geometry. The surface lies in the xy plane. Laser pulses are y-polarized in most of this work, and fluorescence is observed along the z axis. For analysis, dye transition moments are assumed to be randomly distributed on a cone of half-angle θ^* from surface normal

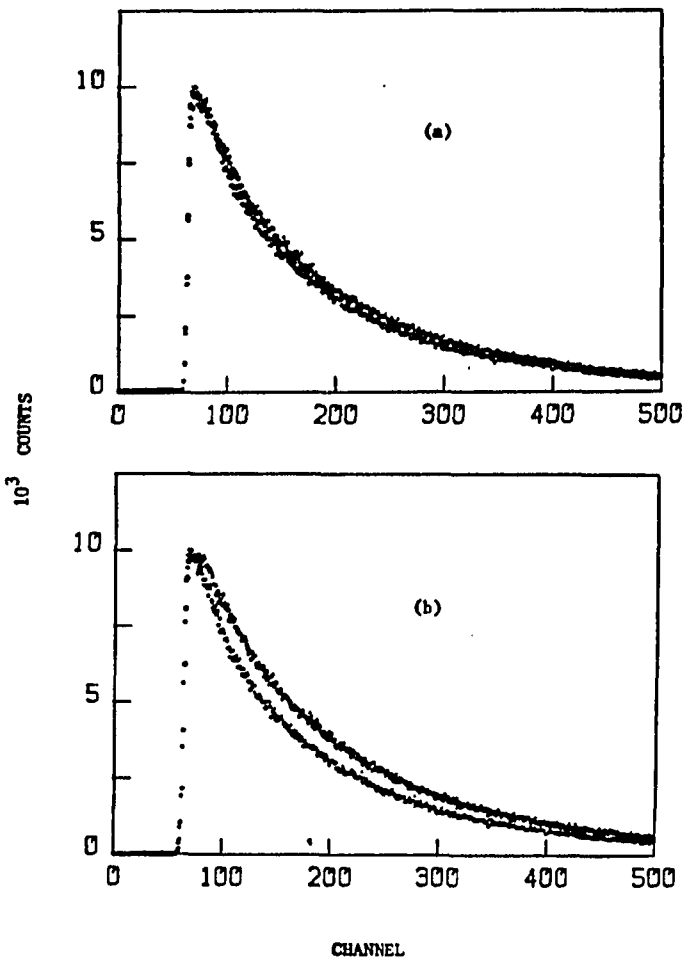

Figure 2. Fluorescence profiles from R3B on optically flat quartz, viewed along surface normal (a) without analyzing polarizer for out-of-plane (upper) and in-plane (lower) laser polarizations and (b) for in-plane laser excitation with a perpendicular analyzing polarizer (upper) and with no analyzing polarizer (lower). Counting times were adjusted to yield 10^4 peak counts in each profile. R3B coverage is similar to that of sample 3 in Table I. Time calibration is 20 ps/channel

depolarization in our R3B/quartz systems is dominated by changes in the azimuthal adsorption angle ϕ attending excitation transport, rather than by ensemble variations in the orientation of the cone axis. A a first approximation, it will therefore be assumed that the R3B transition moments are restricted to lie on the surface of a single cone of half-angle θ^* (whose value does not enter in the relationship between $G^S(t)$ and the time-dependent fluorescence polarization components) aligned parallel to the macroscopic surface normal.

In the Calculation Section, we derive expressions for $I_{//}(t)$ and $I_{\perp}(t)$ in terms of $G^S(t)$ for our experimental geometry and obtain the two-dimensional, two-body Green's function $G^S(t)$ using Förster dipole-dipole transition rates w_{jk} with the correct orientation dependence [12]. The Experimental Section contains the experimental procedure. In the Data Analysis Section we describe the data treatment, a nonlinear least-squares convolute-and-compare analysis which uses model decay functions derived from the two-body Green's function and which fits the isotropic and anistropic parts of $I_{//}(t)$ and $I_{\perp}(t)$ independently in order to avoid covariance between the isotropic lifetime parameters and the parameters in $G^S(t)$. The results and discussion are presented in the Data Analysis Section, where several factors which specifically influence the

interpretation of surface fluorescence anisotropy measurements are discussed.

Calculation of Fluorescence Components and the Two-Body Green's Function $G^S(t)$

The long-axis polarized $S_1 \leftarrow S_o$ absorption and fluorescence transitions in R3B are assumed to have parallel transition moments which are aligned at a fixed angle θ^* from the surface normal (the z axis), but are randomly distributed in ϕ. The excitation polarization lies in the surface plane (the xy plane) and is parallel to the y axis as shown in Fig. 1; the pumping pulses propagate in the xz plane. The orientational probability distribution for excited state transition moments at time t after laser pulse excitation at t = 0 is [21]

$$W(\theta\phi t) = \int_o^{2\pi} d\phi \int_o^{\pi} d\theta \; G(\theta_o\phi_o|\theta\phi t) \; W(\theta_o\phi_o) \qquad (4)$$

where $G(\theta_o\phi_o|\theta\phi t)$ is a Green's function propagator and $W(\theta_o\phi_o)$ is the initial probability distribution created by electric dipole absorption at t = 0. Since θ is fixed at the adsorption angle θ^*, this becomes

$$W(\phi t) = \int_o^{2\pi} d\phi \; G(\phi_o|\phi t) \; W(\phi_o) \qquad (5)$$

with

$$W(\phi_o) = \frac{1}{\pi} \sin^2\theta^* \cos^2\phi_o \ . \tag{6}$$

The angles ϕ and ϕ_o are measured from the y axis. The propagator can be expanded in terms of $\Phi_m(\phi) = (2\pi)^{-1/2}\exp(im\phi)$

$$G(\phi_o|\phi t) = \sum_{m=-\infty}^{\infty} c_m(t)\Phi_m^*(\phi_o)\ \Phi_m(\phi) \tag{7}$$

and obeys the boundary conditions

$$G(\phi_o|\phi 0) = \delta(\phi - \phi_o) \equiv \sum_{m=-\infty}^{\infty} \Phi_m^*(\phi_o)\Phi_m(\phi) \tag{8}$$

$$\int_o^{2\pi} d\phi\ G(\phi_o|\phi t) = 1 \ .$$

This requires that $c_o(t) = 1$ and $c_m\ (0) = 1$. Combining Eqs. 5-8 then implies that the orientational probability distribution must evolve as

$$W(\phi t) = \frac{\sin^2\theta^*}{2\pi}[1 + c_2(t)\ \cos\ 2\phi] \ . \tag{9}$$

The fluorescence components $I_{//}(t)$ and $I_{\perp}(t)$ observed along the z axis are

$$I_{//}(t) = P(t)\int_o^{2\pi} d\phi\ W(\phi t)\sin^2\theta^*\cos^2\phi$$

$$= P(t)\sin^4\theta^* \frac{1}{2}\left[1 + \frac{1}{2}c_2(t)\right] \tag{10a}$$

$$I_\perp(t) = P(t)\int_0^{2\pi} d\phi\, W(\phi t)\sin^2\theta^*\sin^2\phi$$

$$= P(t)\sin^4\theta^* \frac{1}{2}\left[1 - \frac{1}{2}c_2(t)\right] \tag{10b}$$

where P(t) is the isotropic decay law. It may be shown that if all of the fluorescence depolarization proceeds via electronic excitation hopping between stationary dye molecules on the surface, $c_2(t)$ can be identified with $G^s(t)$, the exact probability that the excitation is found on the laser-excited dye molecule at time t. Craver [18] has shown that for the present transition moment adsorption geometry and excitation polarization

$$G^s(t) = 2\,\frac{I_{//}(t) - I_\perp(t)}{I_{//}(t) + I_\perp(t)} \tag{11}$$

which is consistent with Eqs. 10. This equation supersedes Eq. 3, which describes fluorescence depolarization in a three-dimensionally random distribution of transition moments. No knowledge of the adsorption angle θ^* is required to extract $G^s(t)$ from the fluorescence components using Eq. 11, provided fluorescence is observed along the surface normal. If the surface were inclined by an angle λ about the y axis, Eq. 11 would be replaced by

$$G^S(t) = 2\,\frac{I_{//}\cos^2\lambda(1 + 2\tan^2\lambda\cot^2\theta^*) - I_\perp}{I_{//}\cos^2\lambda + I_\perp}\,. \qquad (12)$$

Loring and Fayer [11] derived a self-consistency equation for the Laplace transform of the two-body Green's function $G^S(t)$ in two dimensions in the absence of excitation trapping

$$G^S(\varepsilon) = \left[\varepsilon + \rho\int d\vec{r}_{12}\,\frac{w_{12}}{(1 + 2G^S(\varepsilon)w_{12})}\right]^{-1}. \qquad (13)$$

Here ρ is the surface number density of donor molecules. For simplicity the transfer rate w_{12} was set equal to the orientationally averaged Förster rate $(R_o/r_{12})^6/\tau_D$, leading to

$$G^S(\varepsilon) = \left[\varepsilon + \frac{\pi C}{\tau_D}\left(\frac{4}{27}\right)^{1/2}\left(\frac{2G^S(\varepsilon)}{\tau_D}\right)^{-2/3}\right]^{-1}. \qquad (14)$$

$C \equiv \pi R_o^2\rho$ is the (dimensionless) reduced donor coverage and equals the mean number of donor molecules occupying a circle of radius R_o. Using the correct orientational dependence in w_{12} yields instead the self-consistency equation

$$G^S(\varepsilon) = \left[\varepsilon + \frac{\pi C}{\tau_D}\left(\frac{4}{27}\right)^{1/2}\left(\frac{2G^S(\varepsilon)}{\tau_D}\right)^{-2/3} a^{1/3}\int d\Omega_1 d\Omega_2 |\kappa_{12}|^{2/3}\right]^{-1} \qquad (15)$$

where

$$\kappa_{12} = \hat{d}_1\cdot\hat{d}_2 - 3(\hat{d}_1\cdot\hat{r}_{12})(\hat{d}_2\cdot\hat{r}_{12})$$

$$a = \left[\cos^4\theta^* + \frac{5}{4}\sin^4\theta^*\right]^{-1}.$$

The integral in Eq. 15 is carried out over all orientations Ω_1 and Ω_2 of transition moment pairs randomly distributed on the θ^* cone. Consideration of the anisotropy in w_{12} therefore replaces the reduced coverage C in the two-body Green's function with γC, where

$$\gamma = a^{1/3}\int d\Omega_1 d\Omega_2 |\kappa_{12}|^{2/3} \qquad (16)$$

is a constant which depends on the cone angle θ^*. A similar result is obtained when the anisotropy in w_{12} is incorporated into calculating the two-body, three-dimensional Green's function [13]; in that case, the reduced concentration of donor species becomes multiplied by

$$\gamma = \left[\frac{3}{2}\right]^{1/2}\int d\Omega_1 d\Omega_2 |\kappa_{12}| = 0.846 \ . \qquad (17)$$

This correction brings theoretical fluorescence profiles into excellent agreement with experimental fluorescence components emitted by rhodamine 6G solutions in glycerol [13]. Our reduced dye coverages are far less precisely known than the reduced dye concentrations used in solution

work, since our submonolayer R3B coatings generally exhibit optical densities less than 0.002 at their absorption maximum. We therefore approach comparisons of our experimental profiles with theory by determining to what extent agreement is possible for optimized reduced coverages C in nonlinear least-squares analyses using the two-body, two-dimensional form of $G^s(t)$.

Experimental Section

A Coherent Innova 90 argon ion laser with 5-W plasma tube operated at 26 A was acousto-optically mode-locked by a Harris Corp. H-401 unit driven at 48 MHz. It pumped a cavity-dumped rhodamine 590 dye laser (Coherent CR-599-01 with three-plate birefringent filter), which produced tunable picosecond pulses with ~8-ps fwhm. The cavity dumper combined a Harris Corp. H-100 AOM crystal, an H-102 driver synchronized with the mode-locker driver to provide a 4.8-MHz repetition rate, and optics mounted on Newport Research Corp. beam directors and Line Tool Co. translators. A real-time, rotating-mirror, zero-background autocorrelator [22] provided monitoring and optimization of laser performance.

Rhodamine 3B perchlorate (R3B) was obtained from Eastman Kodak Laser Products, and was used without further purification. Thin-layer chromatography (TLC) of R3B on

Analtech silica gel G plates revealed only one spot with ethanol/acetone, ethanol/acetic acid and 1-propanol/formic acid solvents. The surface substrates were $\lambda/4$ fused quartz. In most experiments, substrates were treated with dichlorodimethylsilane prior to dipping in aqueous R3B solutions with varied concentration (3.7×10^{-9} to 7.4×10^{-7} M), yielding hydrophobic surfaces with macroscopically uniform dye coatings of less than one monolayer. To test for possible effects of adsorption site inhomogeneity of fluorescence properties, some substrates were untreated before dye coating. Untreated substrates yielded visibly less uniform coverage (observed by total fluorescence count rate monitoring during computer-controlled translational surface scanning), but the time-dependent fluorescence profiles were not markedly sensitive to surface pretreatment. Such surface scans identified fluorescence "hot spots" arising from surface scratches or other imperfections, and profile accumulations were limited to uniformly coated areas.

Horizontally polarized dye laser pulses at 575 nm were focused to ~0.1-nm diameter at ~75° incidence on horizontal quartz substrates coated with R3B. Fluorescence was collected vertically with a 5 cm focal length quartz lens and condensed by a 10 cm focal length lens through a variable rectangular aperture onto a Hamamatsu 1564U microchannel plate phototube (MCP) with bialkali

photocathode and borosilicate glass window. The MCP exhibited ~6 x 10^5 gain at 3000 V, 500 nm, and a transit time spread of 76 ps at 3200 V. Three-millimeter Schott filters (two OG-590 and one RG-610) screened 575 nm laser scatter and filter fluorescence from the MCP. The dye laser polarization was purified with a Promaster Spectrum 7 polarizer; an identical polarizer was used as analyzer between the substrate and collecting lens. The differential sensitivity to parallel- and perpendicular-polarized light was less than 2%.

Photocurrent pulses were amplified and inverted with a B&H Electronics AC3011 MIC (3.15 GHz) 21-dB preamplifier and an EG&G IT100 inverting transformer. The amplified pulses were processed in a Tennelec TC455 quad constant-fraction discriminator (CFD) and were used as START pulses in an Ortec 457 time-to-amplitude converter (TAC). The signal from dye laser pulses sampled by an EG&G FOD-100 photodiode in the photoconduction mode was passed through an Ortec 934 quad CFD to provide STOP pulses. TAC output was accumulated in a Canberra Series 30 MCA in the PHA mode, yielding 5.0-, 10.0-, or 20.0-ps channel resolution. Laser pulses scattered from a clean quartz substrate were used for generating instrument functions (~80 ps fwhm) for deconvolution of raw data.

Fluorescence profiles were transferred to a Digital

Equipment Corp. MINC-23 system with dual floppy disk drive operating in an RT-11 environment and analyzed with a Marquardt nonlinear regression [23] program.

Results and Discussion

Details of the convolute-and-compare analysis are given in the Appendix. Following Eq. 10 and the subsequent discussion on the Calculation Section, we use as trial functions for the polarized fluorescence intensities $I_{\parallel}(t)$ and $I_{\perp}(t)$

$$I_{\parallel}(t) = AP(t)[1 + G^{S}(t)/2] \tag{18a}$$

$$I_{\perp}(t) = AP(t)[1 - G^{S}(t)/2] \tag{18b}$$

where $G^{S}(t)$, the two-body, two-dimensional Green's function, is computed as outlined in the Appendix. At this level of approximation, $G^{S}(t)$ depends on the single parameter

$$\alpha = C^{3}/\tau_{D}. \tag{19}$$

Equations 18 imply that the magic analyzing polarizer angle, at which the detected fluorescence profiles will behave as P(t) for our assumed adsorption geometry, is 45° (vs. 54.7° for fluorescence emitted from solutions). Three fluorescence profiles were typically accumulated from each

sample: $I_{\parallel}(t)$, $I_{\perp}(t)$, and a magic-angle profile. Ideally, P(t) should be a single-exponential decay function, and we have in fact obtained excellent single-exponential fits to magic-angle profiles from rhodamine 6G in glycerol in all but the most concentrated solutions, in which excitation trapping by dye dimers distorts the isotropic decay function P(t) [23]. For R3B on quartz, however, single-exponential fits to magic-angle profiles consistently yielded large values of χ^2 (which is defined in the Appendix), even at the lowest R3B coverages. Excellent fits (reduced χ^2 between 0.901 and 1.068) resulted from using a triexponential model function to analyze magic-angle profiles obtained from most of our R3B/quartz samples (Table I). This departure of the isotropic decay function P(t) from single exponentiality can arise from adsorption site inhomogeneity, from dye impurity, or from excitation trapping by adsorbed dye aggregates. The first two causes are unlikely because (i) we obtained results similar to those in Table I for R3B coated onto untreated quartz substrates as well as substrates treated with dichlorodimethylsilane; (ii) the R3B dye purity was verified by TLC (the Experimental Section), and its $-CO_2Et$ functional group cannot produce the carboxylic acid-base equilibrium exhibited by dyes like rhodamine B [16]; and (iii) the nonexponential character of P(t) increases markedly with surface coverage in Table I. In samples 1-3,

Table I. Triexponential fitting parameters for magic-angle profiles

$$N(t) = A_1\exp(-t/\tau_1) + A_2\exp(-t/\tau_2) + A_3\exp(-t/\tau_3)$$

sample	[R3B], M[a]	A_1	τ_1, ns	A_2	τ_2, ns	A_3	τ_3, ns	χ_r^2
1	3.7×10^{-9}	1.0	3.59	19.1	1.86	54.1	4.07	1.068
2	7.4×10^{-9}	1.0	0.194	5.71	2.23	17.0	4.13	0.901
3	3.7×10^{-8}	1.0	0.976	6.27	2.36	17.8	3.95	0.948
4	7.4×10^{-8}	1.0	0.327	4.85	1.65	12.5	3.63	1.031
5	7.4×10^{-7}	1.0	0.186	2.12	1.08	2.88	2.67	1.070

[a]In aqueous coating solution.

the magic-angle profiles are dominated by a long component with lifetime $\tau_3 = 4.05 \pm 0.1$ ns; in the two samples with higher coverage, τ_3 decreases to 3.63 and 2.67 ns, and the shorter lifetime components gain more importance. Excitation trapping by aggregates is therefore a major origin of nonexponentiality in P(t) at our higher coverages. This concentration behavior parallels that observed in solution [13, 23] but is more pronounced because dyes form aggregates more readily on surfaces than in alcoholic solution [15].

The experimental $I_{//}$ and $I_{\perp}$ profiles were then deconvoluted using Eqs. 19 and 20 with the isotropic lifetime parameters in P(t) fixed as determined in the analyses of the magic-angle profiles. Parameter correlation between P(t) and $G^S(t)$ was thus avoided. $G^S(t)$ itself contains only α (defined in Eq. 21) as an adjustable parameter in the two-body approximation, so $G^S(t)$ contributes very little functional flexibility to $I_{//}(t)$ and $I_{\perp}(t)$. Both of the latter profiles were deconvoluted simultaneously, and their combined χ^2 was minimized using a common, optimized α value [24]. The inverse Laplace transform of Eq. A2 in the Appendix was evaluated numerically [25] in order to compute $G^S(t)$ during deconvolution. Our 80-ps-fwhm instrument function was not wide compared to the 20-ps channel spacing used in most of this work. The convolute-and-compare algorithm was

restricted to integral shift parameters s (Eq. A1), so that choosing M = 1 as the initial channel for computing χ^2 (Eq. A3) produced disproportionate contributions to χ^2 from the sharply rising portions of the fluorescence profiles. Channel M was therefore typically placed on the rising edge at 90% peak counts, and the continuous curves which represent convolutions of the optimized model functions with the instrument function in the figures accompanying this Section all begin with channel M.

The quality of data fits using the model functions in Eqs. 18a and 18b can be estimated by evaluating the autocorrelations of residuals [26]

$$A_n = \frac{2N}{N - M} \frac{\sum_{i=1}^{(N-M)/2} Y_i^{-1/2}(C_i - Y_i)Y_{i+n}^{-1/2}(C_{i+n} - Y_{i+n})}{\sum_{i=1}^{N} Y_i^{-1}(C_i - Y_i)^2} \qquad (20)$$

where N is the number of channels comprising the fluorescence profile. The autocorrelation A_o in channel 0 is unity. For model functions which are indistinguishable from the true decay functions, the autocorrelations A_n in other channels consist of random statistical fluctuations about $A_n = 0$. Such statistical autocorrelations were obtained for all of the triexponential fits to the magic-angle profiles summarized in Table I, meaning that the

triexponential decay model is sufficiently flexible to replicate the observed isotropic decays P(t) to within serve only as phenomenological descriptions of P(t) for deconvolution of the $I_{//}$ and $I_{\perp}$ profiles using variable $G^{S}(t)$ in Eqs. 18a and 18b, and physical interpretations of the preexponential and lifetime parameters in Table I do not enter in the data analysis. Strictly speaking, excitation trapping by aggregates influences the fluorescence anisotropy as well as P(t), and the relationship between the fluorescence components $I_{//}(t)$ and $I_{\perp}(t)$ and the Green's function $G^{S}(t)$ in Eq. 18 is applicable only in the limit where the donor-donor excitation hopping rate greatly exceeds the rate of excitation trapping. This approximation is more nearly obeyed in samples 1-3 (in which the isotropic decay behavior varies slowly with donor coverage) than in samples 4 and 5, where the long-component lifetime τ_3 in Table I begins to decrease rapidly with increased coverage. Gochanour and Fayer [13] observed isotropic lifetime shortening from 3.1 to ~2.85 ns in their most concentrated rhodamine 6G/glycerol solutions, and they corrected for this effect by using reduced lifetimes in the isotropic decay portion of their three-dimensional analogues to Eq. 18a and 18b. Such corrections are inherent in our procedure of using the least-squares triexponential parameters from Table I in P(t) while varying α in $G^{S}(t)$ to fit the observed fluorescence anisotropy.

The experimental $I_{\parallel}(t)$ and $I_{\perp}(t)$ profiles are plotted for samples 2-5 in Figure 3; the same spots were irradiated on these surfaces to obtain both these profiles and the magic-angle profiles described in Table I. The continuous curves are convolutions of the model functions in Eqs. 18a and 18b with the instrument function, optimized with respect to α and the shift parameters s in Eq. A1. The upper and lower inset plots in each part of Figure 3 show the autocorrelations of residuals (Eq. 20) for $I_{\parallel}(t)$ and $I_{\perp}(t)$, respectively. The time scale in Figure 3 spans ca. 10 ns, or more than $2\tau_D$ for R3B on quartz. At the lowest coverage shown in Figure 3 (sample 2), the fluorescence depolarization is relatively small because $I_{\parallel}/I_{\perp}$ changes comparatively little between $t = 0$ and $2\tau_D$; much larger depolarizations are evident in samples 3-5.

In Table II, we list the final least-squares fitting parameter α, the reduced χ^2, and the reduced coverage computed from $C = (\alpha\tau_D)^{1/3}$ using $\tau_D = 4.05$ ns, for samples 1-5. The optimized reduced coverage C generally increases with the concentration of R3B coating solution used; a notable exception is the fact that C turns out to be larger for the irradiated point on sample 3 than for that on sample 4. At the highest coverage studied ($C = 0.651$ for sample 5 in Table II), the mean separation between nearest-neighbor donor molecules is still larger than R_o ~51 Å for R3B on quartz [27]. At and above such coverages, the fluorescence

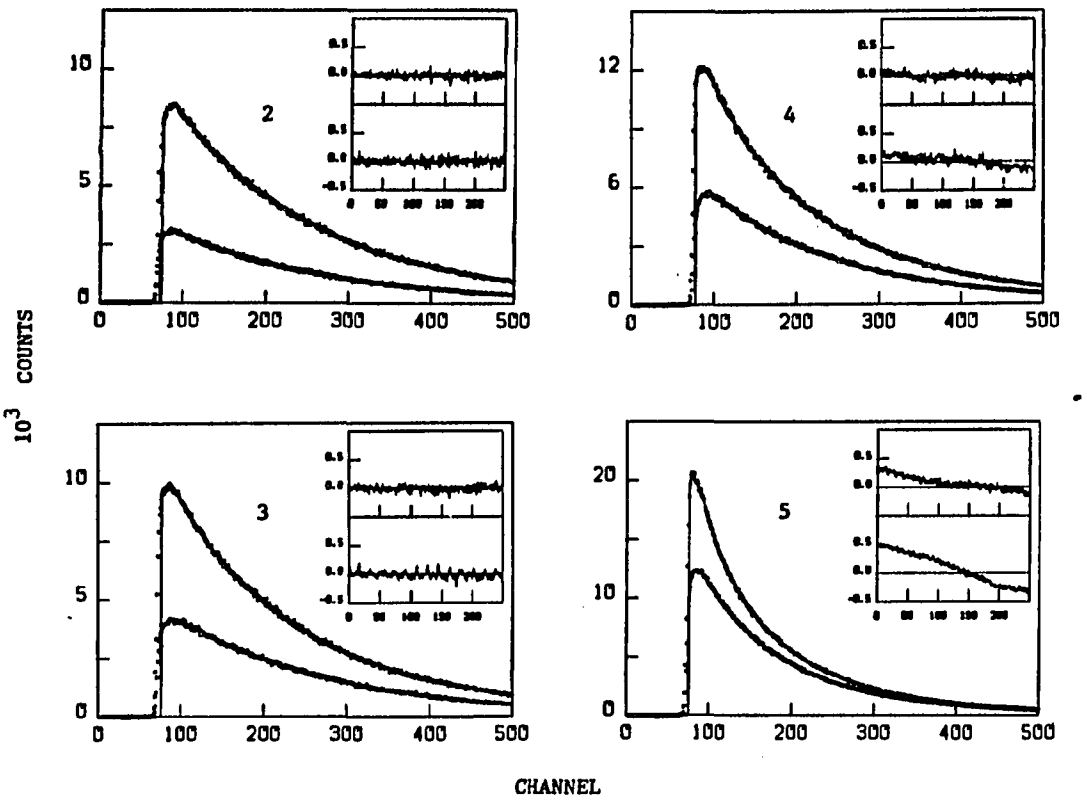

Figure 3. Fluorescence profiles $I_{\parallel}(t)$ and $I_{\perp}(t)$ for sample 2-5 in Table I. Continuous curves are optimized convolutions of the model functions in Eqs. 18a and 18b with the instrument function. Upper and lower inset plots show autocorrelations of residuals for $I_{\parallel}(t)$ and $I_{\perp}(t)$, respectively. Time calibration is 20 ps/channel; all fluorescences were excited with in-plane laser polarization

Table II. Fitting parameters for anisotropic fluorescence profiles[a]

$$I_{//}(t) = P(t)\ [1 + \frac{1}{2}G^S(t)]$$

$$I_{\perp}(t) = P(t)\ [1 - \frac{1}{2}G^S(t)]$$

sample	α, ns^{-1}	Cp[b]	χ_r^2
1	1.29×10^{-4}	0.0805	1.004 1.119
2	2.75×10^{-4}	0.104	1.104 1.055
3	2.16×10^{-2}	0.444	1.009 1.046
4	1.75×10^{-2}	0.414	1.288 1.229
5	6.80×10^{-2}	0.651	1.676 2.155

[a]Triexponential parameters in P(t) fixed at values listed in Table I.

[b]Computed assuming τ_D = 4.05 ns.

count rate decayed noticeably during a typical counting period of ~5 min. Stable count rates were obtained at lower coverages, implying that coverage-dependent photochemistry depleted the surface density of R3B monomers at sufficiently high densities. This photochemistry precluded studying coverages higher than that in sample 5; in the latter case, excitation trapping visibly accelerates the decay in the profiles of sample 5 in comparison to the decay observed in samples 2-4 (Figure 3).

In Figure 4, we plot optimized reduced coverages vs. concentration of aqueous R3B coating solution for triads of profiles obtained by (i) pumping of a given spot, (ii) consecutive pumping of the same spot, and (iii) pumping of a new spot. Photochemistry tends to produce spreads in C values which are largest at the highest coverage, although considerable scatter is also observed at the lowest coverage because in this regime $G^S(t)$ is a weak function of α ($G^S(t) \rightarrow 1$ for all t when $\alpha \rightarrow 0$). These reduced coverages are not linear in the coating solution concentration, but their locus resembles a Langmuir isotherm in that C levels off at the higher concentrations [28]. The continuous curves are plots of the Langmuir type I isotherm function

$$C = \frac{\alpha M}{1 + \beta M} \qquad (21)$$

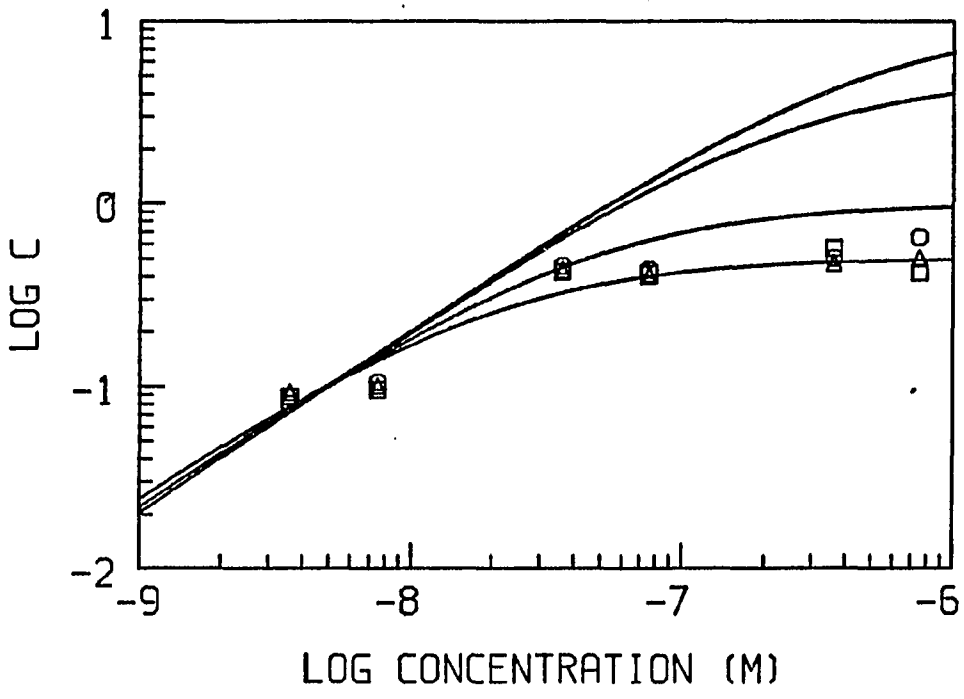

Figure 4. Optimized reduced coverages C for nonlinear least-squares fits to $I_{//}(t)$ and $I_{\perp}(t)$ profiles for samples 1–5, plotted vs. concentration M of R3B coating solution for (O) irradiation of an initial spot, (Δ) consecutive irradiation of the same spot, and (□) irradiation of a new spot on R3B-coated quartz. Continuous curves are Langmuir adsorption functions $C = \alpha M/(1 + \beta M)$ for limiting reduced coverages α/β = 0.5, 1.0, 5.0, and 10.0 (bottom through top), adjusted to pass through C = 0.1 at 5.0×10^{-9} M. The numerical value of γ = 0.837, computed from Eq. 16 with θ^* = 52° [19], was used to adjust the optimized reduced coverages for this figure

for several values of the ratio α/β, which equals the limiting coverage at large coating solution molarities M. Near-Langmuir adsorption behavior has been reported for rhodamine B solution-coated onto SnO_2 and glass [29], and the implications of Figure 4 for the interpretation of our data will be discussed below.

The visual agreement between the optimized convolutions and the fluorescence profiles in Figure 3 is so close that the autocorrelation functions are useful for determining how well Eq. 19 model the decay behavior. The autocorrelations are statistical for the $I_{//}(t)$ and $I_{\perp}(t)$ profiles from samples 1 (not shown), 2, and 3; systematically nonstatistical autocorrelations appear in samples 4 and 5. The latter deviations are not a consequence of modeling artifices in the <u>isotropic</u> decay functions P(t), since our triexponential fits to the magic-angle profiles (Table I) yielded statistical autocorrelations similar to those of sample 2 in Figure 3 in all five samples. Close inspection of the unreduced plots for sample 5 in Figure 3 reveals that the deviations in $I_{//}$ and $I_{\perp}$ anticorrelate, and so they arise from disagreement between the optimized two-body Green's function $G^{s}(t)$ and the observed anisotropy function $c_2(t)$, which enters with opposite sign in the parallel and perpendicular components of Eq. 10. The two-body Green's function contributes appreciably to the observed decay in $I_{//}(t)$ and $I_{\perp}(t)$ even for C = 0.08 (sample 1), since $G^{s}(t)$ in

this approximation decays from 1.0 to 0.916 by $t = 2\tau_D$ for this value of C. The nonexponential character in $G^s(t)$ evolves rapidly as C is increased from 0.1 to 1.0 (Figure 5), and it appears remarkable that statistical autocorrelations are obtainable for C as large as 0.444 (sample 3). The quality of any self-consistent approximation to $G^s(t)$ declines as the reduced coverage or concentration is increased [8, 15], and in this context the nonstatistical autocorrelations obtained at the highest coverages in Figure 2 are not surprising.

However, a likelier cause for the larger deviation at higher coverage is excitation trapping. The R3B coverages which are spanned in Figure 4 are all too low for direct spectroscopic measurement of the actual R3B surface number density ρ ($= C/\pi R_o^2$). The optical density of a quartz surface coated with 7.4×10^{-5} M aqueous R3B was determined to be $0.002 \pm .00025$ using a Perkin-Elmer 320 UV-visible spectrophotometer, corresponding to a reduced coverage of $C \sim 9.0$. This fixes a minimum value for $\alpha/\beta \sim 9.0$ in the isotherms of Figure 4 (all of which are adjusted to pass between the sets of points representing samples 1 and 2), if Langmuir adsorption behavior is indeed followed. The isotherms for $C = 5.0$ and $C = 10.0$ pass near the points for samples 1-3, but at the higher coverages (samples 4 and 5) the optimized coverages from least-squares fitting of the fluorescence profiles lie far below the isotherms. These

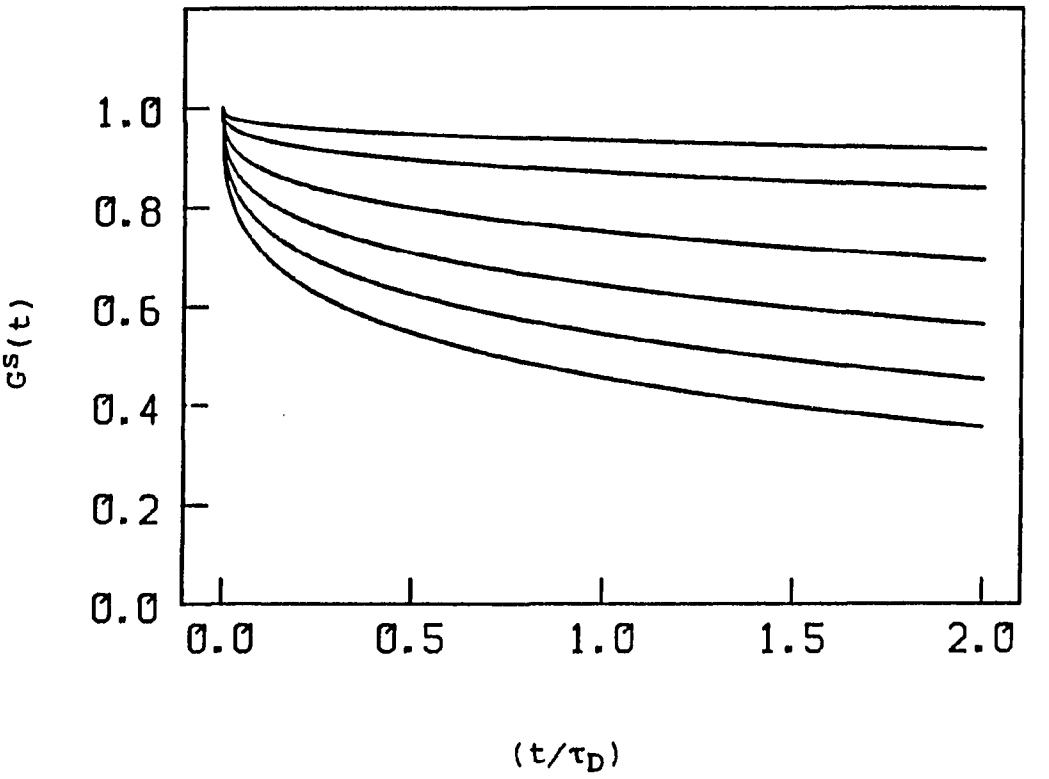

Figure 5. Two-body approximations to the two-dimensional Green's function $G^s(t)$, plotted vs. (t/τ_D) for reduced coverages C = 1.0, 0.8, 0.6, 0.4, 0.2, and 0.1 (bottom through top, respectively)

shortfalls arise physically from the fact that lifetime shortening by excitation trapping interrupts the depolarization process, so that the apparent value of the dynamical parameter C becomes smaller than the actual reduced coverage of donors. It appears certain that the true isotherm in the neighborhood of coating solution concentrations 10^{-7} to 10^{-6} M resembles the plotted isotherm for C = 10.0 more than it resembles the locus of optimized reduced coverages from the fluorescence data, since C must be on the order of 9.0 at 7.4×10^{-5} M. At the highest coverage, then, the optimized reduced coverage is about an order of magnitude too low.

In summary, the model functions which use the two-body Green's function $G^s(t)$ in Eqs. 18a and 18b yield optimized convolutions which are statistically indistinguishable from the experimental profiles from the three samples with lowest coverage (1-3). Figure 4 shows that large distortions in the optimized reduced coverage are caused by excitation trapping in the other samples, and poorer autocorrelations are found in those samples. These disagreements do not arise primarily from inaccuracy in the two-body Green's function at these higher coverages; an effective test of the theory for C larger than ~0.4 requires samples in which aggregation and excitation trapping are more completely suppressed than was possible in our systems.

Solution-coated optically flat quartz systems were used

in the present work, because such dye coatings have been more widely studied than, for example, vacuum-sublimed coatings. Systems can be designed to provide better tests of excitation transport theory. Improved surface flatness can be provided in dye-dodecanoic acid layers in N_2-water interfaces [30] or on LiF surfaces, which can be cleaved to within one molecule of flatness. Such systems may also exhibit more uniformity in transition moment geometry. In this work, the presence of aggregation in R3B (as evidenced by excitation trapping at the higher coverages) indicates that the donor distribution is not truly random, so that strictly speaking the surface density ρ cannot be factored out of the integral in Eq. 13. Use of less polar molecules such as tetracene may both mitigate the trapping problem and provide a more disordered spatial distribution. This is of interest, because improved tests of excitation transport theory will require an ability to investigate fluorescence profiles at higher coverages and longer times, where larger divergences between the two-body theory and the exact Green's function can be expected. Such experiments are in progress in this laboratory.

Fedorenko and Burshtein [31] have recently shown that the Laplace transform $\hat{G}^S(\varepsilon)$ can be inverted analytically for the two- and three-body self-consistent approximations in three-dimensional disordered systems. They demonstrated that both approximations to $G^S(t)$ exhibit incorrect long-

time asymptotic behavior for systems in which the trap density greatly exceeds the donor density (the "static quenching limit") by comparing them to the exact $G^s(t)$ [3] for this limit. The three-body Green's function does describe static quenching dynamics rather accurately for $C_T^2(t/\tau_D) \lesssim 5$ [31], where C_T is the reduced trap density. This regime encompasses the limits of most existing time-resolved excitation transport experiments, where the decay kinetics are typically followed for two or three donor lifetimes and $C_T \lesssim 1.5$ No comparison of the three-body $G^s(t)$ with the exact Green's function is possible in the "migration limit" where the donor density is much larger than the trap density, since no exact theory exists for this case. We have recently shown [23] that for depolarized fluorescence profiles obtained from rhodamine 6G in 10-μm-thick glycerol solutions using the present photon counting techniques, the discrepancies between the experimental profiles and optimized profiles calculated from the three-body theory for $0.06<C<1.26$ are dominated by small experimental artifacts (principally self-absorption at the lower dye concentrations), rather than by inaccuracy in the three-body theory. This suggests that the $C^2(t/\tau_D)$ range of applicability for the three-dimensional three-body theory in the migration limit may resemble the $C_T^2(t/\tau_D)$ range of applicability in the static quenching limit and that the three-body theory accurately describes excitation transport

in many physically realizable situations.

Since the differences between exact dynamics and self-consistent theories are likely to be magnified in systems with lower dimensionality and since the exact dynamics are generally unknown in systems of any dimensionality in the migration limit, we were motivated to try the present two-dimensional systems to determine whether systematic errors in $G^s(t)$ calculated from the two-body theory could be identified and measured. Improved sample preparation and characterization will facilitate accomplishment of this goal over a broad range of surface coverages.

Acknowledgment

The Ames Laboratory is operated for the U.S. Department of Energy by Iowa State University under contract No. W-7405-Eng-82. This work was supported by the Office of Basic Energy Sciences. We thank Professor Michael Fayer for helpful discussions.

References

1. Fayer, M. D. Annu. Rev. Phys. Chem. 1982, 33, 63.
2. Förster, Th. Ann. der Physik (Leipzig) 1948, 6, 55.
3. Förster, T. Discuss. Faraday Soc. 1959, 27, 7.

4. Galanin, M. D. Tr. Fiz. Inst. im. P. M. Lebedeva, Akad. Nauk SSSR 1950, 5, 339.

5. Vavilov, S. I. JETP Lett. (Engl. Transl.) 1943, 13, 13.

6. Ore, A. J. Chem. Phys. 1959, 31, 442.

7. Craver, F. W.; Knox, R. S. Mol. Phys. 1971, 22, 385.

8. Gochanour, C. R.; Andersen, H. C.; Fayer, M. D. J. Chem. Phys. 1979, 70, 4254.

9. Loring, R. F.; Andersen, H. C.; Fayer, M. D. J. Chem. Phys. 1982, 76, 2015.

10. Loring, R. F.; Fayer, M. D. Chem. Phys. 1984, 85, 149.

11. Loring, R. F.; Fayer, M. D. Chem Phys. 1982, 70, 139.

12. Miller, R. J. D.; Pierre, M.; Fayer, M. D. J. Chem. Phys. 1983, 78, 5138.

13. Gochanour, C. R.; Fayer, M. D. J. Phys. Chem. 1981, 852, 1989.

14. Fayer, M. D., Dept. of Chem., Stanford University, private communication.

15. Anfinrud, P.; Crackel, R. L.; Struve, W. S. J. Phys. Chem. 1984, 88, 5873.

16. Sadkowski, P. J.; Fleming, G. R. Chem. Phys. Lett. 1978, 57, 526.

17. Faraggi, M.; Peretz, P.; Rosenthal, I.; Weinraub, D. Chem. Phys. Lett. 1984, 103, 310.

18. Craver, F. W. Mol. Phys. 1971, 22, 403.

19. DiLazzaro, P.; Mataloni, P.; DeMartin, F. Chem. Phys. Lett. 1985, 114, 103.

20. Heinz, T. F.; Shen, C. K.; Richard, D.; Shen, Y. R. Phys. Rev. Lett. 1982, 48, 478.

21. Tao, T. Biopolymers 1969, 8, 609.

22. Yasa, Z. A.; Amer, N. M. Opt. Commun. 1981, 36, 406.

23. Anfinrud, P. A.; Hart, D. E.; Hedstrom, J. F.; Struve, W. S. J. Phys. Chem. 1986, 90, 3116.

24. Knutson, J. R.; Beechem, J. M.; Brand, L. Chem. Phys. Lett. 1985, 102, 501.

25. Stehfest, H. Commun. ACM 1970, 13, 47.

26. Grinvald, A.; Steinberg, I. Z. Anal. Biochem. 1974, 59, 583.

27. This value for R_0 was evaluated for R3B with Eq. 4 of ref 3 by using measured absorption and fluorescence spectra for R3B adsorbed on quartz.

28. Langmuir, I. J. Am. Chem. Soc. 1916, 38, 2267.

29. Itoh, K.; Chiyokawa, Y.; Nakao, M.; Honda, K. J. Am. Chem. Soc. 1984, 106, 1620.

30. Subramanian, R.; Patterson, L. K. Phys. Chem. 1985, 89, 1202.

31. Fedorenko, S. G.; Burshtein, A. I. Chem. Phys. 1985, 98, 341.

Appendix

Given a trial decay law N(t), the convolute-and-compare analysis computes the convolution C_n in the nth channel of N(t) with the instrument function x(t)

$$C_n = \sum_{i=1}^{n} x(i - s)\, N(n - i) \; . \qquad \text{(A1)}$$

The variable shift parameter s allows for delay variations between profiles evaluated under changing experimental conditions. As trial functions N(t), we use $I_{\parallel}(t)$ and $I_{\perp}(t)$

in Eqs. 18a and 18b, where $G^S(t)$, the two-body, two-dimensional Green's function, is given by the inverse Laplace transform of

$$G^S(\varepsilon) = \left\{\left[\frac{1}{2\varepsilon} + \left(\frac{1}{4\varepsilon^2} + \frac{0.01637\alpha}{\varepsilon^3}\right)^{1/2}\right]^{1/3} + \left[\frac{1}{2\varepsilon} - \left(\frac{1}{4\varepsilon^2} + \frac{0.01637\alpha}{\varepsilon^3}\right)^{1/2}\right]^{1/3}\right\}^3 . \quad \text{(A2)}$$

The variable parameters s and $\alpha = C^3/\tau_D$ in the convolution C_n are optimized to yield a minimum in

$$\chi^2 = \sum_{i=M}^{N} (C_i - Y_i)^2/Y_i \quad \text{(A3)}$$

where Y_i is the experimental number of counts in channel i and (M,N) is the channel range used in the analysis.

TIME-CORRELATED PHOTON-COUNTING PROBE OF SINGLET EXCITATION TRANSPORT AND RESTRICTED ROTATION IN LANGMUIR-BLODGETT MONOLAYERS

David E. Hart, Philip A. Anfinrud, and Walter S. Struve

Department of Chemistry and Ames Laboratory-USDOE,
Iowa State University, Ames, Iowa 50010

CHAPTER VIII. TIME-CORRELATED PHOTON-COUNTING PROBE OF SINGLET EXCITATION TRANSPORT AND RESTRICTED ROTATION IN LANGMUIR-BLODGETT MONOLAYERS

Introduction

Theories for electronic excitation transport in disordered systems frequently deal with singlet excitation migration among randomly situated molecules in a homogeneous d-dimensional system [1-5]. All molecules in the model system are chemically identical, no excitation trapping occurs at dimers or higher aggregates, and the excited state population decays only through unimolecular radiative and/or nonradiative processes. The molecules are typically separated by such large distances that their electronic wavefunctions have minimal overlap. If the ground and lowest excited singlet states S_0 and S_1 are connected by an E1 transition, the transport then occurs by a long-range resonance dipole-dipole mechanism [6].

A primary objective of transport theories is calculation of the time-dependent probability $G^S(t)$ that the excitation resides on the initially pumped molecule. $G^S(t)$ decays from unity at early times, as excitation hops from the initial site to neighboring molecules. However, the excitation can return to the initial site via an infinite variety of pathways, passing through arbitrary sequences of neighbors.

$G^S(t)$ is therefore strictly given by an infinite-order density expansion, which cannot be summed exactly [2,4]. Recent attention has focussed on the question of whether asymptotic expressions for $G^S(t)$ can approximate the transport behavior in real systems. At long times and/or high concentrations, $G^S(t)$ behaves as $t^{-d/2}$ [4]. For 3-dimensional systems in the short time/low concentration regime, Huber and coworkers have shown [1] that

$$G^S(t) \rightarrow \exp\left[-C\left(\frac{\pi t}{2\tau}\right)^{\frac{1}{2}}\right]. \qquad (1)$$

Here τ is the isotropic excited state lifetime, and the dimensionless reduced concentration

$$C = \frac{4}{3}\pi R_o^3 \rho \qquad (2)$$

depends on the molecule number density ρ and on the Förster parameter R_o which characterizes the strength of the resonance dipole-dipole coupling responsible for transport [6,7]. The Huber limit for $G^S(t)$ physically corresponds to ignoring excitation return pathways which pass through more than one neighbor. Baumann and Fayer [5] have extended this "two-particle" theory to 1- and 2-dimensional random systems. In the latter case the 2-particle limit for $G^S(t)$ is

$$G^s(t) \rightarrow \exp[-1.354\ C\ (t/4\tau)^{1/3}] \qquad (3)$$

where C is now the reduced coverage

$$C = \pi R_0^2 \rho \qquad (4)$$

and ρ is now the surface number density of chromophores.

The Green's function $G^s(t)$ can be directly monitored by obtaining time-resolved fluorescence profiles from disordered systems excited by linearly polarized laser pulses. While such profiles do not give an inherently sensitive probe of excitation transport (in the sense that physically dissimilar models for $G^s(t)$ can give nearly congruent calculated fluorescence profiles), the superb S/N ratios afforded by time-correlated single photon counting can be exploited to yield exacting tests of transport theories. We have recently shown that in the absence of orientational correlation [8] and artifacts such as excitation trapping [9] and self-absorption [10], the two-particle theory accurately predicts the fluorescence depolarization for DODCI [8] and rhodamine 640 [11] solutions at concentrations up to several mM and times up to ~5τ. The most probable nearest-neighbor separations are on the order of 40Å at such concentrations, and fluorescence decays to 0.7% of its peak intensity after five lifetimes. The 3-dimensional two-particle theory therefore works well at nearly all concentrations for which interchromophore

interactions are validly expressed by leading terms in the multipole expansion, and for times accessible to current fluorescence measurement techniques.

It is of particular interest to test the corresponding two-particle theory for 2-dimensional random systems, Eq. 3. Two-dimensional transport plays a potentially important role in energy transfer on modified semiconductor surfaces and micelles, and the two-particle theory has provided a basis for extensions of transport theory to Langmuir-Blodgett (LB) bilayer and multilayer assemblies [5]. To our knowledge, no definitive transport study has been performed on any system resembling the idealized 2-dimensional assembly visualized in the two-particle theory. Desiderata for such a system include good surface flatness, good spatial dispersion of chromophores, and avoidance of trapping by aggregates. In an earlier study [12], we obtained polarized fluorescences from rhodamine 3B adsorbed onto $\lambda/4$ fused silica. Trapping severely distorted the isotropic fluorescence profiles at moderate to high dye coverages. Aggregation is often prevalent in LB assemblies of alkylated chromophores dispersed in visibly transparent fatty acids. Yamazaki et al. [13] identified several excimer and excited dimer fluorescences from 16-(1-pyrenyl)hexadecanoic acid in LB films of stearic acid. In this work, we have obtained excellent dispersion of octadecylrhodamine B (ODRB) chromophores in LB monolayers of dioleoylphosphatidylcholine

(DOL) at air-water interfaces, as evidenced by the nearly constant isotropic fluorescence profiles emitted by these chromophores at reduced coverages up to C≅5. The comparatively short ODRB isotropic lifetime (~2.5ns, similar to that of rhodamine B in alcoholic solvents [14]) precludes excimer formation [15] at these coverages during the measurement time window of ~9ns. Analysis of polarized ODRB fluorescence profiles in terms of theories for $G^S(t)$ requires prior knowledge of (a) the orientational distribution of ODRB transition moments with respect to the interface normal and (b) the nature of these moments' rotational diffusion, which inevitably contributes to depolarization along with transport. These phenomena are characterized in separate experiments at low ODRB density (where negligible transport occurs), and have interesting implications for the microstructure of LB monolayers. We show that when rotational diffusion is properly considered, the two-particle theory for $G^S(t)$ provides an excellent description of the transport dynamics for ODRB reduced coverages between 0.7 and 4.8. Since the latter coverage corresponds to placing an average of 4.8 chromophores in a circle of radius R_0≅45Å for ODRB (the Excitation Transport Section), the range of validity in the two-particle theory appears to be very broad.

Experimental Section

Octadecylrhodamine B was obtained from Molecular Probes, Inc. (Eugene, OR); dioleoylphosphatidylcholine (>99%) was purchased in $CHCl_3$ solution from Avanti Polar Lipids, Inc. (Birmingham, AL). The structures of the chromophore and DOL are shown in Fig. 1. The 18 MΩ water for LB interfaces was deionized by treatment in ion exchange and charcoal columns, and was filtered before use with a 0.2 μm micropore. The LB trough and moveable barrier (Fig. 2) were fashioned from Teflon. The width of the air-water interface was 2.5 cm, and the length could be compressed from a maximum of 5.0 cm using a Newport Research Corporation Model 850-2 linear actuator. The laser beam transmitted at the interface and refracted into the water was passed by a 2.5 cm dia. fused silica window in the bottom of the trough; this minimized laser scatter into the fluorescence detector. The LB monolayer was prepared flush with the top of the trough. The trough was precisely machined to provide smooth, parallel 90° edges, and the barrier was fabricated with a smooth, matching cylindrical edge. These precautions proved critical in preventing leakage of the LB monolayer past the barrier upon compression. The surface pressure Π was monitored <u>in situ</u> during all experiments with a 0.5 cm wide Wilhelmy plate (Whatman #1 Qualitative filter paper) mechanically connected to a Mettler AE100 electronic balance

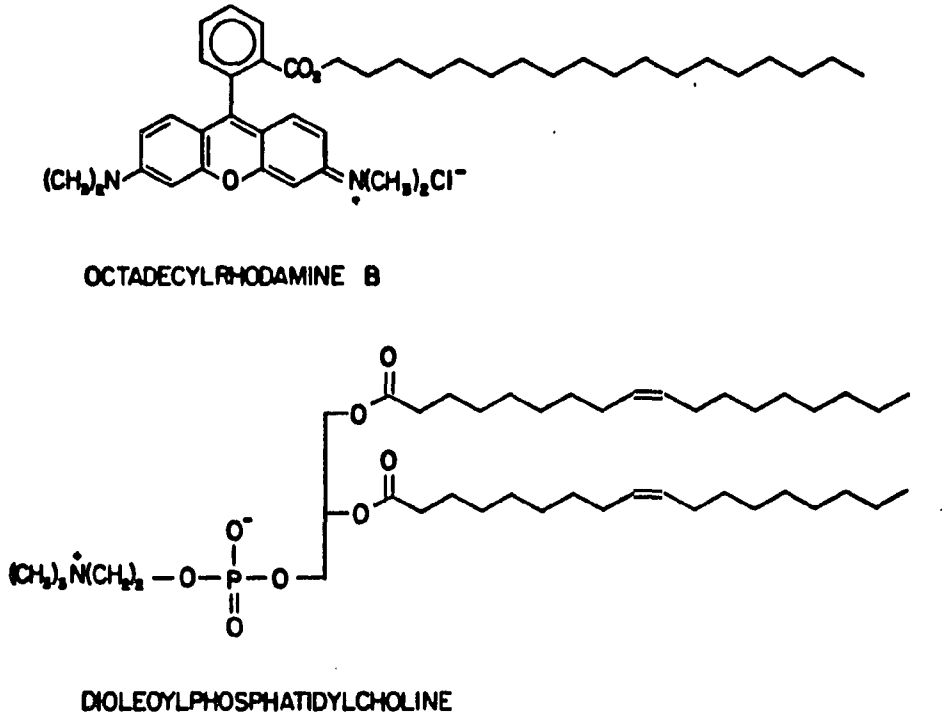

Figure 1. Molecular structures of octadecylrhodamine B (ODRB) and dioleoylphosphatidylcholine (DOL)

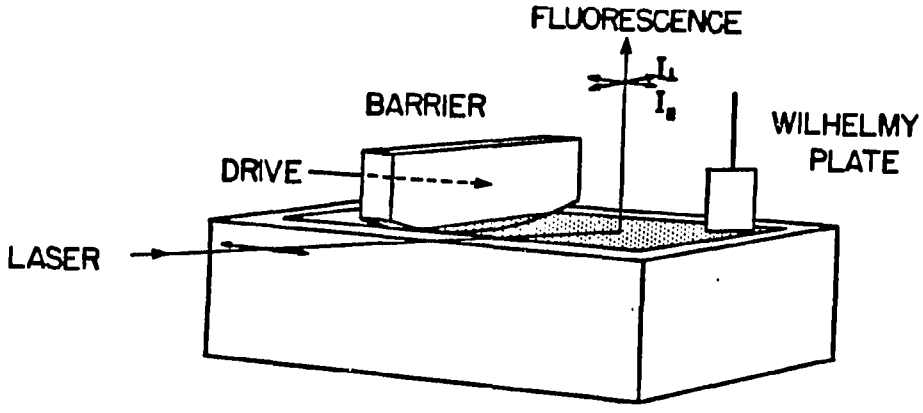

Figure 2. Schematic diagram of Langmuir-Blodgett trough, Wilhelmy plate, and beam geometry

[16,17]. Properly rinsed and prevented from drying, the same Wilhelmy plate could be used indefinitely and reproducibly. By keeping the interface flush with the top of the trough, excessive curvature was avoided near the edges of the assembly, increasing the reliability of surface pressure measurements. Cleanliness of the bare water surface was ascertained prior to monolayer preparation by verifying that the nominal surface pressure remained unchanged to within 0.1 dyne/cm while the surface area was compressed from 12.5 to 1.25 cm^2.

Stock solutions of ODRB were prepared in $CHCl_3$ (Mallinckrodt Nanograde). Aliquots of these solutions were combined with 1.00 cm^3 of the DOL solution (21 mg DOL/cm^3) and diluted to 25 cm^3 with $CHCl_3$. Each ORDB/DOL/$CHCl_3$ mixture was applied to the water surface in a 1.6 μl drop from a 10.0 μl syringe, with the barrier retracted to yield the maximum surface area of 12.5 cm^2. This procedure typically produced no discernible change in Π from that of the bare surface. The barrier was then advanced at a rate of 2 mm/min until Π increased by 0.1 dyne/cm. The advancement rate was then decreased to 0.35 mm/min to achieve near-equilibrium compression of the monolayer. Experiments were conducted at final surface pressures of 5, 15, and 25 dyne/cm (the Rotational Diffusion Section); compression to 25 dyne/cm required some 45 min. The breakdown pressure of LB monolayers of DOL is 44 dyne/cm

[18]. High ambient humidity was required to achieve reproducible compression curves and stable surface films; monolayers with Π stable to ~0.1 dyne/cm over several hours were then readily obtained.

The surface density of ODRB chromophores in LB monolayers may be estimated from the chromophore and DOL molecular weights (M_{ODRB} = 731.5 gm.mol^{-1} and M_{DOL} = 786.15 gm.mol^{-1} respectively), the volume X of the ODRB solution ailquot in cm^3, and the mass Y of the ODRB used per cm^3 of stock solution. The mole ratio of DOL to ODRB in the assembly is then R = 19.54/XY, and the mole fraction of ODRB is $X_{ODRB} = (1+R)^{-1}$. The number density of ODRB chromophores in the monolayer is

$$\rho = \frac{X_{ODRB}}{X_{ODRB}A_{ODRB} + X_{DOL}A_{DOL}} \qquad (5)$$

where A_{ODRB} and A_{DOL} are the areas occupied per molecule of chromophore and lipid, respectively. DOL reportedly occupies ~70Å^2/molecule at Π = 25 dyne/cm [18]. We have evaluated the Π versus A curve at 0.35 mm/min compression speed (which is considerably slower than that in reference [18]), and obtained A_{DOL} = 67Å^2/molecule at 25 dyne/cm. Fatty acids typically fill ~20Å^2/molecule [19]; since the largest ODRB mole fraction in this work was 0.049, the

Table I. Octadecylrhodamine B mole fractions and chromophore densities in Langmuir-Blodgett monolayers at 25 dyne/cm

Monolayer	X_{ODRB}	$\rho(10^{-6}$ Å$^{-2})$
1	0.0496	767
2	0.0321	490
3	0.0254	387
4	0.0163	246
5	0.0129	194
6	0.0082	123
7	0.0065	97

accuracy of this value for A_{ODRB} is not critical to our estimates of ρ. We list in Table I the mole fractions X_{ODRB} and estimated chromophore densities ρ for the LB monolayers used in our transport experiments.

The rhodamine 6G dye laser (synchronously pumped by an acoustooptically mode-locked argon ion laser), optics, and time-correlated single photon counting electronics have been described previously [9,20]. The laser produced linearly polarized 570 nm pulses with ~8 ps FWHM and 4.8 MHz repetition rate. The pulses were incident at 81° from the interface normal with their polarization in the surface plane (Fig. 3). Fluorescence was analyzed using a Promaster Spectrum 7 linear polarizer and detected along the surface normal using a Hamamatsu R1564U microchannel plate phototube (MCP). Two 3mm Schott OG-590 filters discriminated against scattered laser fundamental. The photon counting instrument function (evaluated by scattering laser pulses from a ground glass cover slip 0.15 mm thick) exhibited ~47 ps FWHM.

Appreciable background to the ODRB fluorescence was generated by Raman scattering from the water at the interface. For accurate cancellation of this early-time background from fluorescence profiles, the multichannel analyzer (MCA) was gated ON for a total live time which was proportional to a preset integrated laser intensity, ensuring that profiles could be accumulated with and without LB monolayers with identical background counts. This was

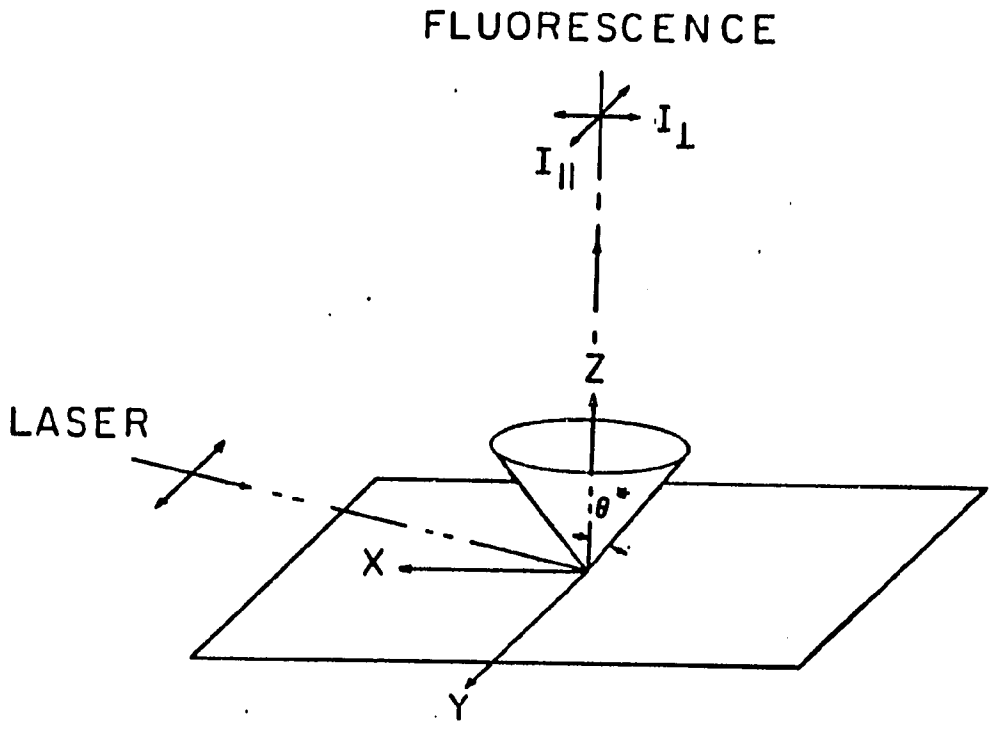

Figure 3. Detailed beam geometry. The Langmuir-Blodgett assembly lies in the xy plane. Laser pulses are y-polarized in most of this work, and fluorescence is observed along the z axis. Laser angle of incidence is 81° from the z axis. For analysis, the dye transition moments are assumed to be randomly distributed on cone of half-angle θ^* (case (b) in text)

achieved by sampling a portion of the laser pulses with an EG&G FOD-100 photodiode, whose output supplied the control voltage to a voltage-controlled oscillator (VCO). The latter oscillated with a frequency (typically 700 kHz) proportional to the laser intensity. The VCO output was enabled only during the live time of the time-to-amplitude converter (TAC), which was itself gated OFF for 125 μs after each true START input in order to eliminate TAC rate dependence for fluorescence counting rates up to 8 kHz [20]. A microprocessor enabled the MCA until a preset number of gated VCO counts was registered. In this way, fluorescence profile accumulation times were scaled to the integrated laser intensities. Such background cancellation was necessary only at the lowest ODRB densities for calibration of rotational diffusion in the absence of excitation transport.

Rotational Diffusion in Langmuir-Blodgett Assemblies

In the absence of excitation transport, the fluorescence intensity components $I_{//}(t)$ and $I_{\perp}(t)$ polarized parallel and perpendicular to the laser polarization are related to the rotational anisotropy function r(t) by

$$I_{//}(t) = P(t)[1 + d_{//}r(t)]$$

$$I_{\perp}(t) = P(t)[1 + d_{\perp}r(t)] \qquad (6)$$

if the chromophore absorption and emission transition moments are parallel. The isotropic decay function P(t), often presumed to be single-exponential in homogeneous systems [9,12], frequently acquires multiexponential character from solvent reorganization and trapping artifacts [8]. The constants $d_{//}$, $d_{\perp}$ depend on the orientational distribution of ODRB transition moments, which is unknown a priori. Conceivable distributions include (a) orientations which are isotropically random over 4π steradians, for which $d_{//} = 0.8$, $d_{\perp} = -0.4$ [21]; (b) moments which are constrained to lie on a cone of fixed half-angle θ^* (Fig. 3), but are random in the azimuthal angle ϕ about the surface normal ($d_{//} = 0.5 = -d_{\perp}$ [12]); and (c) moments which are randomly oriented inside the cone, with $0 \leq \theta < \theta^*$ and $0 \leq \phi < 2\pi$. While the isotropic distribution in case (a) appears improbable for ODRB in DOL monolayers, it is specifically considered in our transport data analysis in the Excitation Transport Section. Examples of cases (b) and (c) occur in xanthene dyes adsorbed on fused silica [22] and nonpolar lipid bilayers in vesicles [23], respectively. Apart from influencing the relationship between the rotational anisotropy function and the fluorescence

observables in Eq. 6, the moment distribution controls the magic angle θ_m at which the analyzing polarizer must be aligned in order to isolate the isotropic decay P(t). According to Eqs. 6, θ_m is 54.7° and 45° respectively for cases (a) and (b). In case (c), the magic angle and the constants $d_{//}$, $d_{\perp}$ depend on the cone half-angle θ^*.

The nature of the ODRB rotational diffusion in the DOL monolayers may be appreciated in Fig. 4, which contrasts the polarized fluorescence profiles observed in the limits of high and low chromophore density. Rapid excitation transport occurs at high density in Fig. 4(a), where essentially complete depolarization merges the $I_{//}$ and $I_{\perp}$ profiles within 5 ns after excitation. Negligible transport occurs at the low chromophore density in Fig. 4(b); here the depolarization is governed by the rotational anisotropy function according to Eq. 6. Since r(t) clearly does not tend to zero at long times ($I_{//}$ and $I_{\perp}$ do not converge together), the ODRB rotational diffusion necessarily occurs over a <u>restricted</u> range of azimuthal angles ϕ. An antecedent for restricted rotational diffusion exists on surfaces of micelles, where the chromophore transition moments are free to move inside cones with their symmetry axes parallel to the local surface normals [24]. The anisotropy function is well described in such cases by

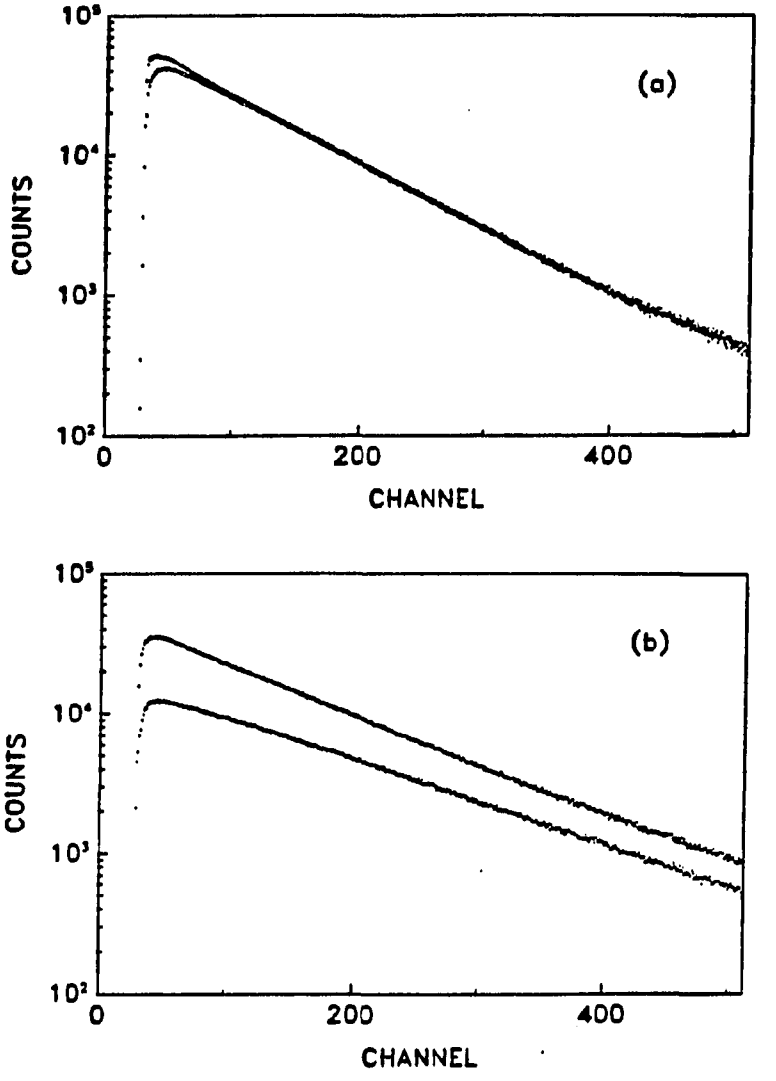

Figure 4. Polarized ODRB fluorescence profiles $I_{//}(t)$, $I_{\perp}(t)$ for chromophore densities 767 x $10^{-6}/Å^2$ (a) and 1.24 x $10^{-6}/Å^2$ (b). The time calibration is 20 ps/channel. In each figure, $I_{//}(t)$ is the upper profile. The counting periods were scaled according to the integrated laser intensities (the Experimental Section), so that these figures accurately represent the relative intensities of $I_{//}(t)$ and $I_{\perp}(t)$

$$r(t) = r(0)\ [a_\infty + (1 - a_\infty)\exp(-Dt)] \qquad (7)$$

where $a_\infty \equiv r(\infty)/r(0)$ is a measure of the restrictedness of the rotational motion and D is a "wobbling" diffusion constant. Lipari and Szabo have shown [24] that a_∞ is related to the cone half-angle θ^* by

$$a_\infty = \langle P_2(\cos\theta)\rangle^2 = 1/4\cos^2\theta^*(1 + \cos\theta^*)^2 \qquad (8)$$

so that in the limit of isotropic diffusion ($\theta^* = \pi/2$), $a_\infty \to 0$. The restricted rotation in our ODRB/DOL systems is physically different from that in micelles in that the air/water interface establishes a single, unique orientation for the cone axis if the moment distribution belongs to either type (b) or (c). The rotational depolarization observed in Fig. 4(b) cannot accompany diffusion over $0 \leq \theta < \theta^*$ and $0 \leq \phi < 2\pi$ inside the cone surface. Such diffusion processes would produce anisotropy functions r(t) which decay to zero at long times. Restrictions of diffusion to a limited range $\Delta\phi < 2\pi$ is a prerequisite for observation of the rotational anisotropy in Fig. 4(b), since only motion in the azimuthal angle ϕ leads to rotational depolarization in our beam geometry.

To characterize this rotational motion quantitatively, polarized fluorescence profiles $I_{//}(t)$ and $I_{\perp}(t)$ were obtained for several surface pressures at a chromophore

density $\rho = 1.24 \times 10^{-6}/\text{Å}^2$, low enough to suppress excitation transport. Magic-angle profiles were obtained with the analyzing polarizer aligned at 45° from the laser polarization. (The impact of this choice for θ_m on our data analysis is examined in the Excitation Transport Section; it is consistent with the moment distribution described in case (b).) Some 35,000 counts were typically accumulated in the peak channel, corresponding to S/N ~190. The magic-angle profiles were fitted with multiexponential functions P(t) using a nonlinear least-squares convolute-and-compare analysis [8,9,20] based on the Marquardt algorithm [25]. All profiles were fitted with biexponential functions; profiles obtained at 25 dyne/cm (the surface pressure used in subsequent transport studies) were also fitted with more accurate triexponential functions. The optimized multiexponential parameters (Table II) are not markedly sensitive to surface pressure, implying that the environmental factors influencing ODRB fluorescence decay change little between 5 and 25 dyne/cm.

The polarized profiles $I_{//}(t)$ and $I_{\perp}(t)$ were analyzed by a linked deconvolution procedure [9,20] using Eqs. 6 with $d_{//} = 0.5 = -d_{\perp}$ as model functions. The isotropic decay function P(t) was expressed as a multiexponential function at each surface pressure, with parameters fixed at the values listed in Table II. The rotational anisotropy was modeled by the function

Table II. Magic angle fits of ORDB fluorescence profiles

$$\rho = 1.24 \times 10^{-6}/\text{Å}^2$$

$$P(t) = \sum_i A_i \exp(-t/\tau_i)$$

Π(dyne/cm)	A_1	τ_1,ps	A_2	τ_2,ps	A_3	τ_3,ps	χ_r^2
5	0.884	2542	0.116	1859			1.28
15	0.888	2541	0.112	1934			1.14
25	0.918	2594	0.083	1998			1.44
25	0.903	2597	0.097	1874			1.41
25	0.647	2659	0.107	1779	-0.247	54.8	1.08
25	0.664	2672	0.192	1936	-0.144	95.4	1.65

$$r(t) = a + (1 - a)\exp(-t/\tau_{rot}) \quad (9)$$

where a and τ_{rot} were the only parameters varied (apart from a fluorescence intensity scaling factor) in the convolute-and-compare analyses. The results are given in Table III. Unlike the isotropic fluorescence parameters, the rotational parameters vary considerably with surface pressure. The ODRB diffusion time τ_{rot} becomes dilated as Π increased, presumably due to increased frictional drag from neighboring DOL molecules at higher surface pressure. The a parameter also increases, reflecting more restricted rotation as the monolayer becomes compressed.

The rotational parameters in Table III form a basis for analysis of the polarized fluorescence profiles at higher chromophore densities (the Excitation Transport Section), where excitation transport also contributes to the depolarization. These transport studies were performed at 25 dyne/cm, a surface pressure which affords considerable slewing of the rotational diffusion (thereby casting the transport depolarization into sharper relief) but which is still well below the DOL monolayer breakdown pressure at 44 dyne/cm [18]. For these experiments, rotational parameters were derived by averaging the last two lines in Table III, $a = 0.386$ and $\tau_{rot} = 4331$ ps.

Table III. Fitting parameters for anisotropic ODRB fluorescence profiles, $\rho = 1.24 \times 10^{-6}/\text{Å}^2$

$$I_{\parallel,\perp} = P(t)[1 \pm 0.5r(t)]$$

$$r(t) = a + (1 - a)\exp(-t/\tau_{rot})$$

Π(dyne/cm)	a	τ_{rot}, ps	$\chi_r^2(\substack{\parallel \\ \perp})$
5	0.2593	2620	1.44 1.54
15	0.2991	3579	1.22 1.36
25	0.3767	4562	1.62 1.31
25	0.3957	4100	2.79 1.55

If the moment distribution is known to belong to either case (b) or (c), the cone half-angle θ^* can be inferred by measuring the total integrated fluorescence intensity $\int[I_{//}(t) + I_{\perp}(t)]dt$ at low chromophore density for two different laser polarizations. Let I_s and I_p be the total intensities measured for the laser polarization in the surface plane and for the polarization normal to this. It is readily shown that if the moments lie on the cone surface as in case (b), the resulting ratio of integrated intensities is related to θ^* by

$$\theta^* = \tan^{-1}\left[\frac{2\sin^2\lambda}{I_p/I_s - \cos^2\lambda}\right]^{1/2} \qquad (10)$$

where λ is the laser angle of incidence at the surface. The ratio is unaffected by rotational diffusion in case (b). Since the measured ratio I_s/I_p (obtained using the profile integration feature in the MCA) is 1.31 for Π = 25 dyne/cm and λ = 81°, the inferred cone angle is 58.4°. This value is quite insensitive to λ for λ near 90°: using λ = 90° instead of 81° yields θ^* = 58.3°. It is similar to adsorption angles reported [22] for rhodamines on fused silica. (Since the $S_0 \rightarrow S_1$ transition is long axis-polarized in rhodamines [26], these angles are between the chromophore long axis and the surface normal.) For moments randomly distributed inside the cone (case (c)) with λ = 90°,

$$\frac{I_s}{I_p} = \frac{8(1-\cos\theta^*) - 3\sin^2\theta^* \cos\theta^* \left(\frac{4}{3} + \sin^2\theta^*\right)}{4(1-\cos\theta^*) - 6\sin^2\theta^* \cos\theta^* \left(\frac{1}{3} - \sin^2\theta^*\right)} . \qquad (11)$$

To achieve an intensity ratio of 1.31, the angle θ^* must then be almost 80°, which corresponds to a nearly isotropic distribution. This appears inconsistent with the geometric constraints expected in ODRB chromophores attached to vertical alkyl chains in highly organized monolayers, and these arguments (which are approximate in that Eqs. 10-11 overlook the slow rotational diffusion observed at 25 dyne/cm, Table III) suggest that the moments are in fact distributed on a cone, case (b). This result is not critical to our analysis of transport depolarization in the Excitation Transport Section, and is mentioned here only for its glimpse into the apparent structure of the monolayers.

Excitation Transport in Langmuir-Blodgett Assemblies

In the presence of excitation transport, the fluorescence intensity components are given by

$$I_{//}(t) = P(t)[1 + d_{//} r(t) G^S(t)]$$

$$I_{\perp}(t) = P(t)[1 + d_{\perp} r(t) G^S(t)] \qquad (12)$$

if the chromophore absorption and emission transition moments are parallel and if the laser beam is weak enough to avoid perturbing the orientational distribution of unexcited molecules. A fundamental assumption behind Eqs. 12 is that the ensemble average of the residual polarization $(I_{//} - I_{\perp})/(I_{//} + I_{\perp})$ following a single excitation hop from the initial site is zero [27]. We have analyzed the residual polarization in 2- and 3-dimensional systems [28], and determined that the effects of ignoring it are negligible under present photon counting statistics.

For 2-dimensional transport in which the transition moments are distributed on cones, the constants $d_{//}$, $d_{\perp}$ and θ_m are +0.5, -0.5, and 45°. The anisotropy function r(t) is given by Eq. 9, with the rotational diffusion parameters fixed at a = 0.386 and τ_{rot} = 4331 ps for 25 dyne/cm surface pressure. For each of the monolayers listed in Table I, the $I_{//}$, $I_{\perp}$, and magic-angle profiles were obtained, with typically 50,000 peak channel counts in the $I_{//}$ profile. In several of the data sets, the profiles were accumulated in the order $I_{//}$, magic-angle, $I_{\perp}$, magic-angle, $I_{//}$ in order to check reproducibility. In other data sets, the order of the $I_{//}$ and $I_{\perp}$ profiles was interchanged. The first and last files created in such sequences were always virtually identical, indicating that the ODRB chromophore were stable with respect to laser exposure and oxidation in air over accumulation times of several hours.

The magic-angle profiles were fitted with biexponential expressions for P(t) at all densities but the highest ($767 \times 10^{-6}/Å^2$), where trapping by aggregates considerably distorted the decay. The optimized parameters are listed in Table IV. Trapping causes the magic-angle lifetime to decrease by ~20% between the lowest and highest densities. Nonexponentiality due to trapping becomes evident only at the highest density, where P(t) is simulated by a triexponential decay law in Table IV. This distortion of magic-angle profiles considerably exceeds that observed in dye solutions: the isotropic lifetime of DODCI in glycerol drops by only 6% between 0.012 and 2.49 mM [20]. ODRB in DOL shows far less distortion (for comparable chromophore densities) than rhodamine 3B on silica [12]. Several other alkylated chromophores (e.g., 1, 1'-dihexadecyloxadicarbocyanine perchlorate) were tried in monolayers of arachidic acid; aggregation truncated their isotropic lifetimes by at least an order of magnitude from those exhibited by the same chromophore in alcoholic solution. Self-absorption, an important artifact in 3-dimensional systems [10], is of course absent in these monolayer assemblies.

The polarized profiles $I_{//}(t)$, $I_{\perp}(t)$ were fitted with Eqs. 12 using the linked deconvolution algorithm. The parameters in the isotropic decay functions P(t) were fixed at the values in Table IV, and the 2-dimensional two-

Table IV. Magic-angle fits of ODRB fluorescence profiles at high densities[a]

$$P(t) = \sum_i A_i \exp(-t/\tau_i)$$

Monolayer	A_1	τ_1,ps	A_2	τ_2,ps	A_3	τ_3,ps	χ_r^2
1	0.689	1956	0.292	1425	-0.019	228.3	2.86
1	0.686	1966	0.295	1435	-0.020	335.4	2.92
2	0.969	2053	-0.031	185.1			1.69
2	0.965	2041	-0.035	191.1			1.70
3	0.976	2170	-0.024	258.6			2.91
4	0.947	2265	-0.053	146.4			1.61
4	0.955	2264	-0.045	213.5			1.45
5	0.962	2312	-0.038	244.5			1.74
6	0.979	2413	-0.021	242.8			2.94
6	0.985	2405	-0.015	314.3			3.23
7	0.958	2424	-0.042	243.4			2.58

[a] Π = 25 dyne/cm.

particle function (Eq. 3) was used for $G^s(t)$. The isotropic lifetime τ in $G^s(t)$ was held at 2650 ps, which approximates the average long-component lifetime of ODRB at low density. (The value of τ pertinent to transport theory is the isolated-molecule lifetime, not the phenomenological lifetimes characterizing the high-density profiles that are distorted by trapping.) Aside from a scaling factor, the only varied parameter in the polarized fluorescence intensities is the reduced coverage C (Eq. 4), which enters in $G^s(t)$. The optimized reduced coverages are given in Table V, and are plotted versus the true chromophore density ρ (Table I) in Fig. 5. The points in this figure should fall on a straight line if the 2-particle theory for $G^s(t)$ is valid. This appears to be very nearly the case. The reduced coverage C in the two-particle theory for $G^s(t)$ is not the true reduced coverage, because the theory is based on an excitation transport probability which is orientationally averaged over 4π steradians. The actual transport rate is proportional to the dipole-dipole orientational factor

$$\kappa^2 = [\hat{d}_i \cdot \hat{d}_j - 3(\hat{d}_i \cdot \hat{r}_{ij})(\hat{d}_j \cdot \hat{r}_{ij})]^2 \qquad (13)$$

where $\hat{d}_i$, $\hat{d}_j$ are unit vectors along the transition moments of chromophores i, j and $\underset{\sim}{r}_{ij}$ is their separation. Correct

Table V. Fitting parameters for anisotropic ODRB fluorescence profiles at high densities[a]

$$I_{\parallel,\perp} = P(t)[1 \pm 0.5r(t)G^S(t)]$$

$$G^S(t) = \exp[-1.354C(t/4\tau)^{1/3}]$$

Monolayer	C	C_D	$\chi^2_r(\parallel)$ $\chi^2_r(\perp)$
1	4.38	4.95	4.24 2.81
1	4.07	4.60	3.56 2.31
2	2.74	3.10	1.87 1.77
2	2.71	3.06	2.28 1.74
3	2.07	2.34	4.24 2.65
4	1.47	1.66	2.22 1.65
4	1.48	1.67	2.11 1.62
5	1.12	1.27	2.66 1.85
6	0.76	0.86	4.21 2.45
6	0.73	0.82	4.86 2.76
7	0.66	0.75	4.08 2.23

[a] Π = 25 dyne/cm.

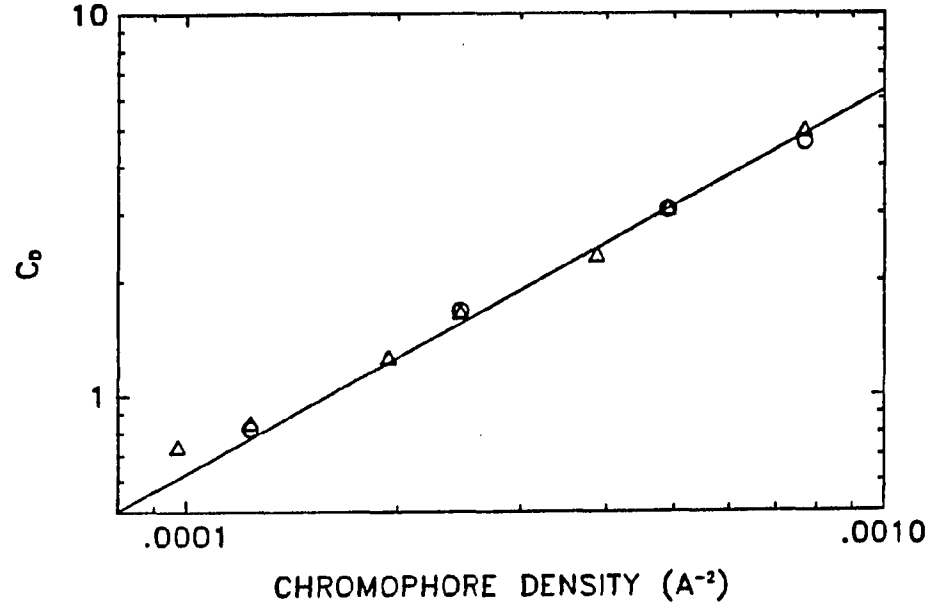

Figure 5. Optimized reduced coverages C_D versus actual ODRB chromophore densities ρ, from linked deconvolutions of $I_{//}$ and $I_{\perp}$ fluorescence profiles using two-particle theory for $G^S(t)$. Straight line gives loci of true reduced concentrations versus ρ for Förster parameter R_O = 44.7Å

averaging of the transport rate over the orientational distribution of moments in the two-particle theory replaces C with the true reduced coverage C_D, where

$$C = C_D\left[\frac{3}{2}\right]^{1/3} \langle\kappa^2\rangle^{1/3} \tag{14}$$

in the dynamic limit where rotational diffusion is rapid compared to transport, and

$$C = C_D\left[\frac{3}{2}\right]^{1/3} \langle|\kappa|^{2/3}\rangle \tag{15}$$

in the static limit of slow rotational diffusion [5]. For moments which are confined to the surface of a cone of half-angle $\theta^* = 58.4°$ (case (b)), the values of $\langle\kappa^2\rangle^{1/3}$ and $\langle|\kappa|^{2/3}\rangle$ are 0.733 and 0.775 respectively. Since the static limit is more appropriate to the ODRB/DOL systems at 25 dyne/cm (Table III), we then take $C = 0.775(3/2)^{1/3}C_D$, or $C_D = 1.13C$. The corresponding values of the "true" reduced coverage (which actually depends on our model for the orientational distribution) are listed in Table V. They are also used for the ordinate in Fig. 5. From the least-squares line which approximates the locus of the points, we derive the value 44.7Å for the Förster parameter R_o. For comparison the value $R_o = 51.5$Å has been inferred

spectroscopically for ODRB in micelles [21]; the difference may reflect environmental effects on R_o.

These conclusions nominally depend on the specific relationships (Eqs. 12) between $G^s(t)$ and the fluorescence observables: our analysis so far has hinged on the assumption that the transition moments are randomly distributed on a cone. We now consider the effects of relaxing this assumption by postulating that while the moments are random in ϕ, the θ-distribution is given by the more general Gaussian function

$$g(\theta) = \exp[-2.77(\theta - \theta^*)^2/\Gamma^2] \tag{16}$$

which has an FWHM of Γ. In the limit $\Gamma \to 0$, $g(\theta)$ becomes proportional to $\delta(\theta - \theta^*)$, as in case (b). When Γ becomes large, the resulting isotropic distribution $g(\theta) = 1$ corresponds to case (a). In the absence of rotational diffusion, the fluorescence intensity components $I_{//}$ and $I_{\perp}$ prior to transport will be proportional to

$$e_{//}^0 = \int_0^{2\pi} d\phi \int_0^{\pi/2} \sin\theta \, d\theta \, g(\theta) \sin^4\theta \cos^4\phi$$
$$e_{\perp}^0 = \int_0^{2\pi} d\phi \int_0^{\pi/2} \sin\theta \, d\theta \, g(\theta) \sin^4\theta \sin^2\phi \cos^2\phi \tag{17}$$

while the component I_n polarized normal to both $I_{//}$ and $I_\perp$ (parallel to the z axis in Fig. 3) will be proportional to

$$e_n^0 = \int_0^{2\pi} d\phi \int_0^{\pi/2} \sin\theta \, d\theta \, g(\theta) \sin^2\theta \cos^2\theta \cos^2\phi. \tag{18}$$

If complete depolarization accompanies a single excitation hop on the average from the initial site [28], the fluorescence components after one hop will be proportional to

$$\begin{aligned} e_{//}^1 &= \int_0^{2\pi} d\phi \int_0^{\pi/2} \sin\theta \, d\theta \, g(\theta) \sin^2\theta \cos^2\phi \\ e_\perp^1 &= \int_0^{2\pi} d\phi \int_0^{\pi/2} \sin\theta \, d\theta \, g(\theta) \sin^2\theta \sin^2\phi \\ e_n^1 &= \int_0^{2\pi} d\phi \int_0^{\pi/2} \sin\theta \, d\theta \, g(\theta) \cos^2\theta. \end{aligned} \tag{19}$$

The polarized fluorescence intensities are then given by

$$\begin{aligned} I_{//}(t) &\propto P(t)[e_{//}^0 G^S(t) + A e_{//}^1 (1 - G^S(t))] \\ I_\perp(t) &\propto P(t)[e_\perp^0 G^S(t) + A e_\perp^1 (1 - G^S(t))] \end{aligned} \tag{20}$$

or equivalently

$$I_{\parallel}(t) = P(t)[1 + d_{\parallel}G^{S}(t)]$$

$$I_{\perp}(t) = P(t)[1 + d_{\perp}G^{S}(t)] \tag{21}$$

with

$$d_{\parallel} = \frac{e_{\parallel}^{0}}{Ae_{\parallel}^{1}} - 1$$

$$d_{\perp} = \frac{e_{\perp}^{0}}{Ae_{\perp}^{1}} - 1. \tag{22}$$

The normalization constant A in Eqs. 20, 22 may be evaluated from the conservation law

$$e_{\parallel}^{0} + e_{\perp}^{0} + e_{n}^{0} = A(e_{\parallel}^{1} + e_{\perp}^{1} + e_{n}^{1}) \tag{23}$$

so that the constants $d_{\parallel}$, $d_{\perp}$ are uniquely determined by the moment distribution function $g(\theta)$. The magic-angle θ_m is then given by

$$\theta_m = \tan^{-1}\left[(-d_{\parallel}/d_{\perp})^{1/2}\right]. \tag{24}$$

In Figure 6, $d_{\parallel}$ and $d_{\perp}$ are plotted as functions of the dispersion Γ in the distribution function $g(\theta)$ for $\theta^{*} = 30°$, 60°, and 90°. When $\Gamma = 0$, we obtain the case (b) limit

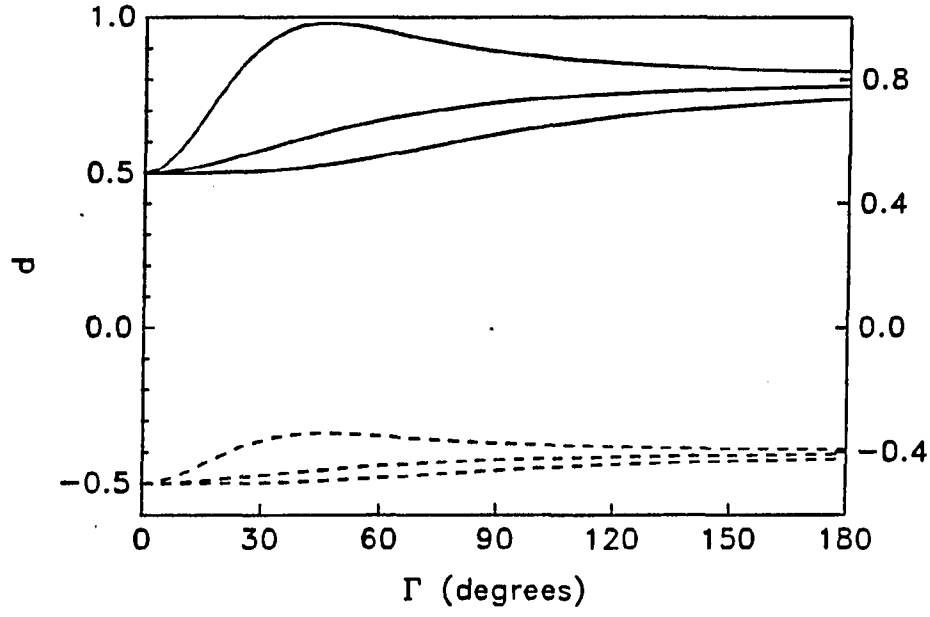

Figure 6. Plots of $d_{\parallel}$ (solid curves) and $d_{\perp}$ (dashed curves) versus the dispersion Γ of the orientational distribution function $g(\theta)$. Values of θ^* in each group of curves are (from top) 30°, 60°, and 90°

$d_{\parallel} = 0.5 = -d_{\perp}$. For large dispersions, the case (a) isotropic limit $d_{\parallel} = 0.8$, $d_{\perp} = -0.4$ is approached. Our measurement of I_s/I_p (the Rotational Diffusion Section) indicate that θ^* is on the order of 60° or larger. For such angles, $d_{\parallel}$ and $d_{\perp}$ increase monotonically with Γ while maintaining the ratio $(d_{\parallel}+ 1)/(d_{\perp}+ 1)$ equal to 3. It is clear in Fig. 6 that $d_{\parallel}$, $d_{\perp}$, and the magic-angle θ_m will be barely affected as the dispersion Γ is increased from 0° to 20°. For such dispersions, the assumption of a case (b) orientational distribution remains valid.

For larger dispersions Γ the use of Eqs. 12 with $d_{\parallel}= 0.5 = -d_{\perp}$ will introduce noticeable errors in the data analysis. In the "worst case" simulation, model fluorescence profiles were generated with the isotropic expressions

$$I_{\parallel}(t) = \exp(-t/\tau_F)[1 + 0.8G^s(t)r(t)]$$
$$I_{\perp}(t) = \exp(-t/\tau_F)[1 - 0.4G^s(t)r(t)]. \qquad (25)$$

A magic-angle profile $I_m(t)$ was simulated by

$$I_m(t) = \exp(-t/\tau_F)[1 + 0.4G^s(t)r(t)] \qquad (26)$$

and represented the profile which would be observed if the magic-angle were mistakenly taken to be 45° instead of

54.7°. The isotropic lifetime τ_F was taken to be 2600 ps. The rotational anisotropy function was generated using $r(t) = a + (1 - a)\exp(-t/\tau_{rot})$, with $a = 0.350$ and $\tau_{rot} = 4300$ ps. The two-particle expression of Eq. 3 was used to simulate $G^S(t)$ for various C_D, and all profiles were convoluted with an experimental instrument function. Gaussian noise was added to all profiles in order to replicate the S/N ratios characteristic for 50,000 counts in the peak channel of $I_{||}(t)$.

The profiles calculated using $C_D = 0$ were analyzed to obtain the rotational parameters, yielding $a = 0.382$ and $\tau_{rot} = 4713$ ps. These shifts from the simulated values (0.350 and 4300 ps respectively) reflect the errors introduced by assuming a case (b) instead of case (a) orientational distribution. The magic-angle profiles $I_m(t)$ simulated at larger C_D were fitted with biexponential models for P(t), and the polarized profiles were then deconvoluted using Eqs. 12 with $d_{||} = 0.5 = -d_{\perp}$. The results of such analyses are shown in Table VI, which lists the input C_D values used in the simulation and the optimized reduced coverages C obtained in the deconvolutions. In spite of the fact that the isotropic simulated data are incorrectly analyzed in terms of a case (b) distribution in the Table, the true C_D values are recovered to within ~15% in the deconvolutions. Moreover, the percent discrepancies Δ are nearly constant, and the linearity of a plot similar to that

Table VI. Fitting parameters for similated anisotropic ORDB fluorescence profiles

$$I_{\parallel,\perp} = P(t)[1 \pm 0.5r(t)G^{s}(t)]$$

$$G^{s}(t) = \exp[-1.354C(t/4\tau)^{1/3}]$$

C_D	$0.886C_D$[a]	$\Delta(\%)$	$\chi^2_r(\frac{\parallel}{\perp})$
0.178	0.140	-11.2	1.15 1.06
0.316	0.236	-15.7	0.992 0.982
0.562	0.433	-13.2	1.11 1.01
1.00	0.755	-14.9	1.18 1.14
1.78	1.33	-15.6	1.28 1.21
3.16	2.41	-14.1	1.28 1.08
5.62	4.47	-10.4	1.06 1.18

[a]Static orientational factor for 2-dimensional system with moments randomly distributed on cone with $\theta^* = 58.4°$.

in Fig. 5 is hardly affected. Hence, our conclusion that the 2-dimensional two-particle theory for $G^S(t)$ works well for all of the densities shown in Fig. 5 is not sensitive to the model assumed for the orientational distribution of transition moments.

Polarized fluorescence profiles obtained at higher chromophore densities than those shown in Table I show an interesting anomaly in that the fluorescence components $I_{\parallel}$, $I_{\perp}$ do not converge together at long times. At 1511×10^{-6} chromophores/Å^2, the two profiles intersect after ~1 ns, and $I_{\perp}$ decays more slowly than $I_{\parallel}$ at long times. At 2932×10^{-6} chromophores/Å^2, $I_{\perp}$ remains below $I_{\parallel}$ at all times, and the phenomenological decay times are markedly reduced. These ODRB densities are extremely large (the latter density corresponds to packing and average of ~16 chromophore per circle of radius R_o = 44.7Å), and these polarization effects may result from excimer formation.

Acknowledgments

The Ames Laboratory is operated for the U.S. Department of Energy by Iowa State University under Contract No. W-7405-Eng-82. This work was supported by the Office of Basic Energy Sciences. We thank Professors Michael Fayer, Charles Harris, and Larry Patterson for valuable discussions.

References

1. Huber, D. L.; Hamilton, D. S.; Barnett, B. Phys. Rev. B 1977, 16, 4642.
2. Gochanour, C. R.; Anderson, H. C.; Fayer, M. D. J. Chem. Phys. 1979, 70, 4254.
3. Loring, R. F.; and Fayer, M. D. Chem Phys. 1982, 70, 139.
4. Fedorenko, S. G.; Burshtein, A. I. Chem. Phys. 1985, 98, 341.
5. Baumann, J.; Fayer, M. D. J. Chem. Phys. 1986, 85, 4087.
6. Dexter, D. L. J. Chem. Phys. 1953, 21, 836.
7. Förster, Th. Discuss. Faraday Soc. 1959, 27, 7.
8. Anfinrud, P. A.; Struve, W. S. J. Chem. Phys. in press.
9. Anfinrud, P. A.; Hart, D. E., Hedstrom, J. F.; and Struve, W. S. J. Phys. Chem. 1986, 90, 2374.
10. Hammond, P. R. J. Chem. Phys. 1979, 70, 3884.
11. Causgrove, T. P.; Bellefeuille, S.; and Struve, W. S. J. Phys. Chem. to be published.
12. Anfinrud, P. A.; Hart, D. E.; Hedstrom, J. F.; and Struve, W. S. J. Phys. Chem. 1986, 90, 3116.
13. Yamazaki, I.; Tamai, N.; and Yamazaki, T. "Ultrafast Phenomena V" Eds. Fleming, G. R.; and Siegman, A. E.; Springer-Verlag: Berlin, 1986; p. 444.
14. Sadkowski, P. J.; and Fleming, G. R. Chem. Phys. Letters 1978, 57, 526.
15. Subramanian, R.; and Patterson, L. K. J. Am. Chem. Soc. 1985, 107, 5820.
16. Möbius, D.; Bücher, H.; Kuhn, H.; and Sondermann, J. Ber. Bunsenges. Phys. Chemie 1969, 73, 845.

17. Kleinschmidt, A. Proc. Third Intern. Congr. Surface Activity, Deutscher Ausshuss für grenzflächenaktive Stoffe, Universitätsdruckerei, Mainz, 1961, Vol. II, 138.

18. Tancrede, P.; Parent, L.; Paquin, P.; and Leblanc, R. M. J. Colloid and Interface Sci. 1981, 83, 606.

19. Adamson, A. W. "Physical Chemistry of Surfaces" Fourth Ed.; John Wiley & Sons: New York, 1982;

20. Hart, D. E.; Anfinrud, P. A.; Struve, W. S. J. Chem. Phys. 1987, 86, 2689.

21. Ediger, M. D.; Fayer, M. D. J. Phys. Chem. 1984, 88, 6108.

22. Heinz, T. F.; Shen, C. K.; Richard, D.; and Shen, Y. R. Phys. Rev. Lett. 1982, 48, 478. DiLazzaro, P.; Mataloni, P.; and DeMartin, F. Chem. Phys. Letters 1985, 114, 103.

23. Lakowicz, J. R. "Principles of Fluorescence Spectroscopy"; Plenum Press: New York, 1983; chapter 5.

24. Lipari, G.; and Szabo, A. Biophys. J. 1980, 30, 489.

25. Marquardt, D. W. J. Soc. Ind. Appl. Math. 1963, 11, 431.

26. Drexhage, K. H. in "Dye Lasers", Ed. F. P. Schäfer; Springer-Verlag: Berlin, 1973.

27. Craver, F. W.; Knox, R. S. Mol. Phys. 1971, 22, 385.

28. Anfinrud, P. A.; Struve, W. S. J. Phys. Chem. in press.

CHAPTER IX. SUMMARY

Excitation transport in disordered 3-dimensional arrays of chromophores with randomly oriented transition dipoles is addressed in two experimental systems. The results of the earliest experiments on rh 6G in glycerol were influenced by artifacts similar to those which have influenced the results of previous work [25]. The ~10 μm absorption cell could not eliminate the effects of fluorescence self-absorption. In addition, excitation trapping by dye aggregates at the higher concentrations quenched the transport and fluorescence and skewed the isotropic and polarized emission profiles. The data analysis procedure used does not properly account for these effects. The fluorescence lifetime τ is a parameter of both $e^{-t/\tau}$ and $G^s(t)$ in Eqs. 2 of Chapter V. In view of the artifacts present, attempts to optimize τ as well as C in the fitting procedure probably adversely affects the convergence of C to accurate values.

The 3-dimensional transport studies on DODCI in glycerol address the problems encountered in the rh 6G in glycerol work. THe effects of fluorescence self-absorption were nearly eliminated by reducing the optical density of the samples with a ~2 μm absorption cell. The effects of trapping by dye aggregates were compensated for in the data fitting procedure. The isotropic decay, P(t) in Eqs. 3 of Chapter VI, was accurately fit to a phenominological model

(biexponential decay) and entered as a fixed quantity in the fitting model for the polarized emission profiles. The value of the fluorescence lifetime τ was determined in a separate experiment at low concentration where it could not be influenced by self-absorption or fluorescence quenching by dye aggregates. This value of τ is entered as a fixed parameter for $G^S(t)$ in the fitting model for the polarized emission profiles. This leaves only a model scaling parameter and the reduced concentration C as variables in the polarized emission fitting model. With this procedure $G^S(t)$ as a function of C is modeling the difference in behavior between the isotropic decay and the polarized emission profiles. That difference is due to depolarization due to excitation transport.

The DODCI in glycerol work also demonstrates the equivalence of the 3-body GAF theory and a much simpler 2-particle theory over the concentration and time range studied ($C \lesssim 1.0$ and $t \lesssim 6\tau$). The close agreement between these models suggests that the deviations from theoretical predictions observed in our data (Fig. 5, Chapter VI) may be due to a nonrandom distribution of the dye molecules in glycerol. Recent work by Anfinrud and Struve [49] suggests that much of the deviation observed can be accounted for by orientational correlation of the DODCI transition dipoles imposed by long range structure of the liquid glycerol.

Two-dimensional energy transport was studied in two very different experimental systems. The preliminary work was performed of 2-dimensional arrays of R3B adsorbed onto optically flat fused silica. Several problems prevented a detailed comparison of the experimental data with theory. An accurate estimate for the chromophore surface density could not be obtained because of the unknown nature of the dye adsorption isotherm from aqueous solution. Also, the optical densities of the samples were too low to permit useful adsorption measurements. Inhomogeneity of the adsorption sites and a surface which is not likely to be flat on the molecular level leads to uncertainty in the distribution of the transition dipole orientations. Aggregation of the dye adsorbed onto the surface proved to be severe and limited the range of concentrations which could be studied.

Many of these problems were overcome in the work on 2-dimensional arrays of ODRB dispersed in DOL in a Langmuir-Blodgett film at an air-water interface. The air-water interface provides a flat homogeneous surface. Compression curves (surface pressure vs. area) even at the highest dye surface concentrations (0.05 mole fraction ODRB) are smooth indicating no breakdown in the organization of the film. Aggregation problems were minimal. Energy transport at reduced donor concentrations up to ~5.0 are possible.

Depolarization due to the restricted rotational motion of the dye in the film was modeled at low concentrations where energy transport is negligible. At higher concentrations, the additional depolarization of the fluorescence due to excitation transport is modeled quite accurately by a 2-dimensional model developed by Baumann and Fayer [26] based on the 2-particle model of Huber et al. [22].

LITERATURE CITED

1. Beddard, G. S.; Porter, G. Nature 1976, 260, 366.
2. Kenney-Wallace, G. A.; Flint, J. H.; Wallace, S. C. Chem. Phys. Lett. 1975, 32, 71.
3. Ediger, M. D.; Fayer, M. D. J. Phys. Chem. 1984, 88, 6108.
4. Ediger, M. D.; Fayer, M. D. J. Chem. Phys. 1983, 78, 2518.
5. Ediger, M. D.; Fayer, M. D. Macromolecules 1983, 16, 1839.
6. Avouris, Phaedon; Gelbart, W. M.; El-Sayed, M. A. Chem. Rev. 1977, 77, 793.
7. Förster, Th. Ann. der Phys. 1948, 6, 55.
8. Förster, T. Discuss. Faraday Soc. 1959, 27, 7.
9. Fleming, G. R. "Chemical Applications of Ultrafast Spectroscopy"; Oxford University Press: New York, 1986.
10. Dexter, D. L. J. Chem. Phys. 1953, 21, 836.
11. Knox, R. S. Physica 1968, 39, 361.
12. Hemenger, R. P.; Pearlstein, R. M. J. Chem. Phys. 1973, 59, 4064.
13. Lakowicz, J. R. "Principles of Fluorescence Spectroscopy"; Plenum Press: New York, 1983.
14. Chuang, T. J.; Eisenthal, K. B. J. Chem. Phys. 1972, 57, 5094.
15. Galanin, M. D. Tr. Fiz. Inst. Akad. Nauk USSR 1950, 5, 339.
16. Weber, G. Trans. Faraday Soc. 1954, 50, 552.
17. Jablonski, A. Acta Phys. 1955, 14, 295.
18. Hedstrom, J. F. Ph.D. Dissertation, Department of Physical Chemistry, Iowa State University, 1987.

19. Haan, S. W.; Zwanzig, R. J. Chem. Phys. 1978, 68, 1879.

20. Gochanour, C. R.; Andersen, H. C.; Fayer, M. D. J. Chem. Phys. 1979, 70, 4254.

21. Loring, R. F.; Fayer, M. D. Chem Phys. 1982, 70, 139.

22. Huber, D. L.; Hamilton, D. S.; Barnett, B. Phys. Rev. B. 1977, 16, 4642.

23. Stehfest, H. Commun. ACM 1970, 13, 47.

24. Anfinrud, P. A.; Struve, W. S. J. Phys. Chem. 1987, 91, in press.

25. Gochanour, C. R.; Fayer, M. D. J. Phys. Chem. 1981, 85, 1989.

26. Baumann, J.; Fayer, M. D. J. Chem. Phys. 1986, 85, 4087.

27. Knoester, J.; Van Himbergen, J. E. J. Chem. Phys. 1984, 80, 4200.

28. Fedorenko, S. G.; Burshtein, A. I. Chem. Phys. 1985, 98, 341.

29. Klafter, J.; Silbey, R. J. Chem. Phys. 1980, 72, 843.

30. O'Connor, D. V.; Phillips, D. "Time-correlated Single Photon Counting"; Academic Press: New York, 1984.

31. Coates, D. B. J. Phys. E. 1968, 1, 878.

32. Bevington, P. R. "Data Reduction and Error Analysis for the Physical Sciences"; McGraw-Hill Book Co.: New York, 1969.

33. Yasa, Z. A.; Amer, N. M. Opt. Commun. 1981, 36, 406.

34. Klann, H.; Kuhl, J.; von der Linde, D. Optics Comm. 1981, 38, 390.

35. Robbins, R. J. Ph.D. Dissertation, Department of Physical Chemistry, University of Melbourne, 1980.

36. Bebelaar, D. Rev. Sci. Instrum. 1986, 57, 1116.

37. Yamazaki, I.; Tamai, N.; Kume, H.; Tsuchiya, H.; Oba, K. Rev. Sci. Instrum. 1985, 56, 1187.

38. Manufacturer's test sheet, March 28, 1985.

39. Tennelec Instruction Manual for TC455 Quad Constant Fraction Discriminator, June 1, 1984.

40. Haugen, G. R.; Wallin, B. W.; Lytle, F. E. Rev. Sci. Instrum. 1979, 50, 64.

41. Hammond, P. R. J. Chem. Phys. 1979, 70, 3884.

42. Tancrede, P.; Parent, L.; Paquin, P.; and Leblanc, R. M. J. Colloid and Interface Sci. 1981, 83, 606.

43. Kuhn, H.; Möbius, D.; Bücher, H. in "Physical Methods of Chemistry Part IIIB Optical, Spectroscopic and Radioactivity Methods" Weissberger, A.; Rossiter, B. W. Eds.; Wiley-Interscience: New York, 1972.

44. Grinvald, A.; Steinberg, I. Z. Anal. Biochem. 1974, 59, 583.

45. Marquardt, D. W. J. Soc. Ind. Appl. Math. 1963, 11, 431.

46. Knight, H. E. W.; Selinger, B. K. Spectrochimica Acta 1971, 27A, 1223.

47. Svec, H. J.; Peterson, N. C. in "Physical Chemistry Experiments, Revised Edition", Unpublished, Chemistry Department, Iowa State University, Copyright 1978.

48. Knutson, J. R.; Beechem, J. M.; Brand, L. Chem. Phys. Lett. 1983, 102, 501.

49. Anfinrud, P. A.; Struve, W. S. J. Chem. Phys. 1987, 87, in press.

ACKNOWLEDGMENTS

As with any undertaking of this magnitude, much time and work has been invested by the author. However, no project such as this is the result of a single individual's efforts. The assistance and support of coworkers, friends, and family deserves to be recognized and praised.

Professor Walter Struve, my research advisor, possesses an incredible reserve of patience from which he was required to make frequent withdrawals. His guidance was essential to the completion of this work. Both Dr. Struve and his wife, Helen, deserve thanks for the generous use of their home for group parties and the use of their dog, Taco, for wrestling.

Phil Anfinrud and Jack Hedstrom were my coworkers and companions in the laboratory. The friendships which developed because of these associations are surely as valuable as the work produced from them. Phil's contagious enthusiasm for science provided the necessary catalyst to carry on when the road was rough.

In addition to being a coworker, Jack also turned out to be a tolerable housemate and first-rate friend. Many of my experiences with Jack and another friend, Cris Morgante, are among the most memorable (remember the time you crated my desk, or the time...) I will take with me as I leave Ames.

Bob Crackel and Tim Causgrove round out the list of friends who made "lab life" more bearable. The Cyclone

wrestling and basketball seasons will surely suffer from our absence in the stands.

The typing and assembling of this dissertation are due in large part to the dedicated efforts of my wife Lynn Patterson. She deserves special thanks for these efforts and for the love and support she has given me throughout this project. If there were an award for "The Most Understanding Newlywed", Lynn would certainly walk away with the trophy.

The continued support and encouragement of other friends and my family has always been important to me. I thank them all, especially my mother for whom this dissertation is a modest "thank you" for all of her sacrifices over my years of study.

APPENDIX A. NONLINEAR LEAST SQUARES FITTING PROGRAM

An example of a convolute-and-compare program used in the data analysis for the work presented in Chapters V-VIII is provided. The program is based on the Marquardt algorithm [45] for the least squares estimation of nonlinear parameters. A global analysis technique is used to provide more accurate convergence of the parameters.

```
C     NGSRR2.FOR-----------------------------------------
C
      NGSRR2 uses the 2-D two-particle Gs(t) model to fit
the parallel and orthogonal polarization files. A multi-
exponential (fixed) form for the isotropic decay P(t) must
be provided.  Restricted Rotational diffusion is also taken
into account.  A histogram representation of the decay model
is generated before convolution with the instrument response
function.
C
C     Input is supplied from the file NGSRR.DAT.
C
C     restricted rotation model: ROT=[a+(1-a)*exp(-t/trot)]
C
C     Gs(t)=exp{-1.354*C*[t/(4*tau)]**.33333}
C
C     I(parallel)=CS(1)*P(t)[1+0.5*ROT*Gs(t)]
C     I(perp.)=   CS(2)*P(t)[1-0.5*ROT*Gs(t)]
C
C     to compile this program:
C        FORT/NOLINENUMBERS NGSRR2
C
C     to link this program:
C        R LINK
C        *NGSRR2/P:350=NGSRR2
C        *[ctrl c]
C
C
C     MAIN PROGRAM---------------------------------------
C
      VIRTUAL X(512),Y(512,2),WTS(512,2),YFIT(512,2),
          BKG(512,2)
      VIRTUAL EMP(512),EMO(512),BKP(512),BKO(512)
```

```
      DIMENSION B(10),IB(10),ILINK(5),IMAP(5,2),F(2)
      BYTE OUTFIL(16),FPFIL(16),FOFIL(16),NPFIL(16),
           NOFIL(16)
      BYTE EMPFIL(16),BKPFIL(16),EMOFIL(16),BKOFIL(16),
           BFIL(16)
      BYTE EXCFIL(16),REV,NFIX,NTYPE,NBKP,NBKO,ERR,STAT
      COMMON/CONST/N,NMIN,NMAX
      COMMON/TERMS/K,NEXPON,IFIX(5),KK,M,REV,STAT
      COMMON/PTMA/A(4),TAU(4),TF
      COMMON/RANGES/NEMLO,NEMHI,NEXLO,NEXHI,NLEMAV,NHEMAV,
           NLEXAV,NHEXAV,BASEMP,BASEMO,BASEXC
      COMMON/FILES/OUTFIL,FPFIL,FOFIL,EMPFIL,EMOFIL,EXCFIL,
           BKPFIL,BKOFIL
      DATA BFIL/'N','O','T',' ','U','S','E','D',' ',' ',' '
           ,' ',' ',' ',' ',' ',' '/
      KK=5
      M=2
      OPEN(UNIT=1,NAME='NGSRR.DAT',READONLY,TYPE='OLD',
           ERR=100)
      READ(1,*) IQUIT
      READ(1,*) (B(J),J=1,KK)
      READ(1,*) (IFIX(J),J=1,KK)
      READ(1,*) (ILINK(J),J=1,KK)
      READ(1,*) NEXPON
      DO 20 J=1,NEXPON
20       READ(1,*) A(J),TAU(J)
      READ(1,*) TF
      READ(1,925) REV
      READ(1,905) EMPFIL,BKPFIL
      READ(1,905) EMOFIL,BKOFIL
      READ(1,905) EXCFIL
      READ(1,*) NEMLO,NEMHI
      READ(1,*) NEXLO,NEXHI
      READ(1,*) NLEMAV,NHEMAV
      READ(1,*) NLEXAV,NHEXAV
      READ(1,*) DELX
      READ(1,925) NTYPE
      READ(1,925) STAT
      CLOSE(UNIT=1)
100   TYPE 1010,IQUIT
      TYPE 1020
      TYPE 1025,(B(J),J=1,KK)
      TYPE 1030,(IFIX(J),J=1,KK)
      TYPE 1040,(ILINK(J),J=1,KK)
      TYPE 1050,NEXPON
      TYPE 1060
      DO 60 J=1,NEXPON
60       TYPE 1065,J,A(J),TAU(J)
      TYPE 1066,TF
      TYPE 1070,REV
      TYPE 1080,EMPFIL,BKPFIL
```

```
      TYPE 1090,EMOFIL,BKOFIL
      TYPE 1100,EXCFIL
      TYPE 1110,NEMLO,NEMHI
      TYPE 1120,NEXLO,NEXHI
      TYPE 1130,NLEMAV,NHEMAV
      TYPE 1140,NLEXAV,NHEXAV
      TYPE 1150,DELX
      TYPE 1160,NTYPE
      TYPE 1165,STAT
      TYPE 1170
      TYPE 1180
      TYPE 1200
1010  FORMAT('0   1: # of Iterations                ',I2)
1020  FORMAT('    2: Shift   Pre-exp.   R.R. anis.   CD
           Tau(rot)')
1025  FORMAT(2X,F8.3,3X,1PE10.3,2X,0PF8.5,3X,F6.3,3X,F10.1)
1030  FORMAT('    3: Fixed  [1=yes]  ',10I1)
1040  FORMAT('    4: Linked [1=yes]  ',10I1)
1050  FORMAT('    5: # of Exponentials  (0-4) ',I2)
1055  FORMAT(/'$Enter Exponential #:  ')
1060  FORMAT('    6: Exp. #        Pre-exponent
           Lifetime(ps)')
1065  FORMAT(12X,I1,9X,1PE10.3,6X,0PF8.1)
1066  FORMAT('    7: Tau [used in Gs(t)] (psec)     '
           ,0PF8.1)
1070  FORMAT('    8: Reverse files  [Y/N]     ',1A1)
1080  FORMAT('    9: Parallel Emission, Bkg. File Names  ',
           16A1,1X,16A1)
1090  FORMAT('   10: Orthog.  Emission, Bkg. File Names  ',
           16A1,1X,16A1)
1100  FORMAT('   11: Excitation File Name  ',16A1)
1110  FORMAT('   12: Emission File Fitting Range    ',I3,',
           'I3)
1120  FORMAT('   13: Excitation File Fitting Range  ',I3,',
           'I3)
1130  FORMAT('   14: Emission Baseline Range        ',I3,',
           'I3)
1140  FORMAT('   15: Excitation Baseline Range      ',I3,',
           'I3)
1150  FORMAT('   16: Picoseconds Per Channel        ',F7.3)
1160  FORMAT('   17: Desire Terminal Output [Y/N]     ',
           1A1)
1165  FORMAT('   18: Photon Counting Statistics [Y/N] ',
           1A1)
1170  FORMAT('   19: Reset Default With The Above Values')
1180  FORMAT('   20: EXECUTE PROGRAM')
1200  FORMAT(/'$Enter Source Number:  ')
1220  FORMAT(/'$ENTER NEW PARAMETER(S):  ')
      ACCEPT*,NSC
      IF(NSC.LT.1.OR.NSC.GT.20) GO TO 100
```

```
      GOTO (110,120,130,140,150,160,166,170,180,190,
     ,        200,210,220,230,240,250,260,265,300,350),NSC
110   TYPE 1010,IQUIT
      TYPE 1220
      ACCEPT *,IQUIT
      GO TO 100
120   TYPE 1020
      TYPE 1025, (B(J),J=1,KK)
      TYPE 1220
      ACCEPT *,  (B(J),J=1,KK)
      GO TO 100
130   DO 136 J=1,KK
136      IFIX(J)=0
      TYPE 1030,(IFIX(J),J=1,KK)
      TYPE 131
      ACCEPT 925,NFIX
      IF(NFIX.EQ.'Y') IFIX(1)=1
      TYPE 132
      ACCEPT 925,NFIX
      IF(NFIX.EQ.'Y') IFIX(2)=1
      TYPE 133
      ACCEPT 925,NFIX
      IF(NFIX.EQ.'Y') IFIX(3)=1
      TYPE 134
      ACCEPT 925,NFIX
      IF(NFIX.EQ.'Y') IFIX(4)=1
      TYPE 135
      ACCEPT 925,NFIX
      IF(NFIX.EQ.'Y') IFIX(5)=1
131   FORMAT('$ Fix the time shift?                ')
132   FORMAT('$ Fix the pre-exp.?                  ')
133   FORMAT('$ Fix the resid. rot. anisotropy?    ')
134   FORMAT('$ Fix the Donor Conc.?               ')
135   FORMAT('$ Fix the rot.   lifetime?           ')
      GO TO 100
140   DO 146 J=1,KK
146      ILINK(J)=0
      TYPE 1040,(ILINK(J),J=1,KK)
      TYPE 141
      ACCEPT 925,NFIX
      IF(NFIX.EQ.'Y') ILINK(1)=1
      TYPE 142
      ACCEPT 925,NFIX
      IF(NFIX.EQ.'Y') ILINK(2)=1
      TYPE 143
      ACCEPT 925,NFIX
      IF(NFIX.EQ.'Y') ILINK(3)=1
      TYPE 144
      ACCEPT 925,NFIX
      IF(NFIX.EQ.'Y') ILINK(4)=1
```

```
      TYPE 145
      ACCEPT 925,NFIX
      IF(NFIX.EQ.'Y') ILINK(5)=1
141   FORMAT('$ Link the time shift?              ')
142   FORMAT('$ Link the pre-exp.?                ')
143   FORMAT('$ Link the resid. rot. anisotropy?  ')
144   FORMAT('$ Link the Donor Conc.?             ')
145   FORMAT('$ Link the rot.   lifetime?         ')
      GO TO 100
150   TYPE 1050,NEXPON
      TYPE 1220
      ACCEPT *, NEXPON
      GO TO 100
160   IF(NEXPON.EQ.0) GO TO 100
      L=1
      IF(NEXPON.EQ.1) GO TO 165
      TYPE 1055
      ACCEPT *,L
165   TYPE 1065,L,A(L),TAU(L)
      TYPE 1220
      ACCEPT *,A(L),TAU(L)
      GO TO 100
166   TYPE 1066,TF
      TYPE 1220
      ACCEPT *,TF
      GO TO 100
170   TYPE 1070,REV
      TYPE 1220
      ACCEPT 925,REV
      GO TO 100
180   TYPE 1080, EMPFIL,BKPFIL
      TYPE 181
181   FORMAT('$Emission file:   ')
      ACCEPT 905,EMPFIL
      TYPE 182
182   FORMAT('$Background file: ')
      ACCEPT 905,BKPFIL
      IF(BKPFIL(1).NE.'') GO TO 100
      DO 184 I=1,16
184      BKPFIL(I)=BFIL(I)
      GO TO 100
190   TYPE 1090, EMOFIL,BKOFIL
      TYPE 181
      ACCEPT 905,EMOFIL
      TYPE 182
      ACCEPT 905,BKOFIL
      IF(BKOFIL(1).NE.'') GO TO 100
      DO 195 I=1,16
195      BKOFIL(I)=BFIL(I)
      GO TO 100
200   TYPE 1100,EXCFIL
```

```
      TYPE 1220
      ACCEPT 905,EXCFIL
      GO TO 100
210   TYPE 1110,NEMLO,NEMHI
      TYPE 1220
      ACCEPT *,NEMLO,NEMHI
      GO TO 100
220   TYPE 1120,NEXLO,NEXHI
      TYPE 1220
      ACCEPT *,NEXLO,NEXHI
      GO TO 100
230   TYPE 1130,NLEMAV,NHEMAV
      TYPE 1220
      ACCEPT *,NLEMAV,NHEMAV
      GO TO 100
240   TYPE 1140,NLEXAV,NHEXAV
      TYPE 1220
      ACCEPT *,NLEXAV,NHEXAV
      GO TO 100
250   TYPE 1150,DELX
      TYPE 1220
      ACCEPT *,DELX
      GO TO 100
260   TYPE 1160,NTYPE
      TYPE 1220
      ACCEPT 925,NTYPE
      GO TO 100
265   TYPE 1165,STAT
      TYPE 1220
      ACCEPT 925,STAT
      GO TO 100
300   OPEN(UNIT=1,NAME='NGSRR.DAT',TYPE='NEW')
      WRITE(1,*) IQUIT
      WRITE(1,*) (B(J),J=1,KK)
      WRITE(1,*) (IFIX(J),J=1,KK)
      WRITE(1,*) (ILINK(J),J=1,KK)
      WRITE(1,*) NEXPON
      DO 330 J=1,NEXPON
330      WRITE(1,*) A(J),TAU(J)
      WRITE(1,*) TF
      WRITE(1,930) REV
      WRITE(1,910) EMPFIL,BKPFIL
      WRITE(1,910) EMOFIL,BKOFIL
      WRITE(1,910) EXCFIL
      WRITE(1,*) NEMLO,NEMHI
      WRITE(1,*) NEXLO,NEXHI
      WRITE(1,*) NLEMAV,NHEMAV
      WRITE(1,*) NLEXAV,NHEXAV
      WRITE(1,*) DELX
      WRITE(1,930) NTYPE
      WRITE(1,930) STAT
```

```
      CLOSE(UNIT=1)
      GO TO 100
350   CONTINUE
C
C     .....................generate file names.....
C
      IPEMC=0
      IOEMC=0
      DO 370 I=1,16
         IF(EMPFIL(I).EQ.'.') IPEMP=I
         IF(EMPFIL(I).EQ.':') IPEMC=I
         IF(EMOFIL(I).EQ.'.') IOEMP=I
         IF(EMOFIL(I).EQ.':') IOEMC=I
         NPFIL(I)=' '
         NOFIL(I)=' '
         FPFIL(I)=' '
         FOFIL(I)=' '
370      OUTFIL(I)=' '
      DO 375 I=1,16-IPEMC
         NPFIL(I)=EMPFIL(I+IPEMC)
375      FPFIL(I)=EMPFIL(I+IPEMC)
      DO 385 I=1,16-IOEMC
         NOFIL(I)=EMOFIL(I+IPEMC)
385      FOFIL(I)=EMOFIL(I+IOEMC)
      DO 395 I=1,IPEMP-IPEMC-1
395      OUTFIL(I)=EMPFIL(I+IPEMC)
      DO 400 I=IPEMP-IPEMC,15-IPEMC
400      OUTFIL(I+1)=EMPFIL(I+IPEMC)
      OUTFIL(IPEMP-IPEMC)=EMOFIL(IOEMP-1)
      FPFIL(1)='H'
      FOFIL(1)='H'
      NPFIL(1)='N'
      NOFIL(1)='N'
      OUTFIL(1)='G'
C
C     .....................read data files.................
C
      CALL RFILE(EXCFIL,X,ERR)
         IF(ERR.EQ.'N') GO TO 410
         TYPE 405,EXCFIL
405      FORMAT(/' EXCITATION FILE ',16A1,'NOT FOUND')
         GO TO 100
410   CALL RFILE(EMPFIL,EMP,ERR)
         IF(ERR.EQ.'N') GO TO 420
         TYPE 415,EMPFIL
415      FORMAT(/' PARALLEL EMISSION FILE ',16A1,
           'NOT FOUND')
         GO TO 100
420      TMP=EMP(1)
      CALL RFILE(EMOFIL,EMO,ERR)
         IF(ERR.EQ.'N') GO TO 430
```

```
          TYPE 425,EMOFIL
425       FORMAT(/' ORTHOG.  EMISSION FILE ',16A1,
            'NOT FOUND')
          GO TO 100
430       TMO=EMO(1)
        CALL RFILE(BKPFIL,BKP,NBKP)
          IF(NBKP.EQ.'N') GO TO 440
          TYPE 435
435       FORMAT(/' PARALLEL BACKGROUND FILE NOT USED')
440       TBP=BKP(1)
        CALL RFILE(BKOFIL,BKO,NBKO)
          IF(NBKO.EQ.'N') GO TO 450
          TYPE 445
445       FORMAT(/' ORTHOG.  BACKGROUND FILE NOT USED')
450       TBO=BKO(1)

C
C       ....change lifetimes and shift to channels, degrees
C       to radians....
C
        B(1)=B(1)/DELX
        TF=TF/DELX
        B(5)=B(5)/DELX
        DO 455 J=1,NEXPON
455       TAU(J)=TAU(J)/DELX
C
C       ..construct IMAP, IB, and B(J) from ILINK and IFIX...
C
        I=KK
        IP=0
        DO 460 JJ=1,M
           DO 460 J=1,KK
              IMAP(J,JJ)=J
              IF(ILINK(J).EQ.1) IMAP(J,JJ)=IMAP(J,1)
              IF(JJ.GT.1.AND.ILINK(J).EQ.0) I=I+1
              IF(JJ.GT.1.AND.ILINK(J).EQ.0) IMAP(J,JJ)=I
              B(IMAP(J,JJ))=B(J)
              IF(IFIX(J).EQ.0) GO TO 460
              IF(JJ.GT.1.AND.IMAP(J,JJ).EQ.IMAP(J,1)) GO TO
460
              IP=IP+1
              IB(IP)=IMAP(J,JJ)
460     CONTINUE
        K=I
C
C       ..............reverse data (if necessary).............
C
        IF(REV.EQ.'N') GO TO 500
        CALL REVERS(EMP)
        IF(NBKP.EQ.'N') CALL REVERS(BKP)
        CALL REVERS(EMO)
```

```
      IF(NBKO.EQ.'N') CALL REVERS(BKO)
      CALL REVERS(X)
      NTEMP=NEMLO
      NEMLO=512-NEMHI
      NEMHI=512-NTEMP
      NTEMP=NEXLO
      NEXLO=512-NEXHI
      NEXHI=512-NTEMP
      NTEMP=NLEMAV
      NLEMAV=512-NHEMAV
      NHEMAV=512-NTEMP
      NTEMP=NLEXAV
      NLEXAV=512-NHEXAV
      NHEXAV=512-NTEMP
C
C     ..............pulse pile-up correction.............
C
500   CONTINUE
C
C     ....subtract background file and/or counts, determine
C     weights....
C
      DO 600 I=1,512
         Y(I,1)=EMP(I)
         Y(I,2)=EMO(I)
         WTS(I,1)=1.
         WTS(I,2)=1.
         IF(EMP(I).GT.0.) WTS(I,1)=1./EMP(I)
600      IF(EMO(I).GT.0.) WTS(I,2)=1./EMO(I)
      IF(NBKP.EQ.'Y') GO TO 610
      CP=(TMP/TBP)**2.
      DO 605 I=1,512
         Y(I,1)=Y(I,1)-BKP(I)*TMP/TBP
         SUM=EMP(I)+BKP(I)*CP
605      IF(SUM.GT.0.) WTS(I,1)=1./SUM
610   IF(NBKO.EQ.'Y') GO TO 615
      CO=(TMO/TBO)**2.
      DO 612 I=1,512
         Y(I,2)=Y(I,2)-BKO(I)*TMO/TBO
         SUM=EMO(I)+BKO(I)*CO
612      IF(SUM.GT.0.) WTS(I,2)=1./SUM
615   BASEXC=0.
      DO 620 I=NLEXAV,NHEXAV
620      BASEXC=BASEXC+X(I)
      BASEXC=BASEXC/FLOAT(1+NHEXAV-NLEXAV)
      BASEMP=0.
      DO 625 I=NLEMAV,NHEMAV
625      BASEMP=BASEMP+Y(I,1)
      BASEMP=BASEMP/FLOAT(1+NHEMAV-NLEMAV)
      PVAR=0.
```

```
      DO 628 I=NLEMAV,NHEMAV
628      PVAR=PVAR+(Y(I,1)-BASEMP)**2.
      PVAR=PVAR/FLOAT(1+NHEMAV-NLEMAV)
      BASEMO=0.
      DO 630 I=NLEMAV,NHEMAV
630      BASEMO=BASEMO+Y(I,2)
      BASEMO=BASEMO/FLOAT(1+NHEMAV-NLEMAV)
      OVAR=0.
      DO 635 I=NLEMAV,NHEMAV
635      OVAR=OVAR+(Y(I,2)-BASEMO)**2.
      OVAR=OVAR/FLOAT(1+NHEMAV-NLEMAV)
      DO 640 I=1,512
         X(I)=X(I)-BASEXC
640      IF(I.LT.NEXLO.OR.I.GT.NEXHI) X(I)=0.
      DO 650 I=1,512
         Y(I,1)=Y(I,1)-BASEMP
         Y(I,2)=Y(I,2)-BASEMO
         IF(STAT.NE.'Y') WTS(I,1)=1./PVAR
         IF(STAT.NE.'Y') WTS(I,2)=1./OVAR
         IF(I.LT.NEMLO.OR.I.GT.NEMHI) WTS(I,1)=0.
650      IF(I.LT.NEMLO.OR.I.GT.NEMHI) WTS(I,2)=0.
      N=NEMHI
C
C     ..........write out modified emission files.........
C
      IF(NBKP.EQ.'Y') GO TO 675
      OPEN(UNIT=2,NAME=NPFIL,TYPE='NEW')
      DO 670 I=1,512,8
670      WRITE(2,935) I-1,(Y(I+J,1),J=0,7)
      CLOSE(UNIT=2)
675   IF(NBKO.EQ.'Y') GO TO 685
      OPEN(UNIT=2,NAME=NOFIL,TYPE='NEW')
      DO 680 I=1,512,8
680      WRITE(2,935) I-1,(Y(I+J,2),J=0,7)
      CLOSE(UNIT=2)
685   CONTINUE
C
C     ..........estimate B(1) and scaling parameters.......
C
      XSUM=0.
      PMAX=0.
      OMAX=0.
      XMAX=0.
      DO 690 I=3,510
         IF(X(I).GT.XMAX) XMAX=X(I)
         IF(XMAX.EQ.X(I)) IXCHAN=I
         IF(Y(I,1).GT.PMAX) PMAX=Y(I,1)
         IF(Y(I,2).GT.OMAX) OMAX=Y(I,2)
690      XSUM=XSUM+X(I)
      PT0=0.
```

```
      DO 695 I=1,NEXPON
695      PT0=PT0+A(I)
      PSCALE=PMAX/(XSUM*PT0*1.8)
      OSCALE=OMAX/(XSUM*PT0*0.6)
      IF(IFIX(2).EQ.0) B(IMAP(2,1))=PSCALE
      IF(IFIX(2).EQ.0) B(IMAP(2,2))=OSCALE
      DO 700 I=3,510
700      IF((PMAX/2.).LT.Y(I,1)) GO TO 702
702   IPCHAN=I
      DO 704 I=3,510
704      IF((OMAX/2.).LT.Y(I,2)) GO TO 706
706   IOCHAN=I
      IF(IFIX(1).EQ.0) B(IMAP(1,1))=IPCHAN-IXCHAN
      IF(IFIX(1).EQ.0) B(IMAP(1,2))=IOCHAN-IXCHAN
      IF(IFIX(1).EQ.0.AND.ILINK(1).EQ.1) B(1)=(IPCHAN+
           IOCHAN)/2.-IXCHAN
      OPEN(UNIT=2,NAME=OUTFIL,TYPE='NEW')
      CALL LSQENP(N,K,X,Y,WTS,B,IMAP,KK,M,IP,IB,IQUIT,
           NTYPE)
      CHISQ1=0.
      CHISQ2=0.
      DO 710 L=1,M
         DO 710 I=1,512
710         YFIT(I,L)=0.
      DO 720 I=1,N
         MI=I
         CALL FCODE(F,X,IMAP,B,MI)
         CHISQ1=WTS(I,1)*((F(1)-Y(I,1))**2.)+CHISQ1
         CHISQ2=WTS(I,2)*((F(2)-Y(I,2))**2.)+CHISQ2
         YFIT(I,1)=F(1)
720      YFIT(I,2)=F(2)
      IPS=0
      DO 725 I=1,KK
725      IF(IFIX(I).EQ.1) IPS=IPS+1
      NFREE=NEMHI-NEMLO-KK+IPS
      CHISQ1=CHISQ1/FLOAT(NFREE)
      CHISQ2=CHISQ2/FLOAT(NFREE)
      DO 750 I=1,512
         IF(I.LT.NEMLO.OR.I.GT.NEMHI) YFIT(I,1)=0.0
750      IF(I.LT.NEMLO.OR.I.GT.NEMHI) YFIT(I,2)=0.0
      IF(REV.NE.'Y') GO TO 800
      NTEMP=NEMLO
      NEMLO=512-NEMHI
      NEMHI=512-NTEMP
      NTEMP=NEXLO
      NEXLO=512-NEXHI
      NEXHI=512-NTEMP
      NTEMP=NLEMAV
      NLEMAV=512-NHEMAV
      NHEMAV=512-NTEMP
      NTEMP=NLEXAV
```

```
      NLEXAV=512-NHEXAV
      NHEXAV=512-NTEMP
800   CALL DECOUT(B,BSAVE,IMAP,IQUIT,DELX,CHISQ1,CHISQ2)
      CLOSE(UNIT=2)
      OPEN(UNIT=2,NAME=FPFIL,TYPE='NEW')
      DO 850 I=1,501,10
850      WRITE(2,940) I,(YFIT(J,1),J=I,I+9)
      I=511
      WRITE(2,945) I,(YFIT(J,1),J=511,512),BASEMP
      CLOSE(UNIT=2)
      OPEN(UNIT=2,NAME=FOFIL,TYPE='NEW')
      DO 860 I=1,501,10
860      WRITE(2,940) I,(YFIT(J,2),J=I,I+9)
      I=511
      WRITE(2,945) I,(YFIT(J,2),J=511,512),BASEMO
      CLOSE(UNIT=2)
905   FORMAT(16A1)
910   FORMAT(X,16A1)
925   FORMAT(A1)
930   FORMAT(X,A1)
935   FORMAT(X,I4,X,8F7.0)
940   FORMAT(X,I4,10F7.0)
945   FORMAT(X,I4,2F7.0,3X,E16.8,3X,I4)
      STOP
      END
```

```
C
C     BlOCK DATA-----------------------------------------
C
        BLOCK DATA
        COMMON /PARAM/ PARAM(6)
        DATA PARAM/.0001,.00005,.001,.01,45.,.1E-35/
        END
C
C     subroutine REVERS----------------------------------
C
      SUBROUTINE REVERS(Z)
      VIRTUAL Z(512),TEMP(512)
      DO 100 I=1,512
100      TEMP(I)=Z(513-I)
      DO 110 I=1,512
110      Z(I)=TEMP(I)
      RETURN
      END
C
C     subroutine RFILE-----------------------------------
C
      SUBROUTINE RFILE(FNAME,Z,ERROR)
      VIRTUAL Z(512)
      BYTE FNAME(16),ERROR
      ERROR='N'
      OPEN(UNIT=1,NAME=FNAME,READONLY,TYPE='OLD',ERR=300)
      DO 100 I=1,505,8
100      READ(1,900,END=200,ERR=300) L,(Z(I+J),J=0,7)
200   CLOSE(UNIT=1)
      GO TO 500
300   ERROR='Y'
500   CONTINUE
900   FORMAT(I4,X,8F7.0)
      RETURN
      END
```

```
C
C     subroutine DECOUT-----------------------------------
C
      SUBROUTINE DECOUT(B,BSAVE,IMAP,IQUIT,DELX,CHISQ1,
           CHISQ2)
      DIMENSION B(1),BSAVE(1),IMAP(5,2)
      BYTE DAY(9),TIM(8)
      BYTE OUTFIL(16),FPFIL(16),FOFIL(16),NPFIL(16),
           NOFIL(16)
      BYTE EMPFIL(16),BKPFIL(16),EMOFIL(16),BKOFIL(16)
      BYTE EXCFIL(16),REV,STAT
      COMMON/CONST/N,NMIN,NMAX
      COMMON/TERMS/K,NEXPON,IFIX(5),KK,M,REV,STAT
      COMMON/PTMA/A(4),TAU(4),TF
      COMMON/RANGES/NEMLO,NEMHI,NEXLO,NEXHI,,NLEMAV,NHEMAV,
           NLEXAV,NHEXAV,BASEMP,BASEMO,BASEXC
      COMMON/FILES/OUTFIL,FPFIL,FOFIL,EMPFIL,EMOFIL,
           EXCFIL,BKPFIL,BKOFIL
      CALL DATE(DAY)
      CALL TIME(TIM)
      WRITE(2,490)
      WRITE(2,500) OUTFIL
      WRITE(2,510) EMPFIL,BKPFIL
      WRITE(2,520) EMOFIL,BKOFIL
      WRITE(2,525) FPFIL,FOFIL
      WRITE(2,528) EXCFIL
      WRITE(2,530) DAY,TIM
      WRITE(2,535) IQUIT
      WRITE(2,540) REV
      WRITE(2,545) STAT
      WRITE(2,550) (NEMHI-NEMLO+1)
      WRITE(2,560) NEMLO,NEMHI,NEXLO,NEXHI
      WRITE(2,570) NLEMAV,NHEMAV,BASEMP,BASEMO
      WRITE(2,580) NLEXAV,NHEXAV,BASEXC
      WRITE(2,590) NEXPON
      WRITE(2,600) DELX
      WRITE(2,605) TF*DELX
      WRITE(2,610)
      DO 100 I=1,NEXPON
100      WRITE(2,620) I,A(I),(TAU(I)*DELX)
      WRITE(2,700)
      WRITE(2,710) ((B(IMAP(1,J))*DELX),J=1,M)
      WRITE(2,720) (B(IMAP(2,J)),J=1,M)
      WRITE(2,740) (B(IMAP(4,J)),J=1,M)
      WRITE(2,730) (B(IMAP(3,J)),J=1,M)
      WRITE(2,750) ((B(IMAP(5,J))*DELX),J=1,M)
      WRITE(2,760)
      WRITE(2,770) CHISQ1,CHISQ2
490   FORMAT('1','2-DIM. TWO PARTICLE Gs(t)*ROT. DIFFUSION
           GLOBAL FIT:  NGSRR2.FOR')
500   FORMAT(' DATA FILE: ',16A1)
```

```
510   FORMAT(' PARALLEL   EM. AND BKG. FILES: ',16A1,1X,
          16A1)
520   FORMAT(' ORTHOGONAL EM. AND BKG. FILES: ',16A1,1X,
          16A1)
525   FORMAT(' PAR. AND ORTHOG. FITTED FILES: ',16A1,1X,
          16A1)
528   FORMAT(' EXCITATION FILE:                ',16A1)
530   FORMAT(X,'DATE:  ',9A1,3X,'TIME:  ',8A1)
535   FORMAT(/' MAX # OF ITERATIONS =',I2)
540   FORMAT(' REVERSED FILES              [Y/N]: ',1A1)
545   FORMAT(' PHOTON COUNTING STATISTICS [Y/N]: ',1A1)
550   FORMAT(' TOTAL NUMBER OF DATA POINTS USED:  ',I4)
560   FORMAT(' EMIS, EXCIT CHAN RANGES USED: ',I4,',',I4,
          3X,I4,',',I4)
570   FORMAT(' CHAN RANGE FOR P & O EMIS BASE AVE:',I4,',',
          I4,2X,
     ,'AVE=',F6.2,2X,'AVE=',F6.2)
580   FORMAT(' CHAN RANGE FOR EXCIT BASE AVE:     ',I4,',',
          I4,2X,
     ,'AVE=',F6.2)
590   FORMAT(' NUMBER OF EXPONENTIAL TERMS IN P(t): ',I1)
600   FORMAT(' PSEC/CHANNEL=  ',F5.2)
605   FORMAT(' TAU [used in Gs(t)] (psec) = ',0PF8.1,/)
610   FORMAT(' P(t) TERM',12X,' PRE-EXPONENT',2X,' LIFETIME
          (psec)',/)
620   FORMAT(3X,I2,19X,1PE10.3,5X,E10.3)
700   FORMAT(/,24X,' PARALLEL',5X,' ORTHOGONAL')
710   FORMAT(/,' XSHIFT (psec)          ',2(1PE10.3,5X))
720   FORMAT(' SCALE FACTOR           ',2(1PE10.3,5X))
730   FORMAT(' RESID. ROT. ANISOTROPY ',2(1PE10.3,5X))
740   FORMAT(' RED CONC               ',2(1PE10.3,5X))
750   FORMAT(' ROT.   LIFETIME (psec) ',2(1PE10.3,5X))
760   FORMAT(/'   REDUCED')
770   FORMAT(' CHI SQUARED     ',5X,2(F10.3,5X))
      RETURN
      END
```

```
C
C     subroutine FCODE ----------------------------------
C
      SUBROUTINE FCODE(F,X,IMAP,B,I)
      DIMENSION B(1),F(2),IMAP(5,2),XS(2),CS(2),AR(2),CD(2)
     ,TR(2)
      DIMENSION C(2),GS(2),ROT(2)
      VIRTUAL X(1)
      COMMON/DECAY/DECP(512),DECO(512)
      COMMON/PASS/XSP(512),XSO(512)
      COMMON/CONST/N,NMIN,NMAX
      COMMON/TERMS/K,NEXPON,IFIX(5),KK,M,REV,STAT
      COMMON/PTMA/A(4),TAU(4),TF
      DATA PI/3.14159265359/
      IF(I.NE.1) GO TO 100
      DO 10 L=1,M
         XS(L)=B(IMAP(1,L))
         CS(L)=B(IMAP(2,L))
         AR(L)=B(IMAP(3,L))
         CD(L)=B(IMAP(4,L))
         TR(L)=B(IMAP(5,L))
10       C(L)=CD(L)*0.852966/(TF**0.333333)
      CALL SHIFT(X,XS(1),XS(2))
      PT0=0.
      DO 20 J=1,NEXPON
20       PT0=PT0+A(J)
      DECP0=1.5*CS(1)*PT0
      DECO0=0.5*CS(2)*PT0
      DO 40 J=1,512
         YY=FLOAT(J)
         PT=0.
         DO 30 JJ=1,NEXPON
30          PT=PT+A(JJ)*EXP(-YY/TAU(JJ))
         ROT(1)=AR(1)+(1.-AR(1))*EXP(-YY/TR(1))
         ROT(2)=AR(2)+(1.-AR(2))*EXP(-YY/TR(2))
         GS(1)=EXP(-C(1)*YY**0.333333)
         GS(2)=EXP(-C(2)*YY**0.333333)
         DECP(J)=CS(1)*PT*(1.+0.5*ROT(1)*GS(1))
40       DECO(J)=CS(2)*PT*(1.-0.5*ROT(2)*GS(2))
      CALL HIST(DECP0,DECP)
      CALL CONVOL(DECP0,DECP,XSP)
      CALL HIST(DECO0,DECO)
      CALL CONVOL(DECO0,DECO,XSO)
100   F(1)=DECP(I)
      F(2)=DECO(I)
        RETURN
        END
```

```
C
C     subroutine PCODE-----------------------------------
C
      SUBROUTINE PCODE(P,X,IMAP,B,I)
      DIMENSION B(1),F(2),P(5,2),IMAP(5,2)
      DIMENSION C(2),D(2),GS(2),CS(2),AR(2),CD(2),TR(2),
           ROT(2)
      DIMENSION DXSP(512),DXSO(512)
      VIRTUAL X(1),PXSP(512),PXSO(512)
      VIRTUAL PCSP(512),PCSO(512),PARP(512),PARO(512)
      VIRTUAL PCDP(512),PCDO(512),PTRP(512),PTRO(512)
      COMMON/PASS/XSP(512),XSO(512)
      COMMON/DECAY/DECP(512),DECO(512)
      COMMON/CONST/N,NMIN,NMAX
      COMMON/TERMS/K,NEXPON,IFIX(5),KK,M,REV,STAT
      COMMON/PTMA/A(4),TAU(4),TF
      DATA PI/3.14159265359/
      IF(I.GT.1) GO TO 100
      DO 10 L=1,M
         CS(L)=B(IMAP(2,L))
         AR(L)=B(IMAP(3,L))
         CD(L)=B(IMAP(4,L))
         TR(L)=B(IMAP(5,L))
         C(L)=CD(L)*0.852966/(TF**0.333333)
10       D(L)=0.852966/(TF**0.333333)
      PT0=0.
      DO 20 J=1,NEXPON
20       PT0=PT0+A(J)
      DO 40 J=1,512
         YY=FLOAT(J)
         PT=0.
         DO 30 JJ=1,NEXPON
30          PT=PT+A(JJ)*EXP(-YY/TAU(JJ))
         E1=EXP(-YY/TR(1))
         E2=EXP(-YY/TR(2))
         ROT(1)=AR(1)+(1.-AR(1))*E1
         ROT(2)=AR(2)+(1.-AR(2))*E2
         GS(1)=EXP(-C(1)*YY**0.333333)
         GS(2)=EXP(-C(2)*YY**0.333333)
         PXSP(J)=CS(1)*PT*(1.+0.5*ROT(1)*GS(1))
         PXSO(J)=CS(2)*PT*(1.-0.5*ROT(2)*GS(2))
         PCSP(J)=DECP(J)/CS(1)
         PCSO(J)=DECO(J)/CS(2)
         PCDP(J)=-CS(1)*PT*0.5*ROT(1)*D(1)*GS(1)*
     YY**0.333333
         PCDO(J)=+CS(2)*PT*0.5*ROT(2)*D(2)*GS(2)*
     YY**0.333333
         PARP(J)=+CS(1)*PT*0.5*(1.-E1)*GS(1)
         PARO(J)=-CS(2)*PT*0.5*(1.-E2)*GS(2)
         PTRP(J)=+.5*CS(1)*PT*GS(1)*(1.-AR(1))*E1*YY/
     (TR(1)*TR(1))
```

```
40          PTRO(J)=-.5*CS(2)*PT*GS(2)*(1.-AR(2))*E2*YY/
         (TR(2)*TR(2))
         DO 50 J=2,511
            DXSP(J)=0.5*(XSP(J-1)-XSP(J+1))
50          DXSO(J)=0.5*(XSO(J-1)-XSO(J+1))
         DXSP(1)=0.
         DXSP(512)=0.
         DXSO(1)=0.
         DXSO(512)=0.
         PXSP0=1.5*CS(1)*PT0
         PXSO0=0.5*CS(2)*PT0
         PARP0=0.
         PARO0=0.
         PCDP0=0.
         PCDO0=0.
         PTRP0=0.
         PTRO0=0.
            IF(IFIX(1).EQ.0) CALL VHIST(PXSP0,PXSP)
            IF(IFIX(1).EQ.0) CALL VONVOL(PXSP0,PXSP,DXSP)
            IF(IFIX(1).EQ.0) CALL VHIST(PXSO0,PXSO)
            IF(IFIX(1).EQ.0) CALL VONVOL(PXSO0,PXSO,DXSO)
            IF(IFIX(3).EQ.0) CALL VHIST(PARP0,PARP)
            IF(IFIX(3).EQ.0) CALL VONVOL(PARP0,PARP,XSP)
            IF(IFIX(3).EQ.0) CALL VHIST(PARO0,PARO)
            IF(IFIX(3).EQ.0) CALL VONVOL(PARO0,PARO,XSO)
            IF(IFIX(4).EQ.0) CALL VHIST(PCDP0,PCDP)
            IF(IFIX(4).EQ.0) CALL VONVOL(PCDP0,PCDP,XSP)
            IF(IFIX(4).EQ.0) CALL VHIST(PCDO0,PCDO)
            IF(IFIX(4).EQ.0) CALL VONVOL(PCDO0,PCDO,XSO)
            IF(IFIX(5).EQ.0) CALL VHIST(PTRP0,PTRP)
            IF(IFIX(5).EQ.0) CALL VONVOL(PTRP0,PTRP,XSP)
            IF(IFIX(5).EQ.0) CALL VHIST(PTRO0,PTRO)
            IF(IFIX(5).EQ.0) CALL VONVOL(PTRO0,PTRO,XSO)
100      P(1,1)=PXSP(I)
         P(2,1)=PCSP(I)
         P(3,1)=PARP(I)
         P(4,1)=PCDP(I)
         P(5,1)=PTRP(I)
         P(1,2)=PXSO(I)
         P(2,2)=PCSO(I)
         P(3,2)=PARO(I)
         P(4,2)=PCDO(I)
         P(5,2)=PTRO(I)
         RETURN
         END
```

```
C
C     subroutine SHIFT-------------------------------------
C
      SUBROUTINE SHIFT(X,SP,SO)
      VIRTUAL X(512)
      COMMON/PASS/XSP(512),XSO(512)
      COMMON/CONST/N,NMIN,NMAX
      ISHIFT=INT(SP)
      FSHIFT=ABS(SP-FLOAT(ISHIFT))
      LL=-1
      IF(SP.GE.0.) LL=1
      DO 5 JJ=1,512
      L=JJ-ISHIFT
      XSP(JJ)=0.
5     IF(L.GT.1.AND.L.LT.512) XSP(JJ)=FSHIFT*X(L-LL)+(1.-
           FSHIFT)*X(L)
      ISHIFT=INT(SO)
      FSHIFT=ABS(SO-FLOAT(ISHIFT))
      LL=-1
      IF(SO.GE.0.) LL=1
      DO 10 JJ=1,512
      L=JJ-ISHIFT
      XSO(JJ)=0.
10    IF(L.GT.1.AND.L.LT.512) XSO(JJ)=FSHIFT*X(L-LL)+(1.-
           FSHIFT)*X(L)
      DO 15 JJ=1,512
      NMIN=JJ
      IF(XSP(JJ).NE.0..OR.XSO(JJ).NE.0.) GO TO 20
15    CONTINUE
20    DO 25 JJ=512,1,-1
      NMAX=JJ
      IF(XSP(JJ).NE.0..OR.XSO(JJ).NE.0.) GO TO 30
25    CONTINUE
30    RETURN
      END
C
C     subroutine HIST--------------------------------------
C
      SUBROUTINE HIST(Z0,Z)
      VIRTUAL ZV(512)
      DIMENSION Z(512)
      ZV0=Z0
      DO 60 I=1,512
60       ZV(I)=Z(I)
      Z0=ZV0/3.+(5.*ZV(1)-ZV(2))/24.
      Z(1)=11.*ZV(1)/12.+(ZV0+ZV(2))/24.
      DO 100 I=2,511
100      Z(I)=11.*ZV(I)/12.+(ZV(I-1)+ZV(I+1))/24.
200   Z(512)=ZV(512)
      RETURN
      END
```

```
C
C     subroutine VHIST-----------------------------------
C
      SUBROUTINE VHIST(Z0,Z)
      VIRTUAL ZV(512),Z(512)
      ZV0=Z0
      DO 60 I=1,512
60       ZV(I)=Z(I)
      Z0=ZV0/3.+(5.*ZV(1)-ZV(2))/24.
      Z(1)=11.*ZV(1)/12.+(ZV0+ZV(2))/24.
      DO 100 I=2,511
100      Z(I)=11.*ZV(I)/12.+(ZV(I-1)+ZV(I+1))/24.
200   Z(512)=ZV(512)
      RETURN
      END
C
C     subroutine CONVOL----------------------------------
C
      CONVOL convolutes the array Z with X and the result is
returned in Z.  The convolution requires Z0 which is the
value of Z at time equals zero.
C
      SUBROUTINE CONVOL(Z0,Z,X)
      VIRTUAL ZV(512)
      DIMENSION X(1),Z(512)
      COMMON/CONST/N,NMIN,NMAX
      DO 100 I=1,N
         C=0.
         IF(I-NMIN) 100,90,70
70       DO 80 J=NMIN,MIN0(NMAX,I-1)
80          C=C+X(J)*Z(I-J)
90       C=C+X(I)*Z0
100   ZV(I)=C
      DO 110 I=1,N
110      Z(I)=ZV(I)
      RETURN
      END
```

```
C
C      subroutine VONVOL-----------------------------------
C
       VONVOL convolutes the VIRTUAL array ZV with X and the
result is  returned in Z.  The convolution requires Z0 which
is the value of ZV at time equals zero.
C
       SUBROUTINE VONVOL(Z0,ZV,X)
       VIRTUAL ZV(512)
       DIMENSION X(1),Z(512)
       COMMON/CONST/N,NMIN,NMAX
       DO 60 I=1,512
60        Z(I)=ZV(I)
       DO 100 I=1,N
          C=0.
          IF(I-NMIN) 100,90,70
70        DO 80 J=NMIN,MIN0(NMAX,I-1)
80           C=C+X(J)*Z(I-J)
90        C=C+X(I)*Z0
100    ZV(I)=C
       RETURN
       END

C
C       subroutine BCHECK----------------------------------
C
       This is a user supplied subroutine which checks the
values of B(I) to determine if they are appropriate (e.g. of
the correct sign). If the values are deemed inappropriate,
control is sent to 299, which determines whether to increase
XL or decrease XKDB before calculating a new set of B(I).
This bypasses the calculation of FCODE, minimizing execution
time (particularly valuable when using the Fayer model).
C
       SUBROUTINE BCHECK(B,IMAP,IBCK)
       DIMENSION B(1),IMAP(5,2)
       COMMON/TERMS/K,NEXPON,IFIX(5),KK,M,REV,STAT
       IBCK=1
       DO 100 L=1,M
          DO 50 I=2,KK
            IF(B(IMAP(I,L)).LT.0.) IBCK=2
50        CONTINUE
100    CONTINUE
       RETURN
       END
```

```
C
C      subroutine LSQENP----------------------------------
C
C
      SUBROUTINE LSQENP(N,K,X,Y,WTS,B,IMAP,KK,M,IP,IB,IQUIT
           ,NTYPE)
      DIMENSION IMAP(5,2),CHISQ(2),PHD(2)
      DIMENSION DB(10),G(10),A(10,11),AXL(10,11)
      DIMENSION SA(10),BS(10),P(5,2),B(1),IB(1),F(2)
      VIRTUAL X(1),Y(512,2),WTS(512,2)
      BYTE NTYPE
      COMMON /PARAM/XTEST,E,TAU,AL,GAMCR,ZETA
      IF(IQUIT.EQ.0) RETURN
      IWS4=IQUIT+1
      GAMMA=0.0
      XKDB=1.
      XL=AL*10.
90    IF(IWS4.EQ.0) GO TO 96
      IF(IWS4.GT.1) GO TO 94
      PHIZ=PHI
      IDONE=1
      GO TO 700
94    IWS4=IWS4-1
96    CONTINUE
      DO 100 I=1,K
         G(I)=0.
         DO 100 J=1,K
100         A(I,J)=0.
      DO 105 JJ=1,M
105      PHD(JJ)=0.
      DO 135 J=1,N
         I=J
         CALL FCODE(F,X,IMAP,B,I)
         CALL PCODE(P,X,IMAP,B,I)
         IF(IP.LE.0) GO TO 125
         DO 120 II=1,IP
            IWS=IB(II)
            DO 120 ICOL=1,M
               DO 120 IROW=1,KK
                  IF(IMAP(IROW,ICOL).EQ.IWS) P(IROW,ICOL)=0.
120   CONTINUE
125   DO 130 ICOL=1,M
         DO 130 JROW=1,KK
            JJ=IMAP(JROW,ICOL)
            G(JJ)=G(JJ)+(Y(I,ICOL)-F(ICOL))*P(JROW,ICOL)*
                 WTS(I,ICOL)
            DO 130 IROW=JROW,KK
               II=IMAP(IROW,ICOL)
               A(II,JJ)=A(II,JJ)+P(IROW,ICOL)*P(JROW,ICOL)*
                        WTS(I,ICOL)
130   A(JJ,II)=A(II,JJ)
```

```
      DO 135 JJ=1,M
135      PHD(JJ)=PHD(JJ)+WTS(I,JJ)*((Y(I,JJ)-F(JJ))**2.)
      PHIZ=0.
      DO 137 JJ=1,M
         CHISQ(JJ)=PHD(JJ)
137      PHIZ=PHIZ+PHD(JJ)
      WRITE(2,845) (IQUIT-IWS4)
      WRITE(2,850) (B(J),J=1,K)
      WRITE(2,855) PHIZ,XL,GAMMA,XKDB
      IF(NTYPE.EQ.'Y') TYPE 845, (IQUIT-IWS4)
      IF(NTYPE.EQ.'Y') TYPE 850, (B(J),J=1,K)
      IF(NTYPE.EQ.'Y') TYPE 855, PHIZ,XL,GAMMA,XKDB
      IF(IP.EQ.0) GO TO 150
      DO 145 JJ=1,IP
         IWS=IB(JJ)
         G(IWS)=0.
         DO 140 II=1,K
            A(IWS,II)=0.
140         A(II,IWS)=0.
145   A(IWS,IWS)=1.
150   DO 155 I=1,K
155      SA(I)=SQRT(A(I,I))
      DO 175 I=1,K
         DO 165 J=I,K
            WS=SA(I)*SA(J)
            IF(WS.GT.0.) GO TO 160
            A(I,J)=0.
            GO TO 165
160         A(I,J)=A(I,J)/WS
165         A(J,I)=A(I,J)
         IF(SA(I).GT.0.) GO TO 170
         G(I)=0.
         GO TO 175
170      G(I)=G(I)/SA(I)
175      A(I,I)=1.
C
C     ..........adjust XL & XKDB for optimum step.........
C
      IF(XL.GT..00000001) XL=XL/10.
      XKDB=1.
      IBK1=1
      DO 190 J=1,K
190      BS(J)=B(J)
      GO TO 500
200   DO 205 J=1,K
205   IF(ABS(DB(J)/(ABS(B(J))+TAU)).GE.E) GO TO 600
      IDONE=2
      DO 210 J=1,K
210      B(J)=BS(J)
      GO TO 700
215   IF(PHI.GT.PHIZ) GO TO 235
```

```
      IF(((PHIZ-PHI)/PHI).GE.XTEST) GO TO 90
      IDONE=3
      PHIZ=PHI
      GO TO 700
235   IBK1=2
237   XL=XL*10.
239   DO 240 J=1,K
240      B(J)=BS(J)
      GO TO 500
245   IF(PHI.GT.PHIZ) GO TO 255
      IF(((PHIZ-PHI)/PHI).GE.XTEST) GO TO 90
      IDONE=3
      PHIZ=PHI
      GO TO 700
255   IF(GAMMA.GE.GAMCR) GO TO 237
      XKDB=XKDB/2.
      DO 260 J=1,K
260      IF(ABS(DB(J)/(ABS(B(J))+TAU)).GE.E) GO TO 239
      IDONE=4
      DO 265 J=1,K
265      B(J)=BS(J)
      GO TO 700
C
C     .................find B(J) and DB(J).................
C
500   DO 505 I=1,K
         DO 505 J=1,K
505         AXL(I,J)=A(I,J)
      DO 510 I=1,K
510      AXL(I,I)=AXL(I,I)+XL
      CALL GJR(AXL,K,ZETA,MSING)
      IF(MSING.EQ.2) RETURN
      DO 520 I=1,K
         DB(I)=0.
      DO 515 J=1,K
515      DB(I)=AXL(I,J)*G(J)+DB(I)
520   DB(I)=XKDB*DB(I)
      XLL=0.0
      DTG=0.0
      GTG=0.0
      DO 525 J=1,K
         XLL=XLL+DB(J)**2
         DTG=DTG+DB(J)*G(J)
         GTG=GTG+G(J)**2
         DB(J)=DB(J)/SA(J)
525      B(J)=B(J)+DB(J)
      IF((K-IP).EQ.1) GO TO 540
      CGAM=DTG/SQRT(XLL*GTG)
      GAMMA=1.570796-ATAN(CGAM/SQRT(1.-CGAM*CGAM))
      GAMMA=GAMMA*360./6.283185
      IF(ABS(GAMMA).LT.90.0.OR.XL.LE.1.0) GO TO 545
```

```
      IDONE=5
      DO 537 J=1,K
537      B(J)=BS(J)
      GO TO 700
540   GAMMA=0.
545   CALL BCHECK(B,IMAP,IBCK)
      GO TO (550,255) IBCK
550   GO TO (200,600) IBK1
C
C     ....................calculate PHI.....................
C
600   DO 555 JJ=1,M
555      PHD(JJ)=0.
      DO 560 J=1,N
         I=J
         CALL FCODE(F,X,IMAP,B,I)
         DO 560 JJ=1,M
560         PHD(JJ)=PHD(JJ)+WTS(I,JJ)*((Y(I,JJ)-F(JJ))**2.)
      PHI=0.
      DO 570 JJ=1,M
570      PHI=PHI+PHD(JJ)
      GO TO (215,245) IBK1
C
C     ....................exit LSQENP.....................
C
700   WRITE(2,840)
      WRITE(2,850) (B(J),J=1,K)
      WRITE(2,855) PHIZ,XL,GAMMA,XKDB
      IF(NTYPE.EQ.'Y') TYPE 840
      IF(NTYPE.EQ.'Y') TYPE 850, (B(J),J=1,K)
      IF(NTYPE.EQ.'Y') TYPE 855, PHIZ,XL,GAMMA,XKDB
710   GO TO (720,730,740,750,760) IDONE
720   WRITE(2,800)
      IF(NTYPE.EQ.'Y') TYPE 800
      GO TO 900
730   WRITE(2,805)
      IF(NTYPE.EQ.'Y') TYPE 805
      GO TO 900
740   WRITE(2,810)
      IF(NTYPE.EQ.'Y') TYPE 810
      GO TO 900
750   WRITE(2,815)
      IF(NTYPE.EQ.'Y') TYPE 815
      GO TO 900
760   WRITE(2,820)
      IF(NTYPE.EQ.'Y') TYPE 820
900   CALL CONLIM(N,K,IMAP,M,KK,IP,IB,SA,A,CHISQ)
800   FORMAT(' FORCE OFF')
805   FORMAT(' EPSILON TEST')
810   FORMAT(' CHISQR TEST')
815   FORMAT(' GAMMA EPSILON TEST')
```

```
820    FORMAT(' GAMMA LAMBDA TEST')
840    FORMAT(' FINAL VALUES:')
845    FORMAT(' ITERATION #:',I2)
850    FORMAT(1P6E12.4)
855    FORMAT(' CHISQR=',F12.3,' XL=',F11.8,' GAMMA=',F6.2,
      1' XKDB=',F11.8/)
       RETURN
       END
C
C      subroutine GJR-------------------------------------
C
C      GAUSS-JORDAN-RUTISHAUSER matrix inversion with double
C      pivoting.
C
       SUBROUTINE GJR(A,N,EPS,MSING)
       DIMENSION A(10,11),B(10),C(10),P(10),Q(10)
       INTEGER P,Q
       MSING=1
       DO 39 K=1,N
C      .........determination of the pivot element.........
       PIVOT=0.
       DO 13 I=K,N
       DO 13 J=K,N
       IF(ABS((A(I,J)))-ABS(PIVOT))13,13,10
   10  PIVOT=A(I,J)
       P(K)=I
       Q(K)=J
   13  CONTINUE
       IF(ABS(PIVOT)-EPS)56,56,15
C
C      ....exchange of the pivotal row with the Kth row.....
C
   15  IF(P(K)-K)16,21,16
   16  DO 20 J=1,N
       L=P(K)
       Z=A(L,J)
       A(L,J)=A(K,J)
   20  A(K,J)=Z
C
C      .exchange of the pivotal column with the Kth column..
C
   21  IF(Q(K)-K)22,27,22
   22  DO 26 I=1,N
       L=Q(K)
       Z=A(I,L)
       A(I,L)=A(I,K)
   26  A(I,K)=Z
   27  CONTINUE
```

```
C
C     .....................JORDAN step.....................
C
      DO 36 J=1,N
      IF(J-K)33,30,33
   30 B(J)=1./PIVOT
      C(J)=1.
      GO TO 35
   33 B(J)=-A(K,J)/PIVOT
      C(J)=A(J,K)
   35 A(K,J)=0.
   36 A(J,K)=0.
      DO 39 I=1,N
      DO 39 J=1,N
   39 A(I,J)=A(I,J)+C(I)*B(J)
C
C     .................reordering the matrix..............
C
      DO 54 M=1,N
      K=N-M+1
      IF(P(K)-K)43,48,43
   43 DO 47 I=1,N
      L=P(K)
      Z=A(I,L)
      A(I,L)=A(I,K)
   47 A(I,K)=Z
   48 IF(Q(K)-K)49,54,49
   49 DO 53 J=1,N
      L=Q(K)
      Z=A(L,J)
      A(L,J)=A(K,J)
   53 A(K,J)=Z
   54 CONTINUE
   55 RETURN
   56 WRITE (2,57) P(K),Q(K),PIVOT
   57 FORMAT(16H0SINGULAR MATRIX3H I=I3,3H J=I3,7H
PIVOT=E16.8/)
      MSING=1
      GO TO 55
      END
```

```
C
C     subroutine CONLIM-----------------------------------
C
      SUBROUTINE CONLIM(N,K,IMAP,M,KK,IP,IB,SA,A,CHISQ)
      DIMENSION A(10,11),SA(10),C(10,11),SC(10)
      DIMENSION IMAP(5,2),IC(10),IB(1),STDERR(10),CHISQ(2)
      COMMON /PARAM/XTEST,E,TAU,AL,GAMCR,ZETA
C
C     ..........construct matrix for each data set........
C
      DO 500 ICOL=1,M
      DO 185 I=1,K
         DO 185 J=1,K
185         C(I,J)=A(I,J)
      IQ=0
      DO 200 I=1,K
         DO 190 IROW=1,KK
190         IF(IMAP(IROW,ICOL).EQ.I) GO TO 200
            DO 195 J=1,K
               C(I,J)=0.
195            C(J,I)=0.
            C(I,I)=1.
            IQ=IQ+1
            IC(IQ)=I
200   CONTINUE
C
C     ......calculate the parameter correlation matrix.....
C
      CALL GJR(C,K,ZETA,MSING)
      IF(MSING.EQ.2) RETURN
      DO 205 I=1,K
         IF(C(I,I).LT.0.) RETURN
205      SC(I)=SQRT(C(I,I))
      DO 220 I=1,K
         DO 220 J=I,K
            WS=SC(I)*SC(J)
            IF(WS.GT.0.) GO TO 210
            C(I,J)=0.
            GO TO 220
210         C(I,J)=C(I,J)/WS
220         C(J,I)=C(I,J)
      DO 230 I=1,K
230      C(I,I)=1.
```

```
C
C     .................find the standard error.............
C
      SE=SQRT(CHISQ(ICOL)/(N-KK+IP))
      DO 235 I=1,K
235      STDERR(I)=SE*SC(I)/SA(I)
         IF(IQ.LE.0) GO TO 245
         DO 240 J=1,IQ
240         STDERR(IC(J))=0.
245      IF(IP.LE.0) GO TO 255
         DO 250 J=1,IP
250         STDERR(IB(J))=0.
255   CONTINUE
C
C     ....................write the results...............
C
      WRITE(2,840) ICOL
      WRITE(2,850) (STDERR(I),I=1,K)
      KST=-6
      WRITE (2,860) ICOL
260   KST=KST+7
      KEND=KST+6
      IF (KEND.GT.K) KEND=K
      DO 270 I=1,K
270      WRITE (2,870)I,((C(I,J)),J=KST,KEND)
      IF (KEND.LT.K) GO TO 260
500   CONTINUE
840   FORMAT(/' STANDARD ERROR ESTIMATE FOR DATA SET #:
',I2)
850   FORMAT(1P6E12.4)
860   FORMAT(/' PARAMETER CORRELATION MATRIX FOR DATA SET #:
',I2)
870   FORMAT (3X,I3,2X,7F8.3)
      RETURN
      END
```

APPENDIX B. GLOSSARY OF PARAMETERS FOR NONLINEAR LEAST SQUARES FITTING PROGRAM

The most commonly used variables for a program utilizing least-squares estimation of nonlinear parameters and a global analysis strategy are defined. All of these parameters can be found in NGSRR2.FOR (Appendix A). This list of variables is not exhaustive. References are made to Marquardt [45] and Bevington [32] throughout the glossary.

TABLE B.1 is a listing of the COMMON BLOCK names and the subroutines to which they pass information.

TABLE B.2 is a listing of the nonlinear least squares programs in use in our laboratory as of August 1987. The model used by each program is briefly described. The date on which the program was created is included.

Glossary

A — In MAIN: Real array of the preexponential factors for the isotropic decay P(t).

In LSQENP: Curvature matrix for the Taylor's series search for a minimum in χ^2.

AL — Initial value of the portion of gradient search used in LSQENP (corresponds to λ in Bevington or Marquardt).

AXL — A matrix modified to include the interpolation between the Taylor's series and gradient search of the Marquardt algorithm.

B — Real array containing the model function parameter values.

BASEMO Baseline average for the orthogonal emission datafile.

BASEMP Baseline average for the parallel emission datafile.

BASEXC Baseline average for the excitation datafile.

BFIL Alphanumeric array defined in a DATA statement of MAIN; used when a background file is not necessary.

BKO Real array containing the background correction data for the orthogonal emission datafile.

BKP Real array containing the background correction data for the parallel emission datafile.

BKOFIL Alphanumeric array containing the name of the orthogonal emission datafile.

BKPFIL Alphanumeric array containing the name of the parallel emission datafile.

BS In LSQENP: Temporary storage for the values in the array B.

BSAVE In MAIN: Same as BS.

CGAM Cosine GAMMA (Marquardt Eq. 23).

CHISQ In LSQENP: Real array whose elements contain the contributions of χ^2 from each model function.

CHISQ1 In MAIN: χ^2 contributions of parallel emission datafile.

CHISQ2 In MAIN: χ^2 contributions of orthogonal emission datafile.

DB Real array containing the step sizes for the parameter values in array B (corresponds to δ in Marquardt and δa in Bevington).

DECO Real array containing the values of the convolution of the excitation function and the model for I (t).

DECO0 DECO evaluated at t = 0.

DECP Real array containing the values of the convolution of the excitation function and the model for I (t).

DECP0	DECP evaluated at t = 0.
DELX	Time per channel used on the MCA (ps/channel).
DIG	Variable used to define CGAM (Marquardt Eq. 23).
DXSO	Real array containing an estimation of the derivative of the shifted excitation file used with the orthogonal emission datafile.
DXSP	Real array containing an estimation of the derivative of the shifted excitation file used with the parallel emission datafile.
E	Constant supplied to LSQENP by BLOCK DATA and used in the EPSILON TEST and GAMMA EPSILON TEST.
EMO	Real array containing the orthogonal emission datafile.
EMOFIL	Alphanumeric array containing the name of the orthogonal emission datafile.
EMP	Real array containing the name of the parallel emission datafile.
EMPFIL	Alphanumeric array containing the name of the parallel emission datafile.
EXCFIL	Alphanumeric array containing the name of the excitation datafile.
F	Single channel value of the convolution of the shifted excitation function with the model function supplied to MAIN and LSQENP by FCODE.
FOFIL	Alphanumeric array containing the name of the fitted file for the orthogonal emission datafile.
FPFIL	Alphanumeric array containing the name of the fitted file for the parallel emission datafile.
FSHIFT	The fractional portion of the shift to be applied to the excitation function.
G	Real array used to determine the parameter step size and direction (Marquardt Eqs. 9, 10).

GAMCR Constant criterion angle described by Marquardt representing a search direction approximately midway between the Taylor's series and gradient search directions (45°).

GAMMA The angle representing the proportion of Taylor's series and gradient search. GAMMA is a decreasing function of XL (λ in Marquardt or Bevington). GAMMA = 0° represents a search in the direction dictated only by the gradient method. GAMMA = 90° represents a search in the direction dictated only by the Taylor's series method.

GTG Variable used to define CGAM (Marquardt Eq 23).

IB Integer array which contains the array index from IMAP for each fixed parameter.

IBCK Error parameter from the subroutine BCHECK. IBCK = 1 unless BCHECK detects an inappropriate B value; then IBCK = 2.

IBK1 Directs the flow of control in LSQENP at different stages of the search (Fig. 4.2).

ICOL Indicates the column of a matrix which represents a particular model in a global analysis.

IDONE Values range from 1 to 5 and indicate the criteria for terminating a search (Table 4.1).

IFIX Integer array whose values indicate whether or not a parameter value should be adjusted (IFIX(J) = 0) or held constant (IFIX(J) = 1) during a search.

ILINK Integer array whose values indicate which parameters among the separate models used in a global analysis should have equal values (ILINK(J) = 1) and which parameters should be adjusted independently (ILINK(J) = 0); used to construct IMAP.

IMAP 2-dimensional integer array with one column corresponding to each model of a global analysis and a number of rows equal to the number of parameters in a model; the values of the matrix elements establish the correspondence between the parameters of the various models.

IOCHAN The channel number in the orthogonal emission datafile of the first value to exceed half of the peak channel value.

IPCHAN The channel number in the parallel emission datafile of the first value to exceed half of the peak channel value.

IP The number of total fixed parameters for all models in a global analysis; used to increment the index of the array IB.

IPS The number of fixed parameters per model in a global analysis; used to establish the number of degrees of freedom in the fitting procedure for each model.

IQUIT User input maximum number of iterations to be performed in the search procedure. If a value of zero is input the program generates a convolution of a user input excitation profile and the model function evaluated at the user input parameter values.

IROW Indicates the row of a matrix which represents a particular parameter of the fitting model.

ISHIFT The integer portion of the shift to be applied to the excitation function.

IWS In LSQENP: Used in conjunction with the array IB to indicate which parameters are fixed; used to construct the array G and the curvature matrix A.

IWS4 In LSQENP: IQUIT + 1.

IXCHAN The channel number of the peak value in the excitation datafile.

K Total number of independently adjustable parameters in a global analysis.

KK Number of parameters in a single model in a global analysis.

M Number of models used in a global analysis.

N Channel number of the last channel from the emission datafile to be included in the fitting range; N = NEMHI.

NBKO Alphanumeric variable equal to 'Y' or 'N' depending on whether or not a background correction datafile is used to correct the orthogonal emission datafile.

NBKP Alphanumeric variable equal to 'Y' or 'N' depending on whether or not a background correction datafile is used to correct the parallel emission datafile.

NEMLO Early time end of the fitting range for the emission datafile; channel number should be read directly from the datafile regardless of the TAC configuration.

NEMHI Long time end of the fitting range for the emission datafile; channel number should be read directly from the datafile regardless of the TAC configuration.

NEXLO Early time of the fitting range for the excitation datafile; channel number should be read directly from the datafile regardless of the TAC configuration.

NEXHI Long time of the fitting range for the excitation datafile; channel number should be read directly from the datafile regardless of the TAC configuration.

NEXPON Number of exponential terms in the fitting model.

NFIX Alphanumeric variable equal to 'Y' or 'N' depending on whether or not a particular parameter is fixed.

NFREE Number of degrees of freedom for the fitting procedure; used to calculate χ^2_r.

NHEMAV Late time end of the baseline range for the emission data file; channel number should be read directly from the datafile regardless of the TAC configuration.

NHEXAV Late time end of the baseline range for the excitation data file; channel number should be read directly from the datafile regardless of the TAC configuration.

NLEMAV Late time end of the baseline range for the emission data file; channel number should be read directly from the datafile regardless of the TAC configuration.

NLEXAV Early time end of the baseline range for the excitation data file; channel number should be read directly from the datafile regardless of the TAC configuration.

NMIN Channel number of the first nonzero value in the excitation datafile.

NMAX Channel number of the last nonzero value in the excitation datafile.

NOFIL Alphanumeric array containing the name of the background corrected orthogonal emission datafile.

NPFIL Alphanumeric array containing the name of the background corrected parallel emission datafile.

NSC Source number for menu drive input.

NTEMP Temporary storage variable used for the inversion of channel ranges when the TAC is operated in the inverted configuration.

NTYPE Alphanumeric variable equal to 'Y' or 'N' depending on whether or not terminal output is desired upon execution of the program.

OMAX Peak channel value of the orthogonal emission datafile.

OSCALE Initial estimate of the scaling parameter for the orthogonal emission datafile.

OUTFIL Alphanumeric array containing the name of the file listing search iteration data, search input parameters, and final optimized parameters.

P Teal array containing the single channel value of the convolution of the shifted excitation function with the partial derivative of the model function with respect to each model parameter; supplied to LSQENP by PCODE.

P***** Real virtual arrays containing the partial derivatives of the model function with respect to each model parameter; ***** represents the characters used to identify the individual partial derivatives.

P****0 P***** evaluated at t = 0.

PHD — Real array containing the values of χ^2 for the individual models of a global analysis.

PHI — Total χ^2 for a global analysis calculated after the model parameters have been adjusted in LSQENP.

PHIZ — Total χ^2 for a global analysis calculated at the beginning of an iteration before the model parameters have been adjusted in LSQENP.

PMAX — Peak channel value of the parallel emission datafile.

PSCALE — Initial estimate of the scaling parameter for the parallel emission datafile.

PT0 — Isotropic decay P(t) evaluated at t = 0.

REV — Alphanumeric variable equal to 'Y' or 'N' depending on whether or not the datafiles from the MCA need to be reversed. REV = Y if the TAC is used in the inverted configuration.

SA — Real array used to scale the curvature matrix A and the array G (Marquardt Eqs. 27 and 28).

SO — Shift parameter for the excitation datafile to be convoluted with the orthogonal emission datafile.

SP — Shift parameter for the excitation datafile to be convoluted with the parallel emission datafile.

STAT — Alphanumeric variable equal to 'Y' or 'N' depending on whether or not photon counting statistics are being used to determine WTS.

TAU — In MAIN: Real array containing the lifetimes in ps of the exponential terms of the isotropic decay P(t).

In LSQENP: Constant supplied to LSQENP by BLOCK DATA and used in the EPSILON TEST and GAMMA EPSILON TEST.

TBO — Collection time for the background correction file for the orthogonal emission file; for gated MCA data collection the datafile should be edited to reflect the true "live" collection time.

TBP — Collection time for the background correction file for the parallel emission file; for gated MCA data collection the datafile should be edited to reflect the true "live" collection time.

TF — Value of the fluorescence lifetimes in ps in the absence of trapping of self-absorption to be used in the function $G^s(t)$ of the fitting models for time-dependent polarized emission.

TMO — Collection time for the orthogonal emission datafile; for gated MCA data collection the datafile should be edited to reflect the true "live" collection time.

TMP — Collection time for the parallel emission datafile; for gated MCA data collection the datafile should be edited to reflect the true "live" collection time.

WS — Variable used to scale the curvature matrix A (Marquardt Eq. 27).

X — Real virtual array containing the excitation datafile.

XKDB — A multiplier ≤ 1 used to scale the parameter step sizes (corresponds to K in footnote 3 of Marquardt).

XL — Portion of gradient search used in LSQENP (corresponds to λ in Marquardt or Bevington).

XLL — Variable used to define CGAM (Marquardt Eq. 23).

XMAX — Peal channel value of the excitation datafile.

XSO — SO

XSP — SP

XSUM — Integrated area under the excitation function.

XTEST — Constant supplied to LSQENP by BLOCK DATA and used in the CHISQR TEST.

Y — Real virtual array containing the emission datafiles.

YFIT — Real virtual array containing the optimized fitted function.

TABLE B.1 COMMON BLOCK names in NGSRR2.FOR (Appendix A) and their associated subroutines

COMMON BLOCK	Subroutines
CONST	MAIN, DECOUT, FCODE, PCODE, SHIFT, CONVOL, VONVOL
DECAY	FCODE, PCODE
FILES	MAIN, DECOUT
RANGES	MAIN, DECOUT
PARAM	DATA, LSQENP, CONLIM
PASS	FCODE, PCODE,SHIFT
PTMA	MAIN, DECOUT, FCODE,PCODE
TERMS	MAIN, DECOUT, FCODE, PCODE, BCHECK

TABLE B.2 Programs in use as of August 1987

NLIN2.FOR ---------- January 21, 1986 ----------

This program fits photon counting data to any combination of exponential terms (0-4) and 2-dimensional Forster terms (0-1). Before convoluting with the instrument response function X(I), the analytic form of the decay function is integrated between channel I - 1/2, and I + 1/2 to generate a histogram of the decay function.

NGAUS.FOR ---------- October 7, 1986 ----------

This program fits photon counting data to up to four (1-4) Gaussian terms.

NGSPT3.FOR ---------- January 22, 1987 ----------

NGSPT3 uses the 3-dimensional 2-particle $G^S(t)$ model to fit the parallel and orthogonal polarization files. A multi-exponential (fixed) form for the isotropic decay P(t) must be provided. A histogram representation of the decay model is generated before convolution with the instrument response function. The angle between the absorption and emission dipoles may be optimized with this model.

NGSR3.FOR ---------- January 22, 1987 ----------

NGSR3 uses the 3-dimensional 2-particle $G^S(t)$ model to fit the parallel and orthogonal polarization files. A multi-exponential (fixed) form for the isotropic decay P(t) must be provided. Rotational diffusion is also taken into account. A histogram representation of the decay model is generated before convolution with the instrument response function.

NGSR2.FOR ---------- February 18, 1987 ----------

NGSR2 uses the 2-dimensional 2-particle $G^S(t)$ model to fit the parallel and orthogonal polarization files. A multi-exponential (fixed) form for the isotropic decay P(t) must be provided. Rotational diffusion is also taken into account. A histogram representation of the decay model is generated before convolution with the instrument response function.

TABLE B.2 (continued)

NGSRR2.FOR ---------- February 25, 1987 ----------

NGSRR2 uses the 2-dimensional 2-particle $G^S(t)$ model to fit the parallel and orthogonal polarization files. A multi-exponential (fixed) form for the isotropic decay P(t) must be provided. Restricted rotational diffusion is also taken into account. A histogram representation of the decay model is generated before convolution with the instrument response function.

NGSRR3.FOR ---------- February 27, 1987 ----------

NGSRR3 uses the 2-dimensional 2-particle $G^S(t)$ model to fit the parallel and orthogonal polarization files. A multi-exponential (fixed) form for the isotropic decay P(t) must be provided. Restricted Rotational diffusion is also taken into account. A histogram representation of the decay model is generated before convolution with the instrument response function.

This model assumes a random distribution of dipole orientations with the dipoles confined to 2-dimensions. Therefore the coefficients are +0.8 and -0.4 (as opposed to +0.5 and -0.5 when the dipoles are found to make an angle with respect to the surface normal).